BEILSTEIN JOURNAL OF NANOTECHNOLOGY

Noncontact atomic force microscopy III

Edited by Mehmet Z. Baykara and Udo D. Schwarz

Imprint

Beilstein Journal of Nanotechnology
www.bjnano.org
ISSN 2190-4286
Email: journals-support@beilstein-institut.de

The *Beilstein Journal of Nanotechnology* is published by the Beilstein-Institut zur Förderung der Chemischen Wissenschaften.

Beilstein-Institut zur Förderung der Chemischen Wissenschaften
Trakehner Straße 7–9
60487 Frankfurt am Main
Germany
www.beilstein-institut.de

BEILSTEIN JOURNAL OF NANOTECHNOLOGY

Noncontact atomic force microscopy III

Mehmet Z. Baykara*[1] and Udo D. Schwarz*[2]

Editorial

Open Access

Address:
[1]Department of Mechanical Engineering and UNAM-Institute of Materials Science and Nanotechnology, Bilkent University, Ankara 06800, Turkey and [2]Departments of Mechanical Engineering & Materials Science and Chemical & Environmental Engineering and Center for Research on Interface Structures and Phenomena (CRISP), Yale University, P.O. Box 208284, New Haven, CT 06520-8284, USA

Email:
Mehmet Z. Baykara* - mehmet.baykara@bilkent.edu.tr;
Udo D. Schwarz* - udo.schwarz@yale.edu

* Corresponding author

Keywords:
atomic force microscopy, scanning force microscopy

Beilstein J. Nanotechnol. **2016,** *7,* 946–947.
doi:10.3762/bjnano.7.86

Received: 30 May 2016
Accepted: 21 June 2016
Published: 30 June 2016

This article is part of the Thematic Series "Noncontact atomic force microscopy III".

Editor-in-Chief: T. Schimmel

Intense interest in nanoscale science and technology has been the main driving force behind a large number of outstanding discoveries in the last few decades. It may not be an overstatement to claim that the development of the various scanning probe methods in the 1980s was the main pre-requisite for the fields of nanoscience and nanotechnology to take off and ultimately evolve to their current states. While scanning tunneling microscopy (STM) relies on quantum mechanical tunneling of electrons to enable the atomic-resolution imaging of (semi-)conducting sample surfaces, it was the atomic force microscope (AFM) that eventually allowed for nanometer-scale imaging of sample surfaces with no limitations on electrical conductivity. As such, the method was widely adopted shortly after its introduction in 1986 and today it is not unusual to have multiple AFMs available at research universities and R&D departments of industrial companies.

Despite their widespread use, a major drawback of traditional AFM instruments is the fact that they rely on the establishment of light contact between a sharp probe and the sample surface of interest for topographical imaging. This results unavoidably in the formation of a finite contact area and the loss of atomic-scale resolution. The invention of noncontact atomic force microscopy (NC-AFM) in 1994 offered an elegant solution to this problem: Instead of touching the sample surface, the probe hovers a short distance above while the micro-machined cantilever that the probe is attached to is oscillated at its resonance frequency. The attractive interaction forces acting between the outermost atoms of the probe apex and the atoms on the surface then cause a downshift in oscillation frequency, which is employed as the feedback signal during lateral scanning. In this way, the probe apex remains atomically sharp and it becomes possible to attain atomic-scale resolution on a wide variety of sample surfaces.

The method of NC-AFM has evolved significantly since its introduction and it is now possible to employ the technique to visualize the internal structure of individual molecules, controllably manipulate single atoms on surfaces, and measure potential energy landscapes with unprecedented resolution. Moreover, NC-AFM is not only limited to operation under ultrahigh vacuum and it can now be utilized to study the detailed struc-

ture and even the dynamic activity of biological molecules. To keep up with the rapid progress in this exciting field, since 1998 the NC-AFM community meets every year at the annual "International Conference on Non-Contact Atomic Force Microscopy" series, which is typically characterized by lively discussions on the latest technical and scientific developments related to NC-AFM. In parallel with the series of conferences, the last few years have seen the publication of two installments in the Thematic Series titled "Noncontact Atomic Force Microscopy" in the *Beilstein Journal of Nanotechnology* [1,2]. This Thematic Series focusing on NC-AFM complements two other series titled "Advanced Atomic Force Microscopy Techniques" [3,4] and "Scanning Probe Microscopy and Related Methods" [5], making the *Beilstein Journal of Nanotechnology* a well-recognized outlet for scanning probe microscopy research.

The current and third installment in the "Noncontact Atomic Force Microscopy" Thematic Series again demonstrates the constant development in the field. In particular, latest instrumental advances are highlighted in the form of a new design for a large-area SPM used for electrostatic force measurements, improvement of dynamic cantilever response by the utilization of reflective coatings and photothermal conversion layers, and the use of length extension resonators for NC-AFM operation in air. In addition, the ever increasing importance of simulations for dynamic AFM experiments is underlined via two contributions focusing on three-dimensional viscoelastic modeling as well as "sub-atomic" contrast formation on the prototypical Si(111)-7×7 surface.

To conclude, we would like to sincerely thank the authors for submitting their exciting work to the latest installment in the Thematic Series, the reviewers for their careful analysis and appraisal of submitted work, and the great editorial team at the *Beilstein Journal of Nanotechnology*, which provides our community with a unique, Open Access platform for the dissemination of research results.

Mehmet Z. Baykara and Udo D. Schwarz

Ankara, New Haven, May 2016

References

1. Schwarz, U. D. *Beilstein J. Nanotechnol.* **2012,** *3,* 172–173. doi:10.3762/bjnano.3.17
2. Baykara, M. Z.; Schwarz, U. D. *Beilstein J. Nanotechnol.* **2014,** *5,* 289–290. doi:10.3762/bjnano.5.31
3. Glatzel, T.; Hölscher, H.; Schimmel, T.; Baykara, M. Z.; Schwarz, U. D.; Garcia, R. *Beilstein J. Nanotechnol.* **2012,** *3,* 893–894. doi:10.3762/bjnano.3.99
4. Glatzel, T.; Garcia, R.; Schimmel, T. *Beilstein J. Nanotechnol.* **2014,** *5,* 2326–2327. doi:10.3762/bjnano.5.241
5. Meyer, E. *Beilstein J. Nanotechnol.* **2010,** *1,* 155–157. doi:10.3762/bjnano.1.18

License and Terms

BEILSTEIN JOURNAL OF NANOTECHNOLOGY

Boosting the local anodic oxidation of silicon through carbon nanofiber atomic force microscopy probes

Gemma Rius*[1], Matteo Lorenzoni[2], Soichiro Matsui[1], Masaki Tanemura[1] and Francesc Perez-Murano[2]

Full Research Paper

Open Access

Address:
[1]Nagoya Institute of Technology, NITech, Gokiso, Showa, 466-8555 Nagoya, Japan and [2]Institut de Microelectronica de Barcelona, IMB-CNM-CSIC, Campus UAB 08193 Bellaterra, Spain

Email:
Gemma Rius* - rius.gemma@nitech.ac.jp

* Corresponding author

Keywords:
carbon nanofiber; dynamic mode; local anodic oxidation; nanopatterning

Beilstein J. Nanotechnol. **2015,** *6,* 215–222.
doi:10.3762/bjnano.6.20

Received: 28 September 2014
Accepted: 14 December 2014
Published: 19 January 2015

This article is part of the Thematic Series "Advanced atomic force microscopy techniques III".

Guest Editor: U. D. Schwarz

Abstract

Many nanofabrication methods based on scanning probe microscopy have been developed during the last decades. Local anodic oxidation (LAO) is one of such methods: Upon application of an electric field between tip and surface under ambient conditions, oxide patterning with nanometer-scale resolution can be performed with good control of dimensions and placement. LAO through the non-contact mode of atomic force microscopy (AFM) has proven to yield a better resolution and tip preservation than the contact mode and it can be effectively performed in the dynamic mode of AFM. The tip plays a crucial role for the LAO-AFM, because it regulates the minimum feature size and the electric field. For instance, the feasibility of carbon nanotube (CNT)-functionalized tips showed great promise for LAO-AFM, yet, the fabrication of CNT tips presents difficulties. Here, we explore the use of a carbon nanofiber (CNF) as the tip apex of AFM probes for the application of LAO on silicon substrates in the AFM amplitude modulation dynamic mode of operation. We show the good performance of CNF-AFM probes in terms of resolution and reproducibility, as well as demonstration that the CNF apex provides enhanced conditions in terms of field-induced, chemical process efficiency.

Introduction

Scanning probe lithography (SPL) is increasing its relevance among currently employed methods towards miniaturization and investigations at the nanometer scale. Interest of developing SPL-based nanofabrication methods relies on its extraordinary performance in terms of resolution and flexibility, as well as its potential for applications, e.g., in materials/surface science, quantum devices and nanoelectronics [1]. Moreover, SPL has the additional capability of in situ inspection, which provides additional control over the fabrication process including pattern placement [2].

SPL can be performed in a wide variety of instrument configurations and operation modes, such as in scanning tunneling microscopy (STM) or atomic force microscope (AFM). Based on the latter, AFM, it excels in versatility, as its working principle allows AFM to be applied conveniently onto any surface and in a variety of atmospheres [2-4]. Nonetheless, SPL based on AFM can rely on a number of tip–surface interactions (chemical, electrical, thermal, etc.), including tip–sample direct mechanical contact or long range interactions, such as based on van der Waals or electrostatic forces. Because of this, AFM-based SPL can be achieved through oxidation, indentation, as well as various other implementations such as dip-pen nanolithography [5]. Early works on AFM-based SPL logically concerned silicon, as it is the ubiquitous material of modern electronics [6,7]. The application of an electric field between a conductive tip and a silicon substrate under ambient conditions can generate the local anodic oxidation (LAO) of the silicon surface very precisely; intrinsic silicon oxide (SiO_x) patterns are in the single/double-digit nanometer-range [8].

The principle of LAO-AFM is the following: A water meniscus is formed in humid air when the tip comes to close proximity to the surface due to capillary condensation. The formation of the water meniscus can be triggered in non-contact mode by the application of a certain bias voltage between the tip and sample. The water meniscus bridges electrical conduction and provides the anions to enable the chemical reaction. Conditions for oxidation require that hydroxy anions are driven towards the substrate, i.e., the sample should be positively biased [9]. Typical anodic currents are of the order of nanoamperes [10] and their efficiency depends on various conditions, which concern the tip, (e.g., conductance and shape) the tip–sample interplay, (e.g., distance and wetting), and other factors such as sample surface texture or wetting. All those parameters also affect the actual resolution of the LAO-AFM features and process reliability.

The understanding of the conditions for LAO-AFM as well as of the resolution capabilities have been addressed from several viewpoints. Particularly, non-contact LAO-AFM has proven to yield a better resolution and tip preservation than the contact mode [11,12]. The improvement of the water meniscus comes from the control of the water meniscus dimensions, which depends on several parameters, including tip–sample distance, humidity and electrical field. Remarkably, LAO-AFM can be performed in dynamic mode AFM, so it is fully compatible with the standard imaging conditions [7].

One direction for further optimization of LAO-AFM is tip engineering. Tip shape and sharpness plays a crucial role for the LAO-AFM as a main regulator of minimum feature size and electric field [13]. Reversely, when the tip morphologically and chemically degrades during its use, the conditions and the results of LAO-AFM are dramatically affected or even lost. It has been proposed, as one possibility to overcome this issue, the use of carbon nanotube (CNT)-functionalized tips [14,15]. With excellent electronic conduction, mechanical and chemical properties, intrinsic very high aspect ratios and tiny tip radii, CNTs looked very promising for LAO-AFM application. Indeed, both single and multi-walled CNTs showed remarkable patterning capabilities [16]. However, this approach has been nearly abandoned, due to the high cost and poor control upon making CNT probes, as well as characteristic tip-to-tip differences, such as length, diameter, and operational complications, such as CNT buckling [15,16].

In this work, we explore the use of a carbon nanofiber (CNF) as the tip apex of AFM probes for the application of LAO-AFM on silicon substrates in amplitude modulation dynamic mode of operation. In spite of the morphological and chemical resemblance, CNFs and CNTs exhibit fundamental structural differences. Both CNF and CNT are high aspect ratio morphologies (one-dimensional) made primarily of atomic carbon. However, a CNF consists of solid amorphous carbon, while a CNT is a tubular crystalline nanomaterial, therefore we expect both common and distinctive features of CNF as a tool for LAO-AFM, as compared to CNT probes. To the best of our knowledge, we report for the first time the use of CNF for SPL. Our CNFs are batch grown by ion-irradiation upon commercial AFM silicon probes [17,18]. We do not only show the good performance of CNF-AFM probes for LAO-AFM in terms of resolution and reproducibility, but our experimental results demonstrate that CNF apex provides enhanced conditions in terms of field-induced chemical process efficiency.

Experimental

CNFs are grown on arrays of commercially available AFM cantilevers, non-blade tetragonal-type Si tips made by Olympus (force constant, $k = 40\ N{\cdot}m^{-1}$), coated with a thin carbon layer; on typically 3–9 chips per batch [17]. The synthesis is performed in a Kaufman-type ion gun, whose beam diameter is 3 cm, at nearly room temperature. The basal and working pressures are 1.5×10^{-5} Pa and 2×10^{-2} Pa, respectively. The ion beam energy is 600 eV, and the growth duration is 8 min. CNF elliptical cross section is smaller than 50 nm in diameter, and it is systematically and conveniently aligned with respect to the conical probe as seen in Figure 1. A set of 8 CNFs, which had comparable morphological characteristics have been used for the experiments presented below. The irradiation with Ar^+ ions is the main factor to induce CNF growth, as described in detail elsewhere [18]. The arrangement of ion-sputtered atomic carbon in the apex of the silicon tip as a CNF results from the re-depo-

sition of ejected carbon atoms, which have diffused along the surface of the Si conical tip. As-grown CNF morphology is characterized by FE-SEM (Hitachi S-4700 operated at 20 keV) and checked (occasionally) at different stages of the LAO-AFM tests (Zeiss, LEO 1530 operated at 3 keV). For comparison purposes, commercially available non-coated doped Si AFM probes from Nanosensors, OTESPA (force constant, k = 40 N·m^{-1}), are employed.

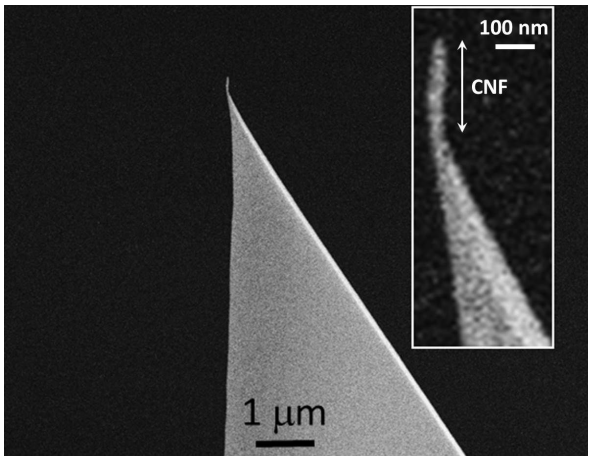

Figure 1: SEM image of a typical example of an as-deposited CNF onto the tip apex of the Si AFM probe.

LAO-AFM and AFM imaging are performed in the amplitude modulation dynamic mode while using relatively stiff cantilevers as specified above. The routines and conditions to perform LAO-AFM in the dynamic mode have been described in [1,19]. In brief, a target location onto the Si substrate is inspected for surface cleanliness. Then, the cantilever free oscillation is set to a low amplitude value (<20 nm), to ensure a close tip–surface distance and the set point amplitude is routinely set to 80% of the free amplitude for imaging when the feedback is active. Under these conditions, attractive forces dominate and, in consequence, it can be inferred that the AFM is operated in non-contact mode. In current experiments we focus on the definition of line patterns. Prior to patterning, the AFM control feedback is disabled and the required voltage is applied. However, in order to keep a constant tip–surface distance, previously the surface inclination with respect to the X–Y piezo-scanning plane is captured and subtracted. All tests are performed at room conditions, with a temperature of 25 °C and under a controlled relative humidity ranging from 20 to 40%. The Si substrates consist of chips cut from Si(100) wafers. Organic contamination on the chips was removed by oxygen plasma etching before the measurements. The native oxide has not been removed.

Results

Kinetics of CNF-LAO-AFM

Figure 2 shows the results of line patterning at several scan rates for both the CNF probe (Figure 2a) and the Si probe (Figure 2b). Eight different writing speeds have been tested, ranging from 0.5 μm/s to 4 μm/s with increments of 0.5 μm/s. The common bias voltage is 20 V. An apparent correlation of line height and width with the writing speed is observed; the slower the scan rate the higher and wider the patterned line. This phenomenon is expected as a result of longer reaction times [20], and clearly applies for both the CNF and the bare Si probe. For this writing speed series, line height ranges are, respectively, 0.7–2 nm and 0.2–1.2 nm for the CNF and Si probe. The lines show a very good uniformity.

A similar comparison test of a CNF probe and a Si probe is performed to evaluate the dependence of LAO-AFM line patterns upon the applied bias voltage. The results are shown in Figure 3. Six different bias voltages have been tested, ranging from 14 V to 24 V with increments of 2 V. Common writing speed is 1 μm/s. Again, an apparent correlation of line height and width with bias voltage is obtained; the higher the bias voltage the higher and wider the line pattern. This phenomenon is understood as an indication of the role of the electric field in the kinetics the oxidation [20], which, similar to the results in Figure 2, it is found for both the CNF (Figure 3a) and the bare silicon probe (Figure 3b). For this series of bias voltages, the obtained line height ranges are, respectively, 1.3–4.2 nm and 0.1–1 nm for the CNF and the Si probe.

The definition of line features is good, although some morphological features arise. On the one hand, for Si probe line patterns done at 14 V and 16 V are nearly not quantifiable; their line height and width are in the limits of AFM resolution and Si surface roughness. On the other side, for CNF-patterned lines, an unexpected widening of the line features is especially characteristic of the 22 V and 24 V tests. The analysis of the line profile suggests that the resulting line is a convolution of the typical sharp line features, as obtained, e.g., when using 14 V, with a more delocalized lateral chemical reaction. This aspect would suggest additional mechanisms in addition to the induced main anodic reaction induced by the electric field, such as an ionic diffusive regime of oxidation, which has already been observed [9,21].

Chemical–mechanical robustness of CNF-AFM probes

The chemical and mechanical robustness of CNF has been preliminarily tested. As an example, we monitored the eventual change of the CNF morphology and orientation upon LAO-AFM, as shown in Figure 4. In the left panel (Figure 4a), a SEM

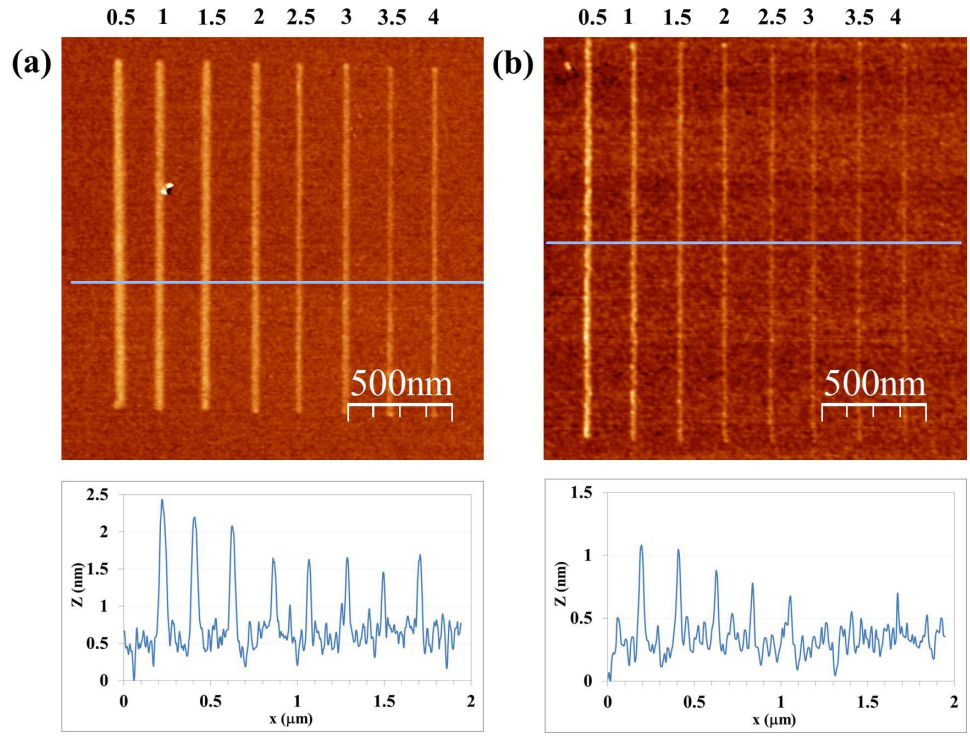

Figure 2: Results of LAO-AFM on Si with CNF (a) and Si (b) probes as a function of the writing speed (µm/s). Bias voltage is 20 V, relative humidity (RH) is 36%.

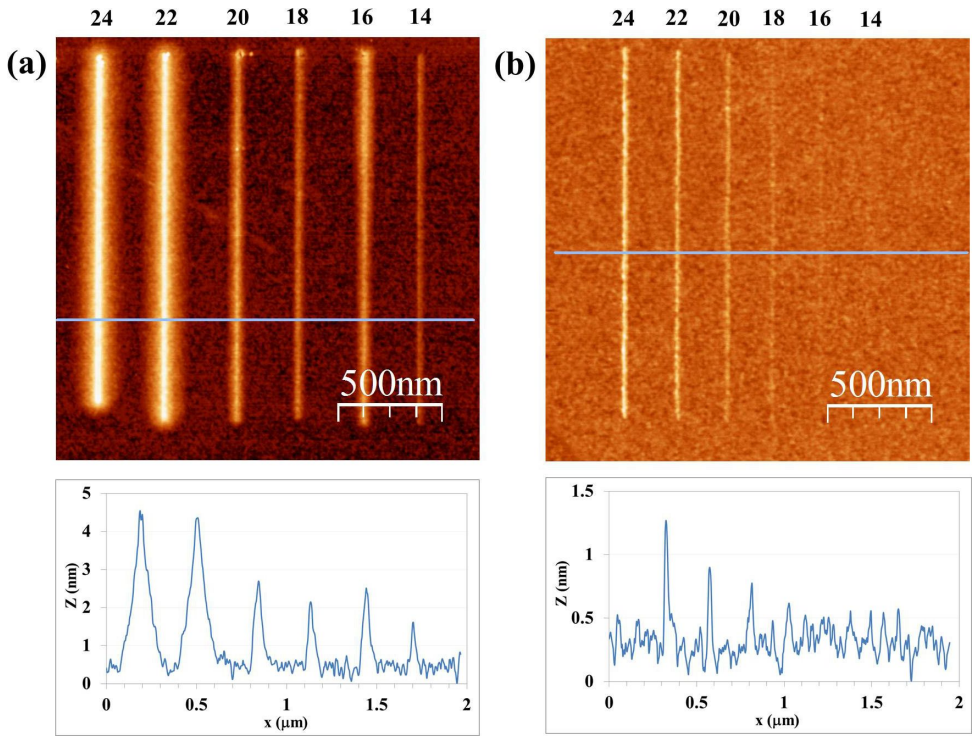

Figure 3: Results of LAO-AFM on Si with CNF (a) and Si (b) probes as a function of the bias voltage (in V). Writing speed is 1 µm/s, RH is 36%.

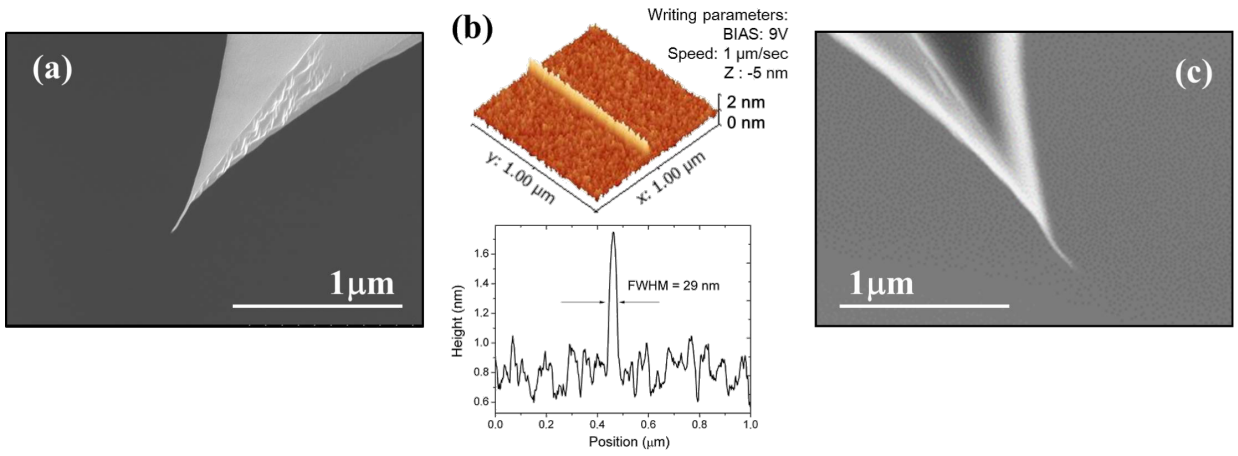

Figure 4: Monitoring chemical and mechanical stability of CNF probes for LAO-AFM. SEM images before (a) and after (c) the definition of 1 μm long line feature, written at 9 V and a writing speed of 1 μm/s (b). The FWHM of the line is about 29 nm.

image of the CNF-AFM probe before the line patterning by LAO-AFM depicted in Figure 4b is shown. It is compared against a SEM image of CNF-AFM probe after LAO-AFM in the right panel (Figure 4c). Morphological changes of the CNF could not be noticed by SEM inspection. Images using a larger magnification have not been performed in order to avoid contamination and eventual electron-beam-induced damage on the CNFs. These simple characterization results support the suitability of using CNF for LAO-AFM in the dynamic mode of operation. It should be noted that this occurs in spite of the relative weakness of the mechanical clamping of the CNF onto the Si apex. The bending elasticity of the CNF-Si probe upon mechanical contact above a few nanonewtons can be compromised to permanent bending (buckling), particularly for longer CNFs, or rupture [22]. Nevertheless, CNF-probes can be ordinarily used for dynamic mode imaging.

Reliability of CNF-LAO-AFM

In Figure 5 we demonstrate another aspect concerning the reliability of CNF probes for LAO-AFM. The images depict two arrays of relatively dense lines defined at two different voltages and at a writing speed of 4 μm/s. Figure 5a corresponds to ten lines defined at 23.4 V, and Figure 5b displays fifteen lines written at 43.2 V. Both voltages were sustained by the CNF and the reproducibility of the line patterning is worth mentioning, because the line variations are well within the intrinsic tolerance of LAO-AFM on Si. Limitations of CNF for pattern density, as well as, for example, chemical inertness upon even stronger electric field should be further investigated by means of dedicated experiments.

Imaging and oxidation is performed in dynamic mode, i.e., under avoidance of tip–surface contact. This is a key aspect of present paper. As far as the tips did not make contact with the surface (either by particle contamination or the surface or problems with feedback loop control) we did not observe tip wear.

Discussion

In Figure 6 the main results of the kinetics study of LAO-AFM are summarized. Figure 6a shows the line height of SiO_x as a function of the writing speed, patterned at a bias voltage of 20 V. The height was determined by averaging ten scan lines. As mentioned above, the oxide growth rate depends inversely upon the writing speed, for both kinds of probes. However, the oxide growth rate by using a CNF probe is significantly higher than that of the bare-Si probe. The proposed exponential decay fit for the experimental data is shown in Figure 6a. The growth rate, expressed here as the oxide height at a certain writing speed, is almost double for the CNF probe.

The linear dependence of oxide line height upon voltage is shown in Figure 6b. Even if there is a higher dispersion for the CNF probes data that could undermine the proposed linear fitting, the linearity of voltage dependence during the LAO process is strongly supported by the literature for Si tips [3,19,23-25]. What limits the thickness of grown SiO_x is not only the decrease of the strength of the electric field as the SiO_x becomes thicker, but also other self-limiting mechanism which decrease the permeability of the hydroxy anions at a given electric field, such as charge build-up in the oxide [21]. Furthermore, one concern when the bias voltage is increased to speed up the oxidation process is the integrity of the tip. Metal-coated probes, as well as Si probes, experience material deposition/sputtering and breakdown voltage at higher bias voltages, like 50 V. We plan to challenge CNF probes in

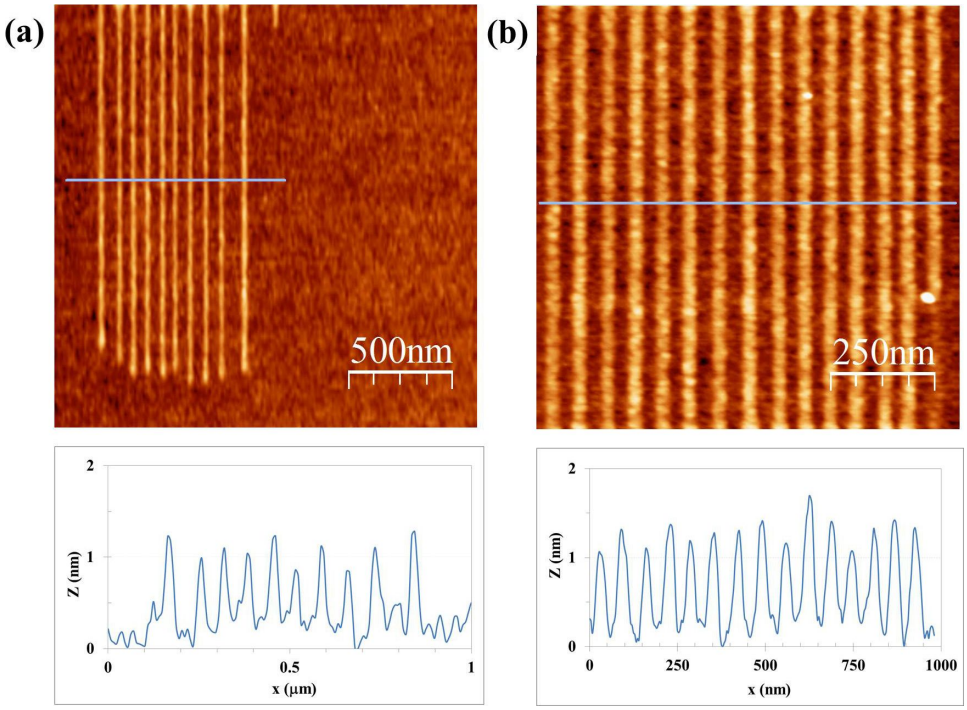

Figure 5: Reproducibility for patterning line arrays by using CNF probes. Array of lines written at a) 23.4 V and b) 43.2 V, having line height of ca. 0.8 nm and ca. 1.2 nm, respectively. The common writing speed is 4 μm/s, RH is 30%.

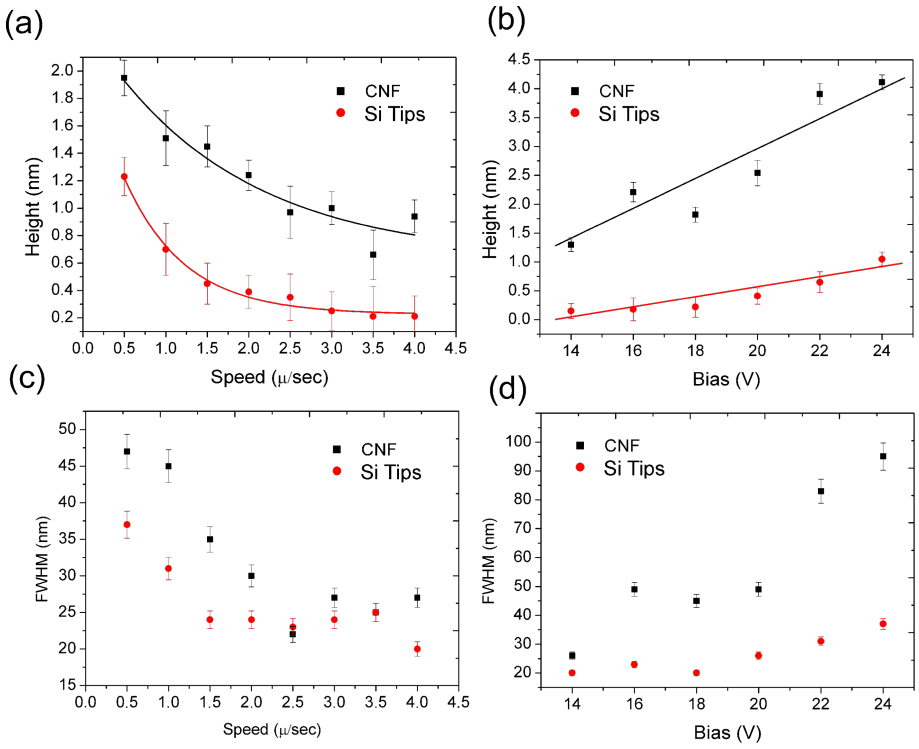

Figure 6: Kinetics of LAO-AFM on Si by using CNF versus Si probes. a) Line height upon writing speed for a bias voltage of 20 V. b) Line height upon bias voltage for a writing speed of 1 μm/s. Full width at half maximum (FWHM) of the same features upon writing speed (c) and upon bias voltage (d).

future experiments. In any case, it is evident that the oxidation rate is enhanced when using CNF probes for a given bias voltage. In Figure 6c and Figure 6d we report full width at half maximum (FWHM) values of the same line features mentioned above. Concerning the exposure time (speed) no great change has been observed when comparing CNF against Si tips. However, in the tested voltage range we could observe a strong widening of the features when the voltage exceeds 14 V. This is probably due to a different wettability of the CNF tips which results in a wider water neck when the voltage exceeds a certain critical value.

Additional features arise from the comparison between CNF probe and Si probe performance for LAO-AFM results. We have observed that high resolution (sub 20 nm line width) patterns are much easily obtainable by using CNF probes. As the water meniscus mediates the oxidation reaction kinetics, we hypothesize that the chemical properties of the CNF benefit the generation of a narrower water meniscus, while at the same time maintaining a higher oxidation rate. In this sense, the limited electrical conduction of CNF is not a restrictive point, and the interplay between chemical and electrical properties of the tip material combines to better regulate the oxidation process. Clearly correlated behaviors have been investigated and confirmed for CNT-based LAO-AFM [26,27].

Conclusion

CNF-AFM probes have been tested for the first time as a tool for nanopatterning based on LAO-AFM in the amplitude modulation dynamic mode. CNF-AFM probes provide suitable electrical, mechanical and chemical properties as required under the experimental conditions of LAO-AFM. We have found experimental evidence that CNF-functionalized Si-probes outperform bare-Si probes for LAO-AFM on a Si surface. Remarkably, CNF-based LAO-AFM shows an increased oxide growth rate, compared to bare-Si probes which we attribute to the shape and chemistry of the CNF tip. Particularly, concentration of the electric field due to the high aspect ratio provided by the CNF apex and changes in wettability, affecting water meniscus shape, with respect to bare Si tip apex are the two mechanisms that would explain the boost in efficiency of CNF for LAO-AFM on silicon. The combination of an increased oxidation rate and an improvement in patterning resolution provided by the geometry of the CNF makes CNF-AFM probes very promising for further developments of LAO-AFM. Future works will fundamentally address the unlocking of CNF-based LAO-AFM variables.

Acknowledgements

Financial support from the Generalitat de Catalunya (SGR) and project number CSIC10-4E-805.

References

1. Garcia, R.; Knoll, A. W.; Riedo, E. *Nat. Nanotechnol.* **2014,** *9,* 577–587. doi:10.1038/nnano.2014.157
2. Martín, C.; Rius, G.; Borrisé, X.; Pérez-Murano, F. *Nanotechnology* **2005,** *16,* 1016. doi:10.1088/0957-4484/16/8/003
3. Lorenzoni, M.; Torre, B. *Appl. Phys. Lett.* **2013,** *103,* 163109. doi:10.1063/1.4825265
4. Garcia, R.; Losilla, N. S.; Martínez, J.; Martínez, R. V.; Palomares, F. J.; Huttel, Y.; Calvaresi, M.; Zerbetto, F. *Appl. Phys. Lett.* **2010,** *96,* 143110. doi:10.1063/1.3374885
5. Salaita, K.; Wang, Y.; Mirkin, C. A. *Nat. Nanotechnol.* **2007,** *2,* 145–155. doi:10.1038/nnano.2007.39
6. Campbell, P. M.; Snow, E. S.; McMarr, P. J. *Appl. Phys. Lett.* **1995,** *66,* 1388. doi:10.1063/1.113210
7. Pérez-Murano, F.; Abadal, G.; Barniol, N.; Aymerich, X.; Servat, J.; Gorostiza, P.; Sanz, F. *J. Appl. Phys.* **1995,** *78,* 6797–6800. doi:10.1063/1.360505
8. Martinez, J.; Martínez, R. V.; Garcia, R. *Nano Lett.* **2008,** *8,* 3636–3639. doi:10.1021/nl801599k
9. Pérez-Murano, F.; Birkelund, K.; Morimoto, K.; Dagata, J. A. *Appl. Phys. Lett.* **1999,** *75,* 199. doi:10.1063/1.124318
10. Kuramochi, H.; Pérez-Murano, F.; Dagata, J. A.; Yokoyama, H. *Nanotechnology* **2004,** *15,* 297–302. doi:10.1088/0957-4484/15/3/012
11. Calleja, M.; Anguita, J.; Garcia, R.; Birkelund, K.; Pérez-Murano, F.; Dagata, J. A. *Nanotechnology* **1999,** *10,* 34–38. doi:10.1088/0957-4484/10/1/008
12. Martínez, R.; Losilla, N.; Martinez, J.; Huttel, Y.; Garcia, R. *Nano Lett.* **2007,** *7,* 1846–1850. doi:10.1021/nl070328r
13. Gómez-Moñivas, S.; Sáenz, J. J.; Calleja, M.; García, R. *Phys. Rev. Lett.* **2003,** *91,* 56101. doi:10.1103/PhysRevLett.91.056101
14. Dai, H.; Hafner, J. H.; Rinzler, A. G.; Colbert, D. T.; Smalley, R. E. *Nature* **1996,** *384,* 147–150. doi:10.1038/384147a0
15. Dai, H. *Surf. Sci.* **2002,** *500,* 218–241. doi:10.1016/S0039-6028(01)01558-8
16. Hongjie, D.; Franklin, N.; Han, J. *Appl. Phys. Lett.* **1998,** *73,* 1508. doi:10.1063/1.122188
17. Tanemura, M.; Kitazawa, M.; Tanaka, J.; Okita, Y.; Ohta, R.; Miao, L.; Tanemura, S. *Jpn. J. Appl. Phys.* **2006,** *45,* 2004. doi:10.1143/JJAP.45.2004
18. Tanemura, M.; Okita, T.; Tanaka, J.; Kitazawa, M.; Itoh, K.; Miao, L.; Tanemura, S.; Lau, S. P.; Yang, H.; Huang, L. *IEEE Trans. Nanotechnol.* **2006,** *5,* 587–594. doi:10.1109/TNANO.2006.880428
19. García, R.; Calleja, M.; Pérez-Murano, F. *Appl. Phys. Lett.* **1998,** *72,* 2295. doi:10.1063/1.121340
20. Calleja, M.; García, R. *Appl. Phys. Lett.* **2000,** *76,* 3427–3429. doi:10.1063/1.126856
21. Dagata, J. A.; Perez-Murano, F.; Abadal, G.; Morimoto, K.; Inoue, T.; Itoh, J.; Yokoyama, H. *Appl. Phys. Lett.* **2000,** *76,* 2710–2712. doi:10.1063/1.126451
22. Inaba, K.; Saida, K.; Ghosh, P.; Matsubara, K.; Subramanian, M.; Hayashi, A.; Hayashi, Y.; Tanemura, M.; Kitazawa, M.; Ohta, R. *Carbon* **2011,** *49,* 4191–4196. doi:10.1016/j.carbon.2011.05.051
23. Garcia, R.; Martinez, R. V.; Martinez, J. *Chem. Soc. Rev.* **2006,** *35,* 29. doi:10.1039/b501599p
24. Kuramochi, H.; Ando, K.; Shikakura, Y.; Yasutake, M.; Tokizaki, T.; Yokoyama, H. *Nanotechnology* **2004,** *15,* 1126. doi:10.1088/0957-4484/15/9/004
25. Snow, E. S.; Jernigan, G. G.; Campbell, P. M. *Appl. Phys. Lett.* **2000,** *76,* 1782–1784. doi:10.1063/1.126166

26. Kuramochi, H.; Tokizaki, T.; Yokoyama, H.; Dagata, J. A. *Nanotechnology* **2007,** *18,* 135703. doi:10.1088/0957-4484/18/13/135703
27. Kuramochi, H.; Tokizaki, T.; Ando, K.; Yokoyama, H.; Dagata, J. A. *Nanotechnology* **2007,** *18,* 135704. doi:10.1088/0957-4484/18/13/135704

License and Terms

BEILSTEIN JOURNAL OF NANOTECHNOLOGY

A scanning probe microscope for magnetoresistive cantilevers utilizing a nested scanner design for large-area scans

Tobias Meier*[1], Alexander Förste[2], Ali Tavassolizadeh[3], Karsten Rott[4], Dirk Meyners[3], Roland Gröger[2], Günter Reiss[4], Eckhard Quandt[3], Thomas Schimmel[2,5] and Hendrik Hölscher[1]

Full Research Paper

Open Access

Address:
[1]Institute of Microstructure Technology, Karlsruhe Institute of Technology (KIT), Hermann-von-Helmholtz-Platz 1, 76344 Eggenstein-Leopoldshafen, Germany, [2]Institute of Nanotechnology, Karlsruhe Institute of Technology (KIT), Hermann-von-Helmholtz-Platz 1, 76344 Eggenstein-Leopoldshafen, Germany, [3]Institute for Materials Science, Christian-Albrechts-Universität zu Kiel, Kaiserstraße 2, 24143 Kiel, Germany, [4]Department of Physics, Bielefeld University, Universitätsstraße 25, 33615 Bielefeld, Germany and [5]Institute of Applied Physics, Karlsruhe Institute of Technology (KIT), Wolfgang-Gaede-Straße 1, 76131 Karlsruhe, Germany

Email:
Tobias Meier* - meier_tobias@gwu.edu

* Corresponding author

Keywords:
atomic force microscopy (AFM); magnetomechanical effects; magnetostriction; scanning probe microscopes and components

Beilstein J. Nanotechnol. **2015,** *6,* 451–461.
doi:10.3762/bjnano.6.46

Received: 10 October 2014
Accepted: 06 January 2015
Published: 13 February 2015

This article is part of the Thematic Series "Advanced atomic force microscopy techniques III".

Guest Editor: U. D. Schwarz

Abstract

We describe an atomic force microscope (AFM) for the characterization of self-sensing tunneling magnetoresistive (TMR) cantilevers. Furthermore, we achieve a large scan-range with a nested scanner design of two independent piezo scanners: a small high resolution scanner with a scan range of 5 × 5 × 5 μm^3 is mounted on a large-area scanner with a scan range of 800 × 800 × 35 μm^3. In order to characterize TMR sensors on AFM cantilevers as deflection sensors, the AFM is equipped with a laser beam deflection setup to measure the deflection of the cantilevers independently. The instrument is based on a commercial AFM controller and capable to perform large-area scanning directly without stitching of images. Images obtained on different samples such as calibration standard, optical grating, EPROM chip, self-assembled monolayers and atomic step-edges of gold demonstrate the high stability of the nested scanner design and the performance of self-sensing TMR cantilevers.

Introduction

Since its invention in the 1980s [1] the atomic force microscope (AFM) became a versatile tool frequently used in nanoscale metrology, biosensing, maskless lithography and high density data storage with nearly as many sensing techniques as applications [2-5]. Current state of the art instruments use micro-fabricated silicon and silicon-nitride cantilevers with an optical read-out [6] and image with high resolution down to the atomic scale. Furthermore, AFMs are often incorporated into quality control systems for the fabrication of micro- and nanostructures, especially for industrial applications. For these applications, not only a high resolution, but also a large scan range (field of view) and a compact instrument design of the read-out is desirable [7].

However, most AFMs feature only a limited scan range of typically tens of micrometers. Unfortunately, it is not possible to expand the scan range by simply scaling the instrument dimensions because of the limitations of piezo actuated scan stages commonly used in AFMs. While piezo scanner stages have huge advantages in terms of dynamic properties and smoothness of motion in comparison with motorized stages, their maximum extension remains limited to hundreds of micrometers by using mechanical levers for motion amplification. Additionally, a large scan range and a high lateral resolution are contradictory. Because of these challenges, previous attempts to realize a high resolution and a large field of view use multiple scanning tips recording individual images and a stitching thereof [8] or a combination of motorized large scan range stages with a fast piezo to compensate for the poor dynamics of such stages [9]. In this work, we applied a different approach and nested a small high resolution scanner on a large piezo scan stage enabling both, a large scan range of $800 \times 800 \times 35\ \mu m^3$ and a high resolution capable of imaging subnanometer features.

The instrument is equipped, like most state-of-the-art instruments for ambient conditions, with an optical read-out of a micro-fabricated cantilever [10,11]. However, the optical read-out contains bulky mechanical parts to focus a laser on the backside of the cantilever and to move the position sensitive photodetector (PSD) or a mirror which puts severe limits on a compact instrument design. Additionally, while adjusting the laser and photodetector is straightforward under ambient conditions under which all components are accessible, it is a challenge in environments such as vacuum or in fluids where the laser light gets scattered and refracted by multiple interfaces [12-15]. Furthermore, optical read-outs have to be readjusted not only after every cantilever exchange but also after temperature drifts which can offset the focal position of the laser and photo-detector due to thermal expansion. Additionally, the optical read-out can influence the cantilevers deflection by photothermal excitation [16] and interfere with the sample as it can cause photobleaching of fluorescence samples [17]. For specific applications and environments like vacuum, self-sensing tuning forks with manually attached tips can greatly simplify instrumentation but at the cost of reduced operation modes [18-20]. Micro-machined cantilevers on the other hand are more versatile and can be mass-produced [21]. Additionally, cantilevers produced by silicon-based microfabrication methods allow for the integration of multiple additional features such as doping for better electrical conductance or the integration of active sensing elements. Previous works incorporated piezoelectric layers [22,23], piezo-resistive layers [24-29] into such cantilevers or added a capacitive readout [30,31] to measure the cantilevers deflection, however, they suffer from a reduced sensitivity compared to the optical read-out. Magnetic sensors [32-34], especially strain sensors based on tunneling magnetoresistive (TMR) junctions [35] had recently shown an enhanced sensitivity compared to piezoresistive sensors [36-40] and are promising candidates for strain sensors incorporated into AFM cantilevers. The instrument presented here has been optimized for the characterization of such self-sensing TMR cantilevers. The microscope is fabricated entirely from non-magnetic materials in order to minimize the instruments influence on magnetic fields which at present are needed to bias the TMR sensors and set their sensitivity at maximum for imaging atomic step edges.

Setup of a nonmagnetic large scan range AFM

In order to characterize magnetoresistive strain sensors integrated into AFM cantilevers, the deflection of the cantilever has to be measured in parallel by independent means. Therefore, our AFM is equipped with an optical beam deflection setup to measure the deflection of the cantilever [10,11]. This setup also allows for the use of conventional silicon and silicon nitrite cantilevers using only the optical beam deflection setup for the feedback. Additionally, the instrument is designed to apply an external in-plane magnetic bias fields, as the strain sensitivity of TMR sensors used in this work strongly depends on their magnetic configuration. This constrained requires a setup in which coils can be integrated for the application of a bias field. The magnetic field has to be homogeneous and should not interact with the materials used to build the instrument.

The optical beam deflection setup has been integrated into an optical microscope that is used to focus the laser spot on the cantilever. By using a long working distance objective, the beam deflection setup is placed outside the coils for the external magnetic bias field. The optical setup is shown in detail in

Figure 1. The use of an infinity-corrected microscope objective and an ocular lens allows one to illuminate the sample and to focus the laser beam on the cantilever with the same objective. Using the microscope objective to focus the laser also simplifies the adjustment of the laser beam deflection setup because the complete optical microscope can be moved instead of adjusting the laser. As a result, the focal spot of the laser is fixed towards the field of view of the optical microscope and the laser is aligned to the cantilever when the cantilever is at a specific position in the optical image. To block scattered light inside the optical path of the laser from the camera, a red mirror is used to couple the laser beam into the objective. As the mirror reflects only light with wavelengths longer than 600 nm, all light from the laser is either reflected towards the objective or the laser itself. The cantilever is tilted towards the optical axis of the microscope and acts as a mirror for the laser beam. As the cantilever gets deflected, the angle of the cantilever tilts towards the incident laser beam and consequently the reflection angle changes. As the reflected beam is divergent (due to the focusing of the microscope objective), it is refocused by using a lens and reflected to the position sensitive photo-detector by a tilting mirror.

To illuminate the sample, a wavelength shorter than the reflection edge of the red mirror was chosen. To suppress stray light within the optical path of the microscope, it is useful to use polarizing optics. In contrast to the laser, the light from the illumination source reaches the sample, is then reflected off the sample, and the reflected light must pass through the complete microscope to reach the camera. By using polarized light for illumination, a polarizing beamsplitter can be used to reflect all light from the light source of the illumination towards the sample. By passing a λ/4 plate, the polarization direction gets rotated by 45°. After being reflected on the sample, the light passes the λ/4 plate again and the polarization is rotated again by 45°. The polarization of the reflected light is now rotated by 90° towards the incident light from the light source. Therefore, the beamsplitter is completely transparent for light reflected from the sample, which can pass towards the camera.

The AFM is operated through a commercial AFM controller (Asylum Research). The controller can directly drive open-loop piezo scanners, because of its integrated high-voltage amplifier, as well as closed-loop scanners with an attached high voltage amplifier and closed-loop controller, as it is also equipped with

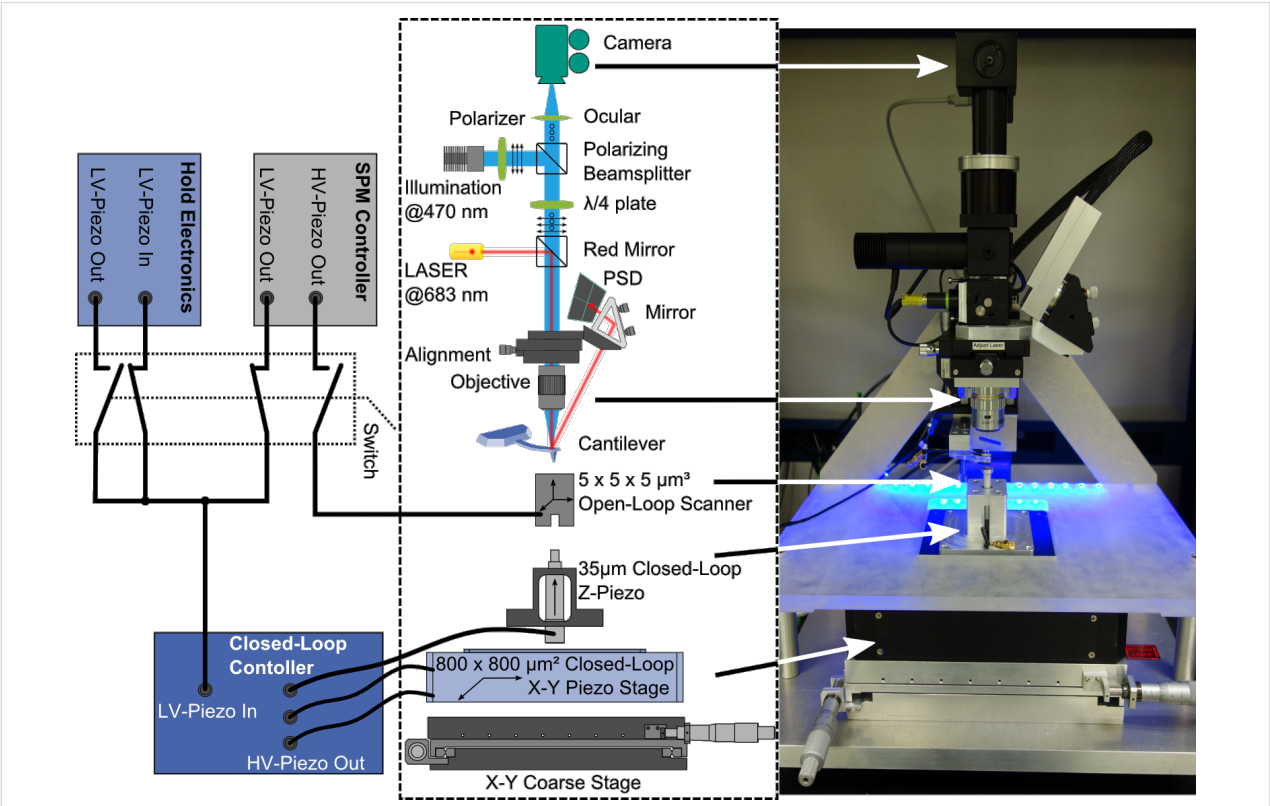

Figure 1: Schematic and photo of the setup including the optical beam deflection and the nested scanner design. The long-working-distance objective of the reflected light microscope is used to focus the laser on the rear side of the cantilever while the reflected beam is focused and reflected on a PSD with a tilting mirror for alignment. To realize both high lateral resolution and large-area scanning, a high resolution open loop scanner is nested on a large-area scanner. For switching between both scanners, the large-area scanner can be held on any position by feeding a constant control voltage to the closed loop controller while small-area scans are performed by the open loop scanner.

a low-voltage piezo-drive output. To drive two scanners independently, external control electronics are attached to the controller, which allow for a switching between the high- and low-voltage output. Additionally, this electronics allows one to hold the low-voltage output at any level when switching from the low-voltage output to the high-voltage output and vice versa. As our AFM setup is equipped with two independent scanners to combine both, a large field of view and a high spatial resolution, these hold electronics allow to drive the small-area scanner directly while holding the large-area scanner at a fixed position. The high resolution open-loop scanner is thereby mounted on a large-area scan stage. The high resolution scanner was realized by using a stack of shear actors for x–y scanning and a stack piezo actor with a travel of 5 µm and a resonance frequency of 50 kHz each. The large-area scanner on the other hand is a combination of an x–y piezo large-travel scan stage and a preloaded piezo stack actor for the z-axis. The large travel is achieved by piezos with a comparable small travel pushing a lever to enhance the stage travel, a principle that is typically called lever motion amplifier. For a large-area scanner, lever motion amplification is a suitable way to reach large travels due to certain constraints, although a lever-motion-amplified piezo stage commonly shows a higher noise level than a directly driven stage. The elongation of a piezo is approximately $\Delta L = \pm E \cdot d \cdot L_0$, where E is the applied electric field, d the piezoelectric coefficient of the material and L_0 the initial length of the piezo with typical values for piezo stack actuators of $U = \pm 220$ V, $d = 350$ pm/V and a distance between two electrodes of 1 mm. To achieve a travel of 800 µm by direct drive, approximately 1 m of piezo ceramic per axis would be required. Such large piezo stacks, however, are neither commercially available nor mechanically stable enough for such a large-area scan stage. However, this design has a reduced mechanical stiffness and resonance frequency.

The reduced resonance frequency increases the response time of the scanner to driving signals. Therefore, lever amplification can only be used for the slow lateral scanning as the z-axis of the scanner needs a high resonance frequency for a fast response to driving signals. The large-area scanner has a motion-amplified x–y piezo stage and a dedicated z-piezo for a short response time. Additionally, the x–y stage must only move in the x–y plane without any cross-talk to the z-axis. This is reached by flexure joints. However, as the stiffness of a lever amplified system is reduced quite significantly, the initial stiffness of the flexure stage has to be quite high. A custom-built scanning stage fulfilling those requirements was therefore developed specifically for this application. Because of the stiff flexure joints, each axis of the stage is equipped with two piezos in parallel movement to increase their pushing force. The piezo elongations and the stage position are each monitored with a capacitive positioning sensor which allows for a linearization of the stage movement by an additional stage controller. The z-piezo of the large-area scanner is a piezo stack with a maximum travel of 35µm and a resonance frequency of 14 kHz while carrying the open-loop scanner. For closed-loop operation of the AFM, this piezo is equipped with a strain gauge sensor which is read out by the AFM controller.

Results and Discussion

Characterization of the microscope

For successful switching from the large scanner to the nested scanner, the stability of the large-area scanner has to be high. The positioning accuracy can be tested during AFM scanning. If scanned with the open-loop scanner, also the stability and drift of the large-area scanner is of interest. In Figure 2a, a scan of polymeric microlenses is shown when using the optical beam deflection setup for the feedback. In parallel, the positioning error (profile after removing the 1st order component) of the fast scan axis was recorded and is shown in Figure 2c. By comparing the measured stage position and the desired position (given by the control signal), the positioning error was extracted. The data shows no drift of the stage during the whole experiment and only small fluctuations around the desired position of ±10 nm, which is a low value for a scan stage that has a maximum travel distance of 800 µm.

As the large-area scanner is mechanically stable, it can be used to carry a second small-area scanner with a higher spatial resolution and better dynamic properties. Using an AFM with multiple scanners allows for both, a large field of view and a high spatial resolution. By using the optical beam deflection setup as well, the potential of such an instrument is demonstrated in Figure 3. By scanning a calibration structure with feature details spanning from hundreds of micrometers to less then 200 nm and a feature height of 22 nm, the topography of the sample can be investigated on all length scales. For a first overview of the sample, the maximum scan size can be used (Figure 3b). Afterwards, sequential zooms into the region of interest are possible (Figure 3c–e). As the desired zoom level results in a scan size below the maximum scan range of the high resolution scanner, the scan position can be held with the large-area scanner while the sample is scanned with the small-area scanner enabling further zoom steps (Figure 3f). Thereby, the instrument can span over three orders of magnitude in scan range, which makes it a helpful tool for micro- and nanomechanical analysis.

One example of such an analysis is given in Figure 4a. For quality control of fabrication steps in microstructure technology, AFMs are often used for spot checks of the fabricated structures. However, as most AFMs are limited to a field of

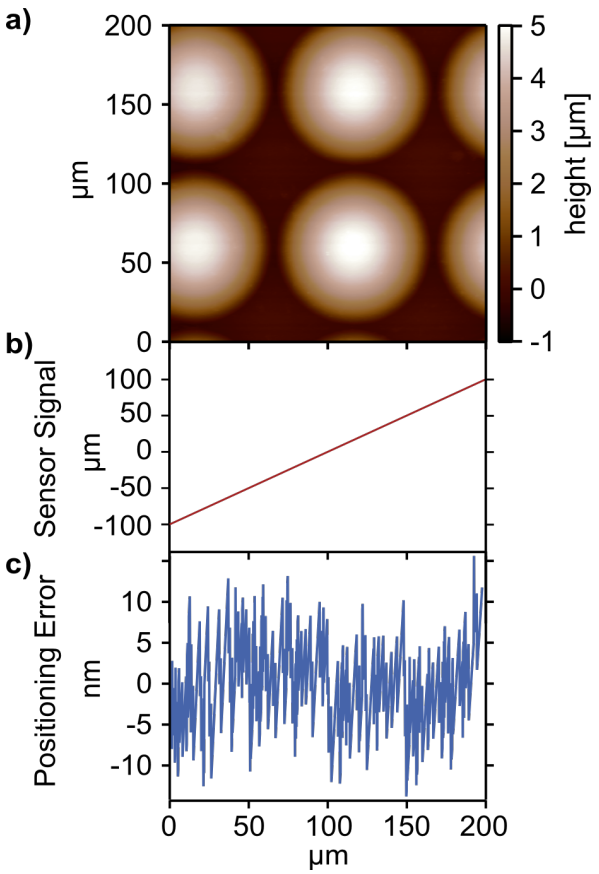

Figure 2: A crucial precondition for a nested high resolution scanner design is the stability of the housing large-area scanner. The position accuracy and positioning error can be tested by reading out the sensing elements for the closed-loop system. a) While scanning the topography of microlenses, b) the read-out of the closed loop sensor in the fast scan direction is recorded. c) The read-out of the fast scan axis is compared with the desired scan position and a positioning error is extracted. The positioning error is below 10 nm for typical scan frequencies. The sensor is read-out with a sampling rate of 1.5 kHz.

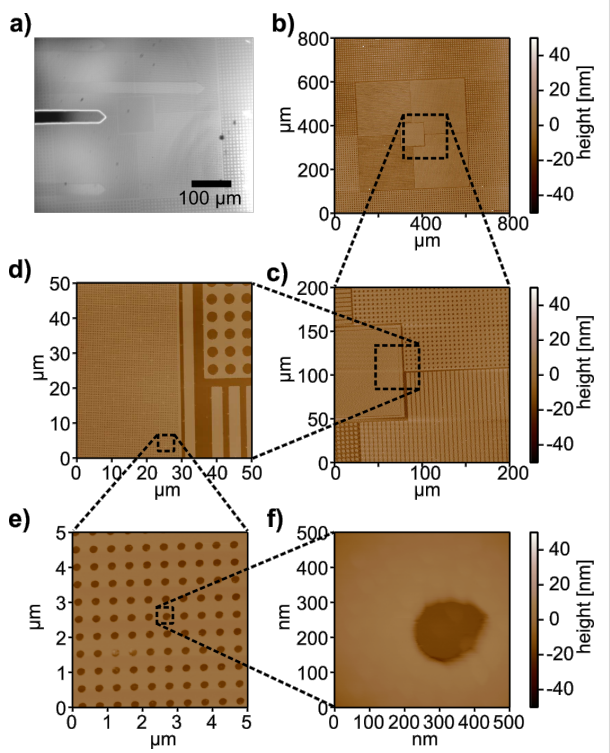

Figure 3: a) Optical microscopy image of a SiO_x calibration grating with various feature sizes. Demonstration of large-area AFM imaging with switching to the small-area scanner for high resolution. b) First, an 800 × 800 µm^2 overview image of the structure was taken. c) Afterwards, the scansize was reduced to 200 × 200 µm^2. d) The scansize was further reduced to 50 × 50 µm^2 before switching to the high resolution scanner. e) After switching, 5 × 5 µm^2 and f) 500 × 500 nm^2 images of the smallest feature sizes of the calibration grating were taken. The nested scanner design which can span over three orders of magnitude in scan range makes this instrument a versatile tool for micro- and nanomechanical analysis.

view of 100 × 100 µm^2, they are only suitable for local imaging. Often, features of structural details will just not fit into this field of view. Optical phase gratings are an example for this type of samples [41]. Imaging such structures with the large-area scanner allows one to image multiple grating periods of 256 × 256 µm^2 in a single AFM picture and to overlay them with the optical microscope image obtained during scanning. Such diffractive structures define the length of the optical path of the light propagating through by their topography. At least one grating period has to be imaged in order to characterize such grating structures which requires a large scan range. An other challenge are high steps in micro- and nanostructures. However, in many cases, the simultaneous investigation of small features such as transistors (on the nanometer or submicrometer scale) and much larger features such as chip architectures (on the millimeter scale) have to be imaged. An example of such structures are microelectronic integrated circuits. Imaging such structures with a special large-area scanning AFM allows for inspection of a wide field of the chip architecture within one scan. Figure 4b shows a portion of the die surface of a UV-erasable CMOS EPROM memory chip (Type 27C256). The image size is 500 × 500 µm^2 imaged with a resolution of 1024 × 1024 pixels. Imaging was done in the intermittent contact mode of the AFM with a setpoint of 89% of the free amplitude of the cantilever. Due to the large step heights of up to 2 µm on the surface of the chip, and the corresponding high demands on the z-feedback loop the scan speed was set to 30 µm/s. The image shows the original raw data, exhibiting no artefacts or defects and despite the relatively soft tapping and large step heights, no loss of contact to the surface occurred over the whole scan area. All elements on the chip are clearly discernible. Due to the hardware-linearized scan and the very low thermal drift of the setup, no further image processing was necessary. The choice of color table allows for a clear

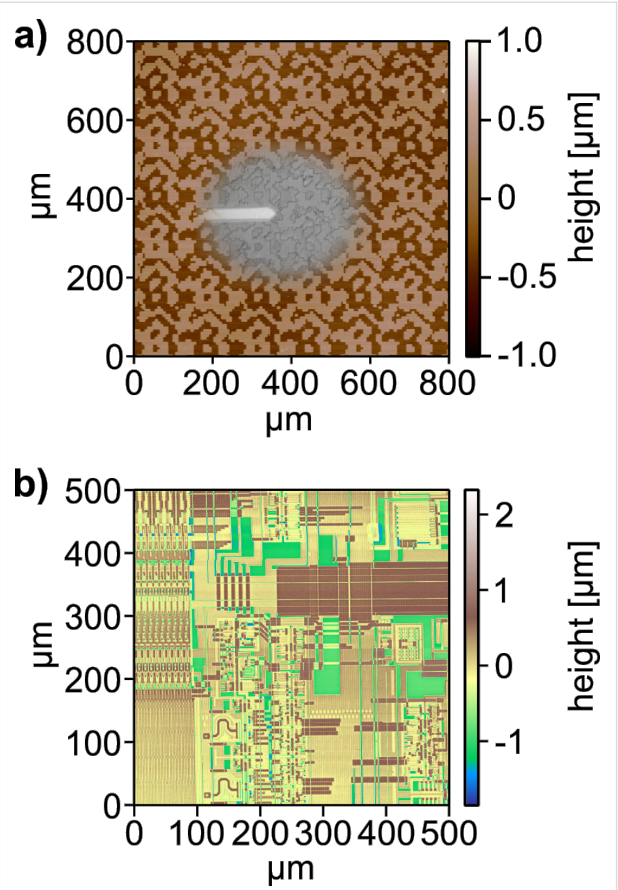

Figure 4: a) Overlay of the optical microscope image with the AFM topography of an optical grating structure with a 256 × 256 µm^2 grating periodicity. b) Large-area AFM topography image of a part of a UV-erasable CMOS EPROM memory chip with a scan size of 500 × 500 µm^2. Despite the large step heights of 2 µm, there no artefacts are visible, no loss of contact happened and the features of the chip architecture are clearly visible. The heights of the different layers are constant over the whole scan area which allows for reliable absolute topography measurements in combination with a fast overview using the optical microscope.

distinction of the different layers of which the circuit is comprised. This shows that also the height scale measured by the AFM is constant over the whole large scan area, a key requirement for reliable quantitative large scale AFM measurements.

Magnetoresistive strain sensors

Driven by the increasing demand for magnetic hard disk drives [42], magnetic tunneling junctions (MTJ) [43-50] are state-of-the-art read-heads in magnetic hard drives. Additionally, they can be adapted for high strain sensitivity [51] and offer remarkable miniaturization opportunities [52]. In combination with already implemented processes of mass production, they are a promising alternative to piezoresistive and piezoelectric sensors for self-sensing AFM cantilevers [23]. Therefore, we used such magnetic tunneling junctions with magnetostrictive electrodes deposited and patterned on Si substrates as strain sensor on AFM cantilevers. The Si substrates were structured into AFM cantilevers by means of microelectromechanical systems (MEMS) technology [35]. The magnetic tunneling junction consists of two ferromagnetic CoFeB-electrodes separated by a thin dielectric MgO layer, which acts like a spin-valve. The electrical conductance of the magnetic tunnel junction, therefore, strongly depends on the orientation of the magnetization of the electrodes towards each other. When magnetostrictive materials are used in the electrodes [53], the magnetization of one electrode can rotate if strained because of the inverse magnetostrictive effect [54]. To use this effect for strain sensing, only the magnetization of one electrode must rotate when strain is applied to the junction while the magnetization of the other electrode should remain in its initial orientation. Therefore, the MTJ has to be integrated into a TMR stack, which includes contact electrodes and a pinning mechanism to fix the magnetization of one reference electrode while the second sense electrode is free to rotate. To fix the magnetization of the reference layer, it is magnetically pinned by a 0.9 nm thick Ru layer to a CoFe layer by an antiferromagnetic interlayer coupling. The exchange bias between a natural antiferromagnet (IrMn) and the CoFe then fixes the magnetization of the reference layer. Then, the resistance of the tunneling junction varies by rotating the magnetization of the free sensing layer. Using the inverse magnetostrictive effect in the sensing layer makes the TMR stack sensitive to applied strain.

We used a CoFeB (3 nm)/MgO (1.8 nm)/CoFeB (3 nm) TMR junction with an MnIr (12 nm)/CoFe (3 nm) exchange bias system that was annealed at about 360 °C for 1 h at a pressure of 10^{-6} mbar under a magnetic field of 2 kOe for a crystallization of the CoFeB electrodes and improvement of CoFeB/MgO interfaces. It also aligns the easy axis of the sensing layer and pins the reference layer due to the imposed magnetic exchange bias [55]. The TMR stack is grown by sputtering techniques on a 4" Si(100) wafer substrate with 300 ± 2 µm thickness (Si-Mat Silicon Materials, Germany) with thermally grown 2 µm-thick and 100 nm-thick SiO_2 layers on the rear and front side, respectively. The TMR sensor AFM cantilevers are prepared by a sequence of MEMS techniques including photolithography, reactive ion etching (RIE), ion beam etching (IBE) and wet etching. The cantilevers used in this study were 300 to 350 µm long and 40 µm wide. To ease the fabrication process thicknesses ranging from 10 µm to 20 µm were chosen. The resulting resonance frequencies of the cantilevers vary from 170 kHz to 270 kHz and their spring constants from 40 N/m to 440 N/m.

Measurements with TMR sensors

As shown in Figure 5 the detection principle of a magnetostrictive TMR sensor can be easily applied to measure the bending

of an AFM cantilever. In particular, TMR sensors with a CoFeB/MgO/CoFeB magnetic tunnel junction are well known for their very high TMR values [56]. In addition, the use of a $Co_{40}Fe_{40}B_{20}$ sensing layer leads to high strain sensitivity [57]. Those measurements, however, are done with a 4-point bending apparatus and a magnetic bias field of 60 Oe perpendicular to the magnetization of the pinned reference layer and with tensile stress applied to the junction. On the cantilever level, not only tensile but also compressive stress occurs. The alignment of the initial easy axis of the sensing layer is, therefore, set to 45° against the applied stress. In this way the TMR sensor is sensitive to both compressive and tensile stress what is required for essentially all modes of AFM. Assuming single domain behavior of the two ferromagnetic layers, the conductance of the TMR junction is depending on the angle α between the magnetizations of the two electrodes [58].

To achieve a high resistance change of the TMR junction and a high strain sensitivity, only the sensing layer must be rotated with respect to the reference layer. This can be achieved with the magnetic bias field. The field must be strong enough to rotate the magnetization of the sensing layer but also weak enough to enable strain-induced rotation. We investigated the angular dependence for a magnetic bias field of 60 Oe. The angle α is thereby defined as the angle between the easy axis and the bias field and varies between 0 and 180°. The angle of the bias field was varied in 5° steps while the TMR sensor was saturated along the easy axis between each angle variation. As the setup of our AFM allows for both the measurement of the cantilever deflection by independent means and the response of the TMR sensor as a function of the angle of the magnetic bias field the field can be varied until the optimum is found. The resistance of the 27 µm × 27 µm sized TMR sensor with a resistance area product of 61 kΩ·µm^2 increases and decreases under the applied tensile and compressive stress, respectively, induced by the oscillation of the cantilever at its resonance frequency (see Figure 5b and Figure 5c). To measure the resistance of the TMR sensor, it is integrated into a Wheatstone bridge configuration with a 20 mV bias voltage. We maintained the voltage drop on the TMR sensor in the unstrained configuration at 10 mV and kept the bridge balanced. The voltage between the midpoints was amplified by 60 dB and low-pass filtered with a cut-off frequency of 400 kHz. This readout was directly fed into a 100 MHz analog–digital converter for recording and comparison with the optical beam deflection readout which is used to measure the deflection of the cantilever. With the deflection, the strain at the base of the cantilever can be approximated by using Hooke's law and the Young's modulus of the cantilever beam. In Figure 5c, the sensor response for four chosen field angles is given. The strain sensitivity (slope of the sensor response) varies quite significantly with the incident angle of the magnetic field. The sensor also shows a higher sensitivity for tensile strain (steeper slope for positive values of ε in Figure 5, which can be used in pre-strained junctions or to distinguish between compressive and tensile stress for spectroscopy applications.

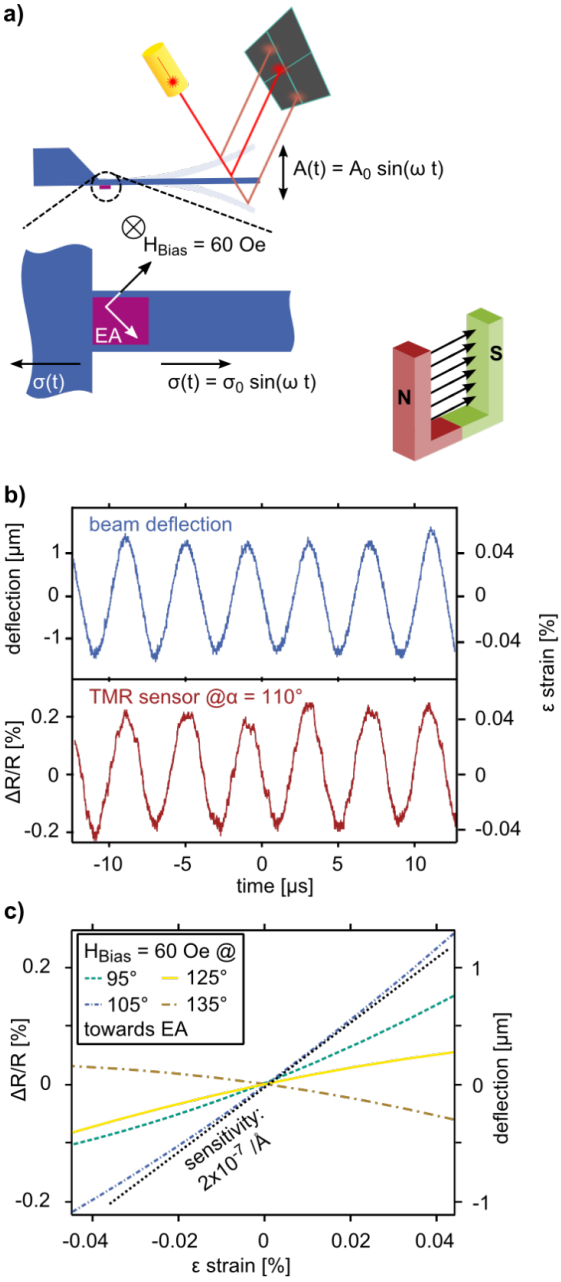

Figure 5: Characterization of AFM cantilevers equipped with strain sensitive TMR sensors. a) The cantilevers deflection can be measured with the beam deflection setup while the strain sensitivity of the TMR sensor can be tuned with a magnetic bias field. b) The oscillation of the cantilever is measured by the beam deflection setup and the strain in the cantilever by the TMR sensor. In this notation, tensile stress corresponds to positive strain. The resistance change of the 27 µm × 27 µm sized TMR sensor can be correlated to the applied strain. c) The resistance change as a function of strain is exemplary plotted for four different angles of the bias field towards the easy axis. The bias field has a strong influence on the strain sensitivity of the TMR sensor.

The TMR junction with a squared geometry used in this work shows the highest strain sensitivity of 2×10^{-7} Å, at a bias field angle α of 115° towards the magnetization of the reference layer. For this measurement, we can extract a signal-to-noise ratio of 900 at a bandwidth of 100 kHz which allows one to measure the oscillation of the cantilever on its resonance. For symmetry reasons, the behavior of the TMR sensor can be assumed to have the same sensitivity for negative values of α, however, the signal from the TMR sensor is inverted with respect to the signal for positive values of α.

To investigate the strain sensitivity and the feedback mechanism when using TMR sensors on AFM cantilevers, we fabricated tipless cantilevers and obtained a suitable resolution on gratings [35]. To increase the lateral resolution, however, sharp tips have to be attached to our cantilevers with TMR sensors. By using a combination of focused ion beam and electron beam deposition, tips can be manually been grown on the apex of the cantilever [59]. The use of such tips enables high lateral resolution as tip radii as small as 30 nm can be achieved. The advantage of this approach is that the tip is subsequently grown and without altering the fabrication process of our TMR cantilevers.

As AFM setups with beam deflection can routinely image smallest features such as atomic step edges, the ability to reveal such features is mandatory to be competitive. Figure 6 demonstrates that atomic-scale resolution can be also obtained with a TMR sensor. The image of atomic step edges on gold(111) was obtained in the amplitude modulation mode in which the cantilever oscillation was detected with the TMR sensor. The applied bias field was chosen for maximum strain sensitivity for the unstrained sensor at 60 Oe and α = 115°. With those parameters, atomic step edges of 2.54 Å height are resolved.

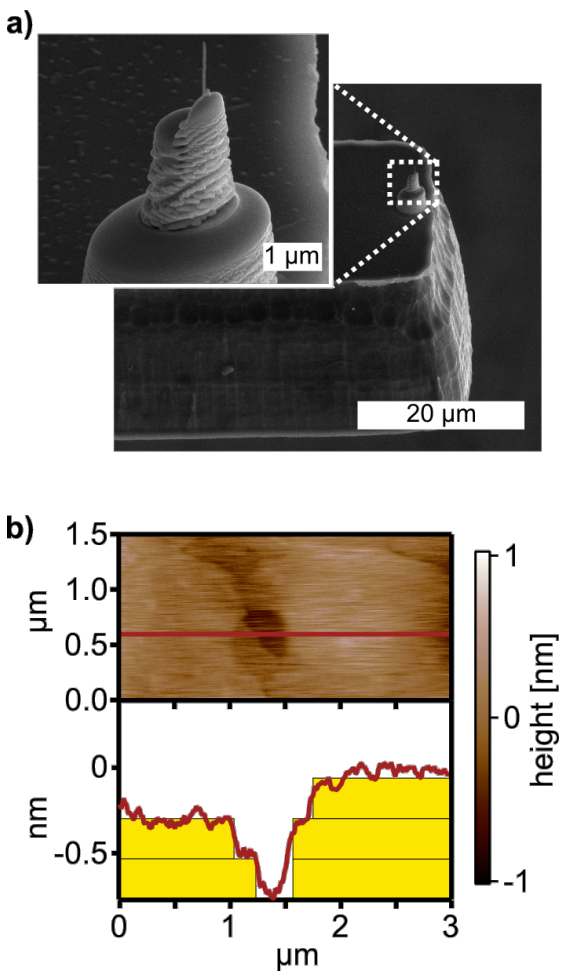

Figure 6: a) To improve lateral resolution, tips with a tip radius of 30 nm were grown by a combination of focused ion beam and electron beam deposition deposition. b) Atomic step-edges on gold(111) terraces can be revealed by amplitude modulation imaging with the feedback on the TMR sensor.

For dynamic-mode experiments, the phase-shift signal is of high interest as it provides information about energy dissipation between tip and sample [60,61] and visualizes chemical contrasts [62]. To demonstrate this kind of measurement also with our TMR sensors, we applied polymer blend lithography to pattern structured self-assembled monolayers (SAMs) on hydrophilic SiO_x [63]. In order to obtain a high chemical contrast we used 1.3 nm high monolayers of FDTS (1*H*,1*H*,2*H*,2*H* - perfluorodecyltrichlorosilane), which are well known for their hydrophobicity [64]. If exposed to ambient conditions with a relative humidity of around 40%, the topographic contrast on those two materials disappears in amplitude modulation imaging. The height difference, however, can be observed if the sample is scanned in a liquid [63]. Therefore, we conclude that the vanishing topography contrast in ambient conditions is most likely caused by the thin water films present on hydrophilic SiO_x under ambient conditions [65]. This effect obscures the height difference between the FDTS and SiO_x. However, as shown in Figure 7a, the difference of the energy dissipation between the two materials is observable and the holes in the FDTS-SAM are visible as bright spots in the phase signal. As the phase contrast on this sample system is higher, we altered the feedback and scanned the same sample in a frequency modulation mode [66]. Thereby, the resonance frequency of the cantilever was tracked with a phase-locked-loop (PLL) while its frequency shift was used as a feedback for the topography feedback loop [6]. As the frequency tracking loop feeds back the cantilevers resonance frequency to the driving signal at a 90°phase shift, the contrast in the phase signal disappears as shown Figure 7b. The topography of the sample, however, is revealed clearly (see Figure 7a).

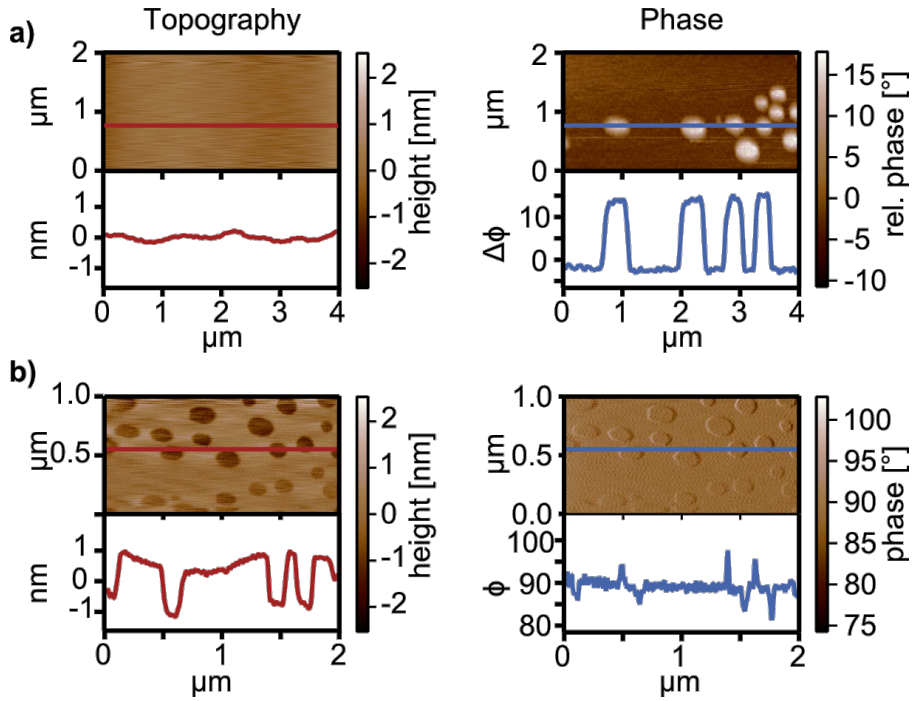

Figure 7: Dynamic mode imaging of FDTS-SAM samples using a TMR sensor with the feedback on amplitude and phase. a) Amplitude modulation mode imaging of FDTS-SAM in SiO_x with a TMR sensor. On this sample system, dissipative tip–sample forces are dominant. Therefore, a high phase-signal contrast can be observed and reveals the different materials of the sample due to different energy dissipation between tip and sample while the amplitude-signal feedback reveals no topographic features. b) On such samples, phase-locked frequency modulation AFM is advantageous and can reveal the topography of the sample. As the cantilevers resonance frequency is fed back to the driving signal by an additional loop, the phase contrast vanishes and is constant at 90°, while the topography with the holes in the SAM is revealed.

Conclusion

To conclude, we presented an atomic force microscope with a nested scanner design of two independent piezo scanners for the imaging of surfaces up to 800 × 800 µm^2. The AFM is capable of switching from the large-area scanner to the small high-resolution scanner. This key feature of the nested scanner design makes the instrument a versatile tool for the analysis of micro- and nanostructures by sequential scanning with both scanners. For the characterization of self-sensing AFM cantilevers based on TMR sensors, the instrument is designed to be operated in externally applied magnetic bias fields to optimize the sensitivity of the TMR sensors. The performance of these sensors has been shown to be sufficient for several operation modes and is capable of imaging smallest feature sizes like atomic step edges.

Acknowledgments

It is a pleasure to thank Hanaul Noh for fruitful discussions. We acknowledge support by the German Science Foundation DFG (HO 2237/4-2, ME 3616/1-2, RE 1052/31-2). This work was partly carried out with the support of the Karlsruhe Nano Micro Facility (KNMF, http://www.kit.edu/knmf), a Helmholtz Research Infrastructure at Karlsruhe Institute of Technology (KIT, http://www.kit.edu).

References

1. Binnig, G.; Quate, C. F.; Gerber, C. *Phys. Rev. Lett.* **1986,** *56,* 930–933. doi:10.1103/PhysRevLett.56.930
2. Vettiger, P.; Cross, G.; Despont, M.; Drechsler, U.; Dürig, U.; Gotsmann, B.; Haberle, W.; Lantz, M. A.; Rothuizen, H. E.; Stutz, R.; Binnig, G. K. *IEEE Trans. Nanotechnol.* **2002,** *1,* 39–55. doi:10.1109/TNANO.2002.1005425
3. Carrascosa, L. G.; Moreno, M.; Álvarez, M.; Lechuga, L. M. *TrAC, Trends Anal. Chem.* **2006,** *25,* 196–206. doi:10.1016/j.trac.2005.09.006
4. Oliver, R. A. *Rep. Prog. Phys.* **2008,** *71,* 076501. doi:10.1088/0034-4885/71/7/076501
5. Pires, D.; Hedrick, J. L.; De Silva, A.; Frommer, J.; Gotsmann, B.; Wolf, H.; Despont, M.; Duerig, U.; Knoll, A. W. *Science* **2010,** *328,* 732–735. doi:10.1126/science.1187851
6. Jalili, N.; Laxminarayana, K. *Mechatronics* **2004,** *14,* 907–945. doi:10.1016/j.mechatronics.2004.04.005
7. Vorburger, T. V.; Dagata, J. A.; Wilkening, G.; Lizuka, K.; Thwaite, E. G.; Lonardo, P. *CIRP Ann.* **1997,** *46,* 597–620. doi:10.1016/S0007-8506(07)60881-6
8. Minne, S. C.; Adams, J. D.; Yaralioglu, G.; Manalis, S. R.; Atalar, A.; Quate, C. F. *Appl. Phys. Lett.* **1998,** *73,* 1742–1744. doi:10.1063/1.122263
9. Dai, G.; Pohlenz, F.; Danzebrink, H.-U.; Xu, M.; Hasche, K.; Wilkening, G. *Rev. Sci. Instrum.* **2004,** *75,* 962–969. doi:10.1063/1.1651638
10. Meyer, G.; Amer, N. M. *Appl. Phys. Lett.* **1988,** *53,* 1045–1047. doi:10.1063/1.100061

11. Marti, O.; Colchero, J.; Mlynek, J. *Nanotechnology* **1990,** *1,* 141–144. doi:10.1088/0957-4484/1/2/003
12. Meyer, G.; Amer, N. M. *Appl. Phys. Lett.* **1990,** *56,* 2100–2101. doi:10.1063/1.102985
13. Allers, W.; Schwarz, A.; Schwarz, U. D.; Wiesendanger, R. *Rev. Sci. Instrum.* **1998,** *69,* 221–225. doi:10.1063/1.1148499
14. Hug, H. J.; Stiefel, B.; van Schendel, P. J. A.; Moser, A.; Martin, S.; Güntherodt, H.-J. *Rev. Sci. Instrum.* **1999,** *70,* 3625–3640. doi:10.1063/1.1149970
15. Drake, B.; Hansma, P. K. Atomic force microscope with optional replaceable fluid cell. U.S. Patent US000000034489E, Dec 8, 1993.
16. Nishida, S.; Kobayashi, D.; Sakurada, T.; Nakazawa, T.; Hoshi, Y.; Kawakatsu, H. *Rev. Sci. Instrum.* **2008,** *79,* 123703. doi:10.1063/1.3040500
17. Kassies, R.; van der Werf, K. O.; Lenferink, A.; Hunter, C. N.; Olsen, J. D.; Subramaniam, V.; Otto, C. *J. Microsc. (Oxford, U. K.)* **2005,** *217,* 109–116. doi:10.1111/j.0022-2720.2005.01428.x
18. Karrai, K.; Grober, R. D. *Appl. Phys. Lett.* **1995,** *66,* 1842–1844. doi:10.1063/1.113340
19. Giessibl, F. J. *Appl. Phys. Lett.* **2000,** *76,* 1470–1472. doi:10.1063/1.126067
20. Hembacher, S.; Giessibl, F. J.; Mannhart, J. *Appl. Surf. Sci.* **2002,** *188,* 445–449. doi:10.1016/S0169-4332(01)00976-X
21. Giessibl, F. J. *Rev. Mod. Phys.* **2003,** *75,* 949–983. doi:10.1103/RevModPhys.75.949
22. Tansock, J.; Williams, C. C. *Ultramicroscopy* **1992,** *42–44,* 1464–1469. doi:10.1016/0304-3991(92)90467-X
23. Doll, J. C.; Pruitt, B. L. *J. Micromech. Microeng.* **2010,** *20,* 095023. doi:10.1088/0960-1317/20/9/095023
24. Tortonese, M.; Yamada, H.; Barrett, R. C.; Quate, C. F. Atomic Force Microscopy Using a Piezoresistive Cantilever. In *International Conference on Solid-State Sensors and Actuators,* Digest of Technical Papers; 1991.
25. Tortonese, M.; Barrett, R. C.; Quate, C. F. *Appl. Phys. Lett.* **1993,** *62,* 834–836. doi:10.1063/1.108593
26. Linnemann, R.; Gotszalk, T.; Hadjiiski, L.; Rangelow, I. W. *Thin Solid Films* **1995,** *264,* 159–164. doi:10.1016/0040-6090(94)05829-6
27. Linnemann, R.; Gotszalk, T.; Rangelow, I. W.; Dumania, P.; Oesterschulze, E. *J. Vac. Sci. Technol., B* **1996,** *14,* 856–860. doi:10.1116/1.589161
28. Gotszalk, T.; Grabiec, P.; Rangelow, I. W. *Ultramicroscopy* **2000,** *82,* 39–48. doi:10.1016/S0304-3991(99)00171-0
29. Fantner, G. E.; Schumann, W.; Barbero, R. J.; Deutschinger, A.; Todorov, V.; Gray, D. S.; Belcher, A. M.; Rangelow, I. W.; Youcef-Toumi, K. *Nanotechnology* **2009,** *20,* 434003. doi:10.1088/0957-4484/20/43/434003
30. Neubauer, G.; Cohen, S. R.; McClelland, G. M.; Horne, D.; Mate, C. M. *Rev. Sci. Instrum.* **1990,** *61,* 2296–2308. doi:10.1063/1.1141354
31. Miller, S. A.; Turner, K. L.; MacDonald, N. C. *Rev. Sci. Instrum.* **1997,** *68,* 4155–4162. doi:10.1063/1.1148361
32. Mamin, H. J.; Gurney, B. A.; Wilhoit, D. R.; Speriosu, V. S. *Appl. Phys. Lett.* **1998,** *72,* 3220–3222. doi:10.1063/1.121555
33. Gurney, B. A.; Mamin, H. J.; Rugar, D.; Speriosu, V. S. Atomic force microscope system with cantilever having unbiased spin valve magnetoresistive strain gauge. U.S. Patent 000005856617A, Sept 2, 1999.
34. Sahoo, D. R.; Sebastian, A.; Häberle, W.; Pozidis, H.; Eleftheriou, E. *Nanotechnology* **2011,** *22,* 145501. doi:10.1088/0957-4484/22/14/145501
35. Tavassolizadeh, A.; Meier, T.; Rott, K.; Reiss, G.; Quandt, E.; Hölscher, H.; Meyners, D. *Appl. Phys. Lett.* **2013,** *102,* 153104. doi:10.1063/1.4801315
36. Gaitas, A.; Li, T.; Zhu, W. *Sens. Actuators, A* **2011,** *168,* 229–232. doi:10.1016/j.sna.2011.04.023
37. Thaysen, J.; Boisen, A.; Hansen, O.; Bouwstra, S. *Sens. Actuators, A* **2000,** *83,* 47–53. doi:10.1016/S0924-4247(00)00299-5
38. Yu, X.; Thaysen, J.; Hansen, O.; Boisen, A. *J. Appl. Phys.* **2002,** *92,* 6296–6301. doi:10.1063/1.1493660
39. Lee, J.; King, W. P. *J. Microelectromech. Syst.* **2008,** *17,* 432–445. doi:10.1109/JMEMS.2008.918423
40. Qazi, M.; DeRoller, N.; Talukdar, A.; Koley, G. *Appl. Phys. Lett.* **2011,** *99,* 193508. doi:10.1063/1.3657467
41. Waddie, A. J.; Taghizadeh, M. R.; Mohr, J.; Piotter, V.; Mehne, C.; Stuck, A.; Stijns, E.; Thienpont, H. *Proc. SPIE* **2006,** *6185,* 61850B. doi:10.1117/12.661912
42. Zhu, J.-G. *Mater. Today* **2003,** *6,* 22–31. doi:10.1016/S1369-7021(03)00729-6
43. Plaskett, T. S.; Freitas, P. P.; Barradas, N. P.; da Silva, M. F.; Soares, J. C. *J. Appl. Phys.* **1994,** *76,* 6104–6106. doi:10.1063/1.358319
44. Moodera, J. S.; Kinder, L. R.; Wong, T. M.; Meservey, R. *Phys. Rev. Lett.* **1995,** *74,* 3273–3276. doi:10.1103/PhysRevLett.74.3273
45. Moodera, J. S.; Gallagher, E. F.; Robinson, K.; Nowak, J. *Appl. Phys. Lett.* **1997,** *70,* 3050. doi:10.1063/1.118168
46. Sousa, R. C.; Sun, J. J.; Soares, V.; Freitas, P. P.; Kling, A.; da Silva, M. F.; Soares, J. C. *Appl. Phys. Lett.* **1998,** *73,* 3288–3290. doi:10.1063/1.122747
47. Moodera, J. S.; Nassar, J.; Mathon, G. *Annu. Rev. Mater. Sci.* **1999,** *29,* 381–432. doi:10.1146/annurev.matsci.29.1.381
48. Wang, D.; Nordman, C.; Daughton, J. M.; Qian, Z.; Fink, J. *IEEE Trans. Magn.* **2004,** *40,* 2269–2271. doi:10.1109/TMAG.2004.830219
49. Yuasa, S.; Nagahama, T.; Fukushima, A.; Suzuki, Y.; Ando, K. *Nat. Mater.* **2004,** *3,* 868–871. doi:10.1038/nmat1257
50. Parkin, S. S. P.; Kaiser, C.; Panchula, A.; Rice, P. M.; Hughes, B.; Samant, M.; Yang, S.-H. *Nat. Mater.* **2004,** *3,* 862–867. doi:10.1038/nmat1256
51. Meyners, D.; von Hofe, T.; Vieth, M.; Rührig, M.; Schmitt, S.; Quandt, E. *J. Appl. Phys.* **2009,** *105,* 07C914. doi:10.1063/1.3063662
52. Albon, C.; Weddemann, A.; Auge, A.; Rott, K.; Hütten, A. *Appl. Phys. Lett.* **2009,** *95,* 023101. doi:10.1063/1.3179241
53. Löhndorf, M.; Duenas, T.; Tewes, M.; Quandt, E.; Rührig, M.; Wecker, J. *Appl. Phys. Lett.* **2002,** *81,* 313. doi:10.1063/1.1483123
54. O'Handley, R. C. *Modern Magnetic Materials: Principles and Applications;* Wiley-VCH Verlag: Weinheim, Germany, 2000.
55. Lee, Y. M.; Hayakawa, J.; Ikeda, S.; Matsukura, F.; Ohno, H. *Appl. Phys. Lett.* **2006,** *89,* 042506. doi:10.1063/1.2234720
56. Ikeda, S.; Hayakawa, J.; Lee, Y. M.; Matsukura, F.; Ohno, Y.; Hanyu, T.; Ohno, H. *IEEE Trans. Electron Devices* **2007,** *54,* 991–1002. doi:10.1109/TED.2007.894617
57. Meyners, D.; Puchalla, J.; Dokupil, S.; Löhndorf, M.; Quandt, E. *ECS Trans.* **2007,** *3,* 223–233. doi:10.1149/1.2753255
58. Jaffrès, H.; Lacour, D.; Nguyen Van Dau, F.; Briatico, J.; Petroff, F.; Vaurès, A. *Phys. Rev. B* **2001,** *64,* 064427. doi:10.1103/PhysRevB.64.064427
59. Kindt, J. H.; Fantner, G. E.; Thompson, J. B.; Hansma, P. K. *Nanotechnology* **2004,** *15,* 1131–1134. doi:10.1088/0957-4484/15/9/005

60. Cleveland, J. P.; Anczykowski, B.; Schmid, A. E.; Elings, V. B. *Appl. Phys. Lett.* **1998,** *72,* 2613–2615. doi:10.1063/1.121434
61. Anczykowski, B.; Gotsmann, B.; Fuchs, H.; Cleveland, J. P.; Elings, V. B. *Appl. Surf. Sci.* **1999,** *140,* 376–382. doi:10.1016/S0169-4332(98)00558-3
62. Noy, A.; Sanders, C. H.; Vezenov, D. V.; Wong, S. S.; Lieber, C. M. *Langmuir* **1998,** *14,* 1508–1511. doi:10.1021/la970948f
63. Huang, C.; Moosmann, M.; Jin, J.; Heiler, T.; Walheim, S.; Schimmel, T. *Beilstein J. Nanotechnol.* **2012,** *3,* 620–628. doi:10.3762/bjnano.3.71
64. Maboudian, R.; Ashurst, W. R.; Carraro, C. *Sens. Actuators, A* **2000,** *82,* 219–223. doi:10.1016/S0924-4247(99)00337-4
65. Freund, J.; Halbritter, J.; Hörber, J. K. H. *Microsc. Res. Tech.* **1999,** *44,* 327–338. doi:10.1002/(SICI)1097-0029(19990301)44:5<327::AID-JEMT3>3.0.CO;2-E
66. Dürig, U.; Züger, O.; Stalder, A. *J. Appl. Phys.* **1992,** *72,* 1778–1798. doi:10.1063/1.352348

License and Terms

BEILSTEIN JOURNAL OF NANOTECHNOLOGY

Improved atomic force microscopy cantilever performance by partial reflective coating

Zeno Schumacher*[1], Yoichi Miyahara[1], Laure Aeschimann[2] and Peter Grütter[1]

Full Research Paper

Open Access

Address:
[1]Department of Physics, McGill University, Montreal, Quebec, H3A 2T8, Canada and [2]NanoWorld AG, Neuchâtel, 2002, Switzerland

Email:
Zeno Schumacher* - zenos@physics.mcgill.ca

* Corresponding author

Keywords:
cantilever; force noise; partial coating; Q-factor

Beilstein J. Nanotechnol. **2015,** *6,* 1450–1456.
doi:10.3762/bjnano.6.150

Received: 18 February 2015
Accepted: 18 June 2015
Published: 03 July 2015

This article is part of the Thematic Series "Noncontact atomic force microscopy III".

Guest Editor: U. D. Schwarz

Abstract

Optical beam deflection systems are widely used in cantilever based atomic force microscopy (AFM). Most commercial cantilevers have a reflective metal coating on the detector side to increase the reflectivity in order to achieve a high signal on the photodiode. Although the reflective coating is usually much thinner than the cantilever, it can still significantly contribute to the damping of the cantilever, leading to a lower mechanical quality factor (Q-factor). In dynamic mode operation in high vacuum, a cantilever with a high Q-factor is desired in order to achieve a lower minimal detectable force. The reflective coating can also increase the low-frequency force noise. In contact mode and force spectroscopy, a cantilever with minimal low-frequency force noise is desirable. We present a study on cantilevers with a partial reflective coating on the detector side. For this study, soft (≈0.01 N/m) and stiff (≈28 N/m) rectangular cantilevers were used with a custom partial coating at the tip end of the cantilever. The Q-factor, the detection and the force noise of fully coated, partially coated and uncoated cantilevers are compared and force distance curves are shown. Our results show an improvement in low-frequency force noise and increased Q-factor for the partially coated cantilevers compared to fully coated ones while maintaining the same reflectivity, therefore making it possible to combine the best of both worlds.

Introduction

For cantilever based beam deflection atomic force microscope (AFM) systems, a large variety of commercial cantilevers exist. For each measurement mode, e.g., tapping, contact, non-contact, etc. optimized cantilevers are offered. These cantilevers differ in parameters like dimension, spring constant, resonance frequency and tip size. Most cantilever models are available in two versions, an uncoated version and a version with a reflective metal coating. The reflective coating is added to enhance the poor intrinsic reflectivity of silicon, the material most cantilevers are made of. On average adding a reflective coating increases the intensity of the reflected beam by 2.5 times, hence resulting in higher signals on the photodiode.

In frequency modulated (FM) AFM, the mechanical quality (Q-)factor of the cantilever plays an important role, since the measurable minimal force gradient in FM-AFM is [1]:

$$\delta F'_{\min} = \sqrt{\frac{4k_{\mathrm{L}}k_{\mathrm{B}}TB}{\omega_0 Q\left\langle z_{\mathrm{osc}}^2\right\rangle}} \quad (1)$$

where Q is the mechanical Q-factor of the cantilever, k_{L} the force constant of the cantilever, T the temperature, k_{B} the Boltzman constant, B the measurement bandwidth, ω_0 the resonance frequency of the cantilever and $\left\langle z_{\mathrm{osc}}^2\right\rangle$ the root-mean-square amplitude of cantilever oscillation. Since the minimal detectable force is inversely proportional to the Q-factor, high Q's are desired to achieve a lower minimal detectable force gradient. By using a cantilever in an ultra high vacuum environment (UHV), the Q-factor is drastically increased due to the absence of damping by air atmosphere and is limited by the intrinsic properties of the cantilever.

It is known that adding a metal layer to a cantilever can degrade the Q-factor of the cantilever. A reduction in Q-factor due to a metallic coating of >100 nm thick film [2] and of thinner films [3] have been reported.

Another undesirable effect caused by a metallic coating is the increased low-frequency noise which often exhibits an $1/f$ behavior. Labuda et al. recently published a study on how to reduce the $1/f$ noise of coated cantilevers by patterning the metal coating with a Fresnel lens like pattern [4]. Bull et al. reported the reduction of the cantilever noise in liquid by a partial metallic coating on commercially available short cantilevers [5]. These changes in the cantilever performance can be described by the additional viscoelastic damping and increased susceptibility to temperature fluctuations due to the added metal layer causing a bimetallic effect. Paoline et al. presented a model that uses a complex spring constant in combination with Sader's model of hydrodynamic damping to describe the $1/f$ noise behaviour of coated cantilever [6].

Since the sole purpose of the reflective coating is to increase the intensity of the reflected light, it is only needed at the position of the incident laser beam, i.e., at the tip end of the cantilever. Waggoner et al. presented a study on the effect of a circular gold pad at different positions along a cantilever showing a reduction in Q-factor for pads placed at the base of the cantilever [7]. Sosale et al. reported a study on partially metallized cantilevers and the resulting Q-factor, finding an optimal coating length of 20% at the tip end and high damping due to coating at the base [8,9]. However, they used cantilevers with dimensions of 22.6 to 24.1 mm in length and 73 to 93 µm in thickness with a coating thickness of 110 nm which are mounted on a custom-made holder for minimizing clamping losses. Although, these cantilevers do work well as a model system, they do not represent the dimensions of commonly used commercial cantilevers for AFM.

It is widely believed that a source of the variability of the Q-factor of commercial cantilevers is a bad coupling between the piezo and the cantilever and the resulting clamping losses [10]. We will present a study of the effect of the reflective coating on the Q-factor and the noise of commercially available cantilevers and how these influence the performance in the different AFM operation modes. We will provide evidence that a small change in coating thickness can influence the Q-factor significantly.

Experimental

We measured the dependencies of low-frequency noise and Q-factor on partial metal coating coverage. As previously mentioned, different AFM modes require different cantilevers. Two types of cantilevers were chosen for this study. First, a soft (≈0.01 N/m) cantilever mainly used for contact mode and force–distance measurements, where a low spring constant and low $1/f$ noise are the most important parameters. Second, a stiff (≈29 N/m) cantilever typically used in high resolution UHV AFM applications, where the focus is on the Q-factor, was used. Cantilever specifications are summarized in Table 1. The partial reflective coating was realized by a shadow masking technique with thermal evaporation. The length of the partial coating, as well as the length of the cantilevers were measured with a calibrated optical microscope, with an estimated error of ±1 µm.

Table 1: Specification of the two types of cantilevers used for this study.

Cantilever name	Soft	NCLR
Spring constant	≈0.01 N/m	≈29 N/m
Length	140 µm	225 µm
Width	34 µm	38 µm
Thickness	340 nm	7 µm
Coating thickness	2 nm Cr & 60 nm Au	30 nm Al
Ratio coating/substrate thickness ($h_{\mathrm{f}}/h_{\mathrm{s}}$)	3/17	3/700
Tested coating percentages	15, 19, 21, 26, 32, 55, 60, 100	0, 20, 24, 27, 32, 41, 44, 48, 100

All measurements were performed with a variable-environment compatible commercial AFM (JEOL JSPM-5400) under high vacuum conditions (<5 × 10^{-5} mbar) or in air atmosphere. The

standard laser diode was replaced with a fiber-pigtailed, temperature stabilized and radio frequency modulated laser diode to reduce the mode-hopping noise of the laser beam [11]. The standard cantilever holder with a metal wire across the chip that clamps the cantilever was used for all measurements.

The cantilever deflection noise density spectra were obtained by fast Fourier transform of the digitized photo diode signal. An 8th order Buttherworth low-pass filter with an appropriate cut-off frequency was used as an anti-aliasing filter. The resulting thermal vibration peak was fitted with a Lorentzian to extract its full width at half maximum from which the Q-factor was calculated. The spring constant of the cantilevers and optical-lever sensitivities were measured by fitting the thermal vibration peak of the fundamental flexural mode acquired in air. The obtained optical-lever sensitivities are used to convert the noise density spectra to be expressed in fm/$\sqrt{\text{Hz}}$. More detail of the procedure is found in [12].

The Q-factor was also obtained by exciting the cantilever oscillation with a piezoelectric actuator and measuring the resulting amplitude and phase with varying frequency with a digital lock-in amplifier (HF2LI, Zurich Instrument). The Q-factor was calculated from the measured phase versus frequency curves using $\frac{\partial phase}{\partial f} = \frac{2Q}{f_{\text{resonance}}}$.

Results and Discussion

The sum signal measured on the photodiode was the same for the partially coated cantilever and the fully coated cantilever under constant laser power. The uncoated cantilever shows a 2 and 3 times lower reflectivity for the NCLR and soft type respectively. In the following paragraph we will highlight the advantage of a partial reflective coating on NCLR and Soft cantilevers for FM-AFM and static AFM operation, respectively.

Advantages for FM-AFM: recovering intrinsic Q-factor values

Figure 1 shows the Q-values for the NCLR cantilever with different coating coverages measured in high vacuum. For each of the uncoated and fully coated cantilevers, the average of at least 3 different cantilevers is plotted. As previously mentioned, the minimal detectable force in FM-AFM can be reduced by increasing the Q-factor. Adding a full reflective coating to the NCLR cantilevers reduces the Q-factor by half compared to uncoated cantilevers. However, by minimizing the coating to 20% of the cantilever length the same Q-factor as that of the uncoated cantilever can be achieved.

A thermal vibration measurement (blue) is compared to a piezo driven measurement recorded during the same experiment

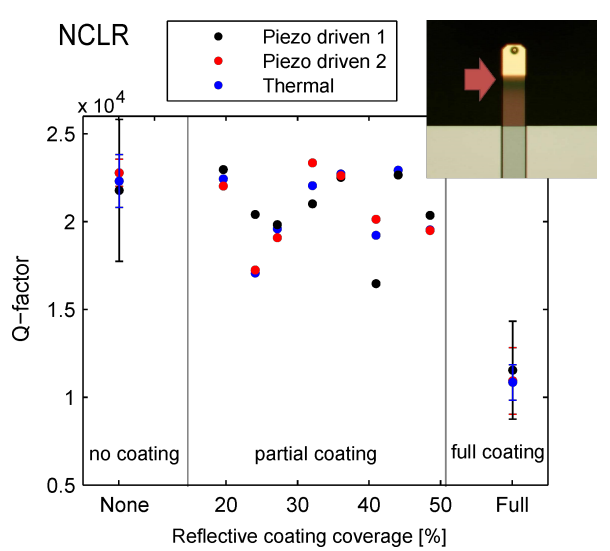

Figure 1: Q-factor of NCLR cantilever with different coating coverage percentages. A 30 nm Al coating was added on the 7 µm thick cantilever. 20% coating coverage show the same Q-factor as uncoated cantilever. The errorbars show standard deviation of the mean of at least 3 different cantilevers.

(Piezo driven 2) and a piezo driven experiment recorded after re-mounting of the cantilever (Piezo driven 1). The Q-factor varies slightly between the thermal and the piezo driven measurement performed with the same clamping. This difference is attributed to multiple possible sources. The thermal vibration measurement is more susceptible to temperature drift as it requires longer acquisition time for measuring the cantilevers with higher Q-factors. The fitting can also contribute to a difference in the measured values due to the high Q-factor. The variation between the two piezo-driven measurements stems from the difference in mounting and therefore possible different clamping losses [10].

In addition, the soft cantilevers show even more pronounced effects under vacuum due to the different coating and cantilever thickness (see Supporting Information File 1, Figure S1 for data).

Advantages for static AFM: reduced low-frequency noise

For static AFM measurement such as contact mode or force spectroscopy, a low 1/f noise is important. In this section, the cantilever deflection noise density spectra of the soft cantilevers measured from 1 Hz to 25 kHz in air is discussed. These spectra include the 1/f noise as well as the fundamental resonance of the cantilever at 11 kHz. In Figure 2, we compare the noise density spectra of a fully coated, two partially coated and an uncoated cantilevers. A nearly an order of magnitude increase in 1/f noise can be observed for the fully coated cantilever compared to the

uncoated one. At 1 Hz, the cantilever with a coating coverage of 27% shows a 4 fold reduction in 1/*f* noise compared to the full coating. When reducing the coating coverage even further to 15% only a slightly higher 1/*f* noise compared to no coating is observed.

The two lowest spectra in Figure 2 show the equivalent deflection noise density due to the instrumental noise measured by reflecting the laser beam off the cantilever chip. The measured spectra were converted to the equivalent deflection noise density spectra by the optical beam lever sensitivities obtained for partially and fully coated cantilevers. It is clear that the instrumental noise is much smaller than the observed cantilever noise and the reduction in 1/*f* noise is therefore a true reduction in the force noise (noise due to the cantilever deflection). The reduction is due to the reduced photothermal (bimetallic) effect. Note that the sharp peaks in the spectra are of electronic origin as they also appear in the detection noise. We observed the similar reduction in 1/*f* noise for the NCLR cantilevers, which can be seen in Supporting Information File 1, Figure S2 and Figure S3.

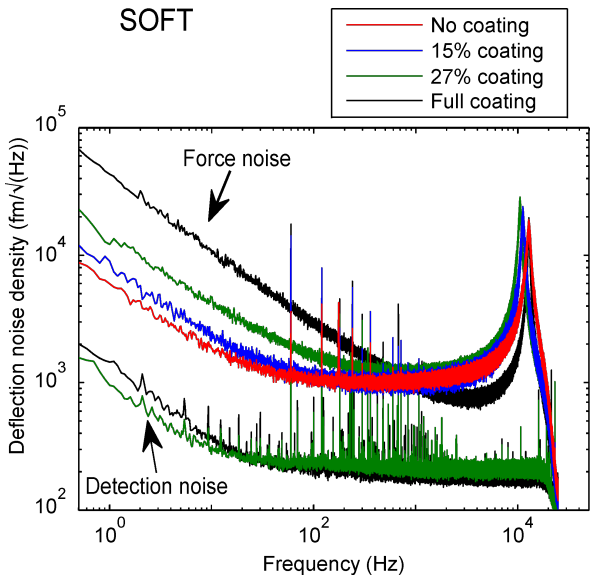

Figure 2: Noise spectra for soft cantilever with different coating coverage acquired in air. Fully coated cantilever shows the highest 1/*f* noise. The 1/*f* noise reduces with reduced coating coverage. The uncoated cantilever shows the lowest 1/*f* noise level.

In force measurements the force noise is more relevant than the deflection noise itself as it directly shows the performance of the cantilevers as a force sensor (see Figure 3a). The equivalent force noise density spectra were obtained by multiplying the deflection noise density shown in Figure 2 with the measured spring constant of each cantilever. Here, the difference between fully and partially coated cantilevers becomes even more pronounced due to the higher spring constant of the fully coated cantilever.

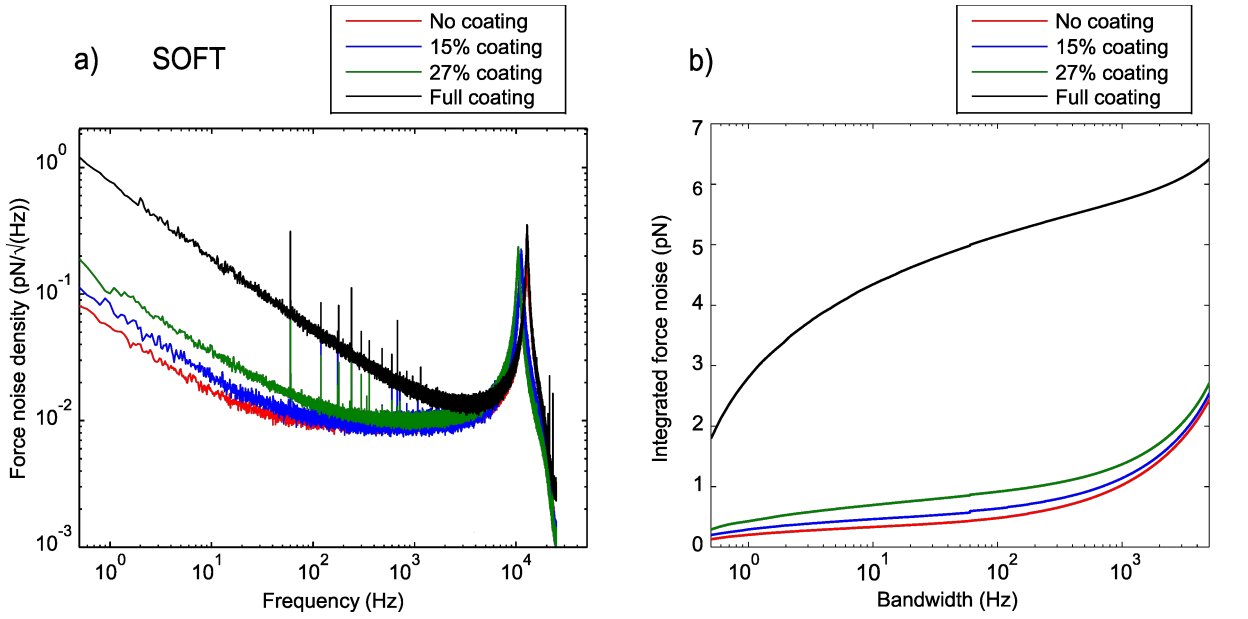

Figure 3: (a) Force noise density spectra for the soft cantilevers obtained from Figure 2 by multiplying with the measured spring constants. (b) The force noise density is integrated to show the expected force noise at a certain bandwidth (0.3 Hz–5 kHz). This sets the minimum force noise with these cantilever, independent of the measured signal. The partially coated cantilever and uncoated cantilever show a sub-pN force noise over a wide range of possible bandwidth (0.5 Hz–1 kHz), whereas the fully coated cantilever shows a strong increase.

An additional measure to quantify the noise for force spectroscopy measurements, is the integrated force noise shown in Figure 3b. The integrated force noise shows the expected noise at the corresponding measurement bandwidth, independent of the measured force. It is therefore the minimum force precision achievable by the cantilever in such a static measurement, not to be confused with the minimal detectable force gradient mentioned for FM-AFM in Equation 1. One can clearly see that the noise on the fully coated cantilever increases rapidly in the low frequency range, whereas the partial and uncoated cantilever show a sub-pN force noise up to 1 kHz bandwidth. Bull, et al. [5] previously used the integrated force noise to characterize the noise of cantilevers and verified this parameter experimentally.

Force–distance curves of the soft cantilever on a silicon wafer were taken to show the noise behaviour under more realistic experimental condition. In Figure 4 one can see the increased noise for the fully coated cantilever with an RMS of 2.14×10^{-9} N compared to the partially coated and uncoated cantilever (1.80×10^{-10} N and 2.01×10^{-10} N, respectively). This order of magnitude difference is larger than the systematic error due to the uncertainty in the spring constant. The slowly varying forces appearing before contact are due to optical interference effect of the detection laser beam. The uncoated cantilever shows the largest variation, possibly due to more light being reflected off the sample underneath the cantilever.

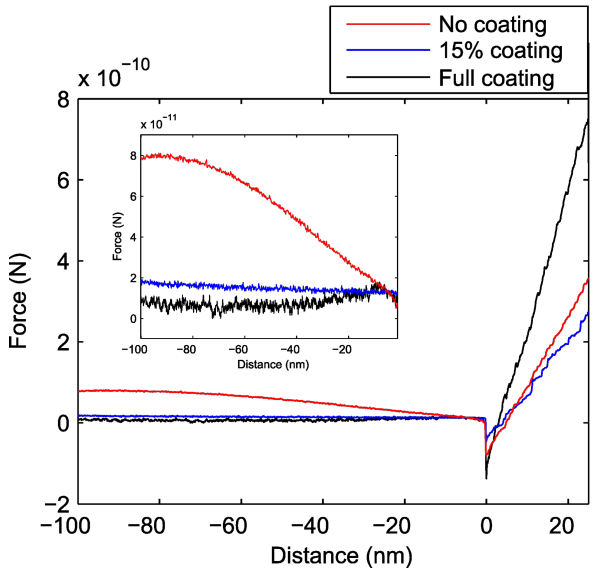

Figure 4: Force–distance curves for an uncoated (red), partial coated (blue) and fully coated soft cantilever (black) with a measurement bandwidth of 1 kHz. In the inset, the approach region is plotted for better illustration of the noise. One can see that the fully coated cantilever shows the highest noise. The uncoated cantilever shows largest variation of the force before contact which is due to the optical interference of the detection laser beam.

Effect of coating thickness on Q-factor

Sosale et al. [8], derived a quantitative theory of how the internal material friction of a partial coating effects the Q-factor of a microcantilever:

$$\delta_c = \delta_s + 3\frac{E_f h_f}{E_s h_s}\left[\frac{\int_{x_1/L}^{x_2/L}\left(\frac{\partial^2\phi(\xi)}{\partial\xi^2}\right)^2 d\xi}{\int_0^{l}\left(\frac{\partial^2\phi(\xi)}{\partial\xi^2}\right)^2 d\xi}\right]\delta_f \qquad (2)$$

with ξ the normalized length (l/L), $\phi(\xi)$ the natural mode shape of the cantilever, E the Young's modulus and h_f, h_s being the coating film thickness and the cantilever thickness. The logarithmic decrement is $\delta = \pi/Q$. The c stands for the composite system, f for the film and s for the substrate. This assumes no clamping losses and a substrate operating at the fundamental thermoelastic limit of dissipation [8].

We calculate the Q-factor dependence on the coating thickness of the NCLR cantilever. Therefore, we measured the Q-factor of fully coated and uncoated NCLR cantilevers, to extract the $\delta_s = 4.18 \times 10^{-5}$, $\delta_f = 8.56 \times 10^{-3}$ term in Equation 2. We used these values to plot the Q-factor vs coating thickness for coating thicknesses between 0–350 nm on a fully coated NCLR cantilever, see Figure 5.

One should notice that a change in coating thickness of a few nanometer around the standard coating thickness of 30 nm can result in a drastic change in the Q-factor, even for a 30 nm coating on a 7 µm thick cantilever. To verify how well this model works for an actual AFM system with clamping losses, the Q-factor of two sets of NCLR cantilevers with a difference in coating thickness of 16 nm was used. For each coating thickness at least 18 cantilevers were measured (horizontal line in Figure 5 inset). The average measured difference in Q-factor between the two different thicknesses was measured to be 6032 with a standard error of 905, which is larger than that expected from Equation 2.

However, if we assume that the logarithmic decrement of the coating film scales linearly with the thickness of the coating such as $\delta_f^* = (\delta_{f,measured}/h_{f,measured})h_f$ we replace δ_f with δ_f^* in Equation 2, the modified Equation 2 gives a better agreement with our observation as shown in Figure 5. Nevertheless, one can see in Figure 5 that a small variation in coating thickness for a fully coated cantilever will influence the Q-factor significantly for both cases.

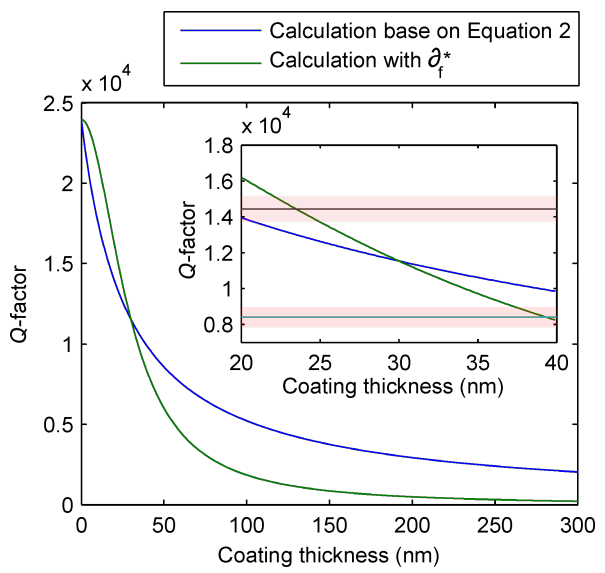

Figure 5: Calculation of the change of Q-factor for a fully coated NCLR cantilever with different coating thicknesses. Blue shows the predicted value according to Equation 2. Green shows the predicted Q-factor value with the added δ_f^* term. The inset shows a zoom to 20–40 nm. The mean measured Q-factor for two sets of NCLR with a coating thickness difference of 16 nm are plotted as a horizontal line with standard error by red bands.

Conclusion

We showed the improved behavior in Q-factor and $1/f$ noise for partially over fully/uncoated commercial AFM cantilevers, which is summarized in Table 2. In general thin-film coatings significantly reduce the Q-factor of any cantilever, even for coating to cantilever thickness ratios as small as 30 nm/7 µm < 10^{-2} and is therefore relevant for AFM applications. This can be described by the additional viscoelastic damping due the metal coating on the cantilever. The effect of this damping increases with increasing coating to cantilever thickness ratio, which was demonstrated with two types of cantilevers used in this study (soft and NCLR). A larger ratio results in an increased damping, hence in a reduction in Q-factor and an increase in $1/f$ noise.

Table 2: Summary of the performance of cantilevers with different coating. The partially coated cantilever combines the advantages of the fully coated with the advantage of the partially coated cantilever.

Coating	Signal on diode	Q-factor	1/*f* noise
Partially coated	high	high	low
Fully coated	high	low	high
Uncoated	low	high	low

However, the damping due to the coating can be overcome if a partial coating at the tip end of the cantilever is used.

We showed that for soft cantilevers (≈0.01 N/m), a significant reduction in $1/f$ noise can be achieved, which is extremely relevant for static force measurements. For stiffer cantilevers commonly used in FM-AFM, a partial coating with 20% coverage at the tip end of the cantilever retains a similar Q-factor as uncoated cantilevers, with the added benefit of a higher signal on the photodiode.

Furthermore, the partial coating of 20% helps to align the laser reliably to the same position on the cantilever since the intensity of the reflective signal decrease significantly when the beam is moved in any of the four direction away from the coating. This should help to achieve more reproducible deflection sensitivity measurement since they depend on the position of the laser beam on the cantilever [13].

We also showed that a slight variation in coating thickness can result in significant changes in the Q-factor of a cantilever. Therefore, fabrication dependent variations of the coating thickness will influence the Q-factor. If a partial coating is used, this effect becomes unimportant, resulting in more reproducible Q-factors from fabrication batch to batch.

In summary, there is no need for fully coated cantilevers since the coating reduces the Q-factor in UHV and adds $1/f$ noise for soft cantilever. The coating at the base of the cantilever is not needed since the sole purpose of the coating is to reflect the laser beam at tip end of the cantilever. Partially coated cantilevers would therefore be a better choice for a variety of AFM applications.

Supporting Information

The Supporting Information includes Q-factor measurments for the soft cantilver and deflection noise density spectra for the NCLR cantilever.

Supporting Information File 1

Detection noise measurement for NCLR cantilever.
[http://www.beilstein-journals.org/bjnano/content/supplementary/2190-4286-6-150-S1.pdf]

Acknowledgements

Funding by NSERC and FRQNT is gratefully acknowledged.

References

1. Albrecht, T. R.; Grütter, P.; Horne, D.; Rugar, D. *J. Appl. Phys.* **1991,** *69,* 668. doi:10.1063/1.347347

2. Sandberg, R.; Mølhave, K.; Boisen, A.; Svendsen, W. *J. Micromech. Microeng.* **2005,** *15,* 2249–2253. doi:10.1088/0960-1317/15/12/006
3. Li, T. J.; Bellon, L. *EPL* **2012,** *98,* 14004. doi:10.1209/0295-5075/98/14004
4. Labuda, A.; Bates, J. R.; Grütter, P. H. *Nanotechnology* **2012,** *23,* 025503. doi:10.1088/0957-4484/23/2/025503
5. Bull, M. S.; Sullan, R. M. A.; Li, H.; Perkins, T. T. *ACS Nano* **2014,** *8,* 4984–4995. doi:10.1021/nn5010588
6. Paolino, P.; Bellon, L. *Nanotechnology* **2009,** *20,* 405705. doi:10.1088/0957-4484/20/40/405705
7. Waggoner, P. S.; Craighead, H. G. *J. Appl. Phys.* **2009,** *105,* 054306. doi:10.1063/1.3079793
8. Sosale, G.; Das, K.; Fréchette, L.; Vengallatore, S. *J. Micromech. Microeng.* **2011,** *21,* 105010. doi:10.1088/0960-1317/21/10/105010
9. Joshi, S.; Hung, S.; Vengallatore, S. *EPJ Tech. Instrum.* **2014,** *1,* No. 5. doi:10.1140/epjti5
10. Lübbe, J.; Tröger, L.; Torbrügge, S.; Bechstein, R.; Richter, C.; Kühnle, A.; Reichling, M. *Meas. Sci. Technol.* **2010,** *21,* 125501. doi:10.1088/0957-0233/21/12/125501
11. Fukuma, T.; Kimura, M.; Kobayashi, K.; Matsushige, K.; Yamada, H. *Rev. Sci. Instrum.* **2005,** *76,* 053704. doi:10.1063/1.1896938
12. Higgins, M. J.; Proksch, R.; Sader, J. E.; Polcik, M.; Mc Endoo, S.; Cleveland, J. P.; Jarvis, S. P. *Rev. Sci. Instrum.* **2006,** *77,* 013701. doi:10.1063/1.2162455
13. Proksch, R.; Schäffer, T. E.; Cleveland, J. P.; Callahan, R. C.; Viani, M. B. *Nanotechnology* **2004,** *15,* 1344–1350. doi:10.1088/0957-4484/15/9/039

BEILSTEIN JOURNAL OF NANOTECHNOLOGY

A simple and efficient quasi 3-dimensional viscoelastic model and software for simulation of tapping-mode atomic force microscopy

Santiago D. Solares

Full Research Paper

Open Access

Address:
Department of Mechanical and Aerospace Engineering, George Washington University, Washington, DC 20052, USA

Email:
Santiago D. Solares - ssolares@gwu.edu

Keywords:
atomic force microscopy (AFM); modeling; multifrequency; multimodal; polymers; simulation; spectroscopy; standard linear solid; tapping-mode AFM; viscoelasticity

Beilstein J. Nanotechnol. **2015,** *6,* 2233–2241.
doi:10.3762/bjnano.6.229

Received: 02 September 2015
Accepted: 13 November 2015
Published: 26 November 2015

This article is part of the Thematic Series "Noncontact atomic force microscopy III".

Guest Editor: M. Z. Baykara

Abstract

This paper introduces a quasi-3-dimensional (Q3D) viscoelastic model and software tool for use in atomic force microscopy (AFM) simulations. The model is based on a 2-dimensional array of standard linear solid (SLS) model elements. The well-known 1-dimensional SLS model is a textbook example in viscoelastic theory but is relatively new in AFM simulation. It is the simplest model that offers a qualitatively correct description of the most fundamental viscoelastic behaviors, namely stress relaxation and creep. However, this simple model does not reflect the correct curvature in the repulsive portion of the force curve, so its application in the quantitative interpretation of AFM experiments is relatively limited. In the proposed Q3D model the use of an array of SLS elements leads to force curves that have the typical upward curvature in the repulsive region, while still offering a very low computational cost. Furthermore, the use of a multidimensional model allows for the study of AFM tips having non-ideal geometries, which can be extremely useful in practice. Examples of typical force curves are provided for single- and multifrequency tapping-mode imaging, for both of which the force curves exhibit the expected features. Finally, a software tool to simulate amplitude and phase spectroscopy curves is provided, which can be easily modified to implement other controls schemes in order to aid in the interpretation of AFM experiments.

Introduction

The quantification of tip–sample dissipation in atomic force microscopy (AFM) has been an ongoing subject of interest since the early days of the technique [1,2]. A significant percentage of the surfaces characterized with AFM exhibit rate-dependent deformation processes that result in dissipative tip–sample interactions. A few examples of these processes include viscoelastic deformation, irreversible molecular structure changes (e.g., in biomolecules) and plastic deformation in

crystals. These phenomena bring challenges into AFM characterization primarily in two ways. First, in delicate samples, such as biomolecules, it becomes necessary to control the maximum tip–sample interaction forces and stresses, such that undesirable irreversible changes do not occur in the sample. Second, the interpretation of the experiment requires the user to make assumptions and/or develop models that properly account for the rate-dependent dissipative processes.

Viscoelasticity, in particular, is a very difficult phenomenon to deal with accurately within AFM spectroscopy, whereby one tries to extract material properties following a set of measurements in which generally one parameter is varied while keeping all other parameters constant. The most common example of a spectroscopic measurement in AFM is the recording of an observable (e.g., phase shift, frequency shift, deflection, specific harmonic amplitudes, etc.), while the base of the microcantilever is brought closer to the sample with a relatively small constant speed, and then retracted at the same speed. Generally the desired information is the tip–sample interaction force curve, which for an elastic body is an analytical expression describing the force sensed by the AFM tip as a function of its vertical position above the sample. From this curve the user can extract properties such as the Young's modulus, which describes the bulk stress–strain relation of the material, or the Hamaker constant, which describes the dispersion forces between the tip and the sample.

In the case of a viscoelastic surface the extraction of material 'properties' is difficult for a number of reasons. First, viscoelasticity itself is a difficult-to-quantify behavior at the nanoscale. In continuum measurements it is common to describe viscoelastic behavior in terms of the loss and storage moduli, but strictly speaking, these quantities are only meaningful in the case when a continuous periodic strain is applied to the sample and the probe–sample system is in steady state, which in AFM requires a contact-mode measurement such as contact-resonance AFM (CR-AFM) [3-5] or dual amplitude resonance tracking (DART) [4]. When the applied strain is not continuous and periodic, and the measurement process is not in steady state, it becomes extremely difficult to quantify viscoelastic behaviors in a meaningful way. Nevertheless, other authors [6-8] have very successfully implemented experimental intermittent-contact multi-frequency AFM methods that allow the extraction of analytical tip–sample interaction expressions in which the force is expressed as the sum of a Hertzian conservative interaction plus an indentation- and velocity-dependent dissipative interaction. Such 1-dimensional (1D) models have, for example, been used in the characterization of polymers [8,9], providing a modulus of elasticity and 'dissipation' parameters, which can be practical and efficient in a variety of situations. Nevertheless, further developments still remain in terms of model improvements that consider the most fundamental behaviors of viscoelastic bodies. Specifically, the above analytical models cannot reproduce stress relaxation and creep [10,11]. Within AFM, this means that when the tip and sample are held in contact at a fixed relative position, the model must exhibit a time-dependent reduction in the stress (stress relaxation). Additionally, when the tip and sample are held in contact at a fixed stress, the model must exhibit a time-dependent relaxation of the position of the sample directly under the tip. That is, the sample must yield, allowing the tip to gradually increase the depth of indentation. Furthermore, if the tip is quickly removed following yielding of the surface, the surface must remain depressed, with a cavity in it, and gradually relax afterwards. In particular, if the tip–sample interaction is of an intermittent contact nature, it may possible that the surface does not fully return to the original (undisturbed) position before the tip impacts it again. That is, during the second impact the tip may find the surface at a lower position than prior to the previous impact. These behaviors are discussed in detail in [10,11].

In an effort to provide a more fundamentally correct viscoelastic description of the surface, in recent intermittent-contact AFM studies we have used the 1D standard linear solid (SLS) model, which is a well-known textbook problem in viscoelasticity. The model is illustrated in Figure 1a and consists of a linear spring (k_1) in parallel with a 'Maxwell arm,' which in turn consists of a linear spring (k_2) in series with a linear damper (c). When a stress (force) or a strain (displacement) is applied to the model, spring k_1 yields and generates a repulsive force that is proportional to the instantaneous displacement of the 'surface.' In the Maxwell arm spring k_2 yields also producing a repulsive force, but in this case the force is proportional to the instantaneous displacement of the 'surface' minus the instantaneous displacement of the damper, which relaxes with a speed that is proportional to the instantaneous force generated by spring k_2. The presence of the Maxwell arm, where complete relaxation of the stress (force) is possible, in parallel with the linear spring k_1 allows the model to exhibit the desired viscoelastic behaviors, namely stress relaxation, creep, and also the ability to fully but gradually (not instantaneously) recover when all forces are removed. Additional details on stress relaxation and creep simulations are provided in [10]. Figure 1b and Figure 1c give examples of tip–sample force curves for intermittent-contact AFM in single- and multifrequency operation, respectively, when using the SLS model to represent the surface. As can be seen, the force curve shows separate force minima for the position where the tip first reaches the sample, and the position where it leaves the sample. These locations can be different due to creep of the surface. Furthermore, the model can be enhanced with multiple relax-

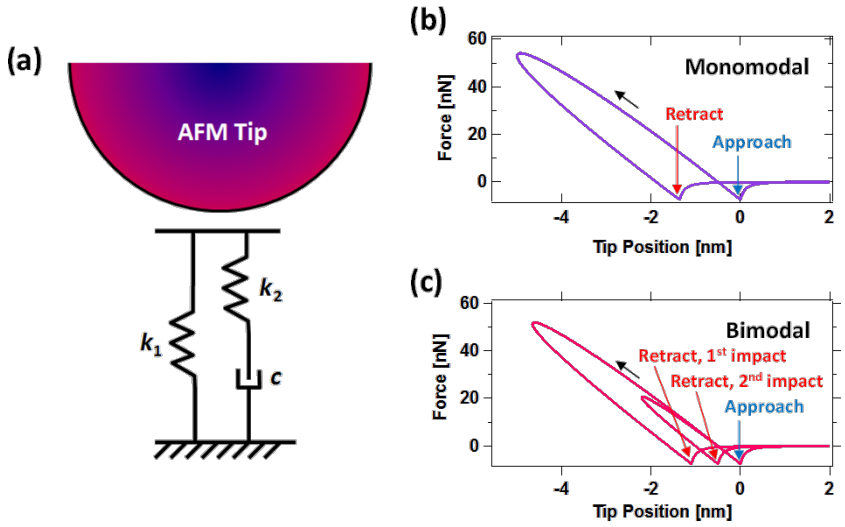

Figure 1: (a) Schematic of AFM tip interacting with the standard linear solid model; (b) example of force curve for monomodal AFM; (c) example of force curve for bimodal AFM, showing a double impact. The blue arrows indicate in each case the position where the tip first reaches the sample, and the red arrows indicate the position where the tip leaves the sample. Van der Waals forces have been included in the attractive (noncontact) region.

ation times by adding additional Maxwell arms (additional elements, each consisting of a linear spring in series with a damper), whereby these combined elements are placed in parallel with the SLS (a more complete description of these models and their advantages and disadvantages in the context of AFM is provided in [10,11]). Although the use of the SLS model in AFM is a step forward in terms of the physics of viscoelasticity, this linear model gives force curves that do not have the correct curvature in the repulsive region. It is clear in Figure 1b and Figure 1c that the force curve is concave downward instead of concave upward. The linear springs in the model lead to straight (linear) force curves, which become concave downwards as the surface creeps, via relaxation of the damper and spring k_2. The incorrect curvature of the force curve is a serious shortcoming of the 1D SLS model within AFM, because it precludes the quantitative interpretation of the results of an experiment in terms of a real 3D tip interacting with a flat surface, and thus makes it impossible to extract approximate parameters such as the Young's modulus [12]. It is clear in Figure 1a that the geometry of the tip and its indentation depth into the surface have absolutely no effect on the nature of the tip–sample interaction when a 1D model is used, unless the user explicitly programs geometric effects into the model, for example through the use of nonlinear springs [11].

In CR-AFM and DART [3-5] surface viscoelasticity is generally interpreted in terms of the Kelvin–Voigt model, consisting of a linear spring in parallel with a damper. This is appropriate (i) when the tip oscillation amplitude is very small, since in this regime the small segment of the force curve that is involved can be treated as quasi-linear, and (ii) when the tip and sample are in permanent contact (that is, the tip does not oscillate faster than the surface can relax). From this type of measurement one can extract storage and loss moduli, given proper calibration. The method has been enhanced by performing tomographic (volume) scanning [13], such that one can obtain the entire force curve via a 3D measurement. One can then analyze the depth dependence of the contact stiffness by performing a fit to appropriate models of elastic, viscous and adhesive forces, as is demonstrated in [13] for polymer blends. This approach is associated with small tip oscillations and is sensitive to the speed at which the base of the cantilever is approached towards and retracted from the sample. The method can be easily enhanced by relaxing the small oscillation amplitude requirement and using a variety of cantilever speeds to carry out the volume scan, although this may, in general, require the use of more complex tip–sample conservative–dissipative models within a simulation framework, in order to properly interpret the results.

If the highest accuracy is desired in AFM modeling, it is necessary to advance towards a model in which the various types of tip–sample interactions can be incorporated and tuned independently: long-range attractive forces (such as dispersion, electrostatic, magnetic), adhesive forces (such as chemical, capillary), viscoelastic forces, plastic forces, etc. For the case of viscoelasticity, in the most elaborate case one would need to solve the relaxation of the surface in 3D with the appropriate constitutive relation, as in the finite elements method (FEM), coupled with the dynamics of the cantilever. Given the number of research directions in which the AFM community is rapidly advancing, this may be unrealistic in terms of the knowledge and time required on the part of the user and in terms of computational

cost. Nevertheless, it is important to gradually advance in that direction. To this end, the present paper introduces a quasi-3D (Q3D) surface model, along with a basic software tool, which consists of a 2D-periodic array of 1D-SLS models. This intermediate approach naturally incorporates important effects such as tip geometry effects (allowing for ideal and non-ideal tip shapes) and changes in the attractive forces due to changes in the surface geometry, following indentation and incomplete relaxation. Additionally, the Q3D model naturally leads to repulsive force curves that are concave upwards for spherical tips.

The subsequent sections of this paper provide (i) an overview the model features in the context of single- [12] and multifrequency [14,15] AFM characterization, (ii) a description of the simulation methodology, and (iii) a brief description of the software tool, which is provided as supplementary information.

Results and Discussion

Description and illustration of the Q3D model

The Q3D model consists of a 2D array of SLS models, as illustrated in Figure 2a. This is not a true 3D model since it is not based on a constitutive equation that describes the properties of the volume of material under the surface. Instead, it consists of 'small' SLS models distributed evenly in the x- and y-directions of the surface, each of which can relax independently in the z-direction upon interaction with the tip, which is modeled here as a hard sphere attached to the AFM cantilever. As depicted in Figure 2b, the degree of relaxation of each individual SLS model is dictated by the geometry of the tip. Given the spherical symmetry of the ideal AFM tip, it is convenient to use polar coordinates, whereby the surface is modeled as a set of concentric rings (Figure 3), in which the radial coordinate is partitioned into equal segments of length Δr, and the width of each element is defined by Δr. Additionally, we consider that each element is connected to a SLS whose parameters are proportional to its surface area, $A = \pi\left(r_{i+1}^2 - r_i^2\right)$. This reduces significantly the computation time required to calculate the interactions of the model with the tip. However, the imposition of radial or any type of symmetry is not a requirement and any arbitrary distribution of SLS parameters over the 2D surface can be defined either in rectangular or polar coordinates. For brevity and simplicity this paper illustrates only the case of radially

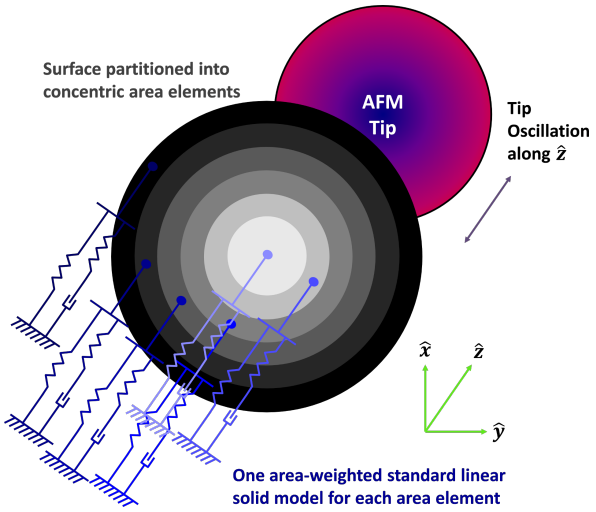

Figure 3: Illustration of the proposed model for a spherically symmetric AFM tip oscillating along the z-axis. Each concentric ring element is connected to an individual SLS model, whose parameters are proportional to the area of the ring.

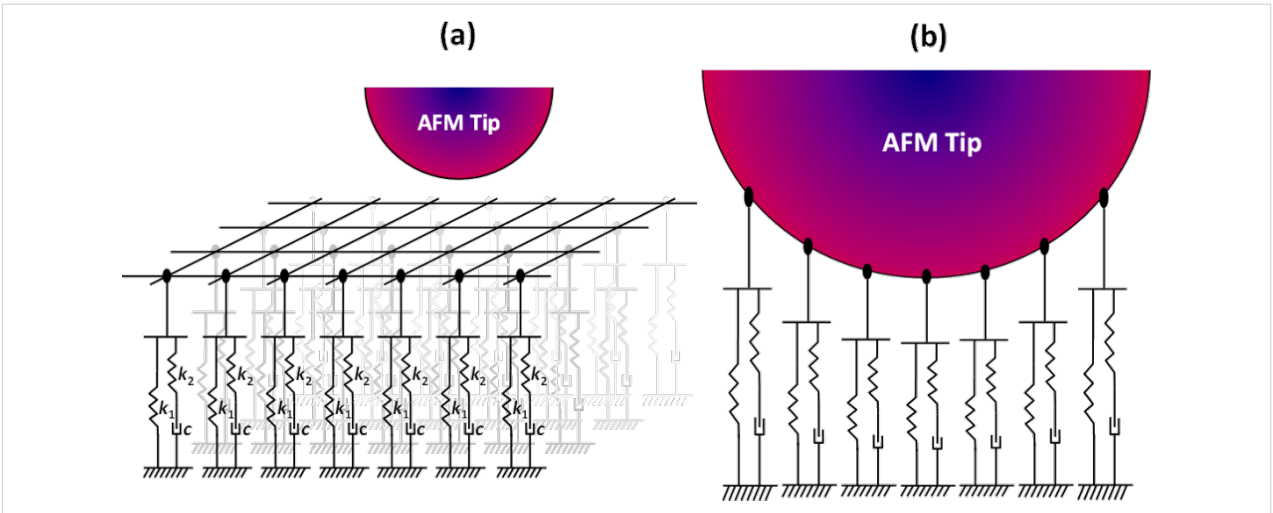

Figure 2: (a) Illustration of AFM tip approaching a 2-dimensional array of SLS models; (b) illustration of AFM tip interacting only with the SLS models directly below it, and interacting to a different depth with each element, as dictated by its geometry. Each SLS model in (a) and (b) is of the same form as the one shown in Figure 1a.

symmetric AFM tips and surfaces, including a defective tip that has a cluster protruding from its apex (this is described below). Similarly, the software tool provided assumes radial symmetry, but it can be easily modified to allow deviations from it.

Figure 4a shows a typical force curve for the Q3D model, which in contrast to the results provided in Figure 1, does have the correct qualitative (upward) concavity in the repulsive region, which occurs because the tip interacts with an increasing number of SLS elements as the indentation increases and the contact area grows. This is illustrated in Figure 4b, which shows an example of the tip–sample force contributions of different area elements that add up to give the total force. Additionally, similar to the SLS, the Q3D force curve shows the qualitatively correct relaxation of the surface, with the surface remaining depressed upon rapid retract of the AFM tip following each impact, depending on the model parameters (see discussion of Figure 1b above). Finally, it is worth noting that the force minima for the approach and retract have a different force magnitude in Figure 4a. This is caused by a temporary cavity that remains on the surface upon tip retract, such that depending on the SLS parameters chosen, this cavity partially encloses the tip as it leaves the sample. This allows the sample surface to interact closely with a larger portion of the tip, compared to a flat sample surface (see Figure 4c), leading to greater van der Waals attractive forces during tip retract (this is also discussed in [10]). Figure 4d shows two force curves for the Q3D model in multifrequency AFM operation for different higher mode amplitudes, which exhibit the expected qualitative features (compare to the curve in Figure 1c). As expected, a larger amplitude in the higher eigenmode also leads to greater indentation during each impact [16].

Even limiting the simulations to radially symmetric tips and samples, there is a wide range of phenomena that can be studied with the Q3D model, such as irregular tips, which are not uncommon. Figure 5a shows an force curve for a tip with a narrow protrusion at the apex, which leads to surprising anomalies, which at first glance may seem unreasonable. However, careful inspection leads to the eye-opening conclusion that this is not so: The region of the curve labeled with the number ‘1’ shows a small force minimum indicating that the apex protrusion is reaching the surface, experiencing van der Waals interactions, but has not yet reached the repulsive regime, which is labeled with the number ‘2’. Region ‘3’ indicates that the rest of the tip is approaching the surface and experiencing a significant attractive force that overcomes the repulsive regime from the small protrusion (this is reasonable because the tip is significantly larger than the protrusion). Finally, in region ‘4’ the entire tip and its apex protrusion are in the repulsive force regime. The retract portion of the curve is similar to the approach but has offsets in the two force minima due to relax-

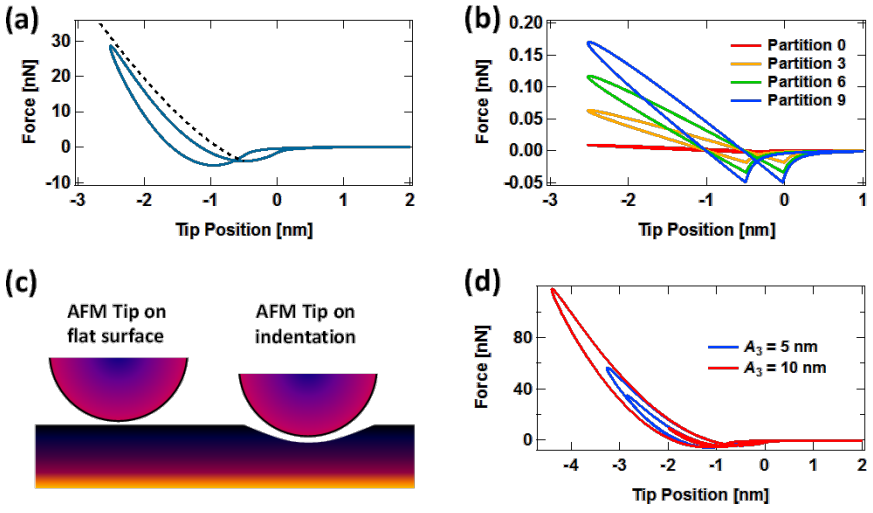

Figure 4: (a) Typical force curve for a spherical tip interacting with the Q3D surface model in monomodal tapping-mode imaging (the dashed line is a plot of a Hertzian curve, for reference); (b) illustration of the contributions to the force curve from different concentric-ring surface elements (numbered starting with the element that intersects the tip vertical axis): as the tip indents deeper into the sample, new surface elements of increasingly larger area become active and contribute to the force curve (recall that the SLS contribution of each surface element is proportional to its area); (c) schematic of the greater van der Waals interaction for a tip interacting with a cavity on the surface with respect to a tip interacting with a flat surface; (d) typical Q3D force curves for bimodal AFM imaging using the first and third eigenmodes. Note that the level of indentation increases as A_3 increases. Note also the resemblance to the force curve shown in Figure 1c. For (a), (b) and (d) the cantilever was placed at a height of 75 nm above the surface and the following parameters were used: first free oscillation amplitude A_1 = 100 nm, third free oscillation amplitude A_3 = 5 and 10 nm (as shown in (d)), fundamental frequency v = 70 kHz, fundamental force constant k = 4 N/m, eigenmode quality factors Q_1 = 150, Q_2 = 450, Q_3 = 750; tip radius of curvature R = 20 nm, and SLS parameters (see Figure 1) $k_1 = k_2 = 7.5 \times 10^{-2}$ N/m/nm^2, and $c = 1.0 \times 10^{-7}$ N s/m/nm^2 (monomodal AFM) and 2.5×10^{-8} N s/m/nm^2 (bimodal AFM).

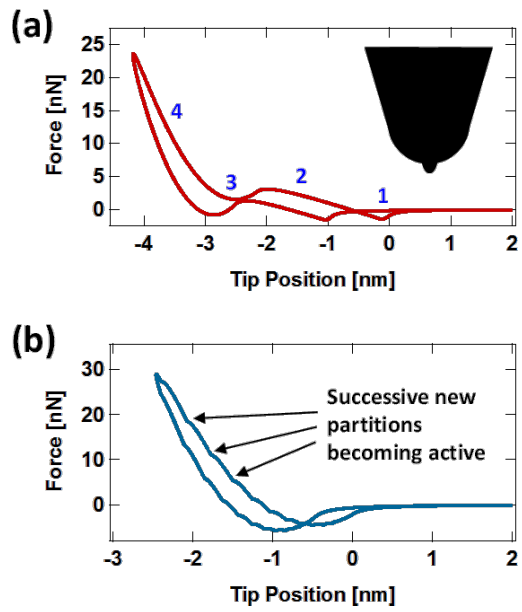

Figure 5: (a) Force curve for a 20 nm radius tip with a 2.5 nm radius protrusion at its apex as shown in the inset. The blue labels on the curve indicate the locations where, (1) the apex protrusion is approaching the surface in the attractive regime, (2) the apex protrusion is experiencing repulsive forces, (3) the rest of the tip is approaching the surface in the attractive regime, and (4) the entire tip is experiencing repulsive forces. The retract portion of the curve is similar to the approach but shows the expected offsets in the force minima, which are a consequence of viscoelastic relaxation. (b) Oscillations in the force curve due to the use of too coarse a surface partition. The simulation parameters are the same as for Figure 4, except for the irregular tip geometry in (a) and the coarser partition in (b) described in the text.

ation of the surface, as previously discussed. There are other types of more subtle tip irregularities which are rarely considered in the literature, but which could be important in a quantitative study and which can be easily evaluated with the Q3D model (without losing sight of its limitations, as discussed below), such as slightly flattened tips or tips with a parabolic profile. Note, however, that anomalies in the calculated force curve may also be the result of non-optimized simulation parameters. For example, the force curve shown in Figure 5b exhibits a series of kinks that are caused by the use of a coarse surface partition (i.e., the concentric ring elements in the surface model are too large or, conversely, too few area elements have been used to describe the surface). The smooth force curves shown in Figure 4 were obtained with a partition where Δr was set to (1/180)R, where R is the tip radius of curvature, while the curve of Figure 5b is based on a partition that is six times coarser.

An important consideration in the use of the Q3D model is the question of calibration against experimental observables. Since the force interactions that are obtained with the model can be highly dependent on the imaging parameters and the geometry of the tip, it is not generally possible to derive analytical expressions that provide the tip–sample force in terms of continuum properties. This is especially true for the intermittent-contact AFM case, where such analytical inversion is not possible even with the simple 1D SLS model, as discussed extensively in reference [10]. Nevertheless, to aid in the interpretation of experiments it is possible to carry out calibration procedures in which an experiment is performed and the Q3D model parameters are adjusted to match the experimental observations. An example of this could be the construction of a frequency response curve (amplitude vs frequency) under different values of the static deflection (with the deflection setpoint fixed for every simulation), which can be directly compared to CR-AFM measurements carried out under the same conditions. This could be especially valuable if, in addition to the CR-AFM observables, an image of the tip geometry is available, which would allow for the incorporation of geometry effects into the simulations. A second type of calibration may be the acquisition of static force distance curves in which the deflection is measured while the cantilever approaches and retracts from the surface at a fixed speed. To enhance the calibration, a collection of such curves could be constructed at different cantilever speeds. These considerations on model calibration suggest that a useful avenue of research may be the study of tip–sample force 'signatures' for different viscoelastic models, as proposed through simulations in [17], where the tip–sample interaction force curve is acquired using spectral inversion methods [18,19] and the force is plotted not only in terms of position but in terms of both position and velocity (that is, the force is expressed as $F(z,\dot{z})$ instead of simply $F(z)$). This enhanced representation may make it possible to invert the AFM observables to obtain viscoelastic model parameters. At this time this approach is still limited by experimental capabilities in the recording of the force spectrum [17,20] as well as by the lack of theoretical development required to infer viscoelastic model properties from such curves.

In order to place the Q3D model in the proper perspective it is important to discuss not only the advantages it offers, but also its shortcomings. The first shortcoming derives directly from its simplicity and computational efficiency: since the individual SLS elements do not interact with one another, the model does not consider material relaxations in the horizontal directions. As a result, it cannot be used as a 'first-principles' simulation tool, but instead only as a fitted tool that requires calibration either via experiments or more elaborate calculations (e.g., FEM simulations). A second limitation, which is related to the above, is that the model surface has no internal cohesiveness. As a result, the indentation profiles at static deflection will always follow the shape of the tip. That is, the largest cavity that the tip

can induce is equal to the size of the tip. This is not the case in practice for most surfaces, where the size of the cavity is often expected to be larger than the diameter of the tip. To understand this, consider an AFM tip that is a perfect cube and impacts the sample with one of its faces oriented parallel to the sample surface. Within the Q3D model the indentation will be a perfectly square hole with vertical side walls, with the perimeter of the hole being exactly the same as the square perimeter of the tip. In a real experiment, the side walls would not be perfectly vertical but would instead be tapered, giving a cavity that is wider than the cross section of the tip. The Q3D model becomes less realistic for very large indentations, near and beyond the tip radius of curvature, and for very sharp tip geometries. These limitations can be partially mitigated by adding additional viscous and elastic elements between adjacent surface locations, although these would come with an added computational cost.

Experimental

Cantilever dynamics modeling

The dynamics of the AFM cantilever were modeled as in previous studies [16] using one equation of motion for each of the first three eigenmodes, whereby the three equations are simultaneously integrated numerically, coupled through the tip-sample force. Each equation is of the form

$$m\ddot{z}_i + \frac{m\omega_i}{Q_i}\dot{z}_i + k_i z_i = F_{ts} + \sum_i F_i \cos\left(\omega_{d,i} t\right), \qquad (1)$$

where m is the cantilever mass, z_i is the eigenmode displacement as a function of time, ω_i is the resonance frequency of the eigenmode, Q_i its quality factor and k_i its dynamic force constant. Additionally, F_{ts} is the total tip–sample force and the last term on the right hand side is the sum of the sinusoidal driving forces included for the various eigenmodes. Each term consists of an excitation force amplitude (F_i) and a cosine term that depends on the respective excitation frequency $\omega_{d,i}$ and time t. Excitation force terms were included for all three eigenmodes, each matching the corresponding eigenfrequency and having a magnitude that yields the desired free oscillation amplitude. The total tip–sample force term F_{ts} consists of the repulsive forces generated by the Q3D model (these are calculated numerically since there does not exist an analytical expression to calculate them [10]) plus attractive van der Waals forces, which are included for each area element in the Q3D model via an equation similar to the Hamaker equation [12]. Thus, the contribution to the van der Waals forces for area element j is

$$F_{\text{vdw},j} = V/d^2 \qquad (2)$$

where V is a van der Waals 'strength' parameter in the code (see c-file in Supporting Information File 1) that adjusts the magnitude of the van der Waals interaction between each individual SLS element and the tip, and d is the distance between element j and the tip surface. The amplitude and phase of each eigenmode were calculated using the in-phase (I_i) and quadrature (K_i) integrals:

$$I_i = \int_{N\tau_i} z_i(t)\cos\left(\omega_{d,i} t\right) dt, \qquad (3)$$

$$K_i = \int_{N\tau_i} z_i(t)\sin\left(\omega_{d,i} t\right) dt, \qquad (4)$$

where $z_i(t)$ is the eigenmode response in the time domain, as in Equation 1, N is the number of periods over which the phase and amplitude were averaged, $\omega_{d,i}$ is the excitation angular frequency, and τ_i is the nominal period of one oscillation of the eigenmode. The amplitude A_i and phase ϕ_i were calculated, respectively, as:

$$A_i = \frac{\omega_{d,i}}{\pi N}\sqrt{I_i^2 + K_i^2}, \qquad (5)$$

$$\varphi_i = \tan^{-1}\left(K_i/I_i\right). \qquad (6)$$

Software tool description

The software tool, written in standard C programming language, provided within Supporting Information File 1, consists of an implementation of the above multifrequency (trimodal) cantilever dynamics in the construction of a point-by-point amplitude-modulation (AM-AFM) spectroscopy curve (amplitude and phase vs cantilever height), although other controls schemes as well as line scanning can easily be implemented, depending on the problem under study. To construct the spectroscopy curve, the user edits an input file which must be located in the same directory as the program executable file and contains the output file root name, the fundamental frequency and force constant (the higher-order frequencies and force constants are estimated based on an ideal rectangular cantilever), the first three quality factors, the starting height of the cantilever above the sample (at the beginning of the spectroscopy experiment), the target oscillation amplitudes for the three eigenmodes and the SLS parameters normalized by surface unit area. The software then performs a simulation in which the cantilever is set at successively lower heights above the surface and driven until it has reached steady state at each

height. At this point, calculation of the phase and amplitude begins along with recording of the data in the output files. The program creates one output file for each cantilever height, which contains the most relevant dynamic information (such as time, instantaneous tip position, instantaneous value of each eigenmode coordinate, instantaneous tip–sample force, instantaneous amplitude, phase). In addition, the program also produces a second output file at the end of the run, which contains the amplitude, phase, peak force and peak indentation recorded for each value of the cantilever height. Figure 6 provides an example of the spectroscopy data obtained, which exhibits the expected features [12,16].

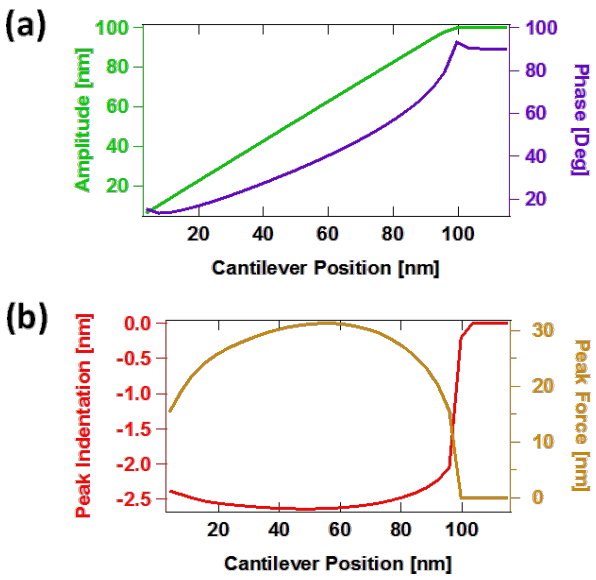

Figure 6: Examples of spectroscopy curves: (a) amplitude and phase vs cantilever position; (b) peak indentation and peak force vs cantilever position (these two quantities are not directly observable in a spectroscopy experiment). The simulation parameters are the same as for monomodal AFM in Figure 4.

A variety of comments are provided throughout the code to aid the user in following the logic. Thus, it is quite easy to modify settings such as the settling time, printstep, the desired quantities in the output files, timestep (a reduction of the timestep should be considered for cantilevers with very high fundamental frequencies, in the MHz regime), number of cantilever height points in the spectroscopy curve, etc.

During benchmarking on an Intel® Xeon® Processor E5-1660 v3 (3.0 GHz) the code completed an equilibrated run at a fixed cantilever height in approximately 120 min. Thus, the total time required to construct the full spectroscopy curve was approximately equal to 120 min times the number of points in the curve.

Conclusion

A quasi-3D viscoelastic model, consisting of a 2D array of standard linear solid elements has been proposed for the simulation of AFM imaging of viscoelatic surfaces. An efficient and easily modifiable software tool for the construction of amplitude and phase spectroscopy curves has also been provided as Supporting Information. The model correctly reproduces the key features of tip–sample interaction force curves acquired on a sample that exhibits stress relaxation and creep. In particular, the model qualitatively reproduces the upward curvature of the force curve in the repulsive region, as well as the relaxation and magnitude variation of the attractive force minima, which are a consequence of temporary variations in the surface geometry, following indentation by the tip. The model is a step forward in terms of introducing more accurate physics into the modeling of viscoelastic soft matter within AFM while keeping the computational cost relatively low, and can be further enhanced through the introduction of additional springs and dampers connecting adjacent SLS elements, through the use of 1D models with more than one relaxation time, or through the use of nonlinear elements [11].

Supporting Information

Supporting Information consists of a ZIP archive containing three files: A program manual (Trimodal_AFM_with_Quasi3D_SLS+-+Files+Description.pdf) describing the content of the software files and their usage, the program source file written in C programming language (Trimodal_AFM_with_Quasi3D_SLS.c) and the input file for user-defined parameters (input.txt).

Supporting Information File 1

Program sources and manual.
[http://www.beilstein-journals.org/bjnano/content/supplementary/2190-4286-6-229-S1.zip]

Acknowledgements

The author gratefully acknowledges support from the U.S. Department of Energy, Office of Science, Basic Energy Sciences through award DESC0011912.

References

1. Cleveland, J. P.; Anczykowski, B.; Schmid, A. E.; Elings, V. B. *Appl. Phys. Lett.* **1998,** *72,* 2613–2615. doi:10.1063/1.121434
2. Martínez, N. F.; García, R. *Nanotechnology* **2006,** *17,* S167–S172. doi:10.1088/0957-4484/17/7/S11
3. Rabe, U.; Janser, K.; Arnold, W. *Rev. Sci. Instrum.* **1996,** *67,* 3281–3293. doi:10.1063/1.1147409

4. Killgore, J. P.; Yablon, D. G.; Tsou, A. H.; Gannepalli, A.; Yuya, P. A.; Turner, J. A.; Proksch, R.; Hurley, D. C. *Langmuir* **2011,** *27,* 13983–13987. doi:10.1021/la203434w
5. Stan, G.; King, S. W.; Cook, R. F. *Nanotechnology* **2012,** *23,* 215703. doi:10.1088/0957-4484/23/21/215703
6. Platz, D.; Forchheimer, D.; Tholén, E. A.; Haviland, D. B. *Nanotechnology* **2012,** *23,* 265705. doi:10.1088/0957-4484/23/26/265705
7. Borysov, S. S.; Platz, D.; de Wijn, A. S.; Forchheimer, D.; Tolén, E. A.; Balatsky, A. V.; Haviland, D. B. *Phys. Rev. B* **2013,** *88,* 115405. doi:10.1103/PhysRevB.88.115405
8. Herruzo, E. T.; Perrino, A. P.; Garcia, R. *Nat. Commun.* **2014,** *5,* 3126. doi:10.1038/ncomms4126
9. Dietz, C.; Schulze, M.; Voss, A.; Rieschc, C.; Stark, R. W. *Nanoscale* **2015,** *7,* 1849–1856. doi:10.1039/c4nr05907g
10. Solares, S. D. *Beilstein J. Nanotechnol.* **2014,** *5,* 1649–1663. doi:10.3762/bjnano.5.176
11. López-Guerra, E. A.; Solares, S. D. *Beilstein J. Nanotechnol.* **2014,** *5,* 2149–2163. doi:10.3762/bjnano.5.224
12. García, R.; Pérez, R. *Surf. Sci. Rep.* **2002,** *47,* 197–301. doi:10.1016/S0167-5729(02)00077-8
13. Stan, G.; Solares, S. D.; Pittenger, B.; Erina, N.; Su, C. *Nanoscale* **2014,** *6,* 962–969. doi:10.1039/c3nr04981g
14. Rodríguez, T. R.; García, R. *Appl. Phys. Lett.* **2004,** *84,* 449–451. doi:10.1063/1.1642273
15. Garcia, R.; Herruzo, E. T. *Nat. Nanotechnol.* **2012,** *4,* 217–226. doi:10.1038/nnano.2012.38
16. Ebeling, D.; Eslami, B.; Solares, S. D. *ACS Nano* **2013,** *7,* 10387–10396. doi:10.1021/nn404845q
17. Williams, J. C.; Solares, S. D. *Beilstein J. Nanotechnol.* **2013,** *4,* 87–93. doi:10.3762/bjnano.4.10
18. Stark, M.; Stark, R. W.; Heckl, W. M.; Guckenberger, R. *Proc. Natl. Acad. Sci. U. S. A.* **2002,** *99,* 8473–8478. doi:10.1073/pnas.122040599
19. Sahin, O.; Magonov, S.; Su, C.; Quate, C. F.; Solgaard, O. *Nat. Nanotechnol.* **2007,** *2,* 507–514. doi:10.1038/nnano.2007.226
20. Solares, S. D.; Hölscher, H. *Nanotechnology* **2010,** *21,* 075702. doi:10.1088/0957-4484/21/7/075702

License and Terms

BEILSTEIN JOURNAL OF NANOTECHNOLOGY

Large area scanning probe microscope in ultra-high vacuum demonstrated for electrostatic force measurements on high-voltage devices

Urs Gysin*[1], Thilo Glatzel[1], Thomas Schmölzer[2], Adolf Schöner[3], Sergey Reshanov[3], Holger Bartolf[2] and Ernst Meyer[1]

Full Research Paper

Open Access

Address:
[1]Department of Physics, University of Basel, Klingelbergstrasse 82, CH-4056 Basel, Switzerland, [2]ABB Corporate Research Center, Segelhofstrasse 1K, CH-5404 Baden-Dättwil, Switzerland and [3]Ascatron AB, Electrum 207, SE-16440 Kista, Sweden

Email:
Urs Gysin* - urs.gysin@unibas.ch

* Corresponding author

Keywords:
copper alloy; electrostatic force microscopy; high-voltage device; Kelvin probe force microscopy; silicon carbide (SiC); surface photo voltage

Beilstein J. Nanotechnol. **2015,** *6,* 2485–2497.
doi:10.3762/bjnano.6.258

Received: 09 October 2015
Accepted: 08 December 2015
Published: 28 December 2015

This article is part of the Thematic Series "Noncontact atomic force microscopy III".

Guest Editor: M. Z. Baykara

Abstract

Background: The resolution in electrostatic force microscopy (EFM), a descendant of atomic force microscopy (AFM), has reached nanometre dimensions, necessary to investigate integrated circuits in modern electronic devices. However, the characterization of conducting or semiconducting power devices with EFM methods requires an accurate and reliable technique from the nanometre up to the micrometre scale. For high force sensitivity it is indispensable to operate the microscope under high to ultra-high vacuum (UHV) conditions to suppress viscous damping of the sensor. Furthermore, UHV environment allows for the analysis of clean surfaces under controlled environmental conditions. Because of these requirements we built a large area scanning probe microscope operating under UHV conditions at room temperature allowing to perform various electrical measurements, such as Kelvin probe force microscopy, scanning capacitance force microscopy, scanning spreading resistance microscopy, and also electrostatic force microscopy at higher harmonics. The instrument incorporates beside a standard beam deflection detection system a closed loop scanner with a scan range of 100 µm in lateral and 25 µm in vertical direction as well as an additional fibre optics. This enables the illumination of the tip–sample interface for optically excited measurements such as local surface photo voltage detection.

Results: We present Kelvin probe force microscopy (KPFM) measurements before and after sputtering of a copper alloy with chromium grains used as electrical contact surface in ultra-high power switches. In addition, we discuss KPFM measurements on cross sections of cleaved silicon carbide structures: a calibration layer sample and a power rectifier. To demonstrate the benefit of surface photo voltage measurements, we analysed the contact potential difference of a silicon carbide p/n-junction under illumination.

Introduction

Scanning probe microscopy (SPM) is nowadays an established technological approach for surface analysis in many different research fields. Applications can be found in areas of life science measuring the properties of cells in buffer solution, submolecular structure of single molecules in ultra-high vacuum (UHV) conditions but also in areas which face the characterization of semiconductor devices. The common technical principle is always related to a conical tip attached to a cantilever which is accurately positioned at the specimen of interest and which is scanned over a certain surface area. The tip height is controlled by a feedback loop correlating the tip–sample interaction with the deflection of the cantilever. However, the interaction force contains many different components which can only be partly suppressed (e.g., magnetic forces when inspecting non-magnetic materials), separated (e.g., electrostatic forces from magnetic forces), or be dynamically compensated (e.g., by tuning the bias voltage in Kelvin probe force microscopy (KPFM)) and measured together with the topological information. For all these properties various experimental approaches have been proposed, successfully demonstrated, and found their way into commercially available SPM systems. However, the unperturbed measurements and the interpretation of the acquired data remains the most challenging task which requires a sophisticated fundamental interpretation.

In recent years, especially the detection of electrostatic forces and the determination of local work function values was intensively discussed and models combining large scale influences with atomistic simulations have been developed [1-4]. As early as in the late 1980s H. Wickramasinghe proposed several SPM based methods for the local analysis of the electrical properties of conducting and semiconducting materials down to the nanometre scale [5-12]. These techniques rapidly emerged [13-17] and were developed further on resulting in more sophisticated methods such as scanning spreading resistance microscopy (SSRM) [18-20] and scanning capacitance microscopy (SCM) [21-23]. However, since atomic force microscopy (AFM) [24] was demonstrated to analyse surfaces down to the nanoscale, most of the commercial microscopes are limited to high resolution in UHV or can only be used under ambient conditions. However, for the characterization of complex semiconductor devices large area scans with the possibility of taking high resolution images at dedicated areas under inert conditions are mandatory.

The instrument described in the first part of this article allows for investigations on a scale of up to 100 µm in lateral and 25 µm in vertical direction under UHV conditions and at room temperature using a large-scale closed-loop scanner. Beside the topographic non-contact AFM mode also contact measurements as well as all major electrical characterization methods (SSRM, SCM, KPFM) are implemented. Additionally, the samples can be optically exited by an external light source (UV–vis) which is introduced by a separate light fibre. An in situ piezo-electric alignment stage allows to focus and position the light exactly below the cantilever tip apex. Therefore, the setup allows for the measurement of the surface photo voltage (SPV) in dependence on the wavelength and light intensity via measuring of the contact potential difference (CPD) values in the dark as well as under illumination [25]. In the second part we present several studies highlighting the potential of the novel instrument. Firstly, we discuss KPFM results from a contact surface of a copper alloy utilized in a power switch. The presence and shape of chromium grains embedded in the copper alloy are clearly visible. The contrast in the measured work function is strongly enhanced by sputtering the sample with argon ions to remove the oxide layer. Second, two different silicon carbide (SiC) devices are analysed and discussed. A calibration layer structure containing precisely defined p/n-interfaces is used to elaborate the challenges associated to KPFM and SPV measurements on semiconducting surfaces. Furthermore, a complex SiC structure of a power semiconductor device is observed by means of large area KPFM measurements. The structure is a junction barrier Schottky (JBS) rectifier-architecture [26]. We observe the termination region of the device, where highly doped p^+-rings are embedded into a large p-type ring. These p-regions diminish the high electric field under reverse bias conditions inside the active area of the device such the the electric field gets properly terminated towards the outer rim of the device without causing unintended field peaks. Such termination regions are relatively large, therefore their detailed inspection by KPFM is only feasible due to the implemented large scan range unit.

Experimental

The atomic force microscope (AFM) [24] developed and built in our physics department is placed in an ultra-high vacuum (UHV) system with a base pressure of $<10^{-9}$ mbar. Operating the instrument under UHV condition has the advantage of a high quality factor ($Q \approx 30{,}000$) due to the suppression of viscous damping and therefore increases the force sensitivity by orders of magnitude [27,28]. To analyse complex and large micro-structures a large positioning and scanning unit is necessary, under ambient conditions scan areas as large as 100×100 µm^2 are available. Furthermore, the novel system provides a dedicated opto-electrical characterization using all major SPM techniques. In the following we will describe the key components of the new AFM.

Beam deflection unit with optical excitation optics

A fundamental design criteria in atomic force microscopy is an accurate oscillation control of the cantilever, allowing to use amplitudes in the range of 0.1–100 nm while keeping a constant tip–sample distance. Furthermore, a good visibility to the tip–sample interface is favourable in order to appropriately align the system. Beam deflection detection of cantilever oscillations is an ideal technique to fulfill these demands [29]. The light source may be placed quite far away (typically some centimetres) from the cantilever allowing for a direct optical access and the beam of light can be focused onto the free oscillating end of the cantilever. The reflected light is detected with a position sensitive diode (PSD, Hamamatsu S5980). In our case the light source is a super luminescent diode (Superlum SLD-371-HP1) with a spectral centre at 838 nm and a bandwidth of 55 nm, which is placed outside the vacuum system for reasons of thermal stability. The maximum optical power output of the diode is 7 mW. The light emitted from the diode is fed into the vacuum chamber through a single mode fibre (Fiberguide ASI4.3/125) and a custom designed optical vacuum feedthrough to the focusing optics consisting of two lenses. The first lens with a focal length of 6 mm collimates the incoming light from the fibre whereas the second lens focuses the light through a beam splitter to the free end of the cantilever. The focal length is 30 mm. The optimum spot size on the cantilever free end is then the inner core diameter of the single mode fibre, in our case 4.3 µm. The optical path of this arrangement provides good visibility with an optical microscope (Olympus SZ61) from the top of the vacuum chamber through a view-port to the tip–sample interface through the beam splitter, as sketched in Figure 1a.

Figure 1b presents a computer aided design (CAD) image of the beam deflection unit. The red arrows indicate the directions of motion of the adjustable parts of the unit. To align the beam of light onto the free end of the oscillating cantilever several shear piezo actuators allow for the movement of parts within the beam deflection unit. The focusing optics is placed on two shear piezo elements in order to allow for horizontal movement and to adjust the light beam across the width of the cantilever. Additionally, the beam splitter is placed on two shear piezo elements rotating the beam splitter and therefore align the light beam along the long axis of the cantilever. The reflected light from the cantilever irradiates directly onto the PSD with an adapted current to voltage converter (*IV*-converter). The detection unit, consisting of the PSD and *IV*-converter, may be moved by three 2D shear piezo elements, adjusting the reflected light beam into the centre of the PSD. The AFM performs best when all four segments of the PSD are equally illuminated.

Surface photo voltage (SPV) effects enable the analysis of optoelectric sample properties and allows to minimize band bending effects at the surface of a semiconducting sample to accurately measure bulk properties by KPFM [25,30-35]. For this purpose we implemented an additional optics based again on two lenses which allows to illuminate the tip–sample interface, as shown in Figure 2. The first lens collimates the incoming light and the second focuses it onto the tip–sample interface. The optics is adjustable by piezo actuators in two directions, too. As a light source we apply an adjustable white light laser (SuperK Extreme EXW-12) with wavelengths from 450 to 2000 nm and a bandwidth ranging from 1 to 100 nm. The integrated optical power of the laser before coupling the light into the fibre of the excitation optics is about 1.2 W.

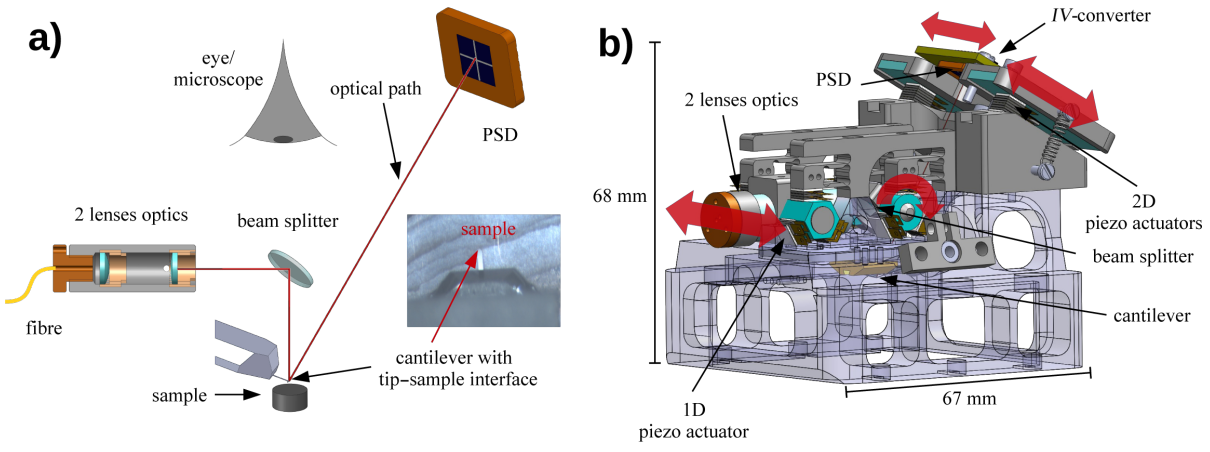

Figure 1: a) Schematic view of the optical path allowing good visibility from the top to the tip–sample setup. The image shows the cantilever above the sample through the beam splitter and an optical microscope. The cantilever is 225 µm long and 28 µm wide. b) Beam deflection unit with the key elements focusing optics, beam splitter and PSD with *IV*-converter. All three elements are adjustable by shear piezo actuators in order to optimally align the light beam. The directions of motion of the mobile parts are shown by the red arrows.

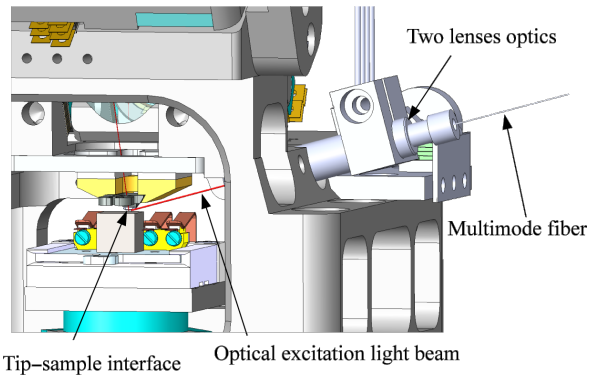

Figure 2: Additional two lenses optics which allows for the illumination of the tip–sample interface.

Scan unit and coarse positioner

CAD images of the scan unit incorporated into the coarse positioner are presented in Figure 3. In panel a the entire unit is shown whereas in panel b the unit is stripped down into smaller parts and the stages with their directions of motion indicated by the red arrows are visible. The desired scan range of 100 µm in lateral (x and y) directions and 25 µm in vertical (z) direction is realized by a commercial closed-loop scanner (nPoint, NPXY100Z25A). The spatial resolution of the scanner is in the sub-nanometre regime for both lateral and vertical directions according to the specifications provided by the manufacturer. Atomic resolution in vertical direction is demonstrated later in our article (see Figure 6). The scan unit is placed on two custom designed piezoelectric stages, which allows for a travel range of 12 mm in lateral directions. A stage consists of three 1D shear piezo actuators and two sapphire sliders. Three flexures compress the two stages together. The scanner has an aperture of 38 mm in which an additional piezo actuator is located with a travel range of 20 mm in vertical direction, used for coarsely approaching the sample to the cantilever tip. All piezo elements are driven with a custom designed controller generating saw tooth voltages with amplitudes ranging from 0 to 400 V and frequencies up to 1 kHz.

Damping system

Figure 4 shows the CAD (panel a) and the photographic (panel b) image of the complete AFM system. The beam deflection and scanner units are mounted together on top of the coarse positioner and represent the heart of the microscope. The system is attached to a CF200 flange and is suspended on four tension springs. Strong magnets (NdFeB magnets) with a horizontal field of about 0.5 T and copper fins serve as an eddy current damper for vertical vibrations. At each corner of the instrument magnets are placed, which can be adjusted in height. The magnets are oriented such that they attract and therefore reduce the weight force of the instrument, allowing for the utilization of softer springs and hence reduction of the resonance frequency of the damping system.

Electronics and SPM software

The current signals from the PSD are converted into voltage signals by a custom designed IV-converter with a bandwidth of 3 MHz, which is located on the rear side of the PSD in UHV. The signals from the converter pass through an electrical vacuum feedthrough to a custom designed electronics that computes the sum and differences of the four diode segment signals and amplifies them. All cables are carefully shielded by a copper mesh to avoid capacitive cross talk between the individual PSD signals, the piezo and electrical excitation, and

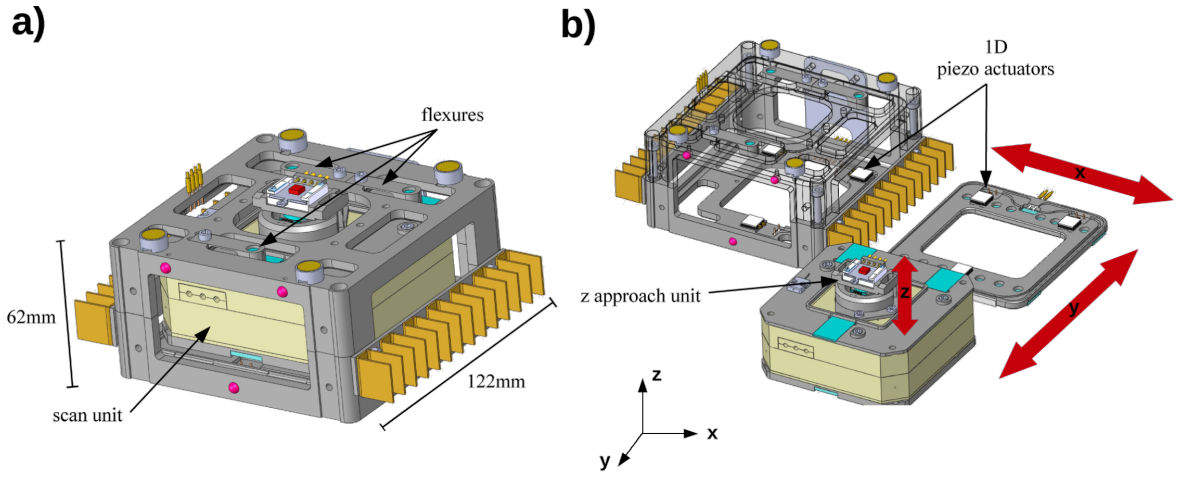

Figure 3: Coarse positioner and scan unit. Panel a shows the entire unit. In panel b the unit is stripped down into smaller parts. The coarse positioner consists of two stages in lateral directions, each driven by three shear piezo actuators. The stages are compressed by three flexures. The piezo step motor in the aperture of the scanner allows to approach the sample to the probe with nanoscale accuracy.

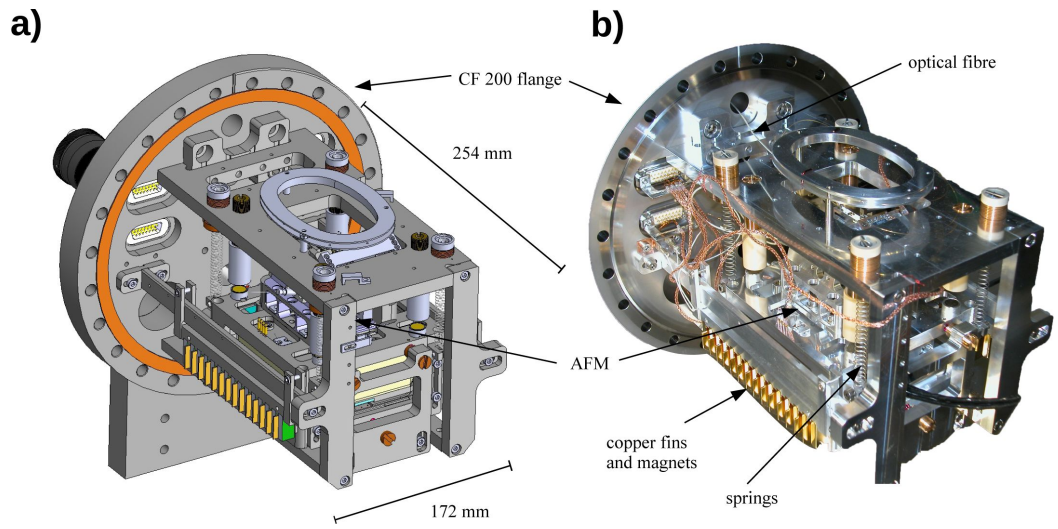

Figure 4: The atomic force microscope is assembled on a CF200 flange with four tension springs. Copper fins and magnets serve as an eddy current damping system to suppress vertical vibrations. In panel a, a CAD image is illustrated, whereas panel b shows a photography of the microscope.

the scanner signal lines. Several separated electrical UHV feedthroughs are implemented for the sample bias voltage, the piezo excitation, the PSD signals, the scanner, and the coarse motion, respectively.

To control the instrument, a commercially available electronic equipment is used (SPECS, Nanonis). For bimodal measurement techniques, such as KPFM and SCFM, two independent phase lock loop (PLL, Nanonis OC4) circuits are necessary. The SPM software consists of several modules allowing to control the PLLs, the beam deflection alignment, the Kelvin controller, the coarse positioner, and the scan unit. The closed loop scanning system includes a control unit with PID-controllers for each axis. The scan area is controlled with analog signals from the SPM electronics.

Results and Discussion

To distinguish between different materials in metallic or differently doped regions in semiconductors several scanning probe microscopy methods are implemented in our novel microscope. KPFM measures the difference of the contact potential difference (CPD) between the tip and the sample by applying a dc voltage V_{CPD} to nullify the electrostatic force acting between them [9,36]. A very sensitive way to measure, separate, and compensate the electrostatic forces is the so-called amplitude modulated KPFM (AM-KPFM) which uses the second eigenmode of the cantilever [17,37]. By applying an ac voltage V_{ac} to the tip–sample system exactly at the second eigenmode, the cantilever starts oscillating at this frequency while the amplitude depends linearly on the dc potential drop ($V_{dc} - V_{CPD}$) between tip and sample. By then applying a dc compensation voltage V_{dc} the amplitude can be minimized and the contact potential difference V_{CPD} can be determined. While this method works fine for metallic surfaces special care has to be taken on semiconducting or insulating surfaces. The main challenge arises from the fact that the tip–sample capacitance is no longer independent of the applied voltage such that higher harmonic contributions between the individual PSD signals, influence the measurements [22]. Furthermore, band-bending effects due to surface defects and the applied ac voltage may change the measured V_{CPD} [38,39]. Hence KPFM is an ideal experimental technique to visualize electronic properties of all kind of surfaces, however, with the aforementioned straight forward interpretation of the results for metallic materials with different work functions as for example in an alloy.

KPFM of a Cu/Cr alloy

Figure 5 presents a copper alloy with incorporated micrometre-sized chromium grains used in high voltage power switches. Each switching process results in a melting of the contact surface and after several hundred events in a degradation of the device properties. Therefore, the chemical and structural properties of these surfaces are of major interest. Since the melting zone is typically macroscopically sized a feature of interest, here a chromium grain, can be localized by a confocal laser microscope (Keyence VK-X100K/X200K) in air (Figure 5a). After transferring the sample into the UHV system, the same grain is approached with the coarse positioner and KPFM experiments are performed on the grain and its surroundings. The large arithmetic average roughness of R_a = 168 nm over a scan range of 50 × 50 µm^2 results in a time of 6 h to acquire these images in a reasonable resolution and stability. For that

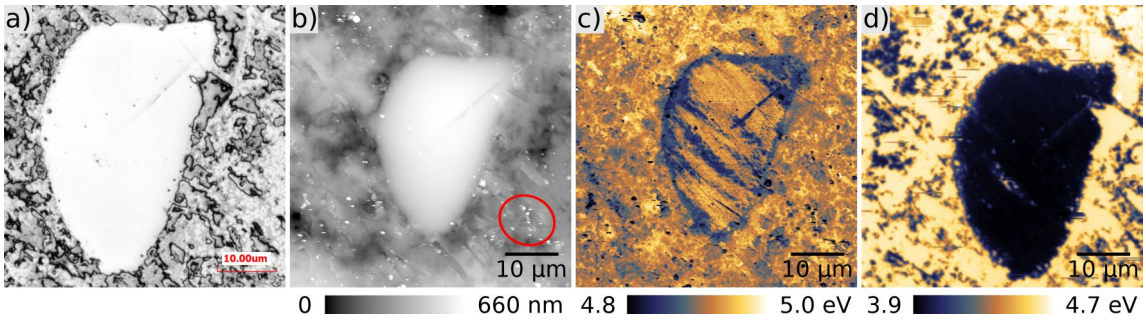

Figure 5: A chromium grain embedded in a polycrystalline copper alloy. a) Measured with a confocal laser microscope. b) Topography and c) KPFM image of the grain before sputtering. d) KPFM image after two sputter cycles for 10 min each with Ar^+-ions and a voltage of 1 kV. Small tip changes, as highlighted by the red circle in panel b, are not influencing the work function measurement sustainably. The work function difference between copper and chromium measures ΔΦ = 720 meV. Scan size: 50 × 50 µm^2.

reason very stable conditions, e.g., in temperature, are required. For these measurements a n^+-doped silicon cantilever with a PtIr-coated tip (Nanosensors, PPP-EFM) was used. The cantilever has frequencies of f_{1st} = 71 kHz for the first and f_{2nd} = 447 kHz for the second eigenmode. In the topography (Figure 5b) as well as in the V_{CPD} (Figure 5c) images the chromium grain is clearly observable. The grain seems to be covered by a residual layer partly smearing out the CPD contrast. The PtIr-coated tip is most probably contaminated by a metal oxide cluster (CuO or CrO) due to slight tip–sample contacts before the measurements, such that the work function is around Φ_{tip} = 5 eV [40]. Also in Figure 5b small tip changes are visible as stripes (some of them indicated by the red circle), however, the work function measurement is not influenced sustainably. After sputtering the surface with Ar^+-ions twice for 10 min with a voltage of 1 kV, the contamination layer is removed and the contrast in the CPD reflects the unperturbed work function values as presented in Figure 5d. The difference in the CPD between copper and chromium is about 0.7 V, while the work function of the chromium grain is reduced to approximately Φ_{Cr} = 3.9 eV and the one for the polycrystalline copper to Φ_{Cu} = 4.6 eV. Both values are in excellent agreement with other experimental values [40]. The new large-area AFM allows not only to image the structural modifications of surfaces but also to acquire quantitative electronic information of the specimen with nanometre-scale resolution.

SiC calibration structure

However, many samples of interest are semiconductor surfaces involving various doping concentrations and even cross-sections of interfaces [41,42]. Such measurements are influenced by surface band-bending effects induced by either intrinsic surface defects, adsorbates, interface states and last but not least by the doping concentration. Since KPFM is a non destructive, surface sensitive technique, e.g., compared to SSRM, information on bulk properties have to be extracted from the surface sensitive information. Several approaches have been applied in recent years for this purpose, e.g., avoiding surface defects by special preparation techniques, depositing additional known termination layers or using additional measurement techniques to separate bulk from surface information as the aforementioned SPV measurements. Recently, the presented SPM system was applied to the analysis of complex SiC structures [43].

To understand the contrast mechanism in KPFM, measurements on a SiC calibration sample have been performed to elucidate the major requirements for getting qualitative and quantitative results. Generally, high p^+-doped regions have Fermi-levels E_F approaching the upper edge of the valence band E_V and hence have a higher work function Φ than lower doped p-areas, where the Fermi level is below the centre E_i of the valence E_V and conduction band E_C. Anyhow n-doped areas have anyway a lower work function than p-doped areas. However, cross-section measurements have already shown, that direct measurements of the Fermi-level position on SiC samples is strongly affected by surface preparation and material properties [44].

Figure 6 shows a KPFM measurement of a SiC calibration sample consisting of a 2 µm thick nitrogen-doped n-type ($N_N = 2 \times 10^{18}$ cm^{-3}) followed by a 4 µm thick aluminium doped p-type ($N_{Al} = 1 \times 10^{16}$ cm^{-3}) epitaxially grown SiC layer stack on top of a highly doped n-type SiC substrate. The cross section of the sample was cleaved right before introducing it into vacuum and the topography (Figure 6a) shows steps running across the differently doped areas. The steps have atomic character, as the difference in height between adjacent steps is 0.2–0.4 nm emphasizing the performance of the developed AFM. The arithmetic average roughness R_a has a value of 0.45 nm. However, traces of the differently doped layers are not directly visible. The simultaneously recorded CPD image is

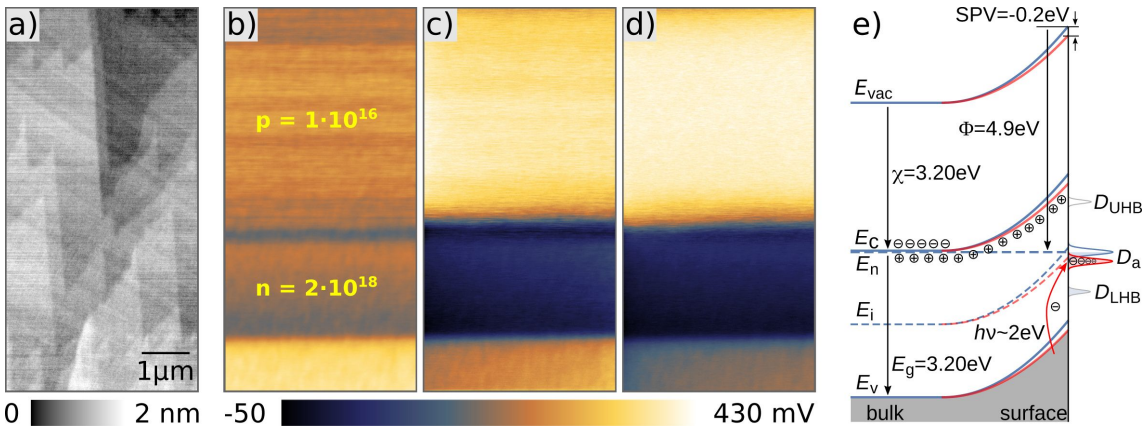

Figure 6: a) Topography, b) dark KPFM and c) 30% laser-power illuminated (470–480 nm and a maximum power of 50 mW) KPFM images of a SiC p/n-junction. The scan size is 4 × 8 µm^2. d) 100% laser- power illuminated KPFM image. e) shows a schematic band diagram of the surface band bending as well as the characteristic energies for the n-doped SiC sample including known defect states in dark (blue) and under illumination (red). Under illumination electrons are excited to the acceptor-type defects D_a and the band-bending is reduced, details are explained in the text.

shown in Figure 6b. In these experiments the bias voltage was applied to the sample while the tip was grounded and the used ac voltage in KPFM was 500 mV tuned to the second eigenmode of the cantilever. The data are measured with a n$^+$-doped silicon cantilever coated with platinum/iridium (Nanosensors, PPP-NCLPt) with eigenfrequencies of 150 kHz for the first and 950 kHz for the second eigenmode. The contrast of the V_{CPD} shows weakly the expected three interfaces but with a much smaller potential difference as one could expect. The variation between the p-type area and the n-type area is expected to be close to the electrical bandgap of SiC which is in the range of $E_{g,SiC}$ = 3.25 eV. Or, more accurately, it should correspond to the built-in potential V_b which one could ideally expect across the interface. The theoretical V_b calculates as [45]:

$$V_b = \frac{kT}{q}\ln\left(\frac{N_A N_D}{n_i^2}\right) \text{ and } n_i = \sqrt{N_C N_V}\exp\left(-\frac{E_g(T)}{2kT}\right), \quad (1)$$

where k is the Boltzmann constant, T the temperature, q the elementary charge, and N_A and N_D the doping concentrations for the p- and n-type materials, respectively. The intrinsic charge carrier concentration can be calculated to be n_i = 9.65 × 10^{-9} cm^{-3} by using the temperature-corrected values (T = 300 K) for the band gap $E_g = E_{g,0} - 6.5 \times 10^{-4}\cdot T^2/(T + 1300)$ = 3.25 eV and the effective density of states in the conduction (N_C = 3.25 × 10$^{15}\cdot T^{3/2}$ = 1.69 × 10^{19} cm^{-3}) and valence band (N_V = 4.8 × 10$^{15}\cdot T^{3/2}$ = 2.49 × 10^{19} cm^{-3}) [46]. This leads to V_b = 3.0 eV, which is a reasonable value taking into account the band gap of 4H-SiC. With a theoretically determined electron affinity of χ = 3.1–3.2 eV [47,48] one gets work function values for the p- and n-type areas of Φ_p = 6.2 eV and Φ_n = 3.2 eV, respectively. Assuming a work function of Φ_{tip} = 4.28 eV for the PtIr-coated tip [49], results in work function values of the SiC cross-section of Φ_{SiC} = 4.5–4.7 eV indicating a Fermi-level pinning at the surface at an energy around mid band gap (E_i = 4.6 eV).

For SiC it was already observed before, that the measured work function seems to be largely independent of the doping concentration indicating a well defined Fermi-level pinning at approx. 4.6 eV due to intrinsic surface-state bands [50]. Furthermore, different surface orientations show variations of the work function of 250 mV and a large statistical variation of the measured values due to different surface preparation techniques is frequently reported [51]. However, a very nice overview on electronic properties of SiC surfaces and interfaces is given by T. Seyller [52]. The electronic structure of SiC surfaces suffers from a strong electron correlation induced by a Mott–Hubbard metal–insulator transition [53] due to a half-filled and hence metallic band arising from dangling bonds. More refined studies employed a 2D Hubbard model indicating that the energy levels of the SiC surface consist of a filled band and an empty band, separated by a Hubbard gap of 1.6 eV. A pinning of the Fermi level was also observed by STM studies differing only by about 200 mV between p- and n-type doped SiC [54]. SiC was found to be in the transition between strong and no Fermi-level pinning which could also be tuned by passivation of the surface states with, e.g., hydrogen [55]. Furthermore, a large density of electrically active defects just below the conduction band of the polytype 4H-SiC has been reported to appear at interfaces and maybe also affecting the electronic structure at surfaces [56]. Especially carbon clusters are responsible for donor states in the lower part of the bandgap as well as a continuum of donor- and acceptor-type states in the central part of the band gap.

Thus, the measurements presented here fit perfectly in this picture of a strongly defect and adsorbate-influenced Fermi-level pinning of the SiC surface. A well-known technique to address and quantify the influence of surface defects in semiconductors are surface photo voltage (SPV) measurements. Charge carriers are excited by an incident photon flux and the generated electron–hole pairs are reducing the surface band bending depending on the illumination intensity and energy even until flat-band conditions. To demonstrate the impact of SPV, we illuminated the SiC p/n-junction with laser light of 470–480 nm and a power of maximum 50 mW. An increase of the CPD contrast is clearly observable by comparing in Figure 6 the KPFM measurements without (panel b) and with (panels c and d) laser illumination with 30% and 100% intensity, respectively. However, the achieved maximum difference between the n- and p-type areas of 430 mV is still far away from the expected built-in voltage. In Figure 6e a schematic band diagram shows the influence of the surface band bending as well as the characteristic energies for the n-doped SiC sample. The surface defect states are placed at energies as determined by T. Seyller [52]. D_{UHB} and D_{LHB} are the upper and lower Mott–Hubbard bands, respectively, located at fixed energies with respect to the Fermi level. In an n-type semiconductor only the acceptor type defects D_a located at the centre of the band gap are responsible for the observed surface band bending. A similar scheme with a downward band bending and donor-type defects is valid for the p-type case. Under illumination electrons are excited from the valence band to the acceptor-type defects at mid bandgap. Consequently, the charge carrier density at the surface is changed and the band bending is reduced, however, only until all acceptor type defect states are filled up. The same process holds true for the p-type SiC where a reduction of the band bending until all donor-type defect states are filled up by holes is expected. Therefore, the measured change of V_{CPD} under illumination corresponds to the width of the defect distribution in the centre of the band gap. To fully diminish the surface band bending in SPV measurements higher light energies overcoming the band gap of SiC are necessary. Figure 7a shows line section data extracted across the SiC p/n-junctions as presented in Figure 6 for various light intensities ranging from 0 to 100%. The evolution of the average CPD of the p- and n-type area with the light intensity is plotted next to it (Figure 7b) and shows an increase of the CPD by 200 mV for the p-type area and a decrease by the same amount for the n-type area. Both values are saturating with increasing light intensity.

Some more detailed features can be observed in the line sections shown in Figure 7a. At the p/n-junction a dip in the CPD can be observed which vanishes under illumination. This might indicated that the interface states are already fully charged before illumination inducing a dip in the surface potential. Furthermore, the linear decrease of the CPD within the n-type layer that is unaffected by the illumination might be related to a constant electric field between the p-type layer and the SiC substrate. More quantitative information can be extracted from the transition of the CPD into the p-type area, which can directly be related to the space charge region (SCR) that develops due to the interdiffusion of oppositely charged carriers at the interface. Following the arguments in chapter 2.2.1 of [45] for a one-sided abrupt junction (p^+/n or p/n^+) the potential distribution across the junction can directly be related to the build in potential (V_b) and the width of the SCR (W):

$$V(x) = \frac{2V_b}{W}\left(x - \frac{x^2}{2W}\right), \qquad (2)$$

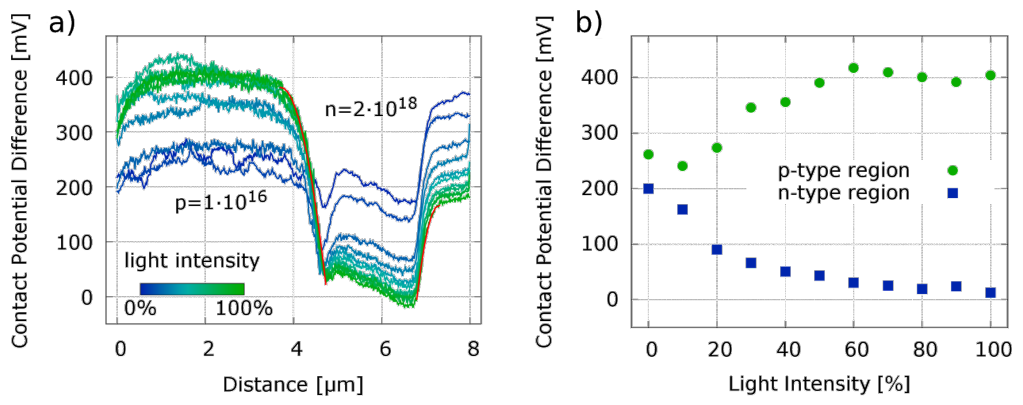

Figure 7: Panel a shows sections across the SiC p/n-junction (Figure 6) extracted from images taken at various light intensities. The data were averaged over five lines taken along the middle of the scan area. The averaged CPD values in the p- and n-type areas approach constant values under illumination as shown in panel b. In red are shown fits of the SCR regions of both junctions from the 100% illuminated sample calculated through Equation 2.

where x corresponds to the distance from the p/n-junction. The total width of such an abrupt SCR is given by:

$$W = \sqrt{\frac{2\varepsilon\varepsilon_0}{q}\frac{V_b}{N}}, \quad (3)$$

where N is N_D or N_A depending on whether $N_A >> N_D$ or vice versa and ε = 9.66 is the relative permittivity of SiC. For the case discussed here most of the depleted SCR will be located in the lowly doped p-type area and a least-square fit of the data by Equation 2 at maximum illumination results in a SCR width of W = 880 nm and a built-in voltage of V_b = 270 mV as shown by the left red curve in Figure 7a. The second fit from the transition of the n-type area to the substrate results in a width of W = 500 nm and a built-in voltage of V_b = 170 mV. As expected the built-in voltage is much smaller than the theoretically expected value calculated by Equation 1, but the SCR width is at least in the same order of magnitude as the value W_{theo} = 570 nm that is analytically calculated through Equation 1 and Equation 3 [57]. A much longer decay of the surface potential was also observed by M. Gao et al. in locally resolved secondary electron emission measurements across a SiC p/n-junction [44]. They attributed the increase of the SCR to near-surface dopant reduction induced during sample surface preparation which in our case would result in a effective doping concentration at the surface of the cross section of $N_{Al,eff} = 4.1 \times 10^{15}$ cm^{-3} utilizing Equation 3. In the case of the n-type substrate we get an effective doping concentration of $N_{N,eff} = 1.3 \times 10^{16}$ cm^{-3}.

SiC JBS device structure

Finally, we applied the technique to analyse the electronic structure of a complex SiC power semiconductor device. SiC material properties enable devices compatible with higher voltages and operating temperatures compared to traditional Si-based architectures for power electronic switches and rectifiers [58]. However, the reduction of the Schottky barrier height as well as tunneling processes are still limiting the voltage and efficiency of SiC Schottky barrier diodes. An alternative approach for such devices is the so-called junction barrier Schottky (JBS) rectifier-architecture, where highly doped p$^+$-regions are embedded into the active device area to shield the Schottky contact from high electric fields and to handle surge-current events at the same time [59,60]. The implantation of dopants as well as the electronic properties of these embedded shields is a key property and needs sophisticated characterization [57].

The KPFM experiment presented in Figure 8a and Figure 8b is an example of a large area 70 × 24 µm^2 cross section from such a SiC power device determined also by the aforementioned AM-KPFM technique and a PtIr-coated Si cantilever in dark. The device was cleaved in air and then transferred into the UHV system, such that a homogeneous distribution of surface defects was expected. The topography (Figure 8a) shows no major contrast, whereas the simultaneously acquired CPD (Figure 8b) clearly distinguishes between the n-, p- and p$^+$-doped regions even without illumination. The arithmetic average roughness of R_A = 5 nm over the entire scan range is astonishing. The measuring time for this image was 2 h and 45 min and the used ac excitation voltage was only 100 mV to avoid any tip-induced band bending effects. In the light of the discussion before the detectable CPD contrast indicates a weaker Fermi-level pinning at the centre of the band gap. However, still the overall contrast of roughly 700 mV does not represent the actual built-in voltage of the interface. The marked areas have been enlarged in Figure 8c and Figure 8d to visualize the JBS-structure of the device. The p$^+$-doped shields

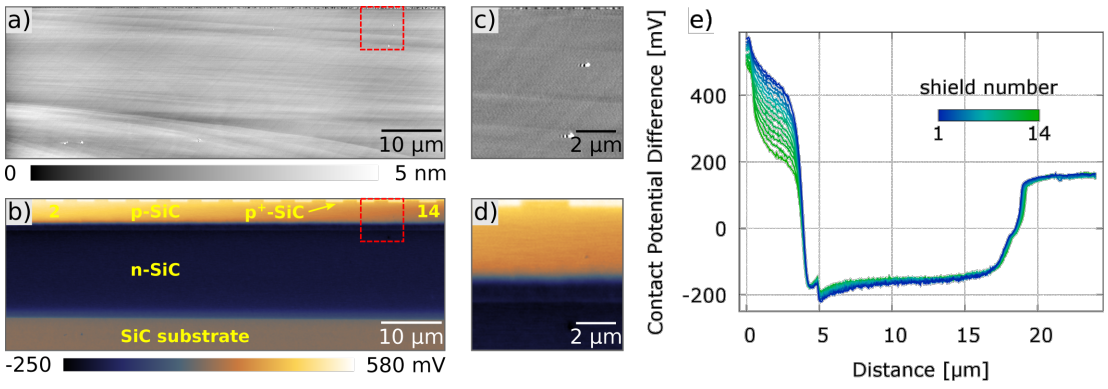

Figure 8: Simultaneously acquired topography (a) and CPD (b) images of a silicon carbide JBS structure. The scan range is 70 × 24 µm^2 with an arithmetic average roughness of R_A = 5 nm. Differently doped regions of the SiC sample are clearly identified in the KPFM-signal. A zoom of the topography and the CPD data marked by the dashed square is shown in c) and d), respectively. Line sections across the different interfaces through each center of a p$^+$-doped area are shown in graph e). The shields (width 2.8 µm) are numbered from left to right and have a periodicity of 4.9 µm.

within the p-type layer are clearly visible as bright areas on top of the CPD image and the n-type areas at the bottom. Taking again a line-section across the interfaces allows to extract more details. Figure 8e shows several vertical line sections across the complete sample always located at a centre of a p^+-doped shield. In total 14 curves starting from the left to the right are presented. Beside the variation between the differently doped areas the most eye-catching feature is the pronounced change of the potential in the p-type SiC layer, while at the same time neither the potential in the substrate nor in the n-SiC is changing noticeably. Also an edge effect on the KPFM signal can be excluded since that should be affecting all other layers, too. Since the sample was contacted homogeneously at all sides also the influence of an external inhomogeneous bias distribution can be neglected, as well as an inhomogeneous surface defect distribution, which should also be apparent at the other layers. Assuming the SiC substrate has the literature work function of $\Phi_{SiC} = 4.6$ eV, the n-type region has a work function of $\Phi_{n-SiC} = 4.2$ eV and the p^+-type region of $\Phi_{p^+-SiC} = 5.0$ eV, which are in reasonable agreement to published values [61].

Figure 9 shows the results of a detailed analysis of the p^+/p- and the p/n-interfaces again dependent on the position along the sample. The length of the line sections corresponds to the scan area presented in Figure 8c and Figure 8d. In Figure 9a and Figure 9b the CPD as well as least-square fits by Equation 2 of the p^+/p and the p/n-interfaces and the corresponding electric field $E = dV_{CPD}/dz$ is shown. This field corresponds to the lateral effective field across the respective junction and should not be confused with the perpendicular field between tip and sample, which is minimized by using KPFM. Starting at around 4.5 µm the n-type area is located showing a zero electric field. The visible kink in the CPD and corresponding spike in E in this area is not changing with position and seems to be related to a defect layer introduced during the growth process of the sample, however, details are unknown. The p/n-junction at around 4 µm exhibits a maximum electric field of $E_{p/n} = -8 \times 10^6$ V/cm, which is slightly decreasing with the position (shield number). However, the curvature neither on the n- nor on the p-side seems to be strongly influenced by the position so that also the least-square fit, as shown in Figure 9a, results in a constant SCR width of $W_{p/n} = 840$ nm and a slightly decreasing built-in voltage of $V_{b,p/n} = 340$–240 mV. Within the p-layer a linear drop of the CPD from the p^+ to the n-layer is observed which is constant with an averaged electric field strength of $E_p = -0.5 \times 10^6$ V/cm at all 14 positions. The p^+/p-

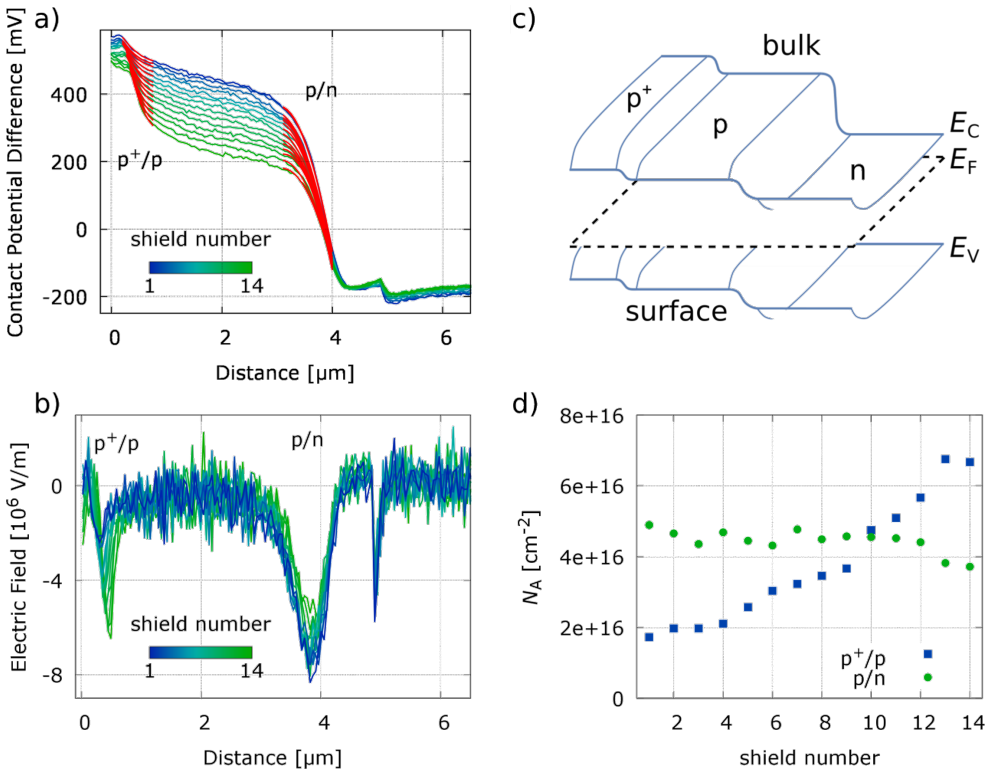

Figure 9: a) Close view of the line sections from Figure 8e at the top layer of the structure, together with least-square fits through Equation 2 of the p^+/p- and p/n-interface in red. b) Calculated electric field from panel a again from shield 1 to 14. The determined built-in voltage V_b and SCR width W from the fits were used to calculate the acceptor concentration N_A, as presented in panel d, of the p-type layer at the 14 different positions for both the p^+/p- and the p/n-interface. c) shows a schematic view of the complex band bending features expected at the surface of the SiC cross section.

interface shows, however, two very distinct effects, the electric field drop across the junction increases with increasing shield number while also the width of the SCR is changing as can be seen by the width of the potential drop (Figure 9b). The results from the least-square fit by Equation 2 show an increase of the built-in potential $V_{b,p^+/p}$ from 400 to 500 mV as well as a clear decrease of the SCR width $W_{p^+/p}$ from 1600 to 900 nm. As discussed before KPFM measurements can only be used under distinct surface conditions to predict bulk information from measured surface properties. Here we have a complex SiC structure influenced by some surface defects and states within the band gap, which induce a laterally homogeneous downward band bending for p-type and opposite for n-type material. Therefore, Equation 2 can be used to evaluate measured surface potentials to get at least surface relevant information. Figure 9c shows a sketch describing the used band structure and the surface effect. However, such effects are not only limited to surfaces but may also occur at interfaces impacting device properties. Assuming that the p^+ and the n-type layers have a higher acceptor and donator concentration than the p-type layer the acceptor concentration N_A of the p-type layer can be calculated via transforming Equation 3 to:

$$N_A = \frac{2 \cdot \varepsilon_0 \varepsilon}{q} \cdot \frac{V_b}{W^2}, \quad (4)$$

resulting in an effective surface-doping concentration for each position and interface as presented in Figure 9d. The value of $N_A = 4 \times 10^{16}$ cm^{-2} is reasonable and under the assumption that only the built-in voltage changes from the surface towards the bulk one calculates a bulk concentration of $N_A = 4 \times 10^{17}$ cm^{-2} for an estimated built-in voltage of 3 V. Therefore, the change of the surface potential can directly be associated with a change in the doping concentration of the p-SiC layer.

Conclusion

A novel atomic force microscope with a large scan area is operated under UHV conditions at room temperature. The instrument is ideal to analyse devices, either conducting or semiconducting, which are the major building blocks of power devices. On the conducting sample we perform KPFM measurements, showing different components in a copper alloy used as contact in power switches. On a SiC calibration structure the differently doped areas were clearly distinguished in the KPFM-signal, whereas the topography did not reflect the different areas, as expected. Surface photo voltage induced reduction of the band bending at the surface is demonstrated on these SiC p/n-junctions illuminated with different laser power levels. The gained knowledge is applied to the analysis of a complex SiC JBS cross section and limitations and challenges of the KPFM technique have been discussed.

Acknowledgements

We thank S. Martin, Y. Pellmont and S. Gentsch for their excellent technical support. This work was supported by the MNT-ERA, Swiss National Science Foundation, Swiss Nanosience Institute and Nanoargovia (Project A1109 WGB-NPA).

References

1. Sadeghi, A.; Baratoff, A.; Ghasemi, S. A.; Goedecker, S.; Glatzel, T.; Kawai, S.; Meyer, E. *Phys. Rev. B* **2012,** *86,* 075407. doi:10.1103/PhysRevB.86.075407
2. Bocquet, F.; Nony, L.; Loppacher, C.; Glatzel, T. *Phys. Rev. B* **2008,** *78,* 035410. doi:10.1103/PhysRevB.78.035410
3. Nony, L.; Foster, A. S.; Bocquet, F.; Loppacher, C. *Phys. Rev. Lett.* **2009,** *103,* 036802. doi:10.1103/PhysRevLett.103.036802
4. Elias, G.; Glatzel, T.; Meyer, E.; Schwarzman, A.; Boag, A.; Rosenwaks, Y. *Beilstein J. Nanotechnol.* **2011,** *2,* 252–260. doi:10.3762/bjnano.2.29
5. Martin, Y.; Williams, C. C.; Wickramasinghe, H. K. *J. Appl. Phys.* **1987,** *61,* 4723. doi:10.1063/1.338807
6. Martin, Y.; Abraham, D. W.; Wickramasinghe, H. K. *Appl. Phys. Lett.* **1988,** *52,* 1103. doi:10.1063/1.99224
7. Abraham, D. W.; Williams, C.; Slinkman, J.; Wickramasinghe, H. K. *J. Vac. Sci. Technol., B* **1991,** *9,* 703. doi:10.1116/1.585536
8. Barrett, R. C.; Quate, C. F. *J. Appl. Phys.* **1991,** *70,* 2725–2733. doi:10.1063/1.349388
9. Nonnenmacher, M.; O'Boyle, M. P.; Wickramasinghe, H. K. *Appl. Phys. Lett.* **1991,** *58,* 2921. doi:10.1063/1.105227
10. Weaver, J. M. R.; Wickramasinghe, H. K. *J. Vac. Sci. Technol., B* **1991,** *9,* 1562. doi:10.1116/1.585424
11. Nonnenmacher, M.; O'Boyle, M.; Wickramasinghe, H. K. *Ultramicroscopy* **1992,** *42–44,* 268–273. doi:10.1016/0304-3991(92)90278-R
12. O'Boyle, M. P.; Hwang, T. T.; Wickramasinghe, H. K. *Appl. Phys. Lett.* **1999,** *74,* 2641. doi:10.1063/1.123923
13. Kitamura, S.; Iwatsuki, M. *Appl. Phys. Lett.* **1998,** *72,* 3154. doi:10.1063/1.121577
14. Kitamura, S.; Suzuki, K.; Iwatsuki, M. *Appl. Surf. Sci.* **1999,** *140,* 265. doi:10.1016/S0169-4332(98)00538-8
15. Kitamura, S.; Suzuki, K.; Iwatsuki, M.; Mooney, C. B. *Appl. Surf. Sci.* **2000,** *157,* 222. doi:10.1016/S0169-4332(99)00530-9
16. Kikukawa, A.; Hosaka, S.; Imura, R. *Appl. Phys. Lett.* **1995,** *66,* 3510. doi:10.1063/1.113780
17. Kikukawa, A.; Hosaka, S.; Imura, R. *Rev. Sci. Instrum.* **1996,** *67,* 1463. doi:10.1063/1.1146874
18. De Wolf, P.; Geva, M.; Hantschel, T.; Vandervorst, W.; Bylsma, R. B. *Appl. Phys. Lett.* **1998,** *73,* 2155. doi:10.1063/1.122408
19. De Wolf, P.; Clarysse, T.; Vandervorst, W.; Hellemans, L.; Niedermann, P.; Hänni, W. *J. Vac. Sci. Technol., B* **1998,** *16,* 355. doi:10.1116/1.589810
20. Eyben, P.; Xu, M.; Duhayon, N.; Clarysse, T.; Callewaert, S.; Vandervorst, W. *J. Vac. Sci. Technol., B* **2002,** *20,* 471–478. doi:10.1116/1.1424280
21. Williams, C. C. *Annu. Rev. Mater. Sci.* **1999,** *29,* 471. doi:10.1146/annurev.matsci.29.1.471
22. Kobayashi, K.; Yamada, H.; Matsushige, K. *Appl. Phys. Lett.* **2002,** *81,* 2629–2631. doi:10.1063/1.1510582
23. Maknys, K.; Douhéret, O.; Anand, S. *Appl. Phys. Lett.* **2003,** *83,* 4205. doi:10.1063/1.1625109

24. Binnig, G.; Quate, C. F.; Gerber, C. *Phys. Rev. Lett.* **1986,** *56,* 930. doi:10.1103/PhysRevLett.56.930
25. Kronik, L.; Shapira, Y. *Surf. Sci. Rep.* **1999,** *37,* 1–206. doi:10.1016/S0167-5729(99)00002-3
26. Wilamowski, B. M. *Solid-State Electron.* **1983,** *26,* 491–493. doi:10.1016/0038-1101(83)90106-5
27. Rast, S. Sensoren mit geringer Dissipation zur Messung kleiner Kräfte. Ph.D. Thesis, University of Basel, Switzerland, 1999.
28. Lübbe, J.; Tröger, L.; Torbrügge, S.; Bechstein, R.; Richter, C.; Kühnle, A.; Reichling, M. *Meas. Sci. Technol.* **2010,** *21,* 125501. doi:10.1088/0957-0233/21/12/125501
29. Meyer, G.; Amer, N. M. *Appl. Phys. Lett.* **1988,** *53,* 2400–2402. doi:10.1063/1.100425
30. Glatzel, T.; Hoppe, H.; Sariciftci, N. S.; Lux-Steiner, M. C.; Komiyama, M. *Jpn. J. Appl. Phys.* **2005,** *44,* 5370–5373. doi:10.1143/JJAP.44.5370
31. Loppacher, C.; Zerweck, U.; Teich, S.; Beyreuther, E.; Otto, T.; Grafström, S.; Eng, L. M. *Nanotechnology* **2005,** *16,* S1–S6. doi:10.1088/0957-4484/16/3/001
32. Hoppe, H.; Glatzel, T.; Niggemann, M.; Hinsch, A.; Lux-Steiner, M. C.; Sariciftci, N. S. *Nano Lett.* **2005,** *5,* 269–274. doi:10.1021/nl048176c
33. Glatzel, T.; Rusu, M.; Sadewasser, S.; Lux-Steiner, M. C. *Nanotechnology* **2008,** *19,* 145705. doi:10.1088/0957-4484/19/14/145705
34. Streicher, F.; Sadewasser, S.; Lux-Steiner, M. C. *Rev. Sci. Instrum.* **2009,** *80,* 013907. doi:10.1063/1.3072661
35. Streicher, F.; Sadewasser, S.; Enzenhofer, T.; Schock, H.-W.; Lux-Steiner, M. C. *Thin Solid Films* **2009,** *517,* 2349–2352. doi:10.1016/j.tsf.2008.11.042
36. Sadewasser, S.; Glatzel, T. *Kelvin Probe Force Microscopy Measuring and Compensating Electrostatic Forces;* Springer Series in Surface Sciences; Springer: Berlin, Germany, 2011.
37. Sommerhalter, C.; Matthes, T. W.; Glatzel, T.; Jäger-Waldau, A.; Lux-Steiner, M. C. *Appl. Phys. Lett.* **1999,** *75,* 286. doi:10.1063/1.124357
38. Rosenwaks, Y.; Shikler, R.; Glatzel, T.; Sadewasser, S. *Phys. Rev. B* **2004,** *70,* 085320. doi:10.1103/PhysRevB.70.085320
39. Sommerhalter, C.; Glatzel, T.; Matthes, T. W.; Jäger-Waldau, A.; Lux-Steiner, M. C. *Appl. Surf. Sci.* **2000,** *157,* 263. doi:10.1016/S0169-4332(99)00537-1
40. Greiner, M. T.; Chai, L.; Helander, M. G.; Tang, W.-M.; Lu, Z.-H. *Adv. Funct. Mater.* **2012,** *22,* 4557–4568. doi:10.1002/adfm.201200615
41. Glatzel, T.; Fuertes Marrón, D.; Schedel-Niedrig, T.; Sadewasser, S.; Lux-Steiner, M. C. *Appl. Phys. Lett.* **2002,** *81,* 2017. doi:10.1063/1.1506205
42. Jiang, C.-S.; Hasoon, F. S.; Moutinho, H. R.; Al-Thani, H. A.; Romero, M. J.; Al-Jassim, M. M. *Appl. Phys. Lett.* **2003,** *82,* 127. doi:10.1063/1.1534417
43. Bartolf, H.; Gysin, U.; Glatzel, T.; Rossmann, H. R.; Jung, T. A.; Reshanov, S. A.; Schöner, A.; Meyer, E. *Microelectron. Eng.* **2015,** *148,* 1–4. doi:10.1016/j.mee.2015.04.011
44. Gao, M.; Brillson, L. J. *J. Vac. Sci. Technol., B* **2007,** *25,* 334–342. doi:10.1116/1.2464117
45. Sze, S. M. *Physics of Semiconductor Devices,* 3rd ed.; John Wiley & Sons, Inc.: Hoboken, NJ, U.S.A., 2007.
46. Goldberg, Y.; Levinshtein, M. E.; Rumyantsev, S. L. Silicon Carbide (SiC). In *Properties of Advanced Semiconductor Materials: GaN, AlN, InN, BN, SiC, SiGe;* Levinshtein, M. E.; Rumyantsev, S. L.; Shur, M. S., Eds.; Wiley: Hoboken, NJ, U.S.A., 2001; pp 93–148.
47. Davydov, S. Yu. *Semiconductors* **2007,** *41,* 696–698. doi:10.1134/S1063782607060152
48. Zhao, J. H.; Sheng, K.; Lebron-Velilla, R. C. Silicon Carbide Schottky Barrier Diode. *SiC Materials and Devices, Volume 1;* Selected Topics in Electronics and Systems, Vol. 40; World Scientific Publishing Co Pte Ltd: Singapore, 2006; pp 117–162. doi:10.1142/9789812773371_0004
49. Sadewasser, S.; Glatzel, T.; Rusu, M.; Jäger-Waldau, A.; Lux-Steiner, M. C. *Appl. Phys. Lett.* **2002,** *80,* 2979. doi:10.1063/1.1471375
50. Pelletier, J.; Gervais, D.; Pomot, C. *J. Appl. Phys.* **1984,** *55,* 994–1002. doi:10.1063/1.333156
51. Wiets, M.; Weinelt, M.; Fauster, T. *Phys. Rev. B* **2003,** *68,* 125321. doi:10.1103/PhysRevB.68.125321
52. Seyller, T. *Appl. Phys. A* **2006,** *85,* 371–385. doi:10.1007/s00339-006-3690-1
53. Ostendorf, R.; Wulff, K.; Benesch, C.; Merz, H.; Zacharias, H. *Phys. Rev. B* **2004,** *70,* 205325. doi:10.1103/PhysRevB.70.205325
54. Ramachandran, V.; Feenstra, R. M. *Phys. Rev. Lett.* **1999,** *82,* 1000–1003. doi:10.1103/PhysRevLett.82.1000
55. Porter, L. M.; Davis, R. F. *Mater. Sci. Eng., B* **1995,** *34,* 83–105. doi:10.1016/0921-5107(95)01276-1
56. Afanas'ev, V. V.; Ciobanu, F.; Dimitrijev, S.; Pensl, G.; Stesmans, A. *J. Phys.: Condens. Matter* **2004,** *16,* S1839. doi:10.1088/0953-8984/16/17/019
57. Bartolf, H.; Gysin, U.; Rossmann, H.; Bubendorf, A.; Glatzel, T.; Jung, T.; Meyer, E.; Zimmermann, M.; Reshanov, S.; Schoner, A. Development of power semiconductors by quantitative nanoscale dopant imaging. In *IEEE 27th International Symposium on Power Semiconductor Devices IC's (ISPSD),* 2015; pp 281–284.
58. Baliga, B. J. *Fundamentals of Power Semiconductor Devices;* Springer: Berlin, Germany, 2008.
59. Ivanov, P. A.; Grekhov, I. V.; Potapov, A. S.; Il'inskaya, N. D.; Samsonova, T. P.; Kon'kov, O. I. *Semiconductors* **2009,** *43,* 1209–1212. doi:10.1134/s106378260909019x
60. Bartolf, H.; Mihaila, A.; Knoll, L.; Sundaramoorthy, V.; Minamisawa, R.; Bianda, E. JBS-Rectifiers with Conduction Properties Close to Pure Schottky-Design Designed for 1.7kV Applications. EPE2015 ECCE Conference, Geneva, Switzerland, Sept 8–10, 2015; Lataire, P., Ed.; 2015.
61. Madelung, O.; Rössler, U.; Schulz, M., Eds. *Landolt-Börnstein - Group III Condensed Matter;* Springer: Berlin, Germany, 2002; Vol. 41A1b.

BEILSTEIN JOURNAL OF NANOTECHNOLOGY

Efficiency improvement in the cantilever photothermal excitation method using a photothermal conversion layer

Natsumi Inada[1], Hitoshi Asakawa[*1,2,3], Taiki Kobayashi[1] and Takeshi Fukuma[1,2,4]

Full Research Paper

Open Access

Address:
[1]Division of Electrical Engineering and Computer Science, Kanazawa University, Kanazawa, Japan, [2]Bio-AFM Frontier Research Center, Kanazawa University, Kanazawa, Japan, [3]PRESTO, JST, Kawaguchi, Japan and [4]ACT-C, JST, Kawaguchi, Japan

Email:
Hitoshi Asakawa[*] - hi_asa@staff.kanazawa-u.ac.jp

* Corresponding author

Keywords:
atomic force microscopy; cantilever excitation; dynamic mode; photothermal conversion; photothermal excitation

Beilstein J. Nanotechnol. **2016,** *7,* 409–417.
doi:10.3762/bjnano.7.36

Received: 06 November 2015
Accepted: 18 February 2016
Published: 10 March 2016

This article is part of the Thematic Series "Noncontact atomic force microscopy III".

Guest Editor: M. Z. Baykara

Abstract

Photothermal excitation is a cantilever excitation method that enables stable and accurate operation for dynamic-mode AFM measurements. However, the low excitation efficiency of the method has often limited its application in practical studies. In this study, we propose a method for improving the photothermal excitation efficiency by coating cantilever backside surface near its fixed end with colloidal graphite as a photothermal conversion (PTC) layer. The excitation efficiency for a standard cantilever of PPP-NCHAuD with a spring constant of ≈40 N/m and a relatively stiff cantilever of AC55 with a spring constant of ≈140 N/m were improved by 6.1 times and 2.5 times, respectively, by coating with a PTC layer. We experimentally demonstrate high stability of the PTC layer in liquid by AFM imaging of a mica surface with atomic resolution in phosphate buffer saline solution for more than 2 h without any indication of possible contamination from the coating. The proposed method, using a PTC layer made of colloidal graphite, greatly enhances photothermal excitation efficiency even for a relatively stiff cantilever in liquid.

Introduction

Atomic force microscopy (AFM) [1] is an analytical technique to investigate nanoscale surface structures and local physical properties of various samples. Dynamic-mode AFM has attracted considerable interests in various fields due to its great potential for many applications. For example, recent advancements in instrumentation of dynamic-mode AFM have enabled atomic-resolution imaging not only in vacuum [2-4] but also in liquid [5,6]. In addition, other advanced AFM techniques such as high-speed AFM [7-9] and multifrequency AFM [10-12] have been developed based on dynamic-mode AFM. In dynamic-mode AFM, a stiff cantilever is mechanically oscillated at a frequency near its resonance frequency. The vibrational characteristics, such as frequency, amplitude and phase are monitored to detect interaction forces between a sharp tip

and a sample. Therefore, an excitation method of cantilever oscillations is an important technique in dynamic-mode AFM.

Acoustic excitation is the most widely used method for cantilever excitation in dynamic-mode AFM. The method is used in many commercially available AFM systems because of its simple setup and high usability. In the method, a cantilever oscillation is excited by vibrating a piezoelectric actuator integrated in a cantilever holder. However, spurious resonances in the surrounding liquid and mechanical parts often deteriorate the stability and accuracy of AFM measurements [13,14]. To solve these problems, alternative methods have been developed such as photothermal excitation [15-17], magnetic excitation [18,19] and electrostatic excitation [20]. In the photothermal excitation method, a power-modulated laser beam irradiates the fixed end of a cantilever. The cantilever oscillation is excited by thermal stress induced by the irradiated laser beam [21]. Owing to the direct excitation of the cantilever, excitation of the spurious resonances is negligible [22].

However, the photothermal excitation method has the disadvantage of low excitation efficiency. Due to the low excitation efficiency, the cantilever oscillation with a desired vibrational amplitude is often difficult to achieve with a moderate laser power (on the order of milliwatts). In particular, a cantilever with a large spring constant requires a large laser power modulation. To overcome this disadvantage, cantilevers are typically coated with a thin metal layer to provide large amplitude response [21,23-25]. The difference in the thermal expansion coefficients between the cantilever material (e.g., silicon or silicon nitride) and thin metal layer (e.g., gold or aluminum) induces a large mechanical stress. Although the metal-coated cantilevers are used in most of the experiments, the excitation efficiency is often insufficient. Therefore, several methods have been proposed to improve the efficiency of the photothermal excitation method. For example, Kiracofe et al. reported that a cantilever with a trapezoidal-shaped cross section showed a higher photothermal efficiency than that with a rectangular-shaped cross section due to difference in thermal distribution in the cantilever [26]. The results indicated that the efficiency of photothermal excitation can be improved by optimizing the cantilever geometry.

As an alternative approach, the improvement of excitation efficiency using a short wavelength laser beam has been reported [27]. The high efficiency when using a short wavelength laser beam compared to a long wavelength laser beam is explained by the optical absorption characteristics of the cantilever material (e.g., silicon was used in [27]). However, the short wavelength light may cause sample damage when biological molecules or organic molecules are studied. To avoid this, an excitation laser with a longer wavelength (e.g., infrared light) is preferred in some cases. Although sample damage can be suppressed by the use of a long wavelength laser beam, the efficiency of photothermal excitation is not as high as that obtained by a short wavelength laser beam. For these reasons, improvement in the photothermal excitation efficiency when using a laser beam with a long wavelength is strongly demanded. Ratcliff et al. reported that a coating layer of black paint or Au/Pd on the cantilever backside enhances the photothermal excitation efficiency by increasing the absorption of the laser light [21]. In this previous study, relatively soft cantilevers with spring constants of 0.58 and 0.12 N/m and a visible laser beam were used. However, since the excitation efficiency decreases with increasing cantilever stiffness (or with increasing the excitation laser beam wavelength), it is important to experimentally confirm the applicability of such a coating method with a relatively stiff cantilever and an infrared excitation laser beam.

In this study, we aimed to improve the photothermal excitation efficiency with relatively stiff cantilevers using a photothermal conversion (PTC) layer made of colloidal graphite. We have established a procedure with a micromanipulator and glass probes to form a PTC layer only at the fixed end of the cantilever to avoid reducing the detection sensitivity of the optical beam cantilever deflection sensor. We demonstrate improvement in cantilever excitation efficiency by using a PTC layer with two types of commercially available cantilevers with nominal spring constants of 42 and 85 N/m (PPP-NCHAuD and AC55). In addition, we demonstrate high stability of the PTC layer in liquid by long-term FM-AFM imaging of mica with atomic resolution in phosphate buffer saline (PBS) solution.

Results and Discussion

Preparation of PTC layers

Figure 1 shows a dynamic-mode AFM setup with two laser beam sources for detection of cantilever deflection and photothermal excitation. The detection and excitation laser beams are irradiated onto the free end and fixed end of a cantilever, respectively. In this study, we chose colloidal graphite as the PTC layer material. This is because carbon materials (e.g., graphite and CNT) provide a high efficiency in conversion of light to heat [28-30] and hence are used in various fields such as printing technology and thermal-type infrared sensing. Since colloidal graphite shows a high absorption efficiency at wide wavelength range [31,32], it may be used for improving the photothermal excitation efficiency. Meanwhile, the cantilever free end should not be coated with a PTC layer because the detection laser beam is irradiated at this position. Thus, a method for coating only at a small region near the cantilever fixed end is necessary. We have established a coating method

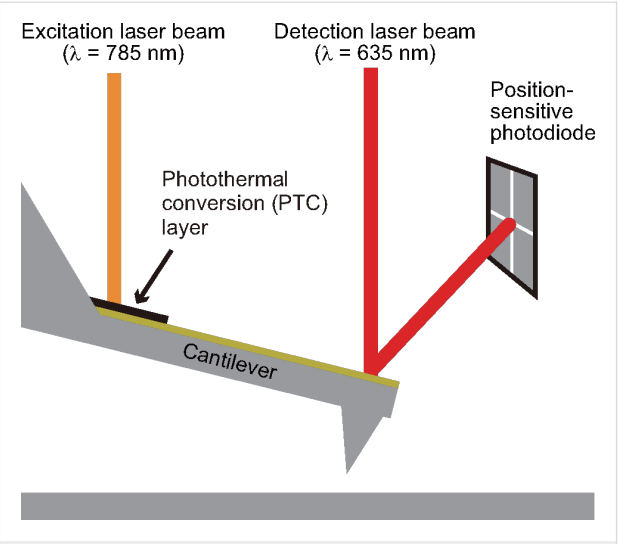

Figure 1: Schematic illustration of the photothermal excitation setup using a cantilever coated with a PTC layer.

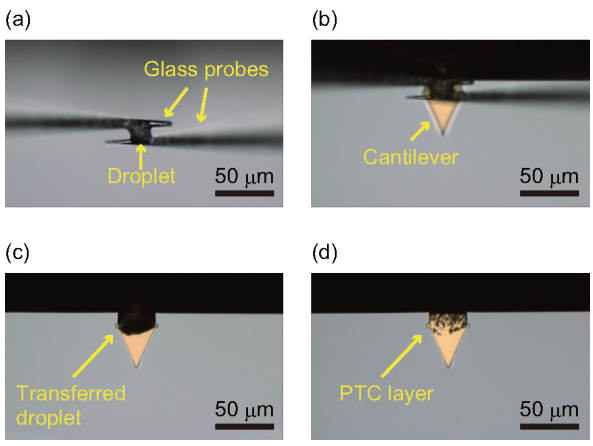

Figure 2: Formation of a PTC layer at a cantilever fixed end with a micromanipulator. (a) Preparation of a small droplet with a diameter of 20 μm by glass probes. (b) Small droplet is deposited on the cantilever fixed end. (c) Before drying. (d) After drying.

for a PTC layer of colloidal graphite using a micromanipulator (AxisProSS, Microsupport, Shizuoka, Japan). In this study, we tested PTC layers on two types of commercially available cantilevers: (1) PPP-NCHAuD (Nanoworld, Neucatel, Switzerland) is widely used for dynamic-mode AFM measurements in liquid and (2) AC55 (Olympus, Tokyo, Japan) is a relatively stiff cantilever with a smaller size than that of PPP-NCHAuD. The backsides of both cantilevers were coated with a thin gold layer.

Figure 2 shows the coating process of a PTC layer on an AC55 cantilever. A small droplet of colloidal graphite dispersion was formed using two glass probes that were controlled by the micromanipulator. The diameter of the small droplet was approximately 20 μm. We found that the coating with aqueous solution was difficult due to water evaporation. Thus, glycerol (23 wt % of total liquid weight) was added to the coating solution. The addition of glycerol enables highly reproducible coating of the PTC layer. To remove the glycerol and water, the coated cantilever was heated at 200 °C for 2 h under reduced pressure ($<3 \times 10^{-3}$ Pa) using a vacuum oven.

Figure 3a,b shows SEM images of PTC layers on AC55 cantilevers before and after the coating. The results suggest that a PTC layer was formed only at a small region near the cantilever fixed end. Thus, the PTC layer should give little influence on the cantilever deflection measurements. In the magnified SEM image (Figure 3c), we found plate-like particles with a diameter between 0.1 and 1 μm. The diameters observed in the SEM images agree with the average diameter of the colloidal graphite (460 nm) measured by dynamic light scattering. The results show that the plate-like particles observed in the SEM images are colloidal graphite.

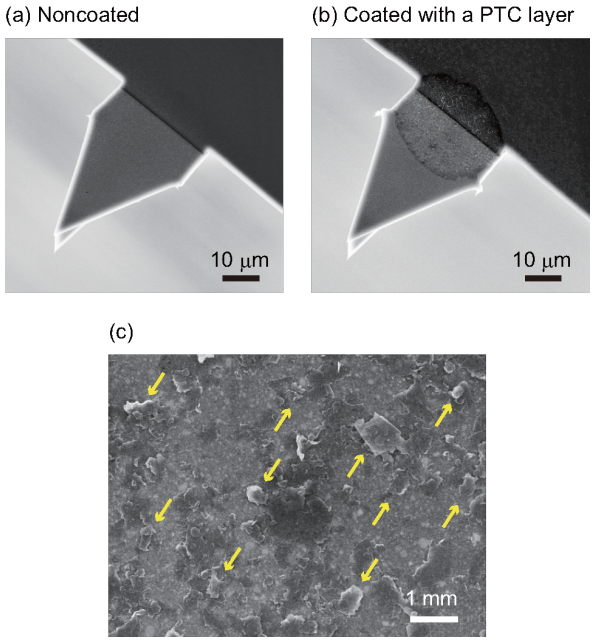

Figure 3: SEM images of AC55 cantilevers. (a) Noncoated and (b) coated with a PTC layer. (c) A magnified SEM image of the PTC layer. The arrows indicate plate-like colloidal graphite.

Performance of PTC layers

Figure 4 shows amplitude and phase versus frequency curves measured with two different types of cantilevers (PPP-NCHAuD and AC55) before and after coating of the PTC layer. To evaluate performance of the PTC layers, we measured the sweep curves with photothermal excitation in water. The amplitude curves obtained for the PPP-NCHAuD cantilever (Figure 4a) show that the peak amplitude measured with the

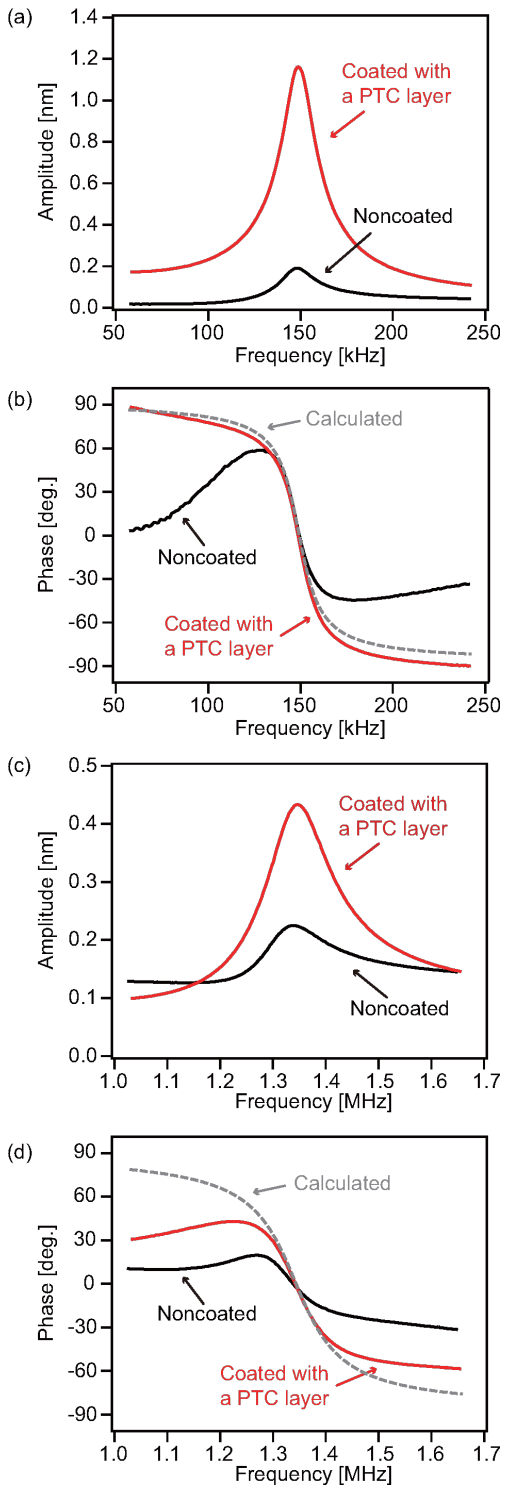

Figure 4: (a) Amplitude and (b) phase versus frequency curves measured with a PPP-NCHAuD in water. (c) Amplitude and (d) phase versus frequency curves measured with an AC55 cantilever in water (Cantilever (iii) in Figure 5a). All curves were measured with the same amplitude of laser power modulation (P_{mod} = 12.9 mW). The dimensions of cantilevers are significant different between PPP-NCHAuD (length; 125 µm, width; 30 µm, thickness; 4 µm) and AC55 (length; 55 µm, width; 31 µm, thickness; 2 µm).

coated cantilever is six times higher than that with the noncoated cantilever. The results suggest the effectiveness of a PTC layer for improving the photothermal excitation efficiency. For a relatively stiff AC55 cantilever, the increase of the peak amplitude is approximately two times. This improvement is not as high as that obtained for a softer PPP-NCHAuD cantilever. However, a doubled increase of the excitation efficiency has significant merit for use of relatively stiff cantilevers in many practical applications as they are difficult to oscillate with a sufficient amplitude.

The lower increase rate of the stiff AC55 cantilever compared to the soft PPP-NCHAuD cantilever is likely to be caused by multiple reasons. However, a quantitative comparison of the increase rates between two cantilevers is difficult in this study due to the use of different objective lenses. Thus, we discuss possible reasons for the large difference in the increase rates. The most likely reason is the difference in the three-dimensional shape of the cantilevers. The two cantilevers have different cross-sectional shapes: AC55 cantilever has a rectangular cross section, and PPP-NCHAuD has a trapezoidal cross section. In addition, they have a large difference in the dimensions (length, width and thickness) as shown in the caption of Figure 4. The excitation efficiency and optimal irradiation positions of an excitation laser should be affected by the three-dimensional shapes of cantilevers as previously reported in [26].

The phase versus frequency curves (Figure 4b,d) show the improvement of the phase response by PTC layer coating. The phase curves measured with the noncoated and coated cantilevers were corrected by subtracting the frequency-dependent phase delay caused by a phase-locked loop circuit. The dotted lines in the figures show ideal phase curves calculated with resonance frequency (f_0) and Q-factor estimated from cantilever thermal vibration spectra as shown in Table 1 and Table 2. The phase curves measured with noncoated cantilevers were not consistent with the calculated ideal curves. In contrast, the curve measured with a coated PPP-NCHAuD showed almost the same profile as that of the ideal one (Figure 4b). In addition, the curve measured with a coated AC55 showed the improvement of phase response compared to that measured with the noncoated AC55 cantilever (Figure 4d). The errors in the measured curves were mostly caused by a reflection of the excitation laser beam into the photodetector and the low excitation efficiency. The results suggest that the coating of a PTC layer improves the phase response obtained by the photothermal excitation method.

Table 1 and Table 2 show the physical properties of PPP-NCHAuD and AC55 cantilevers before and after coating

Table 1: Properties of a PPP-NCHAuD cantilever before and after coating with a PCT layer.

	f_0 [kHz]	Q	k [N/m]	A [nm]	η_{exp} [nm/mW]	Blackened area [%]
Noncoated	149	8.5	35.6	0.19	0.015	—
Coated	149	8.5	36.3	1.16	0.090	100

Table 2: Properties of AC55 cantilevers before and after coating with PCT layers.

	f_0 [MHz]	Q	k [N/m]	A [nm]	η_{exp} [nm/mW]	Blackened area [%]
Noncoated (ii)	1.28	12.9	107	0.25	0.020	—
Coated (ii)	1.28	11.0	121	0.38	0.030	35
Noncoated (iii)	1.34	12.0	132	0.22	0.018	—
Coated (iii)	1.34	10.2	142	0.43	0.034	55
Noncoated (iv)	1.35	10.5	101	0.18	0.014	—
Coated (iv)	1.35	10.7	141	0.44	0.035	70
Noncoated (v)	1.36	11.0	133	0.20	0.016	—
Coated (v)	1.38	10.4	129	0.30	0.024	97

with a PTC layer. The resonance frequency (f_0), Q-factor and spring constant (k) of the cantilevers were estimated from cantilever thermal vibration spectra obtained in water. We found that the PTC layers coating had little influence on the physical properties of these two types of cantilevers. Thus, a PTC layer should not change cantilever performance, such as force sensitivity.

Relationship between excitation efficiency and blackened area with PTC layers

The increase rate in excitation efficiency of a PPP-NCHAuD cantilever (six times) was sufficient for most of the practical applications of dynamic-mode AFM in liquid. In addition, the phase response was also improved and was very close to the ideal curve as shown in Figure 4b. In contrast, the improvements in the excitation efficiency and the phase response obtained with the stiff AC55 cantilever were lower than those obtained with the soft PPP-NCHAuD cantilever. Therefore, we investigated a relationship between excitation efficiency and blackened area with PTC layers on AC55 cantilevers for further improvements.

We found that the photothermal excitation efficiency of the coated cantilevers shows large variation depending on the coating conditions of a PTC layer. Initially, we tried to optimize the excitation efficiency by reducing the graphite concentration in the dispersions. Coarse regulation of the excitation efficiency was possible by this method. However, fine regulation only by controlling the graphite concentration was difficult due to the difference in drop volumes formed by two glass probes and the inhomogeneity of colloidal graphite flakes in the dispersions. Owing to these reasons, it is difficult to estimate the accurate excitation efficiency only from the graphite concentration. To solve this problem, we found the relationship between the blackened area evaluated by optical microscopy and excitation efficiency.

We coated cantilevers with different blackened areas as shown in Figure 5a. The blackened areas near the cantilever fixed end were calculated by a method described in the experimental section. Amplitude and phase versus frequency curves measured with the cantilevers in Figure 5a are shown in Supporting Information File 1, Figure S1. The results suggest that the peak values of the amplitude versus frequency curves measured with these cantilevers are all increased by the coating of the PTC layers. In addition, the phase responses are improved with increasing blackened area. Figure 5b shows the blackened area dependence of the photothermal excitation efficiency (η_{exc}). Here, we define η_{exc} as

$$\eta_{exc} = A / P_{mod}$$

where A and P_{mod} are the peak value of an amplitude versus frequency curve and the modulation amplitude of the excitation laser power, respectively. The result shows that η_{exc} increases with blackened area coverage up to about 70%. This is probably due to the improvement in the photothermal conversion efficiency.

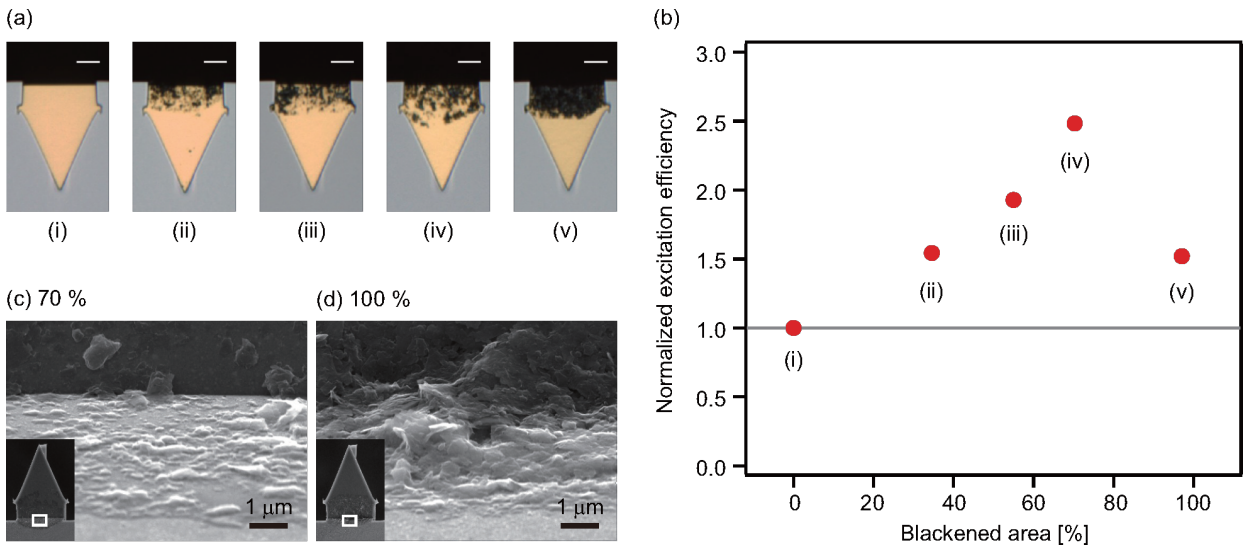

Figure 5: (a) Optical images of AC55 cantilevers having different surface coverage. (i): Noncoated cantilever. The cantilevers were coated with the dispersions in the colloidal graphite concentration of (ii) 0.4 wt %, (iii) 4 wt %, (iv) 2 wt % and (v) 6 wt %. (b) Dependence of excitation efficiency on blackened area of a PTC layer. AC55 cantilevers were used in this experiment. (c, d) SEM images of cantilevers with 70 and 100% blackened area. The rectangles in the insets indicate the location where we took a magnified image.

In contrast, the photothermal excitation efficiency remarkably decreases with increasing blackened area from 70 to 100%. To understand the reason for the decrease, we imaged the cantilevers with blackened area of 70 and 100% by SEM (Figure 5c,d). The SEM images show that the PTC layer with 100% blackened area is much thicker than the one with 70% blackened area. In addition, the PTC layer with 100% blackened area shows relatively large roughness compared with the one with 70%. The large roughness of 100% blackened area in the SEM image indicates that the flakes of colloidal graphite are likely to stack on the surface of the cantilever with hollow spaces. The hollow spaces in the PTC layer may cause the decrease in heat transfer from the PTC layer to the cantilever.

Another possible mechanism is an influence of heat transfer in the lateral direction by connected flakes of colloidal graphite. The lateral connection of colloidal graphite may lead to the increase of heat transfer in the lateral direction, resulting in a small thermal gradient in the cantilever. In fact, the SEM image of the 100% blackened area (Figure 5d) shows that the colloidal graphite flakes are connected. In contrast, most of the flakes are isolated and directly attached to the surface of the cantilever in the 70% blackened SEM image (Figure 5c). The results support that the generated heat is efficiently transmitted to the cantilever with low heat transfer in the lateral direction, resulting in an increase of generated mechanical stress.

The results indicate that the optimal coating of the PTC layer may be slightly lower than 100% as long as a multilayered structure with hollow spaces and/or a lateral connections between the flakes of colloidal graphite are not formed. However, reproducible formation of such a PTC layer is difficult with the present coating method using the micromanipulator and glass probes. Since even a slight increase from 70% blackened area results in a remarkable decrease in the excitation efficiency, we used PTC layers with a blackened area of ≈70% in our experiments.

Long-term stability of PTC layers in liquid

Long-term stability of a PTC layer in liquid is very important for stable operation of a photothermal excitation system in dynamic-mode AFM. To investigate the long-term stability, we measured η_{exc} for 2 h in water with an AC55 cantilever coated with a PTC layer (as shown in Supporting Information File 1, Figure S2). The result reveals that the photothermal excitation efficiency is extremely stable in water. Furthermore, we confirmed that the optical microscope images of the PTC layer before and after the measurement are almost the same (Figure 6a).

Figure 6b–f shows FM-AFM images of a mica surface obtained in PBS solution using an AC55 cantilever coated with a PTC layer. After adjusting the imaging parameters such as Δf, A and feedback gains to obtain atomic resolution, long-term FM-AFM imaging was performed for 2 h without changing the imaging parameters. We found subnanometer-scale contrasts corresponding to the mica surface structure in all the successive AFM images. In addition, no contaminations on the mica sur-

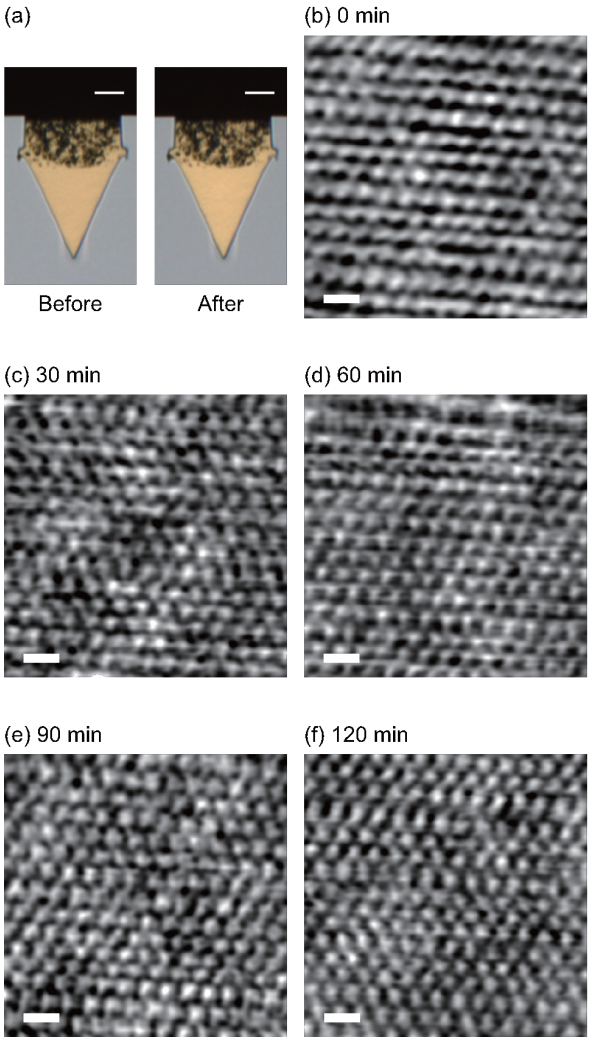

Figure 6: Long-term stability of the PTC layer in liquid. (a) Optical images of an AC55 cantilever before and after use in water. (b)–(f) Successive FM-AFM images of a mica surface in PBS solution. Δf = +3.9 kHz. A = 0.4 nm. Scale bar = 1 nm.

face were found in the AFM images. The results show that a PTC layer does not have any negative influence on the atomic-scale FM-AFM imaging in liquid.

Conclusion

In this study, we proposed a method for improving the photothermal excitation efficiency in dynamic-mode AFM using a PTC layer made of colloidal graphite. We have established a procedure to prepare a PTC layer only at the cantilever fixed end. The photothermal excitation efficiency increases with increasing blackened area of colloidal graphite up to about 70%. In contrast, the excitation efficiency remarkably decreases with increasing the blackened area from 70 to 100%. The results indicate that the decrease is due to formation of multilayered structures of colloidal graphite with hollow spaces and/or lateral connections between flakes. A PTC layer provides six-fold improvement in the excitation efficiency for a standard PPP-NCHAuD cantilever while over two-fold for a stiffer AC55 cantilever. Such an improvement is particularly useful for oscillating a relatively stiff cantilever with a long wavelength laser beam. We experimentally demonstrated the high stability of PTC layers in liquid by the long-term measurements in water and PBS solution. The proposed method should extend the applicability of the photothermal excitation method.

Experimental

Preparation of coating solution used for the formation of PTC layers

A commercially available aqueous dispersion of colloidal graphite (graphite 5–10% and ammonium hydroxide 1–5% in water, Aquadag E, Henkel, Düsseldorf, Germany) was used as the PTC layers material. To control the surface coverage of colloidal graphite on a cantilever, the aqueous dispersion was diluted with Milli-Q water. We added glycerol (Nacalai Tesque, Kyoto, Japan) to each aqueous dispersion to obtain a final concentration of 23 wt % in order to prevent water evaporation in the coating process. The colloidal graphite concentration of the dispersions used in this study are shown in the caption of Figure 5. Sonication of the coating solution was performed before the coating process. The average diameter of colloidal particles in the coating solution was measured by the dynamic light scattering (Zetasizer Nano-ZS, Malvern, Worcestershire, UK).

Measurement of photothermal excitation efficiency

A custom-built AFM equipped with a photothermal excitation setup and a commercially available oscillation controller (Nanonis OC4, SPECS, Zürich, Switzerland) were used for the photothermal excitation efficiency measurement. An infrared laser (λ = 785 nm, Melles Griot, Irvine, CA, USA) was used as an excitation laser source as shown in Figure 1. The laser power was modulated with an external voltage signal from the oscillation controller. The power-modulated laser light was focused on a cantilever fixed end through a collimator lens (F220FC-780, Thorlabs, Newton, USA) and an objective lens (CF Plan Epi 5× for PPP-NCHAuD and CF Plan Epi 10× for AC55, Nikon, Tokyo, Japan). The laser power was measured just after passing through the optical lenses by an optical power meter. The position of laser spot was adjusted near the cantilever fixed end to maximize the amplitude of cantilever oscillation.

Optical and SEM imaging of PTC layers

The PTC layers were imaged by an optical microscope integrated in the micromanipulator system. To calculate the black-

ened area of the PTC layers near the cantilever fixed end, the optical images were taken under the same illumination condition. The obtained optical images were processed using an image processing software (ImageJ [33]). The small areas (10 μm × 10 μm) near the cantilever fixed ends were cut out from optical images and converted to 8-bit gray scale images. The regions coated with colloidal graphite in the gray scale images were selected using a function of Make Binary in ImageJ software. The threshold value of 110 was manually chosen to separate the coated and noncoated regions. SEM (JSM-7100F, JEOL, Tokyo, Japan) was used for imaging colloidal graphite on the cantilevers.

Long-term stability evaluation of PTC layers in liquid

Long-term stability of the PTC layers in liquid was evaluated by monitoring the cantilever excitation amplitude. The signal of excitation amplitude from the oscillation controller (OC4) was recorded by a data logger (ZR-RX40, Omron, Tokyo, Japan) for 2 h every 10 s. An AFM tip was placed far away from the surface (>5 mm) to avoid possible influence of tip–sample interactions.

Long-term FM-AFM imaging in liquid was performed using a custom-built AFM with a low-noise cantilever deflection sensor [34,35] and a commercially available phase-locked loop circuit (OC4, SPECS, Zürich, Switzerland). A commercially available AFM controller (ARC2, Asylum Research, Santa Barbara, CA, USA) was used for the tip–sample distance feedback regulation and acquisition of FM-AFM images. The FM-AFM imaging of a mica surface was performed in PBS solution.

Supporting Information

Supporting Information File 1

Additional figures.
[http://www.beilstein-journals.org/bjnano/content/supplementary/2190-4286-7-36-S1.pdf]

Acknowledgements

We acknowledge support from the JST PRESTO program and the JST ACT-C program.

References

1. Binnig, G.; Quate, C. F.; Gerber, C. *Phys. Rev. Lett.* **1986,** *56,* 930. doi:10.1103/PhysRevLett.56.930
2. Sugawara, Y.; Ohta, M.; Ueyama, H.; Morita, S. *Science* **1995,** *270,* 1646–1648. doi:10.1126/science.270.5242.1646
3. Giessibl, F. J. *Rev. Mod. Phys.* **2003,** *75,* 949–983. doi:10.1103/RevModPhys.75.949
4. Kawai, S.; Sadeghi, A.; Xu, F.; Peng, L.; Orita, A.; Otera, J.; Goedecker, S.; Meyer, E. *ACS Nano* **2015,** *9,* 2574–2583. doi:10.1021/nn505876n
5. Fukuma, T.; Ueda, Y.; Yoshioka, S.; Asakawa, H. *Phys. Rev. Lett.* **2010,** *104,* 016101. doi:10.1103/PhysRevLett.104.016101
6. Voïtchovsky, K.; Kuna, J. J.; Contera, S. A.; Tosatti, E.; Stellacci, F. *Nat. Nanotechnol.* **2010,** *5,* 401–405. doi:10.1038/nnano.2010.67
7. Fantner, G. E.; Schitter, G.; Kindt, J. H.; Ivanov, T.; Ivanova, K.; Patel, R.; Holten-Andersen, N.; Adams, J.; Thurner, P. J.; Rangelow, I. W.; Hansma, P. K. *Ultramicroscopy* **2006,** *106,* 881–887. doi:10.1016/j.ultramic.2006.01.015
8. Ando, T.; Kodera, N.; Takai, E.; Maruyama, D.; Saito, K.; Toda, A. *Proc. Natl. Acad. Sci. U. S. A.* **2001,** *98,* 12468–12472. doi:10.1073/pnas.211400898
9. Miyata, K.; Asakawa, H.; Fukuma, T. *Appl. Phys. Lett.* **2013,** *103,* 203104. doi:10.1063/1.4830048
10. Garcia, R.; Herruzo, E. T. *Nat. Nanotechnol.* **2012,** *7,* 217–226. doi:10.1038/nnano.2012.38
11. Ebeling, D.; Solares, S. D. *Beilstein J. Nanotechnol.* **2013,** *4,* 198–207. doi:10.3762/bjnano.4.20
12. Nievergelt, A. P.; Adams, J. D.; Odermatt, P. D.; Fantner, G. E. *Beilstein J. Nanotechnol.* **2014,** *5,* 2459–2467. doi:10.3762/bjnano.5.255
13. Schäffer, T. E.; Cleveland, J. P.; Ohnesorge, F.; Walters, D. A.; Hansma, P. K. *J. Appl. Phys.* **1996,** *80,* 3622. doi:10.1063/1.363308
14. Buguin, A.; Roure, O. D.; Silberzan, P. *Appl. Phys. Lett.* **2001,** *78,* 2982. doi:10.1063/1.1371250
15. Umeda, N.; Ishizaki, S.; Uwai, H. *J. Vac. Sci. Technol., B* **1991,** *9,* 1318. doi:10.1116/1.585187
16. Marti, O.; Ruf, A.; Hipp, M.; Bielefeldt, H.; Colchero, J.; Mlynek, J. *Ultramicroscopy* **1992,** *42,* 345–350. doi:10.1016/0304-3991(92)90290-Z
17. Ramos, D.; Mertens, J.; Calleja, M.; Tamayo, J. *Appl. Phys. Lett.* **2008,** *92,* 173108. doi:10.1063/1.2917718
18. Han, W.; Lindsay, S. M.; Jing, T. *Appl. Phys. Lett.* **1996,** *69,* 4111. doi:10.1063/1.117835
19. Hoof, S.; Gosvami, N. N.; Hoogenboom, B. W. *J. Appl. Phys.* **2012,** *112,* 114324. doi:10.1063/1.4768713
20. Umeda, K.; Oyabu, N.; Kobayashi, K.; Hirata, Y.; Matsushige, K.; Yamada, H. *Appl. Phys. Express* **2010,** *3,* 065205. doi:10.1143/APEX.3.065205
21. Ratcliff, G. C.; Erie, D. A.; Superfine, R. *Appl. Phys. Lett.* **1998,** *72,* 1911. doi:10.1063/1.121224
22. Labuda, A.; Kobayashi, K.; Kiracofe, D.; Suzuki, K.; Grütter, P. H.; Yamada, H. *AIP Adv.* **2011,** *1,* 022136. doi:10.1063/1.3601872
23. Narayanaswamy, A.; Gu, N. *J. Heat Transfer* **2011,** *133,* 042401. doi:10.1115/1.4001126
24. Pini, V.; Tamayo, J.; Gil-Santos, E.; Ramos, D.; Kosaka, P.; Tong, H.-D.; van Rijn, C.; Calleja, M. *ACS Nano* **2011,** *5,* 4269–4275. doi:10.1021/nn200623c
25. Evans, D. R.; Tayati, P.; An, H.; Lam, P. K.; Craig, V. S. J.; Senden, T. J. *Sci. Rep.* **2014,** *4,* 5567. doi:10.1038/srep05567
26. Kiracofe, D.; Kobayashi, K.; Labuda, A.; Raman, A.; Yamada, H. *Rev. Sci. Instrum.* **2011,** *82,* 013702. doi:10.1063/1.3518965
27. Nishida, S.; Kobayashi, D.; Kawakatsu, H.; Nishimori, Y. *J. Vac. Sci. Technol., B* **2009,** *27,* 964. doi:10.1116/1.3077487
28. Mellouki, I.; Touayar, O.; Ktari, T.; Yacoubi, N. *Infrared Phys. Technol.* **2004,** *45,* 273–279. doi:10.1016/j.infrared.2003.11.010
29. Theocharous, E.; Engtrakul, C.; Dillon, A. C.; Lehman, J. *Appl. Opt.* **2008,** *47,* 3999–4003. doi:10.1364/AO.47.003999

30. Kobayashi, M.; Abe, J. *J. Am. Chem. Soc.* **2012,** *134,* 20593–20596. doi:10.1021/ja310365k
31. Taft, E. A.; Philipp, H. R. *Phys. Rev.* **1965,** *138,* A197. doi:10.1103/PhysRev.138.A197
32. Johnson, L. G.; Dresselhaus, G. *Phys. Rev. B* **1973,** *7,* 2275–2285. doi:10.1103/PhysRevB.7.2275
33. Schneider, C. A.; Rasband, W. S.; Eliceiri, K. W. *Nat. Methods* **2012,** *9,* 671–675. doi:10.1038/nmeth.2089
34. Fukuma, T.; Kimura, M.; Kobayashi, K.; Matsushige, K.; Yamada, H. *Rev. Sci. Instrum.* **2005,** *76,* 053704. doi:10.1063/1.1896938
35. Fukuma, T. *Rev. Sci. Instrum.* **2009,** *80,* 023707. doi:10.1063/1.3086418

License and Terms

BEILSTEIN JOURNAL OF NANOTECHNOLOGY

Length-extension resonator as a force sensor for high-resolution frequency-modulation atomic force microscopy in air

Hannes Beyer*, Tino Wagner and Andreas Stemmer*

Full Research Paper

Open Access

Address:
Nanotechnology Group, ETH Zürich, Säumerstrasse 4, 8803 Rüschlikon, Switzerland

Email:
Hannes Beyer* - hbeyer@ethz.ch; Andreas Stemmer* - astemmer@ethz.ch

* Corresponding author

Keywords:
ambient conditions; drift compensation; frequency-modulation atomic force microscopy; high-resolution; length-extension resonator

Beilstein J. Nanotechnol. **2016,** *7,* 432–438.
doi:10.3762/bjnano.7.38

Received: 14 November 2015
Accepted: 29 February 2016
Published: 15 March 2016

This article is part of the Thematic Series "Noncontact atomic force microscopy III".

Guest Editor: M. Z. Baykara

Abstract

Frequency-modulation atomic force microscopy has turned into a well-established method to obtain atomic resolution on flat surfaces, but is often limited to ultra-high vacuum conditions and cryogenic temperatures. Measurements under ambient conditions are influenced by variations of the dew point and thin water layers present on practically every surface, complicating stable imaging with high resolution. We demonstrate high-resolution imaging in air using a length-extension resonator operating at small amplitudes. An additional slow feedback compensates for changes in the free resonance frequency, allowing stable imaging over a long period of time with changing environmental conditions.

Introduction

Frequency-modulated atomic force microscopy (FM-AFM) is the method of choice to image nanoscale structures on surfaces down to the atomic level. Whereas atomic resolution is routinely achieved in ultra-high vacuum (UHV), it remains a challenge under ambient conditions. However, imaging samples in their natural environment down to the atomic level is key to understanding their properties. Several factors such as contamination of the surface, environmental changes, and water layers on the surface hamper high-resolution imaging under ambient conditions. Especially, water layers present on surfaces exposed to air affect the forces acting on the tip, and as a result the stability. Meniscus forces may dominate the interaction and overshadow forces responsible for atomic contrast, namely short-range forces. A viable strategy to circumvent meniscus forces and to achieve atomic resolution is to measure in liquid [1]. Operation with small amplitudes can further help to stay within a single water layer, minimising disturbances which may arise by penetrating several water layers per oscillation [2].

To avoid stability issues such as “jump-to-contact” while working with small amplitudes, sensors with a high stiffness,

e.g., short cantilevers, quartz tuning forks, or length-extension resonators are required [3]. In UHV tuning forks have outperformed conventional cantilevers because the high stiffness ($k \approx 2$ kN/m) of these sensors allows for stable operation at amplitudes down to tens of picometres, thus increasing the sensitivity to short-range forces. In combination with a functionalised tip (e.g., a CO molecule), this ultimately led to the observation of the chemical structure of single molecules [4,5]. Recently, atomic resolution has been achieved with a qPlus sensor in air on potassium bromide and graphite [2,6].

In this paper, we demonstrate the suitability of the piezoelectric self-sensing length-extension resonator (LER) [7,8] for high-resolution FM-AFM imaging in air. The LER has a resonance frequency of about 1 MHz, a Q-factor of approximately 15,000 in air and an effective stiffness of $k_{\text{eff}} = 1.08$ MN/m. The effective stiffness amounts to twice the stiffness of a single beam ($k = 540$ kN/m) because the LER consists of two oscillating beams fixed at the center [9]. The very high stiffness allows for operation at very small amplitudes down to tens of picometres and atomic resolution has already been achieved in UHV [10-13]. The sensor is also suited for simultaneous measurements of the frequency shift and tunnelling current [12-14]. Only a few applications of the LER in air or liquid have been reported so far, for example on mica [13,15], Si(111) [16], on a grating [17], HOPG, and DNA origami [18]. Froning et al. [18] also discussed the influence of the environmental conditions on the sensor properties. Temperature and humidity changes lead to variations in resonance frequency and Q-factor, a problem also well-known for regular cantilevers. The problem is aggravated for the LER since the measured signal, i.e., the frequency shift Δf, is small due to the high stiffness of the LER ($\Delta f \propto f_0/k_{\text{eff}}$). Hence a controlled environment is essential for stable imaging, especially for measurements over a long period of time.

Several approaches have been reported to adjust scanning parameters such that a constant tip–sample distance can be maintained [19-21]. For example, the variation of the amplitude of the second harmonic resonance has been used to adjust the amplitude setpoint of the first harmonic employed for feedback in amplitude-modulated AFM [19]. Another approach is to adjust the topography feedback parameter according to the difference of trace and retrace, which are scanned with different setpoints [20]. Here, we extend the methods reported by Schiener et al. [19] and Fan et al. [21], applying a feedback based on the Q-factor to stabilise the tip–sample distance. In our implementation the ratio of excitation and amplitude of the first harmonic resonance, and thus the Q-factor, is held constant by a slow feedback to compensate for drift of the free resonance frequency.

Results and Discussion

Experiment

We use unpackaged length-extension resonators (Microcrystal, Switzerland) and solder both gold electrodes at the base of the sensor to conductive tracks on a piece of a circuit board (Figure 1a). The latter is glued to an L-shaped metal piece, which in turn is screwed to a Cypher droplet holder (Figure 1b) for operation in a Cypher AFM (Asylum Research). The resonator is excited electrically by applying a small AC voltage to one of its electrodes (input) and the displacement-induced piezoelectric current is detected on the other electrode which is connected to a charge amplifier (HQA-15M-10T, FEMTO) (output). Input and output are connected to an oscillator and phased-locked loop (HF2, Zurich Instruments), respectively (see Figure 1a). We use the frequency shift Δf as feedback signal for topography while maintaining a constant amplitude with a separate feedback (constant-amplitude FM-AFM). Tips from commercial cantilevers (e.g., Olympus AC160-R3, Nanosensors SSS-NCH) are glued to the front face of the protruding oscillating beam with silver epoxy (E4110-LV, EPO-TEK Epoxy Technology). Environmental conditions are monitored with a digital temperature and humidity sensor (SHT71, Sensirion AG [22]). Basic image processing (e.g., levelling) is done with the Gwyddion software [23].

To determine the sensitivity S of the LER a thermal noise spectrum was acquired around the resonance frequency (Figure 1c). Integration over the noise power spectral density after subtraction of the detector noise floor yields the mean square displacement $\langle U^2 \rangle$ in "V^2" of the resonator. The sensitivity S is then the conversion factor between $\langle U^2 \rangle$ and $\langle z^2 \rangle$ in "nm^2": $\langle U^2 \rangle = S^2 \langle z^2 \rangle$. Taking the equipartition theorem, the potential energy of the oscillating beams equals the thermal energy, we can determine S:

$$\frac{1}{2} k_{\text{eff}} \langle z^2 \rangle = \frac{1}{2} k_{\text{B}} T \longrightarrow S = \sqrt{\frac{\langle U^2 \rangle}{\langle z^2 \rangle}} = \sqrt{\frac{k_{\text{eff}}}{k_{\text{B}} T} \langle U^2 \rangle}, \quad (1)$$

where k_{eff} is the effective stiffness, $\langle z^2 \rangle$ the mean square displacement of the resonator, k_{B} the Boltzmann constant and T the temperature. The inverse sensitivity amounts to $1/S = 2.2$ nm/V_{rms}. Scaling with $1/S$, the detector noise density (noise floor in Figure 1c) is 1.0 fm/$\sqrt{\text{Hz}}$, which is comparable to the value measured by Giessibl et al. for signal-to-noise ratio calculations of the LER [9].

Compensation of environment-induced frequency shift

The frequency shift signal Δf is a measure of the force gradient k_{ts} according to $\Delta f = f_0 k_{\text{ts}}/2k$, where f_0 is the free resonance fre-

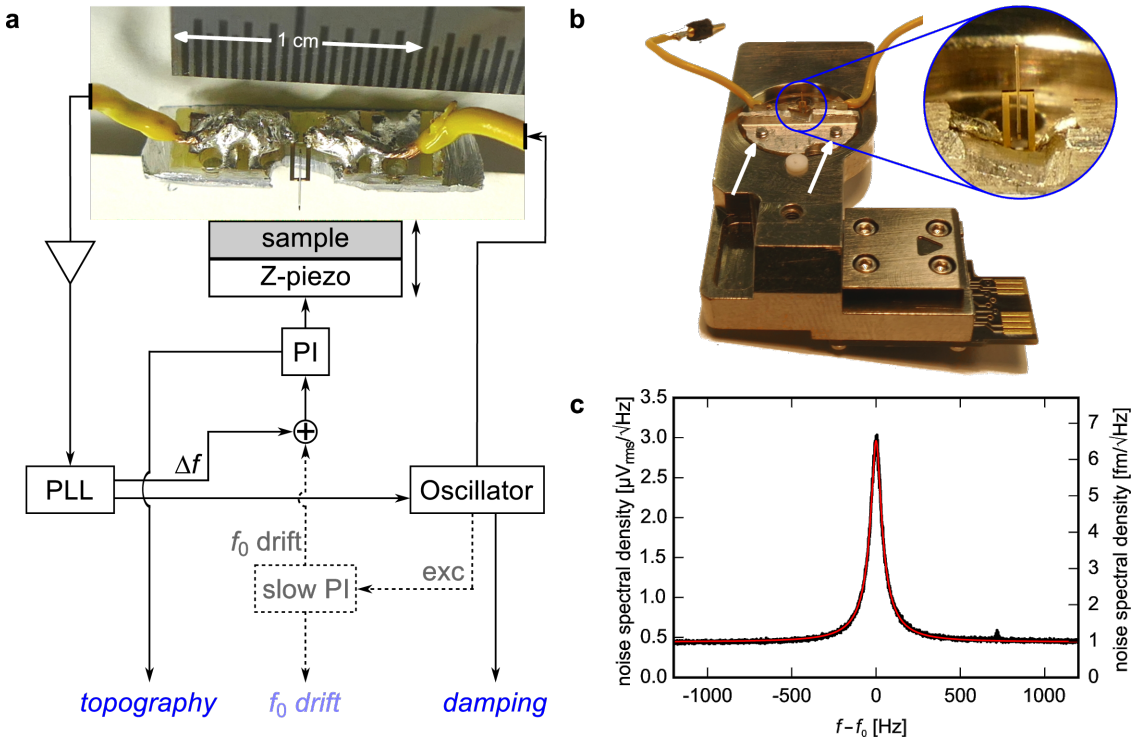

Figure 1: Experimental setup. a) Feedback scheme. The dashed parts enable the slow-drift compensation. Also shown is the LER soldered on a piece of a circuit board, which is glued to an L-shaped metal adapter piece. b) Image of the Cypher droplet holder with LER adapter piece fixed by two screws (white arrows). c) Thermal noise spectrum (black) of a LER with a SSS-NCHR tip attached and a fit of a damped harmonic oscillator (red). The right axis is obtained by multiplying the left axis with the inverse sensitivity $1/S$ = 2.2 nm/V_{rms}. Parameters derived from the fit: Q = 17,000, f_0 = 999.3 kHz. The detector noise density is 1.0 fm/$\sqrt{\text{Hz}}$.

quency. The high stiffness k of the LER leads to a frequency shift signal about 20 times smaller compared to quartz tuning fork sensors. For accurate measurements with the LER it is important to minimise disturbances of the resonance frequency by sources unrelated to the tip–sample interaction.

Figure 2a shows the variation of frequency shift, excitation and dew point [22] over time while the sensor is retracted from the surface and Z-feedback is disabled. Frequency shift and damping correlate with environmental conditions. The resonance frequency decreases whereas the damping increases when the dew point rises. Reasons for this behaviour could be, for example, water condensation on the resonator which would add mass, or expansion/contraction of parts of the setup and the solder joints used for mounting the LER. From Figure 2a we find a change in the dew point of about +0.5 K resulting in a

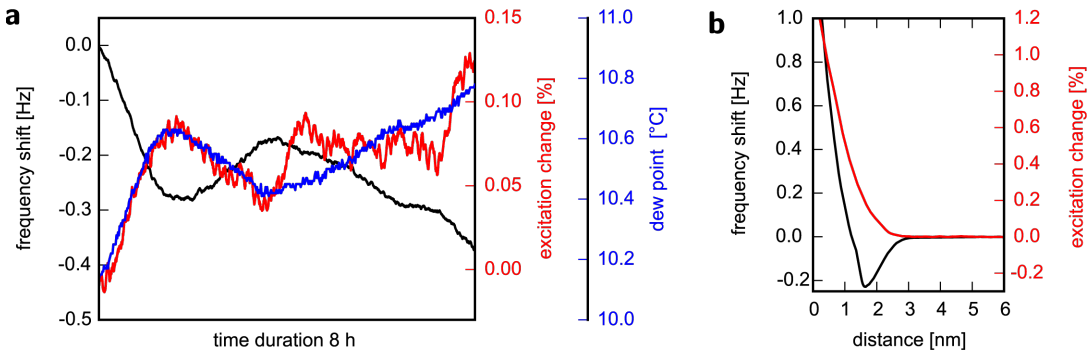

Figure 2: a) Evolution of resonance frequency shift (black), excitation (red), and dew point (blue) over a duration of 8 h. Z-feedback is disabled and the Z-piezo is fully retracted. b) Frequency shift (black) versus distance plot with simultaneously recorded excitation (red) to maintain a constant amplitude of 1.1 nm on a KBr(001) single crystal surface after cleavage in air. The initial excitation is 2.961 mV.

change of −0.27 Hz and +0.08% in the resonance frequency and excitation, respectively.

Let us now consider a real measurement at a setpoint of +0.2 Hz. From Figure 2b, an environment-induced shift of the resonance frequency of +0.27 Hz would lead to a change of the tip–sample distance and the excitation of about 300 pm and 0.42%, respectively. This will strongly affect the desired force gradient setpoint and interpretation of data becomes difficult. Furthermore, in a scenario where operation near the frequency shift minimum Δf_{min} is desired, environment-induced drift could cause the setpoint Δf_{set} to cross Δf_{min}, leading to retraction (extension) of the Z-piezo if Δf_{set} was originally on the negative (positive) slope branch of the Δf–z curve. Again, stable imaging would not be possible.

To overcome such experimental difficulties we have implemented an additional slow feedback to adjust the frequency shift setpoint. The excitation signal is used as input signal of a slow proportional-integral-controller. The setpoint of this slow feedback is determined by the excitation measured at the desired Δf topography setpoint, and thus the desired tip–sample distance. We mainly apply low integrator gain only, resulting in a long time constant ($\tau \approx \mathcal{O}$ (1 min)), which still allows us to determine damping properties of the sample with the much faster regular amplitude-controller ($\tau \approx 5$ ms). The slow controller applies an offset to the Δf-signal in order to maintain the excitation setpoint and thus compensates for slow drifts. This is possible because changes of the dew point affect the excitation directly about five times less than the tip–sample distance alteration caused by drift in f_0. Slow drifts of the excitation constitute a source of error of this method. Hence, heterogeneous samples should be orientated such that material properties primarily change along the fast scan axis.

An example of how this additional slow feedback compensates for environmental changes is shown in Figure 3. Here, consecutive scans over a period of 140 min were performed on a KBr crystal surface with a frequency shift setpoint of +0.15 Hz. The air flow to the AFM housing is controlled via a hose and a reservoir. The air supplied to the reservoir was changed from low humidity air to normal room air after eight minutes. Figure 3a shows dew point ϑ_{dew}, frequency shift Δf, and frequency shift offset Δf_{offset} applied by the slow feedback during the whole duration of the scans. In 140 min the dew point increased by about 12 K. At the beginning (time = 0) the frequency shift drops from Δf = +0.9 Hz to the Δf-setpoint, which is due to piezo engage from the home (retracted) position. During withdrawal of the Z-piezo back to its home position after the scans (time = 138 min), the frequency shift drops to Δf = −1.05 Hz, which results in a total difference of Δf_{drift} = −1.95 Hz attributed to drift. As can be seen from the jump at 133 min (Figure 3a) the tip was retracted before the end of the scans and approached again, most likely due to a bigger contamination on the surface. Note, the frequency shift offset applied for compensation by the slow feedback, Δf_{offset} follows an almost mirrored trace of the dew point, reaching Δf_{offset} = −2.0 Hz just before the end of the scans. This value corresponds very well to the measured Δf_{drift}, demonstrating the reliability of the method. In Figure 3b the topography of the last scan is shown together with a height profile along the line indicated (Figure 3c). A typical KBr surface with terraces separated by steps of approximately 315 pm is observed.

Force regime

As mentioned earlier, the force sensitivity of the LER is lower compared to commercial cantilevers due to the very high stiffness. However, this allows for stable operation with small amplitudes and avoids jump-into-contact. Based on our experi-

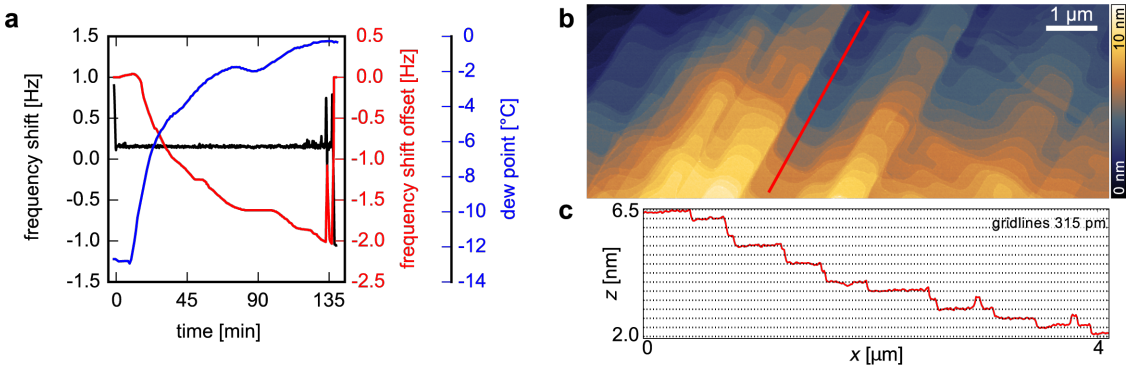

Figure 3: Application of the slow feedback control. a) Evolution of frequency shift Δf (black), frequency shift offset Δf_{offset} (red), and dew point ϑ_{dew} (blue) over 140 min. b) Large scale topography of a KBr surface and c) corresponding height profile along the red line in b). The step height is 315 pm. Scan parameters: A = 1.1 nm, Δf = +0.15 Hz, scan speed 10 µm/s.

ence, imaging in the regime of positive slope of Δf often does not provide high resolution whereas imaging on the negative slope is very stable and yields good resolution. The question arises whether non-destructive scanning on delicate samples is still possible in the repulsive regime. To quantify interaction forces we apply the formula derived by Sader and Jarvis [24] to convert the frequency shift into a tip–sample force:

$$F_{\mathrm{ts}}(z) = \frac{2k}{f_0}\int_z^{\infty} \mathrm{d}t \left[\left(1+\frac{A^{1/2}}{8\sqrt{\pi(t-z)}}\right)\Delta f(t) - \frac{A^{3/2}}{\sqrt{2(t-z)}}\frac{\mathrm{d}(\Delta f(t))}{\mathrm{d}t}\right], \quad (2)$$

where f_0 is the resonance frequency, k the stiffness, A the amplitude, and z the tip–sample distance. A Δf–z curve on HOPG with calculated F_{ts} at an amplitude of 1.1 nm is shown in Figure 4. Only a small attractive force regime is present, which can be explained by the high stiffness of the LER. Depending on the sample and its preparation larger attractive forces have also been observed.

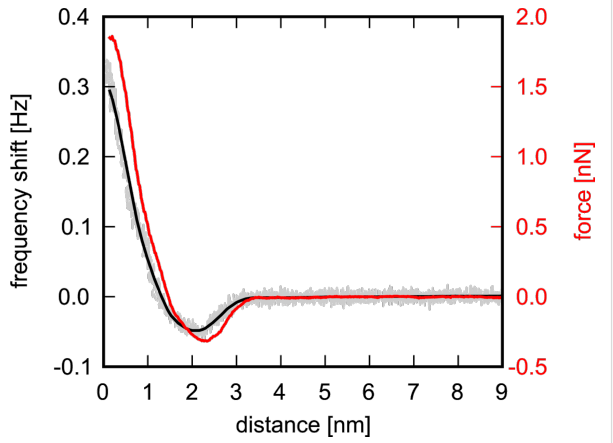

Figure 4: Smoothed frequency-shift (black) versus distance curve on HOPG and tip–sample force F_{ts} (red) calculated from the Sader–Jarvis algorithm. The grey curve corresponds to the frequency shift raw data. A = 1.1 nm.

To prove the feasibility of scanning with small forces a surface decorated by adsorbates was chosen. For this purpose we rinsed a freshly exfoliated (adhesive tape, BT-150E-AT, Nitto Denko) graphite surface with Milli-Q water. It has been reported that in a narrow band of small forces stripes of adsorbed gas molecules can be observed [25]. Indeed, with a setpoint of Δf = +0.2 Hz corresponding to a force of about 1.0 nN three differently orientated domains are observed (Figure 5a). The domains are rotated by an angle of 60° which can be attributed to the underlying hexagonal lattice of graphite. The origin of the stripe pattern is attributed to nitrogen adsorbed through water layers as proposed by Lu et al. [25] from an experiment in a controlled environment. The periodicity of the stripes amounts to 6.2 ± 0.3 nm (Figure 5b). This value differs from the reported 4 nm spacing between the stripes [25,26]. In a later publication Lu et al. also found row spacings of 2 nm for some domains [27], and recently even distances of 6–7 nm have been reported [28,29]. Apparently, several energetically favourable configurations may exist for the adsorption of nitrogen molecules. Further theoretical as well as experimental studies are needed to gain deeper insight into the self-assembly of such molecules on surfaces through water layers.

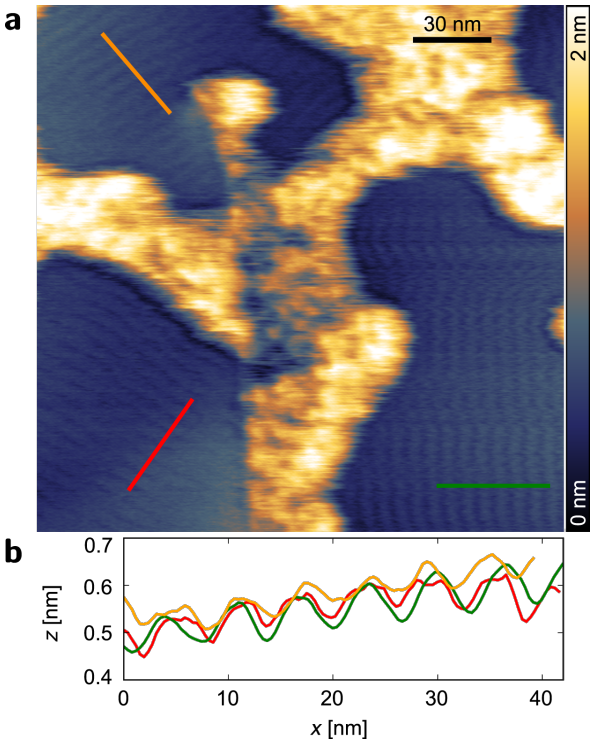

Figure 5: Topography (a) of HOPG after rinsing with Milli-Q water and height profiles (b) along the lines indicated in a) showing the periodic patterns of three domains. A = 1.1 nm, Δf = +0.2 Hz, scan speed 977 nm/s.

Atomic resolution on graphite

To further demonstrate the high-resolution capability in air, a clean HOPG surface was investigated. The topography feedback gains were set low, resulting in a quasi-constant height mode measurement. Starting from a low positive frequency shift setpoint, the tip–sample distance was gradually decreased until atomic contrast was observed. The hexagonal lattice of the graphite surface appeared between Δf = +315 Hz and +400 Hz. Figure 6 shows a frequency shift image (raw data) acquired with a setpoint of +335 Hz. The raw image is distorted due to

drift of the scanner and has been corrected (inset of Figure 6) using a Fourier peak detection method [30]. The drift-corrected image has been processed further by correlation averaging and 3-fold symmetrisation [31]. The honeycomb structure becomes more evident and different repulsive forces for α (above atom in 2nd layer) and β (hollow) sites are observed, too.

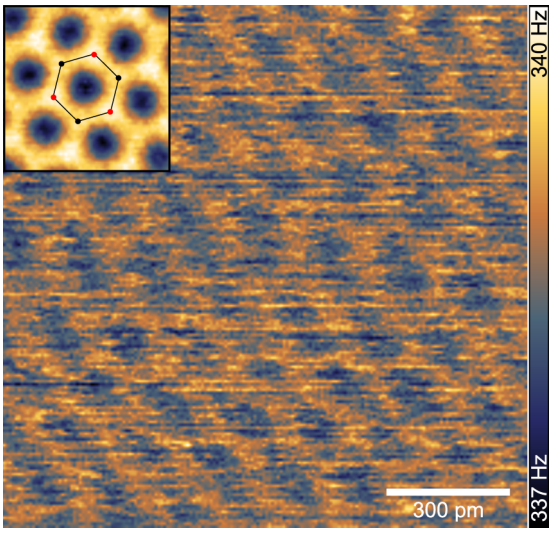

Figure 6: High-resolution detuning image of HOPG in quasi-constant height mode. Inset: 3-fold symmetrised drift-compensated correlation average with overlaid honeycomb structure. *A* = 220 pm, scan speed 58.6 nm/s.

Considering the weaker force sensitivity due to the high stiffness of the sensor, high frequency shifts were required to achieve atomic resolution. The interaction forces amount to hundreds of nanonewtons, exceeding the forces observed in contact-mode AFM. Water layers on the surface can contribute substantially to the interaction forces and lead to higher frequency shifts [6,32]. At this stage the atomic contrast obtained at high forces cannot be fully explained yet and further investigations are needed. The operation regime applied here for atomic resolution is rather a "resonant contact" than non-contact mode.

Conclusion

We have demonstrated high-resolution FM-AFM imaging under ambient conditions with the length-extension resonator. The resonator can be operated stably at small as well as large tip–sample interaction forces. Adsorbates of nitrogen were imaged on HOPG, which paves the road for high-resolution imaging of samples in their natural environment. Furthermore, we have shown atomic resolution imaging on graphite although the interactions are not yet fully understood. A slow feedback maintaining a constant excitation was introduced to compensate for drifts of the free resonance frequency. Stable imaging was demonstrated under extreme variations of the dew point over a period of 140 min. The method could be adapted to other instruments where the Q-factor is rather constant. A modified version could even be used in amplitude-modulated AFM where the average phase signal would be held constant.

Acknowledgements

The authors thank Patrick Reissner for stimulating discussions, Blerim Veselaj for technical support, and Giselher Wichmann for preliminary work on the LER and tip mounting.

References

1. Fukuma, T.; Kobayashi, K.; Matsushige, K.; Yamada, H. *Appl. Phys. Lett.* **2005,** *87,* 034101. doi:10.1063/1.1999856
2. Wastl, D. S.; Weymouth, A. J.; Giessibl, F. J. *Phys. Rev. B* **2013,** *87,* 245415. doi:10.1103/PhysRevB.87.245415
3. Giessibl, F. J. *Phys. Rev. B* **1997,** *56,* 16010–16015. doi:10.1103/PhysRevB.56.16010
4. Gross, L.; Mohn, F.; Moll, N.; Liljeroth, P.; Meyer, G. *Science* **2009,** *325,* 1110–1114. doi:10.1126/science.1176210
5. Pawlak, R.; Kawai, S.; Fremy, S.; Glatzel, T.; Meyer, E. *ACS Nano* **2011,** *5,* 6349–6354. doi:10.1021/nn201462g
6. Wastl, D. S.; Weymouth, A. J.; Giessibl, F. J. *ACS Nano* **2014,** *8,* 5233–5239. doi:10.1021/nn501696q
7. Dinger, R. A Miniature Quartz Resonator Vibrating at 1 MHz. In *Proc. 35th Ann. Freq. Control Symposium,* Fort Monmouth, NJ; IEEE, 1981; pp 144–148.
8. Dransfeld, K.; Fischer, U.; Guethner, P.; Heitmann, K. Akustisches Rastermikroskop zur Untersuchung eines Objektes im Nahfeld eines resonanten akustischen Resonators. German Patent DE3820518, Jan 11, 1988.
9. Giessibl, F. J.; Pielmeier, F.; Eguchi, T.; An, T.; Hasegawa, Y. *Phys. Rev. B* **2011,** *84,* 125409. doi:10.1103/PhysRevB.84.125409
10. Heike, S.; Hashizume, T. *Appl. Phys. Lett.* **2003,** *83,* 3620. doi:10.1063/1.1623012
11. An, T.; Eguchi, T.; Akiyama, K.; Hasegawa, Y. *Appl. Phys. Lett.* **2005,** *87,* 133114. doi:10.1063/1.2061850
12. Torbrügge, S.; Schaff, O.; Rychen, J. *J. Vac. Sci. Technol., B* **2010,** *28,* C4E12. doi:10.1116/1.3430544
13. *Kolibri sensor application notes*; SPECS Surface Nano Analysis GmbH, 2015. http://www.specs.de
14. Morawski, I.; Voigtländer, B. *Rev. Sci. Instrum.* **2010,** *81,* 033703. doi:10.1063/1.3321437
15. Murdfield, T.; Fischer, U. C.; Fuchs, H.; Volk, R.; Michels, A.; Meinen, F.; Beckman, E. *J. Vac. Sci. Technol., B* **1996,** *14,* 877. doi:10.1116/1.589166
16. Nishi, R.; Houda, I.; Aramata, T.; Sugawara, Y.; Morita, S. *Appl. Surf. Sci.* **2000,** *157,* 332–336. doi:10.1016/S0169-4332(99)00547-4
17. Peng, Z.; West, P. *Appl. Phys. Lett.* **2005,** *86,* 014107. doi:10.1063/1.1846156
18. Froning, J. P.; Xia, D.; Zhang, S.; Lægsgaard, E.; Besenbacher, F.; Dong, M. *J. Vac. Sci. Technol., B* **2015,** *33,* 021801. doi:10.1116/1.4906517
19. Schiener, J.; Witt, S.; Stark, M.; Guckenberger, R. *Rev. Sci. Instrum.* **2004,** *75,* 2564–2568. doi:10.1063/1.1777405
20. Kindt, J. H.; Thompson, J. B.; Viani, M. B.; Hansma, P. K. *Rev. Sci. Instrum.* **2002,** *73,* 2305. doi:10.1063/1.1475352

21. Fan, L.; Potter, D.; Sulchek, T. *Rev. Sci. Instrum.* **2012,** *83,* 023706. doi:10.1063/1.3683236
22. For dew point calculation see Datasheet Humidity Sensor SHT7x. http://www.sensirion.com (accessed Nov 12, 2015).
23. Nečas, D.; Klapetek, P. *Cent. Eur. J. Phys.* **2012,** *10,* 181–188. doi:10.2478/s11534-011-0096-2
24. Sader, J. E.; Jarvis, S. P. *Appl. Phys. Lett.* **2004,** *84,* 1801. doi:10.1063/1.1667267
25. Lu, Y.-H.; Yang, C.-W.; Hwang, I.-S. *Langmuir* **2012,** *28,* 12691–12695. doi:10.1021/la301671a
26. Wastl, D. S.; Speck, F.; Wutscher, E.; Ostler, M.; Seyller, T.; Giessibl, F. J. *ACS Nano* **2013,** *7,* 10032–10037. doi:10.1021/nn403988y
27. Lu, Y.-H.; Yang, C.-W.; Hwang, I.-S. *Appl. Surf. Sci.* **2014,** *304,* 56–64. doi:10.1016/j.apsusc.2014.03.084
28. Gallagher, P.; Lee, M.; Amet, F.; Maksymovych, P.; Wang, J.; Wang, S.; Lu, X.; Zhang, G.; Watanabe, K.; Taniguchi, T.; Goldhaber-Gordon, D. *Nat. Commun.* **2016,** *7,* 10745. doi:10.1038/ncomms10745
29. Sivan, U. *An Ultra-Low Noise, Liquid Environment Atomic Force Microscope*; Talk at the NC-AFM: Cassis, France, 2015.
30. Jørgensen, J. F.; Madsen, L. L.; Garnaes, J.; Carneiro, K.; Schaumburg, K. *J. Vac. Sci. Technol., B* **1994,** *12,* 1698. doi:10.1116/1.587266
31. Philippsen, A.; Schenk, A. D.; Signorell, G. A.; Mariani, V.; Berneche, S.; Engel, A. *J. Struct. Biol.* **2007,** *157,* 28–37. doi:10.1016/j.jsb.2006.06.009
32. Arai, T.; Koshioka, M.; Abe, K.; Tomitori, M.; Kokawa, R.; Ohta, M.; Yamada, H.; Kobayashi, K.; Oyabu, N. *Langmuir* **2015,** *31,* 3876–3883. doi:10.1021/acs.langmuir.5b00087

License and Terms

BEILSTEIN JOURNAL OF NANOTECHNOLOGY

Modelling of ‘sub-atomic’ contrast resulting from back-bonding on Si(111)-7×7

Adam Sweetman*, Samuel P. Jarvis and Mohammad A. Rashid

Full Research Paper

Open Access

Address:
The School of Physics and Astronomy, The University of Nottingham, Nottingham, NG7 2RD, United Kingdom

Email:
Adam Sweetman* - adam.sweetman@nottingham.ac.uk

* Corresponding author

Keywords:
NC-AFM; qPlus; sub-atomic; sub-molecular

Beilstein J. Nanotechnol. **2016,** *7,* 937–945.
doi:10.3762/bjnano.7.85

Received: 29 October 2015
Accepted: 09 June 2016
Published: 29 June 2016

This article is part of the Thematic Series "Noncontact atomic force microscopy III".

Guest Editor: M. Z. Baykara

Abstract

It has recently been shown that ‘sub-atomic’ contrast can be observed during NC-AFM imaging of the Si(111)-7×7 substrate with a passivated tip, resulting in triangular shaped atoms [Sweetman et al. *Nano Lett.* **2014**, 14, 2265]. The symmetry of the features, and the well-established nature of the dangling bond structure of the silicon adatom means that in this instance the contrast cannot arise from the orbital structure of the atoms, and it was suggested by simple symmetry arguments that the contrast could only arise from the backbonding symmetry of the surface adatoms. However, no modelling of the system has been performed in order to understand the precise origin of the contrast. In this paper we provide a detailed explanation for ‘sub-atomic’ contrast observed on Si(111)-7×7 using a simple model based on Lennard-Jones potentials, coupled with a flexible tip, as proposed by Hapala et al. [*Phys. Rev. B* **2014**, 90, 085421] in the context of interpreting sub-molecular contrast. Our results show a striking similarity to experimental results, and demonstrate how ‘sub-atomic’ contrast can arise from a flexible tip exploring an asymmetric potential created due to the positioning of the surrounding surface atoms.

Introduction

Recent developments in low temperature scanning probe instrumentation [1], coupled with specific experimental techniques utilising the in situ functionalisation of scanning probe tips with single molecules [2], and operation in the constant-height imaging mode, have resulted in an explosion of interest in high-resolution imaging and force mapping of atomic and molecular structures using non-contact atomic force microscopy (NC-AFM). In particular, suppressing the chemical bonding between tip and sample enables the stable exploration of the repulsive part of the tip–sample force regime, which has allowed outstanding resolution to be obtained during imaging of planar organic molecules [3,4]. An important development in the inter-

pretation of sub-molecular resolution imaging has been the explicit consideration of deflection (i.e., mechanical deformation) in the tip–sample junction [5-7], which can result in contrast enhancement [6], but also unwanted distortions and potential artefacts [5,7-10]. Modelling using computationally inexpensive empirical potentials has produced a surprisingly good agreement with experimental data, and also allows for simulated images to be computed with a comparable size and resolution to experiment, which is essential for meaningful qualitative comparisons.

In this paper we explore the application of a simple Lennard-Jones model with a flexible tip probe [5,7,8] to a case of 'sub-atomic' imaging on the Si(111)-7×7 surface [11,12]. We show that the triangular features observed experimentally arise naturally from the exploration of an asymmetric potential by a flexible tip and do not require consideration of the detailed electronic structure of the surface. By constructing artificial surface slabs utilising different elements of the full Si(111)-7×7 unit cell, we are able to examine the relative influence of the different parts of the surface on the contrast. Our simulations show the influence of the backbonding atoms (that is, the atoms directly behind the topmost adatoms, via which they are bonded to the surface), and also the influence of the rest atoms in the unit cell, on the triangular adatom contrast. We also highlight the limitations of the model when chemical interactions become important at close approach, and explore the qualitative variation in contrast observed between force and Δf images depending on oscillation amplitude.

Simulation Methods

To simulate constant height force images, we used the method proposed by Hapala et al. [7,13] to model the interaction between a functionalized probe and the Si(111)-7×7 unit cell, using simple Lennard-Jones (L-J) potentials. In this model the functionalized tip is assumed to consist of a tip base, representing the end of the bulk tip material, and a single passivated probe particle. In order to simulate the mechanical deformation in the tip–sample junction, the probe particle is allowed to move around the tip base, and acts as a flexible end of the model tip. To model the Si(111)-7×7 surface we imported a relaxed geometry from previous density functional theory simulations performed in our group, details of which are described elsewhere [14]. During the force field calculations the positions of all the atoms in the surface slab were kept fixed. We note that more sophisticated versions of the probe-particle model also incorporate the effect of electrostatics via introduction of the Hartree potential, which has been shown to have important consequences for the imaging of certain classes of molecules [15]. In our simulations the effect of the Hartree potential is not included, primarily as electrostatic forces are not expected to result in significant differences in contrast due to the small variation in electrostatic force over the different atoms of the Si(111)-7×7 unit cell [16].

In the simulations the probe particle is subject to forces from three sources: 1) a L-J-like interaction due to the tip base, 2) a sum of all pairwise forces due to interactions with the atoms in the sample slab, and 3) a lateral harmonic restoring force from the tip base. We used the same L-J parameters as described by Hapala et al. [7], i.e., a tip base with parameters r_α= 2 Å, and ε_α = 1000 meV (artificially large to keep the probe particle attached), and a probe particle with parameters r_α = 1.66 Å and ε_α = 9.106 meV, and a lateral stiffness of 0.5 N/m.

In the L-J model, the interaction between atoms α and β are written as:

$$\mathbf{F}_{\alpha\beta}(\mathbf{R}) = 12\varepsilon_{\alpha\beta}\mathbf{R}\left(\frac{r_{\alpha\beta}^{12}}{r^{14}} - \frac{r_{\alpha\beta}^{6}}{r^{8}}\right) \quad (1)$$

$$U_{\alpha\beta}(r) = \varepsilon_{\alpha\beta}\left(\frac{r_{\alpha\beta}^{12}}{r^{12}} - \frac{r_{\alpha\beta}^{6}}{r^{6}}\right), \quad (2)$$

where $r = |\mathbf{R}|$ is the distance between atoms α and β, $\varepsilon_{\alpha\beta} = \sqrt{\varepsilon_\alpha \varepsilon_\beta}$ is the pair binding energy and $r_{\alpha\beta} = r_\alpha + r_\beta$ is the equilibrium separation of the two atoms with ε_α and r_α being the atomic parameters. In our calculations the L-J parameters for the silicon atoms were set to ε_α = 25.489 meV and r_α = 1.9 Å. We acquired the simulation data by scanning the sample laterally with a step of Δx, Δy = 0.1 Å. At each lateral position we placed the tip base at an initial separation z_0 = 15 Å from the surface molecule and approached the sample in steps of Δz = 0.05 Å, allowing the probe position to be relaxed at each step due to the combined force of the sample and tip base. After calculation of the 3D force field, a complementary Δf grid was calculated using the method proposed by Giessibl et al. [17], assuming cantilever parameters of k_{cant} = 1800 N/m and f_0 = 30 kHz.

It is important to stress that there are a number of differences between the systems normally modelled using this approach and the experimental system to which we compare our results. Typically, in sub-molecular resolution imaging experiments, well defined atoms (such as Xe or Cl), or molecules (such as CO) are picked up from metal surfaces onto metal-coated tips by STM protocols [3]. In our experimental data the initial tip termination is likely silicon due to prior STM treatment of the tip on the clean Si(111)-7×7 surface (although the tip bulk material is tungsten). In addition, the identity of the passivating end group,

which was picked up spontaneously during NC-AFM imaging of the clean surface, is not known. Although CO is a common vacuum contaminant, our tip termination could also easily be a number of other common contaminants (for example H, OH or O), which would also suppress the chemical reactivity of the tip apex. Therefore our modelling, using CO parameters, is only intended to represent a 'generic' passivated tip. In particular, the chemical interaction between the passivating end group and a silicon-terminated tip is likely to be different to the interaction between CO and a metal terminated tip, which may explain the differences between experiment and simulation which we observe at close approach (see later discussion).

Results

Origin of triangular contrast in simulated images

Figure 1 shows a comparison between experimental constant height Δf images (acquired during the same experimental run as [11]), and simulated constant height Δf images using a flexible, and very rigid, tip apex. In both cases the images have been selected from full datasets in order to best illustrate the evolution of the contrast as the tip–sample distance is decreased, full datasets are available in Supporting Information File 1–Supporting Information File 9.

Far from the surface (top row Figure 1) the adatoms of the surface appear as attractive features (i.e., dark depressions resulting from more negative frequency shifts). Likewise, both of the simulated sequences show attractive contrast at large tip–surface separations, as expected for a L-J interaction. Closer to the surface (second row from top Figure 1) the adatoms and rest atoms begin to image as repulsive features (bright regions corresponding to more positive frequency shifts). At this height the triangular shape of the atoms is already visible. In the simulated images the adatoms and rest atoms are visible as repulsive features, but are only slightly non-spherical. Further into the repulsive regime (second row from bottom Figure 1) triangular adatoms and rest atoms are clearly observed experimentally, and these features are reproduced well in the simulations using the flexible tip. At very close approach dark depressions are observed in the center of the adatoms experimentally (bottom row Figure 1), which corresponds to the onset of a strong attractive interaction. It is possible that these features correspond to some reversible change in the tip state due to the strong repulsive tip–sample forces – e.g., either a change in the position of the passivating end group, or some modification of the chemical reactivity of the tip due to mechanical deformation. Interestingly, somewhat similar features are reproduced in simulation using the flexible tip, with an inversion of contrast directly over the adatoms. This results from the deflection of the tip, and is the origin of the contrast inversion during intramolecular imaging described previously by Hapala et al. [7]. However, it is important to note that the simulations do not reproduce the dramatic drop in Δf observed experimentally, as the simple Lennard-Jones potential used does not take into account chemical interactions, or changes in the chemical reactivity of the tip. This evolution in contrast is not reproduced in the simulations using a very stiff tip (right column), where the atoms of the Si(111)-7×7 surface remain spherical throughout. This highlights the essential requirement for considering the flexibility of the tip apex in interpreting contrast obtained in the repulsive regime using passivated tips. There are also some additional minor differences between the simulation and experimental results. Most notably, a difference is observed experimentally in the contrast over the different adatoms of the Si(111)-7×7 unit cell, corresponding to the known differences in chemical reactivity at these sites [18]. As each of the atoms in the simulations has identical properties, this variation is not reproduced in the simulated images. We also note the non-physical asymmetric distortions in the atoms at the edge of the unit cell in the simulations, due to the finite unit cell size. Therefore in comparisons to the experimental data we focus on the appearance of the atoms in the centre of the unit cell, which experience a uniform attractive background.

Although these simulations reveal the key role that relaxation in the tip–sample junction plays in explaining the image contrast, they do not necessarily reveal the origin of the features. Beyond the computational simplicity of the L-J model, an additional advantage compared to more sophisticated modelling techniques is that it is easy to construct "toy" systems that allow us to explore how different parts of the surface contribute to the image contrast. A selection of simulated image sequences using this approach is shown in Figure 2, which helps elucidate the origin of the contrast in the simulations shown in Figure 1. The first column shows a control model, where only the adatoms of the Si(111)-7×7 unit cell have been used as the surface slab. In this sequence the adatoms image as uniform spheres at all heights, with the exception of the previously mentioned contrast inversion in the centre at close approach. When the atoms in the backbonding positions are included (middle column), the evolution of the adatoms goes from spherical to triangular contrast with close approach of the tip. Consequently, it appears that the presence of the backbonding atoms creates an asymmetry in the repulsive part of the potential, producing a complementary asymmetry in the deflection of the probe particle as it explores the tip–sample interaction. Interestingly, when only the adatoms and rest atoms are included in the surface slab (right hand column) the rest atoms appear clearly triangular, and the adatoms also have a triangular symmetry, despite the lack of atoms in the backbonding positions. This separation of the effect of the different elements of the surface slab illustrates

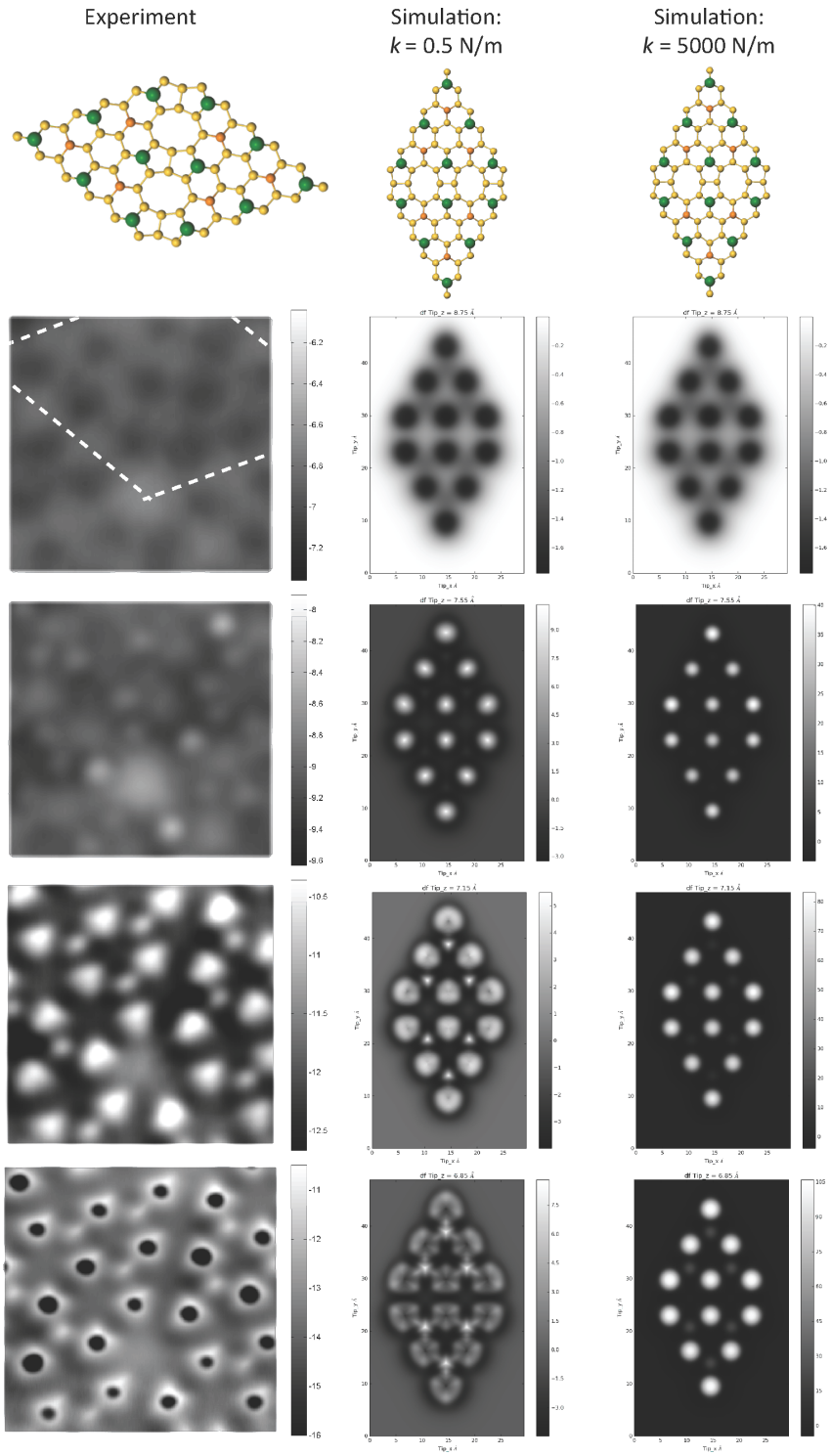

Figure 1: Left column: Experimental constant height Δ*f* images at decreasing tip–sample separation. Note a 10 point gaussian filter has been applied to all images to remove high frequency noise. Experimental parameters: A_0 = 110 pm, V_{gap} = 0 V. Experimental tip heights relative to Δ*f* feedback setpoint (top to bottom): +0.186 nm, +0.104 nm, +0.032 nm, 0 nm. Image size 3.6 nm × 3.6 nm. Data acquired at 77 K. Middle column: simulated constant height force images over a Si(111)-7×7 unit cell using a flexible tip with stiffness k_{xy} = 0.5 N/m. At close approach triangular adatoms and rest adatoms become apparent, strikingly similar to the experimental images. At very close approach an inversion occurs directly over the adatoms resulting in a dark hole in the centre of the atom. Right column: simulated constant height force images using a tip with stiffness k_{xy} = 5000 N/m. The atomic features remain spherically symmetric at all tip–sample separations. Simulated tip heights: (top to bottom) 0.875 nm, 0.755 nm, 0.715 nm, 0.685 nm.

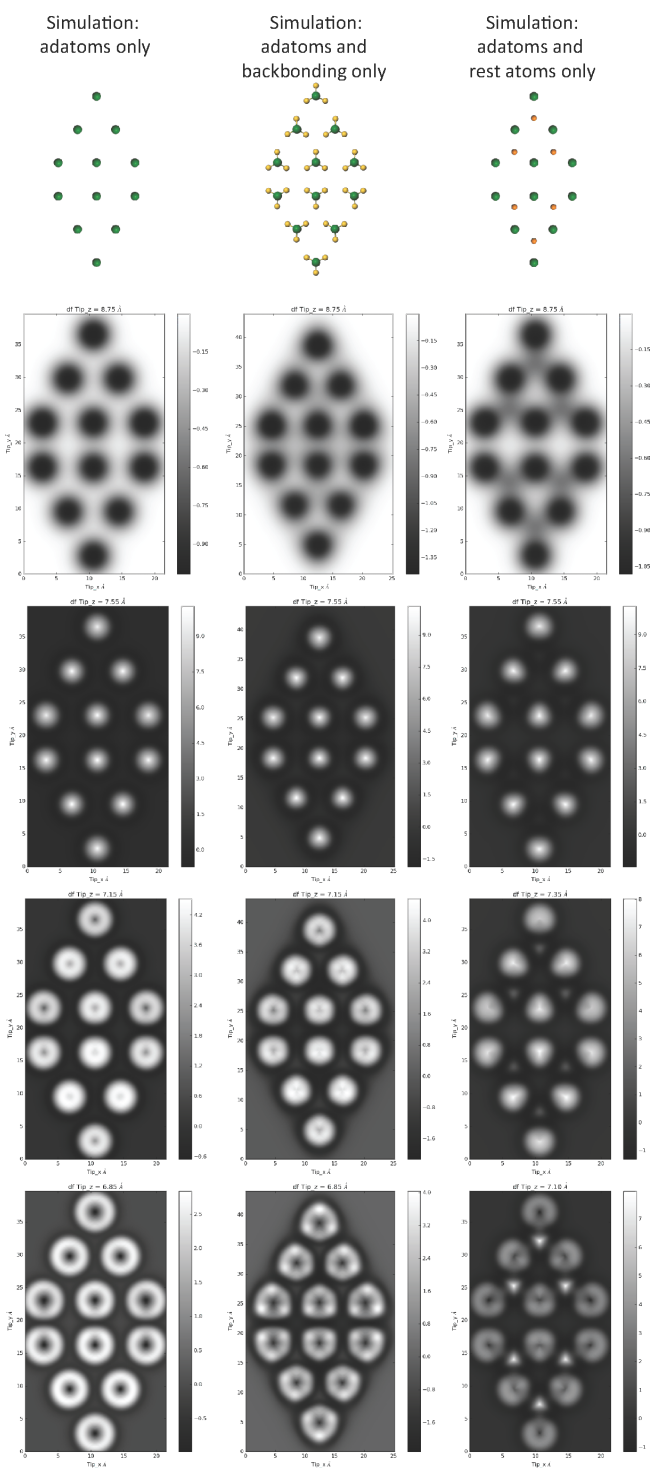

Figure 2: Left column: simulated constant height force images at decreasing tip–sample separation, over a Si(111)-7×7 unit cell containing only the upper adatoms. All atoms image as uniform spheres, at close approach an inversion occurs in the centre of the atoms. Middle column: simulated constant height force images at decreasing tip–sample separation, over a Si(111)-7×7 unit cell containing only the adatoms and their backbonding atoms. At close approach the adatoms appear as triangles with a orientation matching the backbonding atoms, with an inversion in the centre of the atoms. Right column: simulated constant height force images at decreasing tip–sample separation, over a Si(111)-7×7 unit cell containing the adatoms and rest atoms (no backbonding atoms). The rest atoms image as triangles as a result of being positioned in the asymmetric potential of the surrounding adatoms. Also note the weak triangular shape of the adatoms as a result of the potential arising from the position of the rest atoms, in addition to the inversion in the centre of the atom. Simulated tip heights, left and middle column: (top to bottom) 0.875 nm, 0.755 nm, 0.715 nm, 0.685 nm, right column (top to bottom): 0.875 nm, 0.755 nm, 0.735 nm, 0.710 nm. Tip stiffness k_{xy} = 0.5 N/m for all simulations.

how the appearance of the atoms is shaped by the potential created by the entire surface. In the case of the rest atoms, their position within the asymmetric attractive potential of the surrounding adatoms means that a saddle in the potential is created, resulting in an asymmetric deflection of the probe particle – an effect that is enhanced by their lower topographic location relative to the adatoms. The complementary influence of the rest atoms on the appearance of the adatoms is somewhat reduced (due to their lower height), but is still sufficient to produce a noticeable change in their appearance. Consequently, the simulations suggest that the experimentally observed triangular shape of the atoms results from the potential that results from a combination of the effect of the backbonding atoms, and presence of the rest atoms.

Comparison of Δ*f* and force, and effect of oscillation amplitude

In the limit of small oscillation amplitudes, the frequency shift tends towards the force gradient between tip and sample [19], however, it is less trivial to determine how the frequency shift relates to the force with finite oscillation amplitudes [20]. In particular, there has been little consideration of how the use of finite oscillation amplitudes effects the contrast in the Δ*f* images acquired during intramolecular imaging with passivated tips [21], where it is often assumed that the Δ*f* images closely reflect the force and/or charge density associated with the molecule. In Figure 3 we compare constant height force, and Δ*f* images acquired with different oscillation amplitudes, at different tip–sample separations. Intriguingly, the triangular shape of the adatoms is more pronounced in the force images (top row), and importantly, lacks the inversion observed in the Δ*f* images acquired with A_0 = 0.1 nm. The Δ*f* images simulated with A_0 = 0.5 nm (lower row) show a striking qualitative similarity to the force images, being more triangular, and also lacking the contrast inversion over the adatoms. Intuitively, these results may be understood on the basis that at smaller amplitudes the Δ*f* begins to resemble the force gradient, whereas at larger amplitudes the Δ*f* is more strongly dominated by the interaction at the point of closest approach.

Effect of k_{xy} on simulated images

As noted above, the tip used to take the experimental images in Figure 1 was not intentionally functionalised, and, more importantly, the identity of the passivating group at the apex of the tip

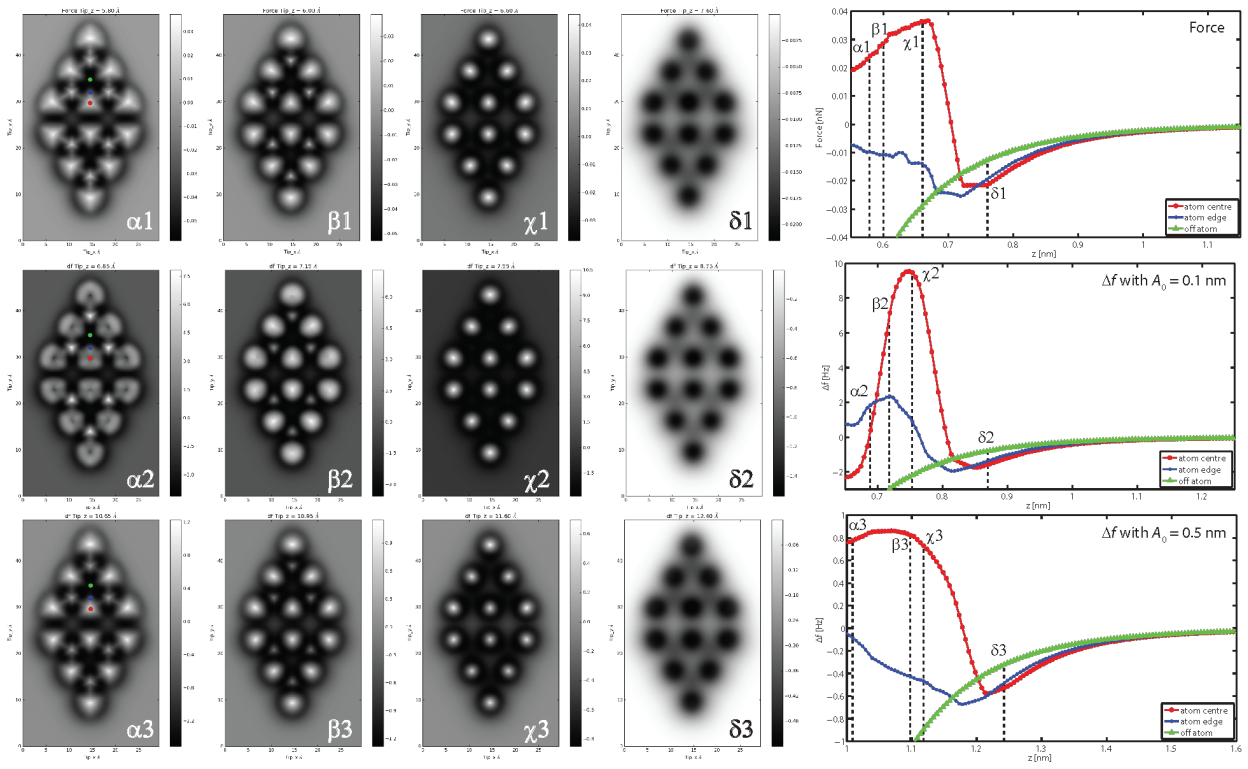

Figure 3: Comparison of the evolution in force (top row) and frequency shift (lower two rows). The evolution in Δ*f* is shown for oscillation amplitudes of 0.1 nm (middle row), and 0.5 nm (lower row). The position of single *F*(*z*) and Δ*f*(*z*) curves are marked on the *xy* images, and the heights of each image is marked on the graphs with the corresponding Greek letter. The Δ*f* contrast and evolution in *z* is qualitatively similar for the force and 0.5 nm oscillation amplitude simulations. The simulations with an oscillation amplitude of 0.1 nm show an dark region in the centre of the adatoms, which is reflected in the inversion observed in the Δ*f*(*z*) curves.

is not known. In the majority of the simulations performed in the previous sections, we have assumed a lateral stiffness k_{xy} = 0.5 N/m, in line with previous work modelling CO terminated tips. However, a priori, we have no knowledge of the actual stiffness of our probe, and it is important to consider what a modification of the lateral stiffness may have on our simulated results. While for small modifications of k_{xy} we find that the contrast is qualitatively similar as previously reported [7], we find that for larger changes in k_{xy} we observe qualitative changes in the appearance of the simulated images. These results are summarised in Figure 4, where we compare the k_{xy} = 0.5 N/m simulations with a very low stiffness tip (k_{xy} = 0.1 N/m), and a relatively rigid tip (k_{xy} = 5 N/m). Although for all stiffnesses we observe triangular shaped adatoms at close approach, the extent and shape of the contrast inversion in the centre of the adatoms is directly affected by the change in lateral stiffness. The choice of k_{xy} = 0.5 N/m therefore appears to be justified empirically for two primary reasons. First, simulations with stiffness's around this value best reproduce the experimental contrast. Second, tips producing similar contrast over the adatoms also produced very similar contrast during intramolecular imaging experiments, [12], including the characteristic sharpening of the bond features typically associated with the tilting of the CO molecule [6].

Conclusion

We have modelled an example of 'sub-atomic' contrast on the Si(111)-7×7 substrate with a passivated tip, using simple L-J potentials and a flexible tip model. Despite lacking information on the electronic or chemical nature of the surface, the model well reproduces the contrast observed over the adatoms and rest atoms. By decomposing the contributions of different parts of the substrate, we are able to show that 'sub-atomic' contrast can in principle arise as the result of a flexible tip exploring an asymmetric potential around an atom unrelated to its electronic orbital configuration. Our simulations show that the local atomic environment (i.e., the position of the other atoms on the surface) can provide such a potential. A distinction must therefore be drawn between what might be termed 'orbital' imaging, which explicitly images the orbitals of single atoms, and 'sub-atomic' imaging, which can arise from a number of multi-atom effects. Therefore, we suggest that interpretation of 'sub-atomic' features that share a symmetry with either the direct backbonding atoms, or even nearby atoms that are not directly bonded to the target atom, must therefore be carried out with the utmost care. We do stress that a simple L-J model cannot reproduce the onset of a repulsive 'halo' that occurs before repulsion over the centre of the atom, as was reported recently [22], and interpretation of features of this type requires full ab-initio modelling of the combined tip–sample system,

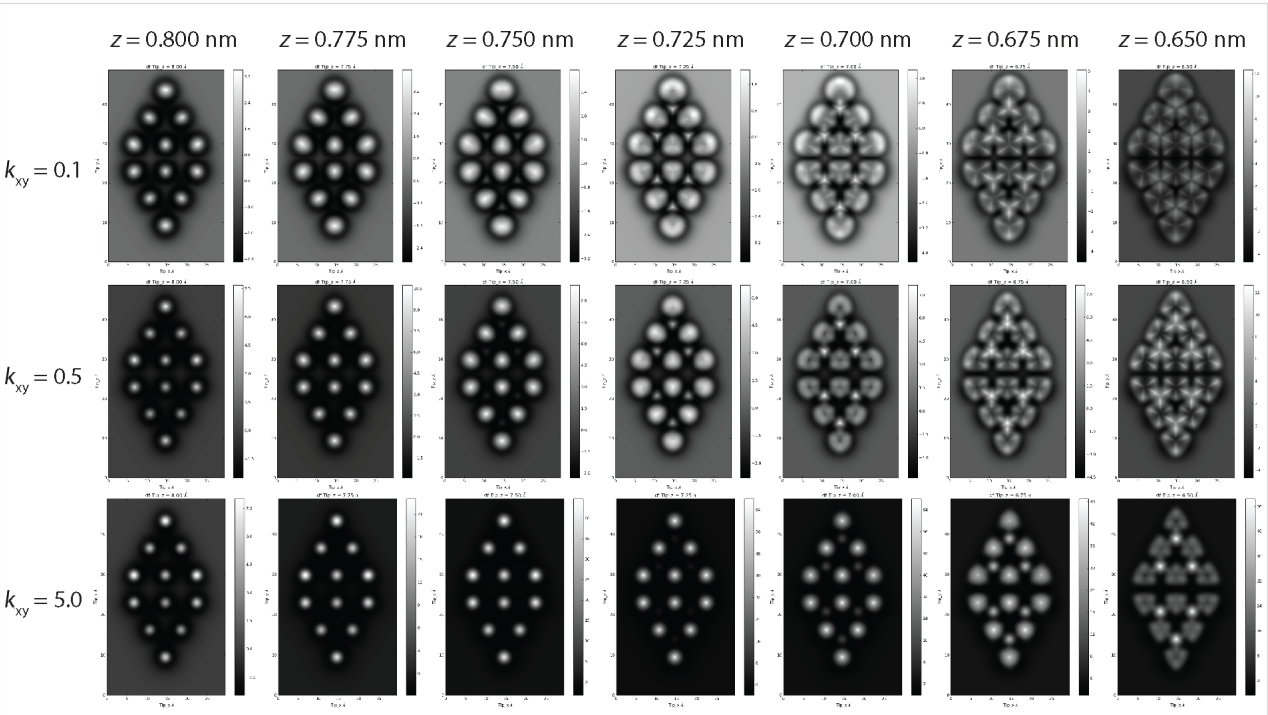

Figure 4: Simulated constant height images at decreasing tip–sample separation for three different probe lateral stiffness (k_{xy}). The triangular appearance of the adatoms, and the subsequent contrast inversion, occurs at larger tip separations for lower stiffness probes. For the lowest stiffness probe the 'hole' produced by the contrast inversion is almost reduced to a point due the the extreme sharpening of the features caused by the deflection of the probe.

with full consideration of the combined charge density, and the relaxation of the atomic positions, in the tip–sample junction.

Supporting Information

Supporting Information File 1

Datasets A0=1A adatoms_backbonds k=0.5.
[http://www.beilstein-journals.org/bjnano/content/supplementary/2190-4286-7-85-S1.zip]

Supporting Information File 2

Datasets A0=1A k=5000.
[http://www.beilstein-journals.org/bjnano/content/supplementary/2190-4286-7-85-S2.zip]

Supporting Information File 3

Datasets A0=1A adatoms_only k=0.5.
[http://www.beilstein-journals.org/bjnano/content/supplementary/2190-4286-7-85-S3.zip]

Supporting Information File 4

Datasets A0=1A adatoms_rest_atoms k=0.5
[http://www.beilstein-journals.org/bjnano/content/supplementary/2190-4286-7-85-S4.zip]

Supporting Information File 5

Datasets A0=1A adatoms_rest_atoms_backbonds k=0.5.
[http://www.beilstein-journals.org/bjnano/content/supplementary/2190-4286-7-85-S5.zip]

Supporting Information File 6

Datasets A0=1A k=0.5.
[http://www.beilstein-journals.org/bjnano/content/supplementary/2190-4286-7-85-S6.zip]

Supporting Information File 7

Datasets A0=1A k=0.5_extendedrange.
[http://www.beilstein-journals.org/bjnano/content/supplementary/2190-4286-7-85-S7.zip]

Supporting Information File 8

Datasets A0=1A k=5.0.
[http://www.beilstein-journals.org/bjnano/content/supplementary/2190-4286-7-85-S8.zip]

Supporting Information File 9

Datasets A0=5A k=0.5.
[http://www.beilstein-journals.org/bjnano/content/supplementary/2190-4286-7-85-S9.zip]

Acknowledgements

The authors wish to gratefully acknowledge valuable discussions with P. Hapala and S. Hämäläinen regarding implementation of the L-J model. A. Sweetman gratefully acknowledges the support of the Leverhulme Trust via fellowship ECF-2013-525. S. P. Jarvis would like to thank the Leverhulme Trust for fellowship ECF-2015-005. M.R.A acknowledges funding from the University of Nottingham via the Vice-Chancellors Scholarship for Research. We also acknowledge the support of the University of Nottingham High Performance Computing Facility (in particular, Dr. Colin Bannister).

References

1. Giessibl, F. J. *Appl. Phys. Lett.* **2000,** *76,* 1470. doi:10.1063/1.126067
2. Bartels, L.; Meyer, G.; Rieder, K.-H.; Velic, D.; Knoesel, E.; Hotzel, A.; Wolf, M.; Ertl, G. *Phys. Rev. Lett.* **1998,** *80,* 2004–2007. doi:10.1103/PhysRevLett.80.2004
3. Gross, L.; Mohn, F.; Moll, N.; Liljeroth, P.; Meyer, G. *Science* **2009,** *325,* 1110–1114. doi:10.1126/science.1176210
4. Jarvis, S. P. *Int. J. Mol. Sci.* **2015,** *16,* 19936–19959. doi:10.3390/ijms160819936
5. Boneschanscher, M. P.; Hämäläinen, S. K.; Liljeroth, P.; Swart, I. *ACS Nano* **2014,** *8,* 3006–3014. doi:10.1021/nn500317r
6. Gross, L.; Mohn, F.; Moll, N.; Schuler, B.; Criado, A.; Guitián, E.; Peña, D.; Gourdon, A.; Meyer, G. *Science* **2012,** *337,* 1326–1329. doi:10.1126/science.1225621
7. Hapala, P.; Kichin, G.; Wagner, C.; Tautz, F. S.; Temirov, R.; Jelínek, P. *Phys. Rev. B* **2014,** *90,* 085421. doi:10.1103/PhysRevB.90.085421
8. Hämäläinen, S. K.; van der Heijden, N.; van der Lit, J.; den Hartog, S.; Liljeroth, P.; Swart, I. *Phys. Rev. Lett.* **2014,** *113,* 186102. doi:10.1103/PhysRevLett.113.186102
9. Moll, N.; Schuler, B.; Kawai, S.; Xu, F.; Peng, L.; Orita, A.; Otera, J.; Curioni, A.; Neu, M.; Repp, J.; Meyer, G.; Gross, L. *Nano Lett.* **2014,** *14,* 6127–6131. doi:10.1021/nl502113z
10. Neu, M.; Moll, N.; Gross, L.; Meyer, G.; Giessibl, F. J.; Repp, J. *Phys. Rev. B* **2014,** *89,* 205407. doi:10.1103/PhysRevB.89.205407
11. Sweetman, A.; Rahe, P.; Moriarty, P. *Nano Lett.* **2014,** *14,* 2265–2270. doi:10.1021/nl4041803
12. Sweetman, A.; Jarvis, S. P.; Rahe, P.; Champness, N. R.; Kantorovich, L.; Moriarty, P. *Phys. Rev. B* **2014,** *90,* 165425. doi:10.1103/PhysRevB.90.165425
13. https://github.com/ProkopHapala/ProbeParticleModel.
14. Chiutu, C.; Sweetman, A. M.; Lakin, A. J.; Stannard, A.; Jarvis, S.; Kantorovich, L.; Dunn, J. L.; Moriarty, P. *Phys. Rev. Lett.* **2012,** *108,* 268302. doi:10.1103/PhysRevLett.108.268302
15. Hapala, P.; Temirov, R.; Tautz, F. S.; Jelínek, P. *Phys. Rev. B* **2014,** *113,* 226101. doi:10.1103/PhysRevLett.113.226101
16. Sadewasser, S.; Jelinek, P.; Fang, C.-K.; Custance, O.; Yamada, Y.; Sugimoto, Y.; Abe, M.; Morita, S. *Phys. Rev. Lett.* **2009,** *103,* 266103. doi:10.1103/PhysRevLett.103.266103
17. Giessibl, F. J. *Appl. Phys. Lett.* **2001,** *78,* 123–125. doi:10.1063/1.1335546
18. Tao, F.; Xu, G. Q. *Acc. Chem. Res.* **2004,** *37,* 882–893. doi:10.1021/ar0400488
19. Giessibl, F. J. *Rev. Mod. Phys.* **2003,** *75,* 949–983. doi:10.1103/RevModPhys.75.949

20. Sader, J. E.; Jarvis, S. P. *Appl. Phys. Lett.* **2004,** *84,* 1801. doi:10.1063/1.1667267
21. Schulz, F.; Hämäläinen, S.; Liljeroth, P. Atomic-Scale Contrast Formation in AFM Images on Molecular Systems. In *Noncontact Atomic Force Microscopy;* Morita, S.; Giessibl, J. F.; Meyer, E.; Wiesendanger, R., Eds.; NanoScience and Technology, Vol. 3; Springer: Berlin, Germany, 2015; pp 173–194. doi:10.1007/978-3-319-15588-3_10
22. Emmrich, M.; Huber, F.; Pielmeier, F.; Welker, J.; Hofmann, T.; Schneiderbauer, M.; Meuer, D.; Polesya, S.; Mankovsky, S.; Ködderitzsch, D.; Ebert, H.; Giessibl, F. J. *Science* **2015,** *348,* 308–311. doi:10.1126/science.aaa5329

BEILSTEIN JOURNAL OF NANOTECHNOLOGY

Noise in NC-AFM measurements with significant tip–sample interaction

Jannis Lübbe[1], Matthias Temmen[1], Philipp Rahe[*2,3] and Michael Reichling[*1]

Full Research Paper

Open Access

Address:
[1]Fachbereich Physik, Universität Osnabrück, Barbarastraße 7, 49076 Osnabrück, Germany, [2]Department of Physics and Astronomy, The University of Utah, 115 South 1400 East, Salt Lake City, UT 84112-0830, USA and [3]now at: School of Physics & Astronomy, The University of Nottingham, University Park, Nottingham NG7 2RD, UK

Email:
Philipp Rahe[*] - philipp.rahe@nottingham.ac.uk;
Michael Reichling[*] - reichling@uos.de

* Corresponding author

Keywords:
amplitude noise; cantilever stiffness; closed loop; detection system noise; frequency shift noise; non-contact atomic force microscopy (NC-AFM); Q-factor; spectral analysis; thermal noise; tip–sample interaction

Beilstein J. Nanotechnol. **2016,** *7,* 1885–1904.
doi:10.3762/bjnano.7.181

Received: 20 August 2016
Accepted: 28 October 2016
Published: 01 December 2016

This article is part of the Thematic Series "Noncontact atomic force microscopy III".

Guest Editor: M. Z. Baykara

Abstract

The frequency shift noise in non-contact atomic force microscopy (NC-AFM) imaging and spectroscopy consists of thermal noise and detection system noise with an additional contribution from amplitude noise if there are significant tip–sample interactions. The total noise power spectral density $D^{\Delta f}(f_m)$ is, however, not just the sum of these noise contributions. Instead its magnitude and spectral characteristics are determined by the strongly non-linear tip–sample interaction, by the coupling between the amplitude and tip–sample distance control loops of the NC-AFM system as well as by the characteristics of the phase locked loop (PLL) detector used for frequency demodulation. Here, we measure $D^{\Delta f}(f_m)$ for various NC-AFM parameter settings representing realistic measurement conditions and compare experimental data to simulations based on a model of the NC-AFM system that includes the tip–sample interaction. The good agreement between predicted and measured noise spectra confirms that the model covers the relevant noise contributions and interactions. Results yield a general understanding of noise generation and propagation in the NC-AFM and provide a quantitative prediction of noise for given experimental parameters. We derive strategies for noise-optimised imaging and spectroscopy and outline a full optimisation procedure for the instrumentation and control loops.

Introduction

Non-contact atomic force microscopy (NC-AFM) [1,2] is an unmatched surface science tool, especially when it comes to studying non-conducting surfaces [3,4], to map sub-molecular structures [5] or to measure forces [6] and force fields [7] with highest resolution. The primary imaging signal in NC-AFM is the frequency shift Δf of a probe resonator carrying a tip inter-

acting with the sample surface [2], typically a cantilever, a tuning fork, or a needle sensor [8].

The resolution of force measurements is limited by the noise in the frequency shift signal [9,10], which strongly depends on the noise floor of the detection system, the frequency response of the frequency demodulator (mostly a phase-locked loop detector, PLL), cantilever properties and ultimately thermal noise [11]. The footing of our work are these precursor studies, and the rigorous system analysis introduced by Polesel-Maris et al. [12], showing that the frequency shift noise at close tip–sample distance is increased due to a coupling of the phase-locked loop with the amplitude and the distance control loops.

While noise in the amplitude control loop itself is essentially independent of the frequency shift noise without tip–sample interaction, amplitude and topography feedback loop noise are coupled into the frequency shift noise in the presence of tip–sample forces [12]. Ultimately, the noise in the frequency shift signal determines the base performance of all downstream processing such as the topography signal or the Kelvin probe force signal [13].

Here, we use the formalism derived by Polesel-Maris et al. [12], introduce realistic transfer functions for the control electronics, cantilever properties and tip–sample interaction, to quantitatively determine the frequency shift noise in the presence of significant tip–sample interaction, to derive predictions for noise spectra and to correlate them with experimental data obtained under realistic measurement conditions. We find excellent agreement between simulated and experimental results for noise in a cantilever-based NC-AFM with optical beam-deflection and measurements performed in an ultra-high vacuum environment, where the cantilever Q-factor is close to the intrinsic value Q_0 [14,15]. Our analysis can, however, be applied to any NC-AFM detection scheme and sample environment, specifically also to measurements in liquids where signal-to-noise-ratio considerations play a paramount role [16-18]. From our findings, we derive a general strategy for adjusting instrumental settings and control loops for noise-optimised operation. A full glossary of all of these settings and further quantities relevant in this context are compiled in appendix A.

Our analysis is based on four fundamental steps: First, the cantilever oscillation amplitude is determined precisely by calibrating the voltage signal proportional to the cantilever displacement with a method described in detail elsewhere [19]. This yields the detection sensitivity S_A^z (see also Supplementary Information section 1 of [11]). Second, S_A^z is used to convert the displacement noise voltage signal into the displacement noise quantities, namely the displacement noise power spectral density $D_{\mathrm{ds}}^z(f)$ of the detection system (frequently referred to as the noise floor) and the thermal noise power spectral density $D_{\mathrm{th}}^{\mathrm{exc}}(f)$ [11]. Note that the latter cantilever thermal excitation noise contribution can be predicted from the oscillator properties and temperature [11]. Third, the frequency response H_{filter} of the PLL system is used for describing the propagation of noise from the cantilever oscillation to the frequency shift signal at the output of the frequency demodulator. This frequency response function strongly depends on the PLL filter settings [11] and will here be modelled for a typical experimental setup described in section "Noise propagation model" and appendix C. Fourth, we determine the explicit frequency response functions H_A and H_z of the amplitude and topography control loops, respectively. This allows an adjustment of the amplitude control loop and the frequency response of the PLL prior to the measurement when tip–sample interaction is absent (i.e., with the tip retracted). The frequency response of the distance control loop, however, inherently depends on the tip–sample interaction which is, in turn, preset by the z-position along the force–distance curve [12]. Therefore, this control loop needs adjustment under conditions of the envisaged measurement.

After describing experimental methods and procedures in section "Experimental", we introduce the NC-AFM model used to simulate noise generation and propagation in section "Noise propagation model". In section "Tip–sample interaction", we then discuss the implications of the tip–sample interaction on the coupling of control loops. After a check of validity and consistency of the model by testing simulation results against measurements for the case of absent tip–sample interaction in section "Noise with negligible tip–sample interaction", we systematically explore cases with significant tip–sample interaction in section "Noise with significant tip–sample interaction". The investigation comprises measurements and simulations for scanning the surface at a constant tip–sample distance (constant-height mode) as well as with the frequency shift kept at a certain value by the z-control loop (topography mode). For the simulations, the filter settings of the control loops are varied over ranges of values typically present in experiments, and an artificial but realistic model potential is used for the tip–sample interaction. We validate the noise model including tip–sample interaction and describe a rational procedure for choosing system parameters for noise-optimised measurements in section "Conclusions and system optimisation". All equations within this work are written using power spectral densities D^X for the quantity X, while simulated and experimental results are described in terms of amplitude spectral densities $d^X = \sqrt{D^X}$.

Experimental

All experiments are performed using a commercial NC-AFM system (UHV 750 variable temperature STM/AFM, RHK Tech-

nology, Inc., Troy, MI, USA) operated at room temperature and employing the beam-deflection method to measure the cantilever displacement. Tip positioning and approach is accomplished by the SPM 100 control system (RHK Technology, Inc.). For this and all other instruments we introduce scaling factors to convert voltage signals delivered by the instruments to physical units. The detection sensitivity S_A^z for the herein presented data is determined to 52.5 nm/V from an amplitude calibration (see [19] and Supporting Information of [11]). A PLLpro2 control system (RHK Technology, Inc., Troy, MI, USA) is used for frequency demodulation and amplitude stabilisation. This control system encodes the frequency shift Δf in volts using $S^{\Delta f} = -30$ Hz/V. For the distance control loop, we employ a digital PI controller of the HF2LI device (Zurich Instruments AG, Zürich, Switzerland) as this instrument provides loop filters with well-defined characteristics. Noise measurements at the Δf and amplitude outputs of the PLL system as well as at the topography output of the distance controller are performed using a SR770 spectrum analyser (Stanford Research Systems, Inc., Sunnyvale, CA, USA). The topography signal is scaled using the sensitivity $S_p^z = 9.36$ nm/V for the scanner z-piezo response. This value was determined from measuring step heights on CaF_2 surfaces.

The cantilever is a commercial silicon cantilever (type PPP-NCH, Nanoworld AG, Neuchâtel, Switzerland) with an eigenfrequency of $f_0 = 305337.6$ Hz at room temperature and a quality factor of $Q_0 = 43900$ determined as described elsewhere [14]. The noise floor is determined to $d_{ds}^z = \sqrt{D_{ds}^z} = 81\ \mathrm{fm}/\sqrt{\mathrm{Hz}}$ and the modal stiffness of the cantilever [20] to $k_0 = 32.4$ N/m from a measurement of the thermally excited cantilever oscillation [11] with the spectrum analyser of the HF2LI device. The cantilever oscillation is stabilised at an amplitude of $A = 13.6$ nm, which corresponds to an amplitude of $A_z = A\cos(\theta) = 12.6$ nm perpendicular to the surface due to the inclination of $\theta = 22.5°$ between cantilever and sample surface given by the cantilever mount. These experimental parameters are used in all simulations presented within this work.

The tip–sample interaction modelled by the parameter β_{ts} (see section "Tip–sample interaction") is derived from a measured $\Delta f(z_p)$ curve shown in Figure 4). Here, Δf is plotted against the piezo position z_p. Depending on the operation mode (constant-height or topography), the parameter β_{ts} can be obtained by using either the frequency shift set-point Δf_{set} for the topography feedback or by the average frequency shift $\langle\overline{\Delta f}\rangle$ measured at the tip–sample distance z_p with deactivated topography feedback loop.

For the numerical evaluation of signal vs time traces and noise spectra, the explicit frequency response functions and system parameters for our experimental setup are used; all frequency response functions are listed in the appendix and the implementation in MATLAB is available in Supporting Information File 1. This approach enables a numeric evaluation in absolute physical units and, therefore, allows the direct comparison between experiment and our model.

Results and Discussion

Noise propagation model

Figure 1 illustrates the signal and noise propagation in a typical NC-AFM setup. The cantilever is excited by a drive signal with frequency f_{exc} and amplitude A_{exc}. Additionally, the cantilever

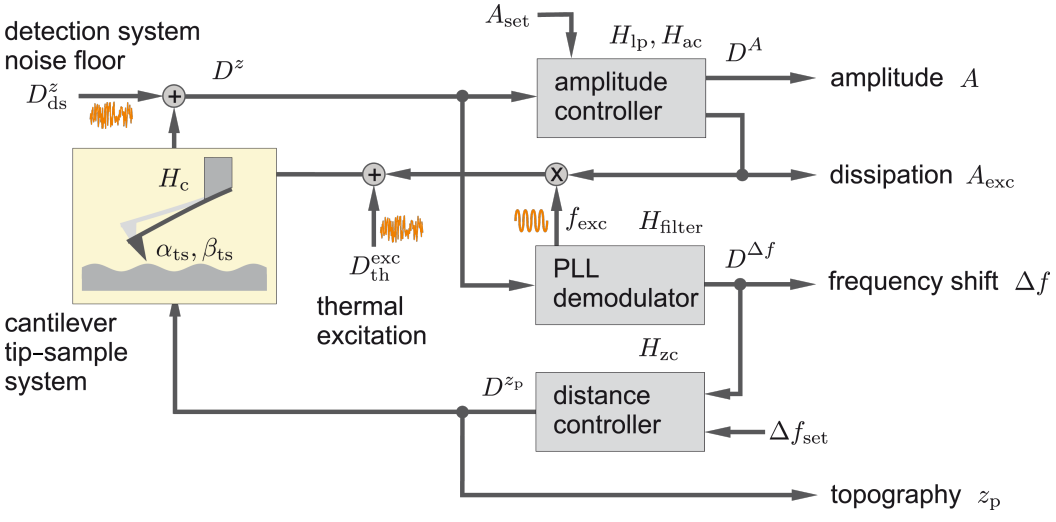

Figure 1: Schematic representation of functional elements of an NC-AFM described by transfer functions H_y. Quantities D^X denote noise power spectral densities of the signal X. Symbols "+" and "×" denote entry points of noise and entanglement of signals, respectively.

experiences an excitation due to thermal noise expressed by the power spectral density $D_{\mathrm{th}}^{\mathrm{exc}} = 2k_{\mathrm{B}}T/(k_0Q_0\pi f_0)$. The cantilever responds to these excitations with an oscillation of amplitude A dictated by the cantilever response function $H_{\mathrm{c}}(f)$. This cantilever oscillation is measured as the cantilever displacement signal. Noise contributions in this signal are described in frequency space by the thermal noise displacement power spectral density $D_{\mathrm{th}}^{z}(f)$ and by the detection system noise power spectral density $D_{\mathrm{ds}}^{z}(f)$, the latter caused by the electronic detection system [11]. The sum of the detection system noise power spectral density $D_{\mathrm{ds}}^{z}(f)$ and the thermal displacement noise power spectral density $D_{\mathrm{th}}^{z}(f)$ yields the total displacement noise power spectral density $D^{z}(f)$.

The cantilever displacement signal is fed into both, the amplitude controller and the PLL demodulator. The amplitude controller measures the oscillation amplitude A typically using a root-mean-square algorithm or lock-in detection and adjusts the excitation amplitude A_{exc} to keep the oscillation amplitude A at the set-point A_{set}. The amplitude measurement includes a low-pass filter with the response function $H_{\mathrm{lp}}(f)$, while the amplitude controller is described by the frequency response $H_{\mathrm{ac}}(f)$. Noise in the amplitude signal is characterised by the amplitude noise power spectral density $D^{A}(f)$.

The PLL demodulator determines the frequency shift $\Delta f = f_{\mathrm{r}} - f_0$, which is the difference between the cantilever resonance frequency f_{r} in the presence of tip–sample interaction and the cantilever eigenfrequency f_0. Furthermore, the demodulator provides the cantilever excitation signal with frequency f_{exc} that is nominally identical to the current resonance frequency f_{r} of the cantilever. The frequency shift noise power spectral density $D^{\Delta f}(f_{\mathrm{m}})$ depends on the filter and loop settings of the PLL demodulator expressed by its frequency response function $H_{\mathrm{filter}}(f_{\mathrm{m}})$, where f_{m} represents the frequencies of the modulation side bands measured relative to the resonance frequency f_{r} [11]. Thus, the cantilever excitation signal contains noise from both, the PLL and the amplitude controller.

The frequency shift signal is fed into the distance controller, which adjusts the tip–sample distance to maintain a frequency shift equal to the set-point Δf_{set}. The tip–sample distance is expressed as the position z_{p} of the z-piezo (see below in Figure 3) and is in this context commonly referred to as the topography signal. The distance-dependent frequency shift $\Delta f(z_{\mathrm{p}})$ is governed by the details of the tip–sample interaction forces, and is herein for a few specific tip–sample distances characterised by the two parameters $\alpha_{\mathrm{ts}}(z_{\mathrm{p}})$ and $\beta_{\mathrm{ts}}(z_{\mathrm{p}})$ as described in section "Tip–sample interaction". These parameters determine how fluctuations in the oscillation amplitude and the tip–sample distance are coupled into the frequency shift signal.

The noise propagation model used for our simulations is based on the approach introduced in [12] and sketched in Figure 2. In

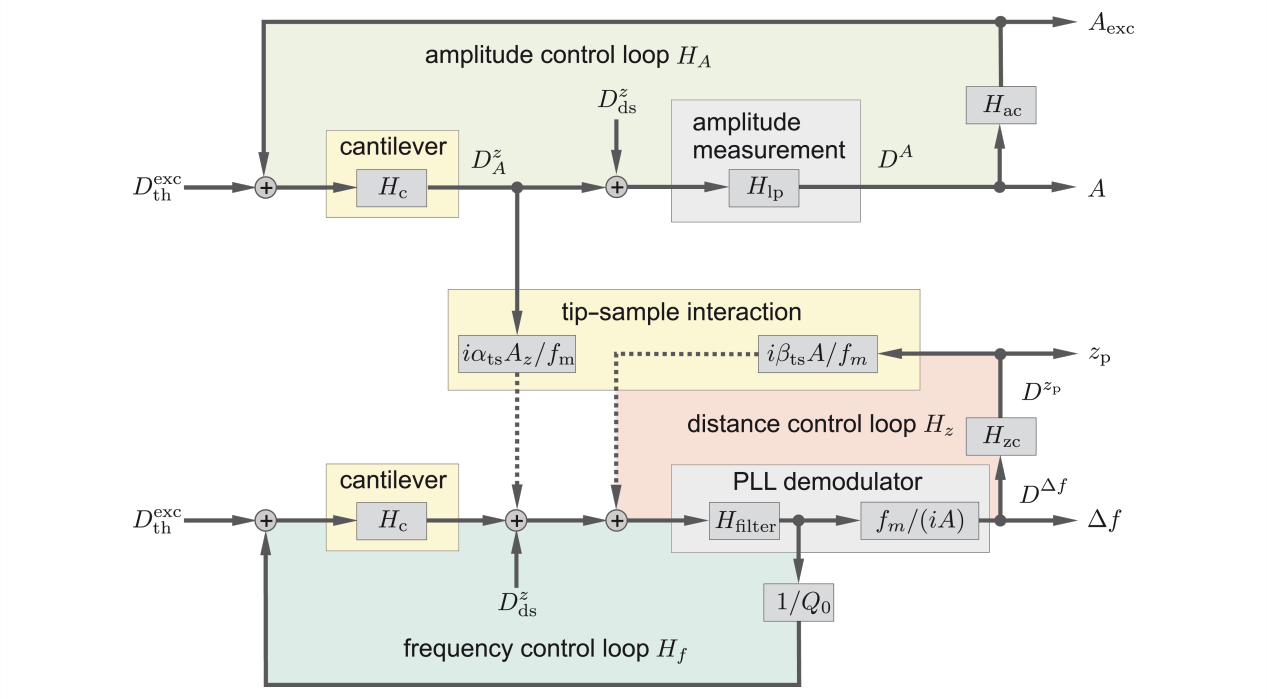

Figure 2: Model for signal and noise propagation in an NC-AFM, highlighting the tip–sample interaction, PLL demodulator and control loops. Signal paths indicated by dotted lines are only relevant for the case of significant tip–sample interaction.

contrast to the NC-AFM functional scheme shown in Figure 1, here we focus on the noise signal paths and transfer blocks relevant to the noise propagation. Furthermore, we investigate amplitude noise and frequency shift noise in two separate loops that are coupled via the tip–sample interaction. Effectively, this approach splits the signal into a purely amplitude-modulated component (controlled by the amplitude control loop) and a signal with pure frequency (or phase) modulation (controlled by the frequency control loop including the PLL) [12]. This separation stems from the small intermixing strength of the two modulations, and will be justified here based on experimental evidence.

In the **amplitude control loop** (top part of Figure 2), the cantilever displacement signal contains amplitude fluctuations described by the noise power spectral density $D_A^z(f)$ and the detection system adds the noise floor $D_{\mathrm{ds}}^z(f)$, yielding the measured displacement noise $D^z(f)$. The amplitude signal A follows from the displacement signal, which is then low-pass-filtered as described by the transfer function H_{lp}, and finally contains noise with the amplitude power spectral density noise $D^A(f_{\mathrm{m}})$. This signal is fed into the amplitude controller described by the transfer function H_{ac}, generating the excitation signal amplitude A_{exc}. The amplitude control loop is closed by feeding this signal to the cantilever. Note that with closing the loop, a fraction of the noise $D^A(f_{\mathrm{m}})$ is fed back to the cantilever, added to the thermal noise $D_{\mathrm{th}}^{\mathrm{exc}}(f)$ and filtered by the narrow-band cantilever response function $H_{\mathrm{c}}(f)$.

In the **frequency control loop** (bottom part of Figure 2), the measured cantilever displacement signal is fed into the PLL demodulator yielding the frequency shift signal Δf as well as the excitation signal for the cantilever in the feedback path. The control loop within the PLL demodulator (not shown in Figure 2) is discussed in appendix C.2. In this frequency control loop feedback path, displacement noise propagating from the PLL to the cantilever excitation is weighted by the reciprocal of the quality factor Q_0. This factor defines the ratio of the cantilever excitation signal to the oscillation amplitude at the cantilever resonance if neither amplitude noise nor amplitude disturbances are present, i.e., in absence of tip–sample interactions. The sum of excitation signal noise and thermal excitation noise $D_{\mathrm{th}}^{\mathrm{exc}}(f)$ is band-pass-filtered by the cantilever response function $H_{\mathrm{c}}(f)$ and added to the detection system noise floor $D_{\mathrm{ds}}^z(f)$. The loop is closed by feeding this signal into the PLL. In the case of negligible tip–sample interaction, the noise in the frequency control loop is virtually independent from the settings of the other control loops shown in Figure 2, although we note that a coupling may become apparent if either of the loops is operated in an unstable ringing configuration. If significant tip–sample interaction is present, two more signals, one from the amplitude and a second from the distance control loop, are added before feeding the signal into the PLL demodulator as described below.

The **distance control loop** employs a controller with transfer function H_{zc} to regulate the frequency shift Δf from the PLL by adjusting the piezo position z_{p}. The slope $\beta_{\mathrm{ts}} = \partial\Delta f/\partial z$ of the frequency shift vs distance curve $\Delta f(z)$ models the tip–sample interaction and is usually a non-linear function of z_{p}. The frequency shift noise $D^{\Delta f}(f_{\mathrm{m}})$ is converted to topography noise $D^{z_{\mathrm{p}}}(f_{\mathrm{m}})$ by the action of the distance controller with transfer function H_{zc}. The topography noise is scaled by the tip–sample interaction transfer function $i\beta_{\mathrm{ts}}A/f_{\mathrm{m}}$ and added to other noise contributions at the PLL demodulator input. The loop is closed across the PLL.

The **coupling** between the amplitude and the frequency control loops, which exists in the presence of significant tip–sample interaction, is modelled by a transfer function $i\alpha_{\mathrm{ts}}A/f_{\mathrm{m}}$ with $\alpha_{\mathrm{ts}} = \partial\Delta f/\partial A$, acting on the amplitude noise D_A^z. The resulting noise is one of the contributions at the PLL demodulator input and increases the frequency shift noise.

Tip–sample interaction

The tip–sample interaction closes the distance control loop and it couples the amplitude control loop with the frequency control loop. Both connections can significantly increase the noise in the frequency shift Δf output signal compared to the case of negligible tip–sample interaction.

The transfer of fluctuations from the piezo position z_{p} into the cantilever deflection signal by the distance control loop (see Figure 2) is described by the parameter β_{ts}. This parameter is defined as the gradient of the frequency shift signal Δf with respect to the tip–sample distance z_{ts} (see [12] and appendix D):

$$\beta_{\mathrm{ts}} = \frac{\partial\Delta f\left(z_{\mathrm{ts}}, A_z\right)}{\partial z_{\mathrm{ts}}}, \tag{1}$$

$$= \frac{\partial\Delta f\left(z_{\mathrm{p}} - A_z, A_z\right)}{\partial z_{\mathrm{p}}}. \tag{2}$$

The parameter β_{ts} can be parameterised by either the z-position of the lower turning point z_{ts} (Equation 1) or using the piezo position z_{p} (Equation 2), which is the centre position of the cantilever oscillation (see Figure 3). We explicitly include the amplitude dependency on the frequency shift Δf by including the oscillation amplitude component A_z perpendicular to the sample surface. This dependency follows from the convolution of

the interaction force with the weighting function due to the cantilever oscillation. For large oscillation amplitudes A_z, the functional dependence $\Delta f \propto A_z^{-3/2}$ has been found [21]. Hence, for a small variation δz_p of the z_p position, β_{ts} can straightforwardly be determined from the slope of the $\Delta f(z_p)$ curve at the working point as illustrated by the model curve in Figure 4. Obviously, β_{ts} strongly varies as a function of z_p.

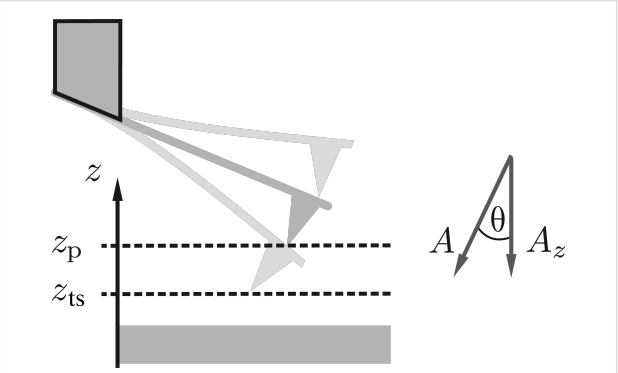

Figure 3: Relations between the piezo position z_p (tip position for resting cantilever), the lower turning point z_{ts} of the cantilever oscillation and the oscillation amplitude A as well as its projection A_z on the sample surface normal.

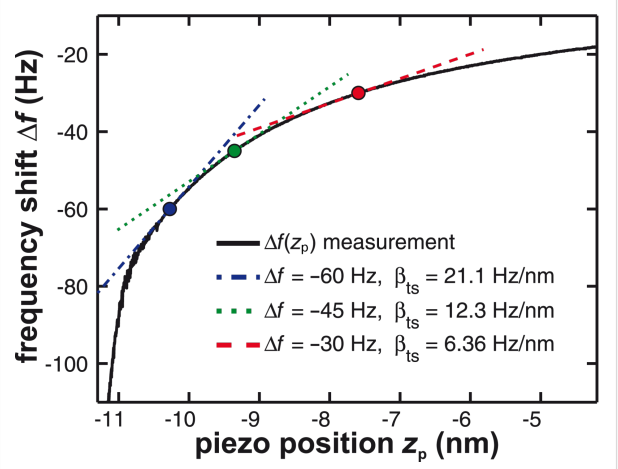

Figure 4: Determination of the tip–sample interaction parameter β_{ts} from the slope of a measured $\Delta f(z_p)$ curve. Frequency shift data are plotted as a function of the z-piezo position z_p.

The parameter α_{ts} describes the transfer of cantilever deflection noise D_A^z from the amplitude control loop into deflection noise in the frequency control loop via two mechanisms. First, a variation δA in the amplitude changes the weighting function in calculating the frequency shift from the cantilever oscillation [21] and, thus, the magnitude of the resulting Δf. Second, the variation leads to a shift of the lower turning point z_{ts}, bringing the sensor into a different tip–sample interaction regime. The coupling parameter α_{ts} is defined by [12]

$$\alpha_{ts} = \frac{\partial \Delta f\left(z_p - A_z, A_z\right)}{\partial A_z}. \tag{3}$$

For the experimental conditions within this work (see appendix D), small fluctuations δA_z of the oscillation amplitude have the same effect as a small fluctuation δz in the center position, namely $\delta z = -\delta A_z$. Therefore, we use the approximation

$$\alpha_{ts} \approx -\beta_{ts}. \tag{4}$$

Further details on the relation between α_{ts} and β_{ts} assuming a model potential for the tip–sample interaction are provided in appendix D. Short-range forces acting between the probing tip and the sample surface are of primary relevance for our discussion as they typically exhibit strong gradients. Thus, the coupling strongly increases with increasing interaction when the tip is closely approached to the surface.

Noise with negligible tip–sample interaction

We first analyse noise in the frequency shift Δf and amplitude A channel for the case of negligible tip–sample interaction ($\alpha_{ts} = \beta_{ts} = 0$) to check for consistency with previous simulations [12] as well as experimental results [11]. In respective experiments, we prepare this situation by retracting the tip several tens of nanometres from the sample surface.

The frequency shift noise power spectral density $D_{\text{free}}^{\Delta f}$ strongly depends on the PLL demodulator parameters [11] and is explicitly given by evaluating the frequency control loop in Figure 2 (see appendix B)

$$D_{\text{free}}^{\Delta f}\left(\omega_m\right) = \left|\frac{H_{\text{filter}}}{1 - H_{\text{filter}} H_c / Q_0}\right|^2 \times \left(2\left(\frac{\omega_m}{2\pi A}\right)^2 \left(D_{\text{ds}}^z + \left|H_c\right|^2 D_{\text{th}}^{\text{exc}}\right)\right), \tag{5}$$

where the system parameters are those introduced in Figure 2. We use the explicit description of our experimental system (see appendix C for the individual frequency response functions) to numerically evaluate Equation 5. Note that the comparison of simulated noise spectra with experimental data is based on these system parameters and not on fitting.

The amplitude noise power spectral density D^A is calculated from evaluating the amplitude control loop in Figure 2

$$D^A\left(\omega_m\right) = 2\left|\frac{H_{\text{lp}}}{1 - H_c H_{\text{lp}} H_{\text{ac}}}\right|^2 \left(\left|H_c\right|^2 D_{\text{th}}^{\text{exc}} + D_{\text{ds}}^z\right). \tag{6}$$

We use the explicit system parameters for our experimental setup to evaluate Equation 6 numerically in absolute physical units.

In Figure 5, we compile measurements (solid lines) and simulations (dotted lines) for the frequency shift noise amplitude spectral density $d^{\Delta f}_{\text{free}}$ (panels (a) and (b)) and the amplitude noise amplitude spectral density d^{A} (panels (c) and (d)). Panels (a) and (c) represent results for optimised amplitude loop gain settings while varying the PLL parameters. In contrast, panels (b) and (d) show results for optimised PLL parameters while varying the amplitude gain settings. In all data, the amplitude control loop filter H_{lp} has a 3rd-order Butterworth characteristics with a cutoff frequency of f_{c} = 500 Hz.

Figure 5a demonstrates the low-pass filter characteristics of the PLL in the case of excessive filtering (low P-gain), optimum operating conditions (optimum P-gain) and gain peaking (high P-gain), respectively. The optimum frequency response is determined as described in appendix C, yielding optimum parameters of P_{PLL} = −2.1 Hz/deg and I_{PLL} = 1 Hz. Note that the PLL frequency response does not depend on the cantilever parameters. Thus, it can be optimised for the desired detection bandwidth by only considering the cantilever parameters. In contrast, the frequency shift noise at the PLL output generated by the frequency control loop depends on cantilever properties and several other system parameters including the PLL settings. The amplitude noise presented in Figure 5c is independent of the PLL loop settings and, similarly, the frequency shift noise shown in Figure 5b is independent of the amplitude loop settings, clearly demonstrating that the amplitude and frequency control loops are not coupled unless the PLL is operated in an unstable regime.

The spectral behaviour of the amplitude noise d^{A} upon changing the amplitude control loop settings is slightly different from the behaviour observed in the frequency shift noise $d^{\Delta f}_{\text{free}}$ upon changing the frequency control loop gain settings as demonstrated in Figure 5a and Figure 5d. When increasing the P-gain of the amplitude control loop, the noise in the low-frequency

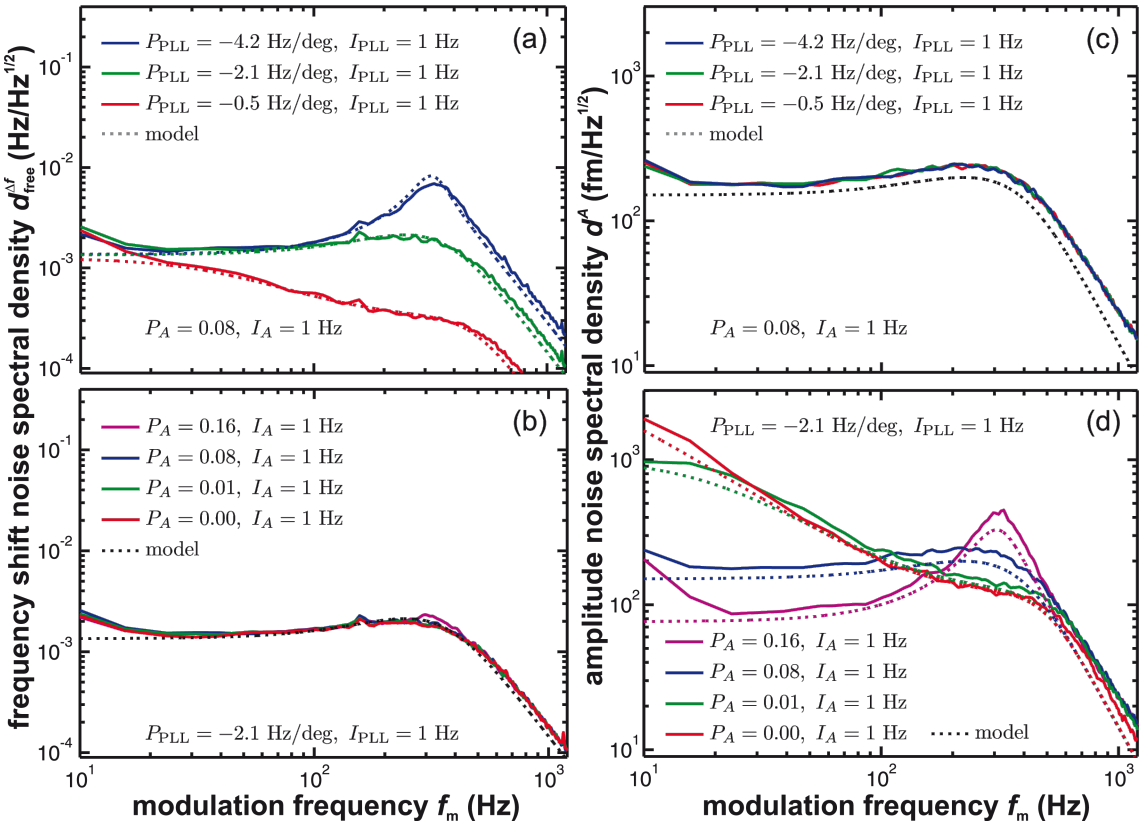

Figure 5: Measured noise spectral density (solid lines) of (a, b) the frequency shift signal and (c, d) the amplitude signal for a variation of the proportional loop gain settings P_{PLL} and P_A of the PLL and amplitude control loop, respectively. The integral cutoff of the PLL loop (I_{PLL}) and of the amplitude loop (I_{A}) are each held constant. The tip is retracted from the surface for the measurements. Model calculations (dotted lines) based on Equation 5 and Equation 6 are performed assuming negligible tip–sample interaction. The loop filter H_{lp} has a 3rd-order Butterworth characteristics with a cutoff frequency of f_{c} = 500 Hz, all other quantities are explicitly given in appendix C.

region decreases while in this case a peak around a frequency of about 300 Hz develops. If the amplitude control loop is disabled (P_A = 0, red line), the noise spectral density becomes large in the low-frequency region as predicted by the simulation (dotted line). Thus, an activated amplitude control loop effectively compensates low-frequency noise in the amplitude signal. Optimum performance of this loop is obtained for the parameters P_A = 0.08 and I_A = 1 Hz using the criteria introduced in appendix C.

In conclusion, we find excellent quantitative agreement between simulated and experimental data for various settings of the amplitude and frequency control loop. The independence of the frequency shift noise (amplitude noise) upon changing the amplitude (frequency) control loop settings, respectively, clearly demonstrates the validity of separating the system in these two control loops as depicted in Figure 2 for the case of negligible tip–sample interaction.

Noise with significant tip–sample interaction

Realistic NC-AFM imaging or force mapping experiments are performed at a small tip–sample distance, or even in the repulsive regime [22], where large gradients of the tip–sample force generate strong gradients in the frequency shift signal. We now extend Equation 5 and Equation 6 to include the additional noise contributions predicted by [12] and our system model in Figure 2.

The noise power spectral density of the cantilever oscillation amplitude D_A^z is not directly accessible experimentally, but can be introduced by analysing the amplitude control loop (see Figure 2)

$$D_A^z(\omega_m) = 2\left|\frac{H_c}{1-H_cH_{lp}H_{ac}}\right|^2\left(D_{th}^{exc}+\left|H_{lp}H_{ac}\right|^2 D_{ds}^z\right). \quad (7)$$

The quantity D_A^z itself is not affected by the tip–sample interaction. However, due to the coupling characterised by the parameter α_{ts}, the noise spectral density D_A^z propagates into the frequency control loop, yielding a significant contribution to the frequency shift noise. From including this contribution in the control loop diagram of Figure 2, we find the frequency shift noise power spectral density $D^{\Delta f}$ as

$$D^{\Delta f}(\omega_m) = \left|\frac{H_{filter}}{1-H_{filter}H_c/Q-\beta_{ts}H_{zc}H_{filter}}\right|^2 \times\left(\alpha_{ts}^2 D_A^z + 2\left(\frac{\omega_m}{2\pi A}\right)^2\left(D_{ds}^z+\left|H_c\right|^2 D_{th}^{exc}\right)\right). \quad (8)$$

Following the approach from the previous section, we use the explicit system parameters and system-specific transfer functions (given in appendix C) to numerically evaluate Equation 8 for comparison with the experimental data.

First, we investigate NC-AFM experiments performed in the constant-height mode, where the tip is in close proximity to the sample surface with the distance control loop disabled, modelled here by setting H_{zc} = 0. Measurements (solid lines) and corresponding simulations using Equation 8 (including tip–sample interaction, dotted lines) and Equation 5 (without tip–sample interaction, dashed lines) of the frequency shift noise spectral density $D^{\Delta f}$ are reproduced in Figure 6. Measurements and simulations are performed with enabled (P_A = 0.08) and disabled (P_A = 0) amplitude control loop as shown in Figure 6a and at two tip–sample distances characterised by the

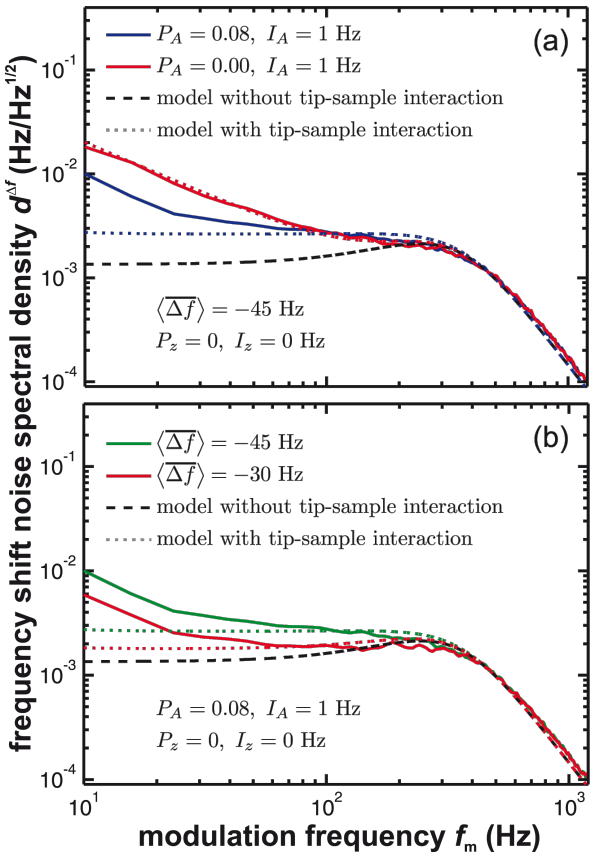

Figure 6: Frequency shift noise spectral density $d^{\Delta f}$ for the case of significant tip–sample interaction measured in the constant height mode (P_z = 0, I_z = 0 Hz) in dependence on (a) the amplitude control loop settings and (b) the tip–sample distance parametrised via the averaged frequency shift $\langle\overline{\Delta f}\rangle$. Measured curves (solid lines) are compared to model predictions including tip–sample interaction (dotted lines, Equation 8) and to the model without tip–sample interaction (dashed lines, Equation 5). The loop filter H_{lp} has a 3rd-order Butterworth characteristics with a cutoff frequency of f_c = 500 Hz.

averaged frequency shift $\langle\overline{\Delta f}\rangle$ as shown in Figure 6b. The increase in the spectral noise at low frequencies in Figure 6a indicates contributions from the cantilever amplitude noise coupling into the frequency shift signal via the tip–sample interaction. Despite some discrepancy at very low frequencies also observed for the case of negligible tip–sample interaction (see Figure 5), we find a good agreement between prediction and experimental results. Here, we can only speculate that the low-frequency deviation is caused by mechanical instabilities within the system, or by instabilities within the piezoelectric excitation system. For example, low-frequency noise has been observed when using photothermal excitation [23].

Disabling the amplitude control loop results in a strong increase of low frequency noise compared to operation with engaged amplitude control using optimum parameters (see previous section and appendix C). The amplitude control loop effectively reduces the frequency shift noise by its negative feedback. Furthermore, we observe an increase of the frequency shift noise $D^{\Delta f}$ for stronger tip–sample interaction (see Figure 6b) due to a strong coupling described by an increase of α_{ts} at smaller tip–sample distances.

Second, we investigate the frequency shift and topography noise in the commonly used constant frequency-shift mode where the tip–sample distance is adjusted by the distance control loop to keep the frequency shift at the set-point Δf_{set}. The topography noise spectral density D^{z_p} is obtained by applying the frequency response H_{zc} of the distance controller to the frequency shift noise $D^{\Delta f}$ (see Figure 2)

$$D^{z_p}(\omega_m) = |H_{zc}|^2 D^{\Delta f}(\omega_m). \quad (9)$$

Figure 7 shows the measured frequency shift (panels (a, b)) and topography (panels (c, d)) noise in the presence of the activated distance control loop (solid lines). These experimental data are

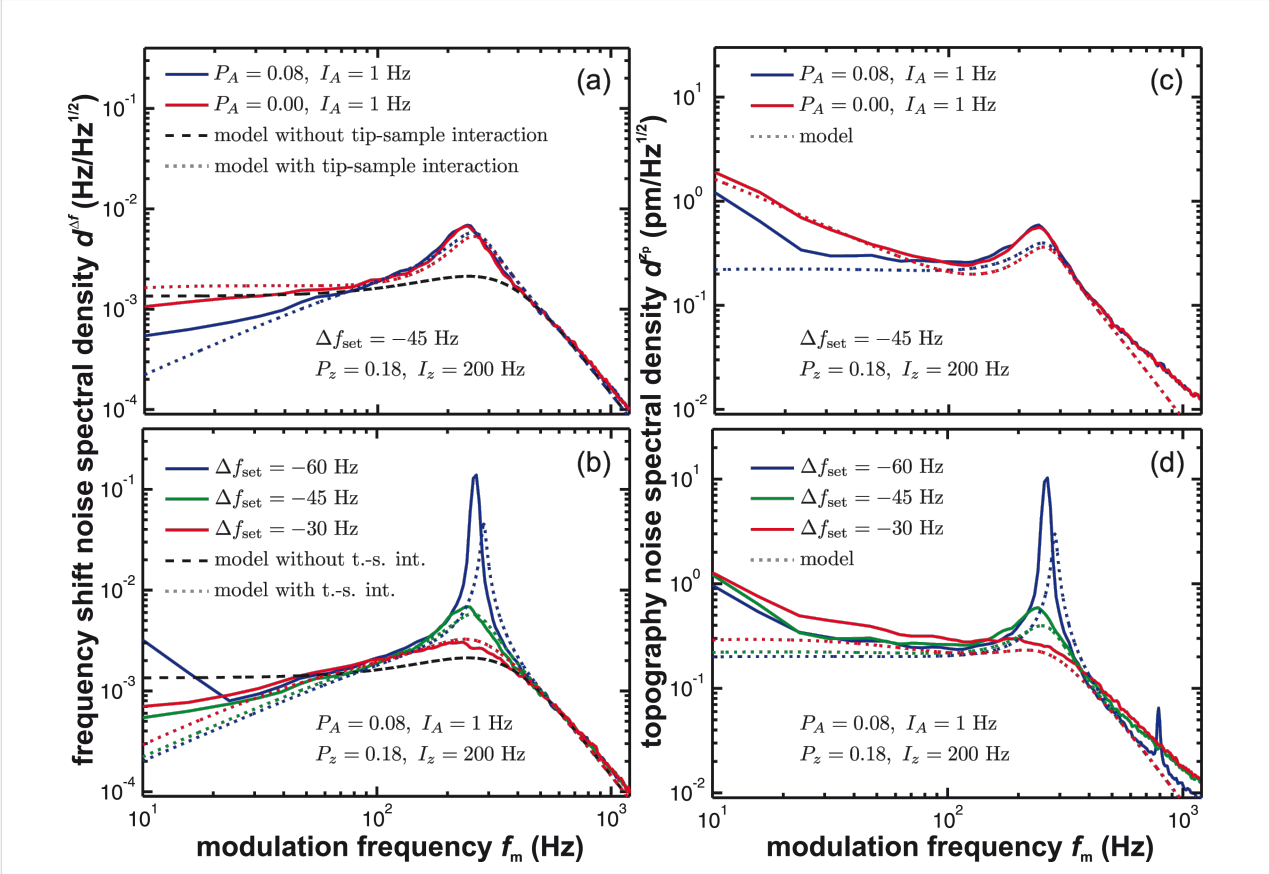

Figure 7: (a, b) Frequency shift noise spectral density $d^{\Delta f}$ and (c, d) topography noise spectral density d^{z_p} with tip–sample interaction using the constant frequency-shift mode in dependence on the amplitude control loop settings and the tip–sample distance defined by the frequency shift set-point Δf_{set}. Measured curves (solid lines) are compared to model predictions including tip–sample interaction (dotted lines, Equation 8 and Equation 9) and without tip–sample interaction (dashed lines, Equation 5). The loop filter H_{lp} has a 3rd-order Butterworth characteristics with a cutoff frequency of f_c = 500 Hz.

compared to simulation results based on Equation 8 including tip–sample interaction (dotted lines) and Equation 5 without tip–sample interaction (dashed lines).

Generally, we observe an increase of noise power in the frequency range from 200 to 300 Hz, where the apparent peaking firsthand appears to be independent from the amplitude control loop settings. Engaging the amplitude control loop (Figure 7a and Figure 7c) results in a reduction of noise in the low-frequency regime as observed in the constant-height measurement mode. However, the active loop has a marginal influence on the peaking in the 200–300 Hz region. In contrast, the appearance of this peak strongly depends on the frequency shift set-point: The peak height increases with increased frequency shift set-point Δf_{set} (Figure 7b and Figure 7d). Interestingly, with activated distance control, the noise level in the low-frequency range may even fall below the values observed without tip–sample interaction. This demonstrates that the distance control loop is effectively able to compensate some of the low-frequency thermal noise by a distance adjustment and directly suggests an optimum frequency response as outlined in appendix C.

Finally, we investigate in Figure 8 the influence of the distance control loop parameters P_z and I_z on the noise characteristics. Frequency shift noise $d^{\Delta f}$ (panels a and c) and topography noise d^{z_p} (panels c and d) experimental data (solid curves) are compared to simulations based on Equation 8 including tip–sample interaction (dotted lines) and Equation 5 without tip–sample interaction (dashed lines). In all cases, the amplitude control loop is set using optimum parameters. Data in Figure 8 are presented for different P_z (I_z) while keeping I_z (P_z) constant, respectively. Choosing the gain factors too large results in gain peaking in the noise spectral density of the frequency shift signal as well as the topography signal. Different P_z (Figure 8a and Figure 8c) shift the gain peak along the frequency axis and

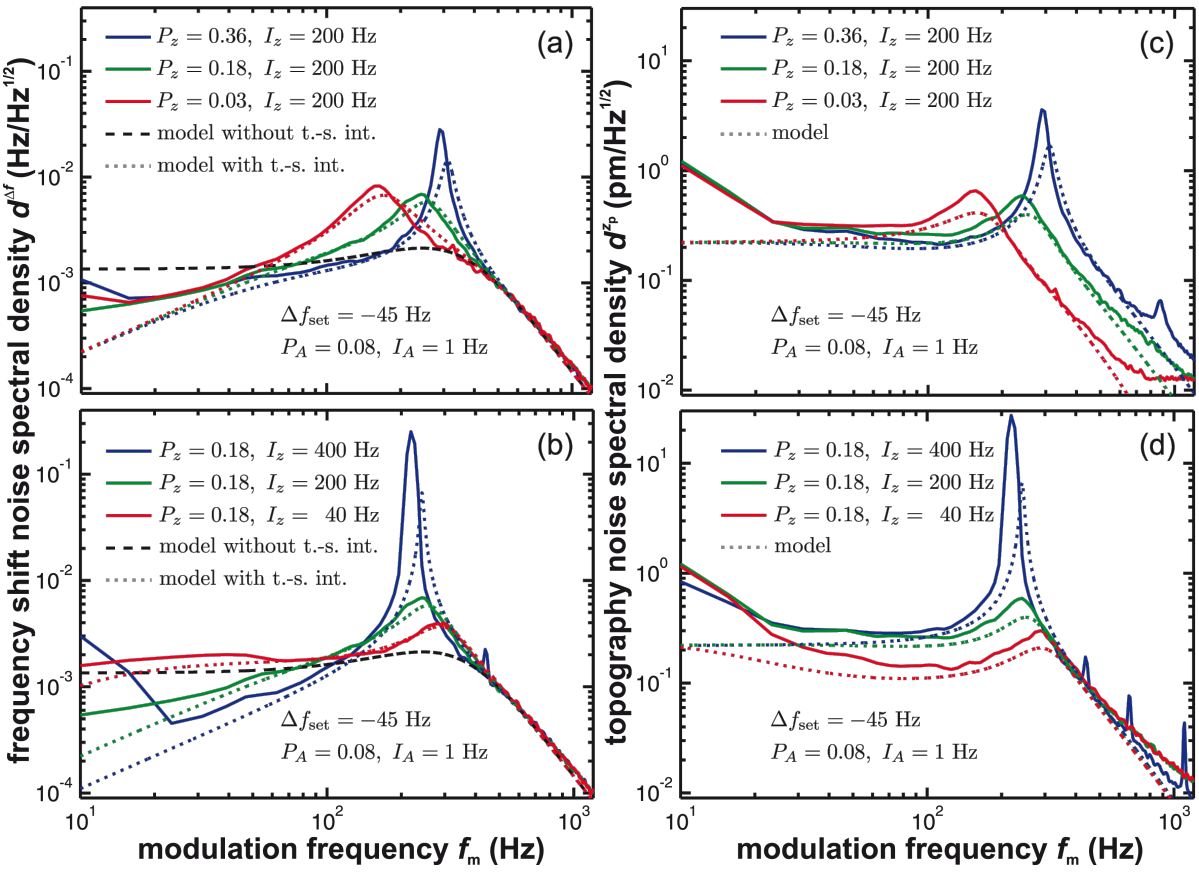

Figure 8: (a, b) Frequency shift noise spectral density $d^{\Delta f}$ and (c, d) topography noise spectral density d^{z_p} with tip–sample interaction in the constant frequency-shift mode in dependence on the distance control loop settings. Measured curves (solid lines) are compared to model predictions including tip–sample interaction (dotted lines, Equation 8 and Equation 9) and without tip–sample interaction (dashed lines, Equation 5). The loop filter H_{lp} has a 3rd-order Butterworth characteristics with a cutoff frequency of f_c = 500 Hz.

we find in this example a minimum of the peak amplitude for $P_z = 0.18$. This behaviour is further illustrated by discussing the frequency and step response of the distance control loop in appendix C. Decreasing I_z (Figure 8b and Figure 8d) reduces the gain peaking but elevates the noise level in the low-frequency range of the frequency shift noise. In the topography noise, a decrease of I_z significantly reduces the total noise. This effect is not surprising as it coincides with a reduction of the gain in the frequency range around 100 Hz and a significant slow-down of the step-response as shown in Figure 12 of appendix C. A small response time of the topography feedback loop causes a reduced noise in D^{z_p}.

Conclusions and System Optimisation

We realise that the control and data acquisition system of a NC-AFM is a complex network of sensing, amplification and processing stages as well as several control loops interacting with each other. Our network analysis demonstrates the quantitative description of all frequency response functions of the NC-AFM system, including the prediction of noise confirmed by an excellent agreement between measurement and network modelling. This analysis especially provides experimental evidence for strong noise amplification by coupling of control loops due to the tip–sample interaction.

In regular NC-AFM operation with state-of-the-art hardware, signal generation and noise amplification is governed by the tip–sample interaction, which introduces the most non-linear transfer function into the system. Therefore, the optimisation of NC-AFM measurements by proper settings for system parameters is not straightforward and has to be carefully adapted to the specific measurement task. Often, corrections are necessary during measurements upon a change in tip–sample interaction, for instance due to a change in tip–sample distance or a tip change. In such situations, best results are commonly obtained by following the instinct of the experienced experimentalist.

However, the basic adjustment of the system to yield the optimum in stability, accuracy and signal-to-noise ratio can be done by a rational, systematic approach following the findings described in this paper, provided the measurement system is well characterised and offers sufficient choice and flexibility in system parameter settings.

The starting point is always the experimental task defining the desired spatial resolution λ that is, for instance, a fraction of the atomic periodicity in atomic resolution imaging, and the available time for the measurement expressed by the scan speed v_{scan}. Assuming perfectly band-limited output signals, the sampling theorem requires the product of scan speed and inverse spatial resolution to be smaller than half of the detection bandwidth Δf_{BW}, or

$$\Delta f_{BW} > 2 \times v_{scan} \frac{1}{\lambda}. \tag{10}$$

This often requires a compromise as using the optimum bandwidth defined by operation at the thermal noise limit [11] may impose a scan speed that is not practical, specifically if thermal drift is not compensated [24]. Considering the interdependence of the control loops and the tip–sample interaction, we suggest four optimisation steps to be performed in following order: (1) the PLL demodulator H_{filter}, (2) the frequency control loop H_f, (3) the amplitude control loop H_A and (4) the distance control loop H_z.

In step (1), the PLL demodulator H_{filter} is optimised purely from simulating the frequency response to have a certain bandwidth Δf_{BW}. For an integral cutoff I_{PLL} of the PLL loop given from the ratio f_0/Q_0 [25] and for a low-pass filter H_{lp} selected according to the requested bandwidth Δf_{BW}, the feedback gain parameter P_{PLL} is increased until the peak threshold of 0.1 dB is reached (see appendix C.2 for an example and further details). As it is most desirable to work with high-Q cantilevers [11], the frequency control loop H_f is in step (2) inherently optimised from step (1) (see appendix C.2 for details). In case of small Q values (i.e., in liquid environment [16]), the optimisation in step (2) can be performed from simulating the frequency response with the knowledge of the system parameters f_0 and Q. Optimising the amplitude control loop response H_A in step (3) requires the cantilever parameters f_0 and Q_0 that can easily be determined [14]. Here, the integral cutoff I_A of the amplitude loop is again set to f_0/Q_0 and the feedback gain parameter P_A is then increased until the threshold of 0.1 dB for gain peaking is reached as outlined in appendix C.1. This optimisation can also be performed purely from simulating the frequency response function. In step (4), the frequency response of the distance control loop is optimised. This requires the acquisition of a $\Delta f(z_p)$ curve, from which the slope β_{ts} is calculated at the working point. The feedback loop gains P_z and I_z are optimised until an acceptable overshoot and a fast step response is achieved as outlined in appendix C.3. Due to the usually imminent risk of tip changes, it is advisable to plan with a safety buffer regarding these two parameters.

Specifically the last step is most crucial and requires utmost care, not only in experiment preparation but also during the experimental run. Following the outlined procedure will yield the best possible result. If this is not satisfactory, the reason is often

that the base value of D_{ds}^{z} is too high or that the detection system noise contains disturbing signals, such as radio frequency interference or spurious cantilever excitation. Therefore, it is always good practice to additionally check the measurement signal with a spectrum analyser from the pre-amplifier all way down to the PLL output. The quality of measurements may dramatically be increased by removing even a minute spurious signal generated at a critical frequency to avoid its amplification by the system network. In this case, our optimisation procedure can bring the NC-AFM setup to noise-optimised performance.

Appendix

A Glossary

Table 1 is a glossary of all symbols used within this work to parametrise noise in an NC-AFM system.

Table 1: Glossary of symbols used within this work.

Function arguments	
$f = \omega/2\pi$	frequency
$f_m = \omega_m/2\pi$	modulation frequency measured relative to f_r
$s = \sigma + i\omega$	complex frequency variable
Frequency response functions	
$H_0(i\omega)$	cantilever frequency response function
$H_c(i\omega_m)$	cantilever frequency response function approximated around f_0
$H_{filter}(i\omega_m)$	frequency response of the PLL system
$H_{lp}(i\omega_m)$	frequency response of the low-pass filter in the amplitude measurement
$H_{ac}(i\omega_m)$	frequency response of the amplitude controller
$H_{zc}(i\omega_m)$	frequency response of the distance controller
$H_A(i\omega_m)$	frequency response of the amplitude control loop
$H_z(i\omega_m)$	frequency response of the topography control loop
$H_f(i\omega_m)$	frequency response of the frequency control loop
Cantilever and tip–sample interaction properties	
f_0	modal eigenfrequency of the cantilever (fundamental mode)
f_r	resonance frequency of the cantilever
k_0	modal stiffness of the cantilever (fundamental mode)
Q_0	modal quality factor of the cantilever (fundamental mode)
A_{exc}	cantilever drive signal amplitude
f_{exc}	cantilever drive signal frequency
Δf_{set}	frequency shift set-point
$\langle\overline{\Delta f}\rangle$	measured average frequency shift
A	cantilever oscillation amplitude
A_z	cantilever oscillation amplitude perpendicular to the sample surface
A_{set}	cantilever oscillation amplitude set-point
α_{ts}	parameter describing the coupling between the amplitude control loop and the frequency control loop
β_{ts}	parameter describing the coupling between the distance control loop and the frequency control loop
System setup parameters	
z_p	scanner piezo position (topography signal)
z_{ts}	lower turning point of the cantilever oscillation relative to the sample surface
S_A^z	sensitivity of the cantilever deflection and the detection system
S_{exc}^z	sensitivity of the cantilever excitation piezo
$S^{\Delta f}$	Δf output signal voltage encoding of the PLL system
S_p^z	sensitivity of the z piezo
f_c	cutoff frequency of the loop filter in the amplitude and in the frequency control loop

Table 1: Glossary of symbols used within this work. (continued)

P_{PLL}	proportional loop gain of the PLL
I_{PLL}	integral cutoff of the PLL
P_A	proportional loop gain of the amplitude control loop
I_A	integral cutoff of the amplitude control loop
P_z	proportional loop gain of the distance control loop
I_z	integral loop gain of the distance control loop
Spectral densities	
D_j^i	power spectral density of noise type *i* due to noise source *j*
$d_j^i = \sqrt{D_j^i}$	amplitude spectral density of noise type *i* due to noise source *j*
D^z	total displacement noise power spectral density
D_{ds}^z	displacement noise power spectral density generated by the detection system
D_A^z	noise power spectral density describing amplitude fluctuations in the cantilever displacement signal
D_{th}^z	displacement noise power spectral density due to the cantilever thermal excitation
D^{z_p}	topography noise power spectral density
D_{th}^{exc}	excitation noise power spectral density, describing the thermal excitation of the cantilever
D^A	amplitude noise power spectral density
$D_{free}^{\Delta f}$	frequency shift noise power spectral density at the PLL output for the case of negligible tip–sample interaction
$D^{\Delta f}$	frequency shift noise power spectral density at the PLL output

B Frequency response of control loops

We briefly outline how we calculate a closed loop response H_{xy} for a loop containing frequency response functions H_i between the input signal X and the output signal Y. For a more detailed discussion we refer to [26]. All frequency response functions are treated as a function of the complex frequency $i\omega$. In the main text, we mostly evaluate the real component with respect to $f = \omega/(2\pi)$ (or f_m) as this "amplitude response" or "gain" can directly be compared to experimental data. Furthermore, we usually do not consider the signal phase in this work, as we are interested in noise that is a result of stochastic processes. However, the frequency response functions $H_i(i\omega)$ are treated as transfer functions $H_i(s)$ using the complex frequency variable $s = \sigma + i\omega$ to calculate step responses from an inverse Laplace transformation.

Figure 9a is a block diagram of the frequency and distance control loop of Figure 2. The model contains two closed loops that are interlaced. Using the corresponding signal-flow graph in Figure 9b and Mason's theorem [26], we are able to describe the interlaced feedback loops by one transfer function. While the block diagram in Figure 9a focuses on the involved transfer functions, the signal-flow graph in Figure 9b represents the topological structure of the system. After using basic signal-flow graph algebra [26] and following the analysis introduced by Shinners [26], this signal-flow graph directly permits to derive a solution for the transfer function.

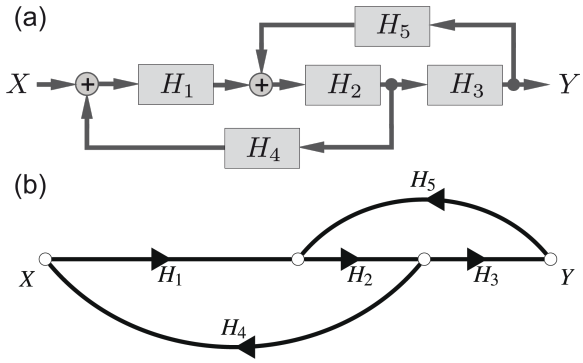

Figure 9: (a) Block diagram of interlaced control loops as introduced in Figure 2 and (b) signal-flow graph to demonstrate the derivation of the frequency response of coupled closed loops.

According to Mason's theorem, the general expression for the signal-flow graph frequency response H_{xy} is

$$H_{xy} = \frac{\sum_{k=1}^{N} H_k^{\Pi} \Delta_k}{\Delta}, \tag{11}$$

where Δ is the determinant of the graph defined as

$$\Delta = 1 - \sum_{a} L_a + \sum_{a,b} L_a L_b - \sum_{a,b,c} L_a L_b L_c + \ldots + (-1)^m \sum_{m} L_m \quad (12)$$

with

L_a : frequency response of each closed loop in the graph
$L_a L_b$: product of loop gains of any two non-touching loops (two loops are non-touching if they share no common node)
$L_a L_b \ldots L_N$: product of loop gains of any N non-touching loops
L_m: as $L_a L_b$, but with m (non-touching) closed loop frequency responses
H_k^{Π} : multiplied frequency responses in the kth forward path
Δ_k : the cofactor value of Δ for the kth forward path, with the loops touching the kth forward path removed.

We exemplarily calculate the full frequency response for the system sketched in Figure 9 where only one forward path ($H_1H_2H_3$) is in the corresponding signal-flow representation. Therefore, the calculation reduces to determine H_1^{Π} and Δ_1. Furthermore, two non-touching closed loops, namely $H_1H_2H_4$ and $H_2H_3H_5$, are present. Consequently, Δ is reduced to $1-\sum L_1$ and reads

$$\Delta = 1 - \left(H_1 H_2 H_4 + H_2 H_3 H_5\right). \quad (13)$$

Evaluating

$$H_1^{\Pi} = H_1 H_2 H_3 \quad (14)$$

and

$$\Delta_1 = 1 \quad (15)$$

allows us to determine the full frequency response from X to Y from Figure 9 as

$$H_{\mathrm{xy}} = \frac{Y}{X} = \frac{H_1^{\Pi}\Delta_1}{\Delta} = \frac{H_1 H_2 H_3}{1 - H_1 H_2 H_4 - H_2 H_3 H_5}. \quad (16)$$

If a noise power spectral density D_x is used as the input signal X and treated by the system response H_{xy} we find

$$D_y = \left|H_{\mathrm{xy}}\right|^2 D_x = \left|\frac{H_1 H_2 H_3}{1 - H_1 H_2 H_4 - H_2 H_3 H_5}\right|^2 D_x \quad (17)$$

for the output noise power spectral density D_y [27].

C Frequency response functions

In this section, we present the explicit form of the frequency response functions and the specific frequency response functions valid for the experimental setup used for this work. The derivation follows [11] and [12].

C.1 Amplitude control loop

The frequency response H_{ac} of the amplitude controller is [25]

$$H_{\mathrm{ac}}\left(i\omega_m\right) = -\left(S_{\mathrm{exc}}^z \big/ S_A^z\right) P_A \left(1 + \pi I_A \big/ \left(i\omega_m\right)\right), \quad (18)$$

using the amplitude and excitation calibration factors S_A^z and S_{exc}^z, respectively, where S_A^z is determined by an amplitude calibration as described in [19] while S_{exc}^z is determined from measuring the oscillation amplitude in resonance for a given excitation voltage V_{exc}. Assuming $Q_0 = A/A_{\mathrm{exc}} = V_A S_A^z / (V_{\mathrm{exc}} S_{\mathrm{exc}}^z)$ allows a straightforward calculation of S_{exc}^z from known parameters of a well-characterised system. Note that by rewriting this formula to $S_A^z / S_{\mathrm{exc}}^z = Q_0 V_{\mathrm{exc}} / V_A$, we can fully describe H_{ac} without performing an amplitude calibration measurement. The characteristics of the loop are defined by two parameters, the gain P_A and the integral cutoff I_A. Assuming that the cantilever is a system of first order, the integral cutoff I_A can be chosen to f_0/Q_0 to avoid loop instabilities [25]. Therefore, the formula is written directly in terms of the integral cutoff and not using the integral loop gain $I = I_A P_A \pi$.

The frequency response of the cantilever follows from the response of a damped harmonic oscillator

$$H_0\left(i\omega\right) = \frac{1}{1 + \left(i\omega/\omega_0\right)^2 + i\omega/\left(Q_0\omega_0\right)}, \quad (19)$$

with the quality factor Q_0 and the eigenfrequency $\omega_0 = 2\pi f_0$. This function can be re-written with the modulation frequency ω_m as the argument by substituting $\omega = \omega_0 + \omega_m$ and can for $\omega_m \ll \omega_0$ be approximated [9] to

$$H_{\mathrm{c}}\left(i\omega_m\right) = \left(1/Q_0 + 2i\omega_m/\omega_0\right)^{-1}. \quad (20)$$

Note that Equation 20 is phase shifted by π/2 relative to Equation 19 [12]. Following procedures outlined in appendix B and Figure 2, the frequency response of the closed amplitude control loop is given as

$$H_A(i\omega_m) = \frac{H_{ac}H_cH_{lp}}{1 - H_{ac}H_cH_{lp}}, \tag{21}$$

with the frequency response of the amplitude controller H_{ac} (see Equation 18), the frequency response of the cantilever H_c (see Equation 20) and the frequency response of the loop filter H_{lp}, which is in our case a Butterworth filter of 3rd order [28] with cutoff frequency f_c

$$H_{lp,B3}(i\omega_m) = \frac{1}{\left(1+\frac{i\omega_m}{2\pi f_c}\right)\left(1+\frac{i\omega_m}{2\pi f_c}+\left(\frac{i\omega_m}{2\pi f_c}\right)^2\right)}. \tag{22}$$

To quantitatively evaluate H_A, we first note that H_c is fully defined by the two cantilever parameters f_0 and Q_0. These can easily be determined in absence of tip–sample interaction [14]. By adding the response functions of the loop filter and amplitude controller according to Equation 21, we calculate the frequency response of the amplitude control loop illustrated in Figure 10a for different proportional gain values P_A. Figure 10b shows the corresponding step response in time space, which is calculated by applying the inverse Laplace transform [29] to the product of the transfer function $H_A(s)$ with $s = \sigma + i\omega$ and the Laplace transform of the unit step function, $1/s$. The result $A(t) = \mathcal{L}^{-1}\left[H_A(s)/s\right]$ is numerically evaluated [30]. The PLLpro2 system provides a feedback test by periodically changing one parameter, here the amplitude set-point, by a given magnitude, while recording the respective response with time. The measurements are normalised to a step height of one to be comparable to the calculated step responses. As shown in panel (c), the calculations are in excellent agreement with the measured step response. The response functions follow the expected behaviour: For small P_A, the frequency response is a decreasing function of frequency and the step response a slowly rising function in time (red curves). For large P_A, gain peaking appears in the frequency response and the step response exhibits ringing (blue curves). The optimum setting is represented by the frequency response being flat over the low pass filter bandwidth followed by a steep decrease. This corresponds to a nearly rectangular step response with a certain rise time and a small overshoot (green curves).

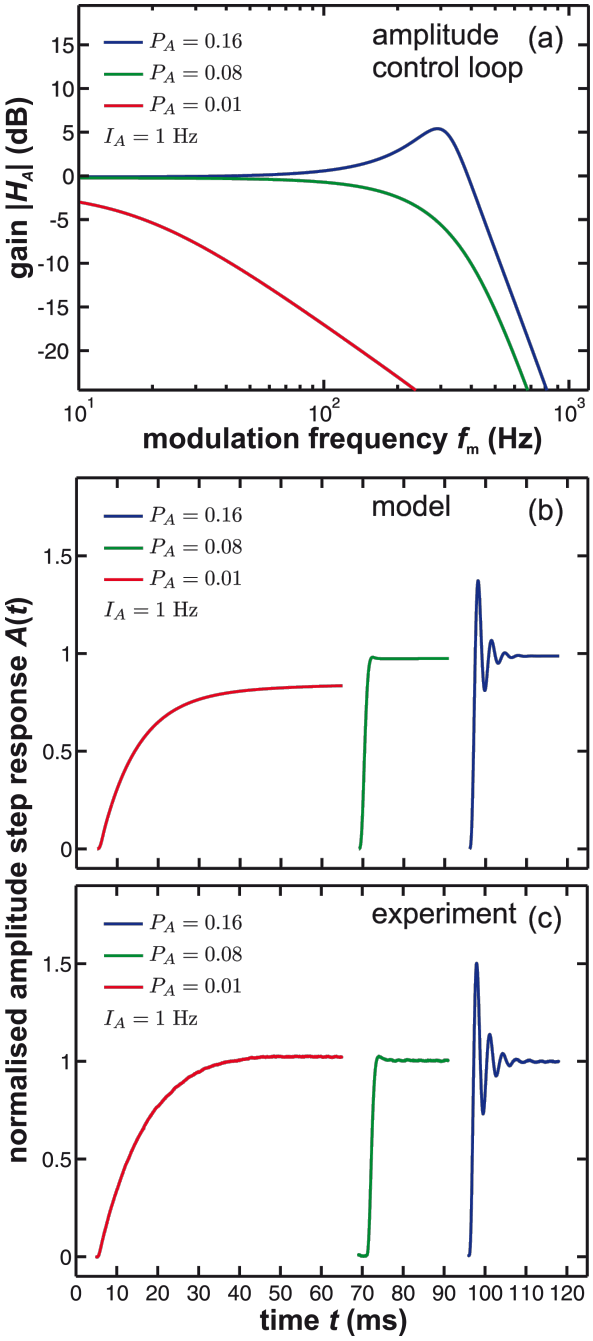

Figure 10: (a) Calculated gain and (b) calculated step response of the amplitude control loop compared to (c) measured step response for different loop gains P_A. I_A is kept fixed at 1 Hz. The loop filter H_{lp} has a 3rd-order Butterworth characteristics with a cutoff frequency of f_c = 500 Hz.

To optimise the amplitude control loop parameters, we first set the integral cutoff I_A of the amplitude controller to f_0/Q_0 [25]. To analyse the frequency response, we then start with a small P_A and increase this value stepwise until a certain threshold for the gain peaking is reached, e.g., 0.1 dB. For the given set of parameters, this response reflects the optimum settings.

C.2 Frequency control loop

The frequency response of the PLL is given by (see Supplemental Information of [11])

$$H_{\text{filter}}(i\omega_m) = \frac{369\,\text{deg} \times P_{\text{PLL}}\left(1+\pi I_{\text{PLL}}/(i\omega_m)\right)}{i\omega_m/H_{\text{lp}} + 369\,\text{deg} \times P_{\text{PLL}}\left(1+\pi I_{\text{PLL}}/(i\omega_m)\right)}, \quad (23)$$

with $H_{\text{lp}}(i\omega_m)$ being the frequency response of the low-pass loop filter. Figure 11a illustrates the calculated gain of the PLL using Equation 23 for different loop gain settings P_{PLL} and a 3rd-order Butterworth filter (see Equation 22) with a cutoff frequency of 500 Hz. We experimentally observe that the integral cutoff I_{PLL} has a minor influence on the frequency response besides the presence of gain peaking for very small values. In Figure 11b, the step response of H_{filter} is calculated and compared to the measured step response of the PLLpro2 system shown in Figure 11c. Here, the inverse Laplace transform is used to calculate the frequency shift $\Delta f(t) = \mathcal{L}^{-1}\left[H_{\text{filter}}(s)/s\right]$ and the PLLpro2 feedback test is experimentally performed by periodically changing the phase setpoint within the PLLpro2 frequency control loop while logging the frequency shift signal.

For the closed frequency control loop, we find from Figure 2 and using procedures outlined in appendix B

$$H_{\text{f}}(i\omega_m) = \frac{H_{\text{filter}}}{1 - H_{\text{filter}}H_{\text{c}}/Q_0}. \quad (24)$$

By using Equation 20, we find $H_{\text{c}}/Q_0 \to 0$ for large Q_0. As high Q_0 values are always desirable in experiments performed under UHV conditions, this analysis suggests an optimisation procedure for the frequency control loop solely based on the frequency response H_{filter} of the PLL. This optimisation is possible from calculating the gain before the cantilever is inserted into the system if the system parameters f_0 and Q_0 are known. The procedure can be performed similar to the optimisation of the amplitude loop, by first setting the integral cutoff I_{PLL} to f_0/Q_0 and then increasing P_{PLL} until the threshold of 0.1 dB for gain peaking is reached. Calculated and experimentally measured frequency and step response functions are acquired as before in case of the amplitude control loop and are presented in Figure 11.

C.3 Distance control loop

The the z-distance controller is a general proportional–integral regulator with frequency response

$$H_{\text{zc}}(i\omega_m) = \left(S_{\text{p}}^z / S^{\Delta f}\right)\left(P_z + I_z/(i\omega_m)\right). \quad (25)$$

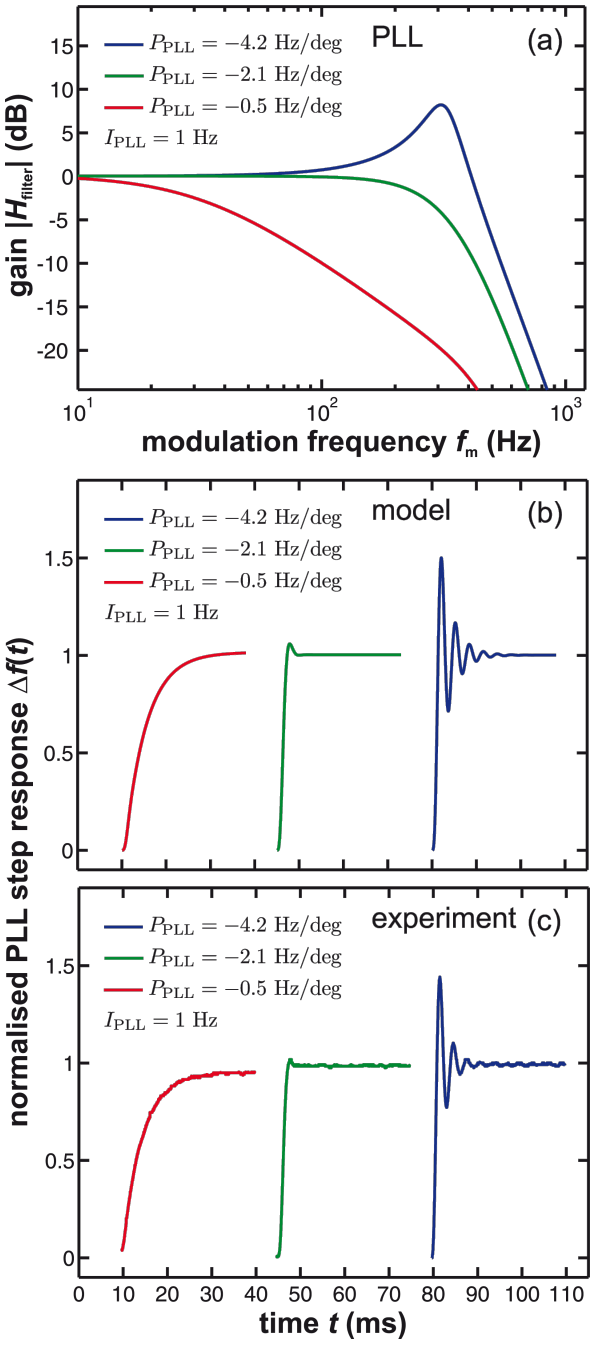

Figure 11: (a) Calculated gain and (b) calculated step response of the PLL compared to (c) the measured step response for different loop gains P_{PLL}. I_{PLL} is kept fixed at 1 Hz. The loop filter H_{lp} has a 3rd-order Butterworth characteristics with a cutoff frequency of f_c = 500 Hz.

The voltage output of the PLL and the signal input of the piezos are both scaled in units of volts. To account for the correct unit of the frequency response function, we include a calibration factor $S^{\Delta f}$ (in units of Hz/V) for the PLL output and a calibration factor S_{p}^z (in units of nm/V) as z-piezo sensitivity.

The frequency response of the closed distance control loop is determined from Figure 2 and using procedures outlined in appendix B

$$H_z\left(i\omega_m\right)=\frac{\beta_{ts}H_{filter}H_{zc}}{1-\beta_{ts}H_{filter}H_{zc}-H_cH_{filter}/Q_0}, \qquad (26)$$

with H_{zc} being the frequency response of the distance controller (see Equation 25) and H_{filter} being the frequency response of the PLL (see Equation 23). Figure 12a,b illustrate the calculated response of the distance control loop using Equation 26 for different settings of the proportional gain P_z and the integral gain I_z. The corresponding calculated step response of the distance control loop is shown in Figure 12c,d.

Figure 12 illustrates that a proper adjustment of the distance controller parameters P_z and I_z is mandatory for stable and fast operation. Compared to the previous loop discussions, a significant complication added is the parameter β_{ts}, which strongly depends on z_p. Therefore, a configuration identified as the optimum for a certain tip–sample distance is most likely obsolete for stronger or weaker tip–sample interaction and would yield creep or overshoot in the step response.

For the optimisation of the distance control loop, a $\Delta f(z_p)$ curve should be obtained first and the slope of the $\Delta f(z_p)$ curve at the desired working point (β_{ts} = 12.3 Hz/nm, see Figure 4) should be used to simulate the frequency response of the distance control loop. As shown in Figure 12a and Figure 12c, an optimum for the lowest gain peaking could be found for P_z = 0.18 (green curve). When changing the integral gain I_z (see Figure 12b and Figure 12d), we start in this case from a strongly damped response (red curve), pass the optimum (I_z = 200 Hz, green curve) and arrive at a ringing behaviour (blue curve). The optimum is characterised by acceptable overshoot. A fast step response is obtained by reducing gain peaking while maintaining a flat response at low frequencies. However, operating on a slightly different position on the $\Delta f(z)$ curve may strongly change the frequency response of the distance control loop. Therefore, it is advisable to plan with a safety buffer regarding the choice of P_z and I_z values to be prepared for unexpected changes of the tip–sample interaction.

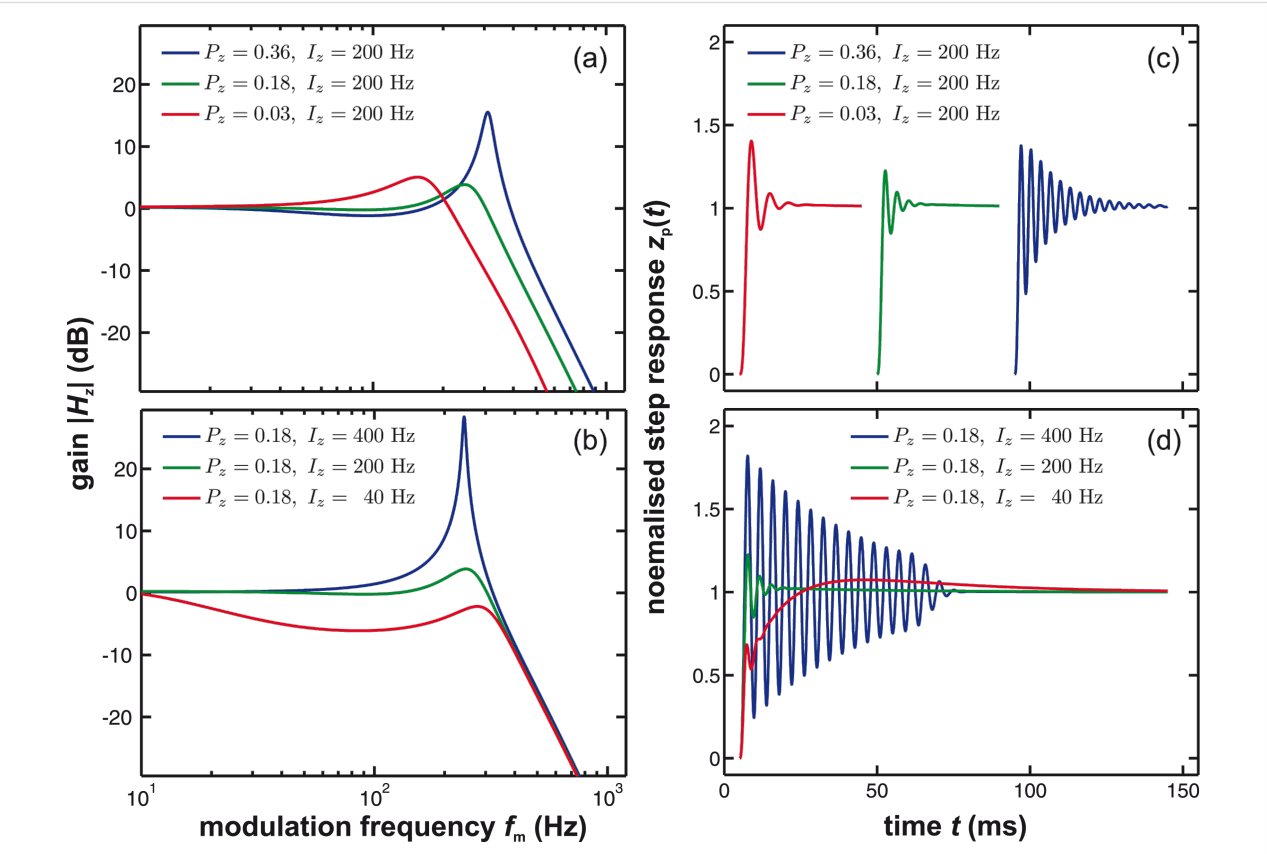

Figure 12: (a, b) Frequency response and (c, d) step response of the distance control loop for a given tip–sample interaction β_{ts} = 12.3 Hz/nm and different settings of P_z and I_z. The calculations are performed using the ratio $S_p^z / S^{\Delta f}$ = −0.312 nm/Hz and for PLL settings P_{PLL} = −2.1 Hz/deg, I_{PLL} = 1 Hz with the loop filter H_{lp} having a 3rd-order Butterworth characteristics with a cutoff frequency of f_c = 500 Hz.

D Relation between α_{ts} and β_{ts}

The theory derived by Polesel-Maris et al. [12] describes the impact of the tip–sample interaction on the measurement signal noise by the two parameters α_{ts} and β_{ts} defined as

$$\alpha_{\mathrm{ts}}\left(z_{\mathrm{ts}}, A_z\right) = \frac{\partial \Delta f\left(z_{\mathrm{ts}}, A_z\right)}{\partial A_z} \tag{27}$$

and

$$\beta_{\mathrm{ts}}\left(z_{\mathrm{ts}}, A_z\right) = \frac{\partial \Delta f\left(z_{\mathrm{ts}}, A_z\right)}{\partial z_{\mathrm{ts}}}. \tag{28}$$

Here, z_{ts} denotes the z-position of the lower turning point of the cantilever oscillation (see Figure 3). This position is related to the piezo position z_p and the oscillation amplitude A_z by

$$z_{\mathrm{ts}} = z_{\mathrm{p}} - A_z. \tag{29}$$

Following an amplitude change of δA, the lower turning point shifts to $z_p - \delta A$ while the centre of the oscillation z_p remains fixed. As a consequence of Equation 29, we find an identity for the derivations with respect to z_{ts} and z_p:

$$\frac{\partial}{\partial z_{\mathrm{ts}}} = \frac{\partial z_p}{\partial z_{\mathrm{ts}}}\frac{\partial}{\partial z_{\mathrm{p}}} = \frac{\partial}{\partial z_{\mathrm{p}}}. \tag{30}$$

Using this identity and Equation 29, we rewrite Equation 27 and Equation 28:

$$\alpha_{\mathrm{ts}}\left(z_{\mathrm{p}}, A_z\right) = \frac{\partial \Delta f\left(z_{\mathrm{p}} - A_z, A_z\right)}{\partial A_z} \tag{31}$$

$$\beta_{\mathrm{ts}}\left(z_{\mathrm{p}}, A_z\right) = \frac{\partial \Delta f\left(z_{\mathrm{p}} - A_z, A_z\right)}{\partial z_{\mathrm{p}}}. \tag{32}$$

Thus, the parameter β_{ts} can be determined directly from the slope of a known $\Delta f(z_p)$ curve as shown in Figure 4. Furthermore, Equation 31 can be rewritten into two terms

$$\alpha_{\mathrm{ts}} = \underbrace{-\left.\frac{\partial \Delta f\left(\tilde{x}, A_z\right)}{\partial \tilde{x}}\right|_{\tilde{x}=z_{\mathrm{p}}-A_z}}_{\alpha_{\mathrm{ts},1}} \underbrace{+\left.\frac{\partial \Delta f\left(z_{\mathrm{p}} - A_z, \tilde{y}\right)}{\partial \tilde{y}}\right|_{\tilde{y}=A_z}}_{\alpha_{\mathrm{ts},2}}. \tag{33}$$

This representation explicitly presents the two effects of an amplitude change on the frequency shift: First, the frequency shift changes due to a different lower turning point ($\alpha_{ts,1}$) and, second, the change in Δf due to a change of the weighting function [21] in the Δf calculation ($\alpha_{ts,2}$).

The first term is a measure of the slope of the $\Delta f(z_p)$ curve with respect to the piezo position z_p. It is identical to $-\beta_{ts}$. The second term is a result from the convolution of the tip–sample force interaction with a weighting function [21]. For large oscillation amplitudes, a dependence $\Delta f \propto A_z^{-3/2}$ has been found, allowing the definition of an amplitude-independent, normalised frequency shift [21]. This second term becomes negligible for large oscillation amplitudes A_z.

We illustrate the latter point by using an analytic expression for a Morse interaction force

$$F_{\mathrm{M}}\left(z_{\mathrm{ts}}\right) = 2\kappa E_{\mathrm{b}}\left[\exp\left(-2\kappa\left(z_{\mathrm{ts}} - \sigma\right)\right) - \exp\left(-\kappa\left(z_{\mathrm{ts}} - \sigma\right)\right)\right], \tag{34}$$

for which the resulting frequency shift Δf_M can be calculated as [31]

$$\begin{aligned}\Delta f_{\mathrm{M}}\left(z_{\mathrm{ts}}, A_z\right) = {} & 2E_{\mathrm{b}}\kappa\frac{f_0}{A_z k}\exp\left(-2\kappa\left(A_z + z_{\mathrm{ts}} - \sigma\right)\right) \\ & \times\left[I_1\left(2\kappa A_z\right) - \exp\left(\kappa\left(A_z + z_{\mathrm{ts}} - \sigma\right)\right) I_1\left(\kappa A z\right)\right],\end{aligned} \tag{35}$$

where $I_n(z)$ is the modified Bessel function of the first kind. Using this expression, parameters α_{ts} and β_{ts} are directly calculated as

$$\alpha_{\mathrm{ts}}\left(z_{\mathrm{p}}, A_z\right) = \alpha_{\mathrm{ts},1} + \alpha_{\mathrm{ts},2}, \tag{36}$$

$$\begin{aligned}\alpha_{\mathrm{ts},1}\left(z_{\mathrm{p}}, A_z\right) = {} & \frac{E_{\mathrm{b}}\kappa^2 f_0}{A_z k}\left[-2\exp\left(\kappa\left(\sigma - z_{\mathrm{p}}\right)\right) I_1\left(\kappa A_z\right)\right. \\ & \left. + \exp\left(2\kappa\left(\sigma - z_{\mathrm{p}}\right)\right) I_1\left(2\kappa A_z\right)\right],\end{aligned} \tag{37}$$

$$\begin{aligned}\alpha_{\mathrm{ts},2}\left(z_{\mathrm{p}}, A_z\right) = {} & \frac{E_{\mathrm{b}}\kappa^2 f_0}{A_z k}\left[\exp\left(\kappa\left(\sigma - z_{\mathrm{p}}\right)\right)\right. \\ & \times\left(-2I_0\left(\kappa A_z\right) + \frac{4}{A_z\kappa} I_1\left(\kappa A_z\right) + 2I_1\left(\kappa A_z\right)\right) \\ & + \exp\left(2\kappa\left(\sigma - z_{\mathrm{p}}\right)\right) \\ & \left.\times\left(4I_0\left(2\kappa A_z\right) + \frac{4}{\kappa A_z} I_1\left(2\kappa A_z\right) - 4I_1\left(2\kappa A_z\right)\right)\right]\end{aligned} \tag{38}$$

$$\beta_{ts}\left(z_p, A_z\right) = \frac{E_b \kappa^2 f_0}{A_z k}\Big[2\exp\left(\kappa\left(\sigma - z_p\right)\right) I_1\left(\kappa A_z\right) - \exp\left(2\kappa\left(\sigma - z_p\right)\right) I_1\left(2\kappa A_z\right)\Big] \quad (39)$$

The statement $\alpha_{ts,1} = -\beta_{ts}$ is directly evident from Equation 37 and Equation 39. To quantify the relation between $\alpha_{ts,1}$ and $\alpha_{ts,2}$, we plot the ratio

$$\delta\alpha = -\frac{\alpha_{ts,2}}{\alpha_{ts,1}} \quad (40)$$

as a function of the amplitude A and the lower turning point position z_{ts} in Figure 13 and using parameters for a Si–Si interaction derived from theory [32], namely E_b = 2.273 eV, κ = 12.76 nm^{-1} and σ = 0.2357 nm. Even at z-positions close to the force minimum ($z_{min} \approx 0.3$ nm) and for amplitudes A larger than 5 nm, the parameter $\alpha_{ts,2}$ is less than 5% of $\alpha_{ts,1}$. Thus, under these conditions, the approximation

$$\alpha_{ts} \approx -\beta_{ts} \quad (41)$$

is fully justified.

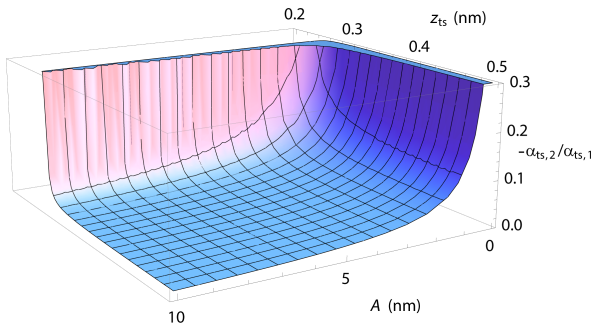

Figure 13: Ratio $\delta\alpha = -\alpha_{ts,2}/\alpha_{ts,1}$ as a function of the z-position and the amplitude. A Morse interaction using parameters from [32] and f_0 = 300 kHz, k = 35 N/m are used to model the tip–sample interaction.

Supporting Information

Supporting Information File 1

Scripts implementing all transfer functions and noise signals defined within this article.
[http://www.beilstein-journals.org/bjnano/content/supplementary/2190-4286-7-181-S1.zip]

Acknowledgements

We thank Steffen Porthun (RHK) and Sadik Hafizovic (Zurich Instruments) for most helpful discussions regarding the system-specific frequency response functions. M.T. gratefully acknowledges support from the Hans-Mühlenhoff-Stiftung. P.R. gratefully acknowledges support from the Alexander von Humboldt foundation. The project has been generously supported by Nanoworld Services GmbH.

References

1. Binnig, G.; Quate, C. F.; Gerber, C. *Phys. Rev. Lett.* **1986,** *56,* 930–933. doi:10.1103/PhysRevLett.56.930
2. Albrecht, T. R.; Grütter, P.; Horne, D.; Rugar, D. *J. Appl. Phys.* **1991,** *69,* 668–673. doi:10.1063/1.347347
3. Barth, C.; Foster, A. S.; Henry, C. R.; Shluger, A. L. *Adv. Mater.* **2011,** *23,* 477–501. doi:10.1002/adma.201002270
4. Lauritsen, J. V.; Reichling, M. *J. Phys.: Condens. Matter* **2010,** *22,* 263001. doi:10.1088/0953-8984/22/26/263001
5. Gross, L. *Nat. Chem.* **2011,** *3,* 273–278. doi:10.1038/nchem.1008
6. Lantz, M. A.; Hug, H. J.; Hoffmann, R.; van Schendel, P. J. A.; Kappenberger, P.; Martin, S.; Baratoff, A.; Güntherodt, H.-J. *Science* **2001,** *291,* 2580–2583. doi:10.1126/science.1057824
7. Sweetman, A. M.; Jarvis, S. P.; Sang, H.; Lekkas, I.; Rahe, P.; Wang, Y.; Wang, J.; Champness, N. R.; Kantorovich, L.; Moriarty, P. *Nat. Commun.* **2014,** *5,* 3931. doi:10.1038/ncomms4931
8. Reichling, M.; Kühnle, A. Scanning probe techniques. In *Surface and Interface Science;* Wandelt, K., Ed.; Wiley-VCH: Weinheim, Germany, 2012; Vol. 1, pp 427–488. doi:10.1002/9783527680535.ch11
9. Kobayashi, K.; Yamada, H.; Matsushige, K. *Rev. Sci. Instrum.* **2009,** *80,* 043708. doi:10.1063/1.3120913
10. Kobayashi, K.; Yamada, H.; Matsushige, K. *Rev. Sci. Instrum.* **2010,** *81,* 129901. doi:10.1063/1.3509402
11. Lübbe, J.; Temmen, M.; Rode, S.; Rahe, P.; Kühnle, A.; Reichling, M. *Beilstein J. Nanotechnol.* **2013,** *4,* 32–44. doi:10.3762/bjnano.4.4
12. Polesel-Maris, J.; Venegas de la Cerda, M. A.; Martrou, D.; Gauthier, S. *Phys. Rev. B* **2009,** *79,* 235401. doi:10.1103/PhysRevB.79.235401
13. Diesinger, H.; Deresmes, D.; Mélin, T. *Beilstein J. Nanotechnol.* **2014,** *5,* 1–18. doi:10.3762/bjnano.5.1
14. Lübbe, J.; Tröger, L.; Torbrügge, S.; Bechstein, R.; Richter, C.; Kühnle, A.; Reichling, M. *Meas. Sci. Technol.* **2010,** *21,* 125501. doi:10.1088/0957-0233/21/12/125501
15. Lübbe, J.; Temmen, M.; Schnieder, H.; Reichling, M. *Meas. Sci. Technol.* **2011,** *22,* 055501. doi:10.1088/0957-0233/22/5/055501
16. Fukuma, T.; Kimura, M.; Kobayashi, K.; Matsushige, K.; Yamada, H. *Rev. Sci. Instrum.* **2005,** *76,* 053704. doi:10.1063/1.1896938
17. Kobayashi, K.; Yamada, H.; Matsushige, K. *Rev. Sci. Instrum.* **2011,** *82,* 033702. doi:10.1063/1.3557416
18. Rode, S.; Stark, R.; Lübbe, J.; Tröger, L.; Schütte, J.; Umeda, K.; Kobayashi, K.; Yamada, H.; Kühnle, A. *Rev. Sci. Instrum.* **2011,** *82,* 073703. doi:10.1063/1.3606399
19. Simon, G. H.; Heyde, M.; Rust, H.-P. *Nanotechnology* **2007,** *18,* 255503. doi:10.1088/0957-4484/18/25/255503
20. Lübbe, J.; Temmen, M.; Rahe, P.; Kühnle, A.; Reichling, M. *Beilstein J. Nanotechnol.* **2013,** *4,* 227–233. doi:10.3762/bjnano.4.23
21. Giessibl, F. J. *Phys. Rev. B* **1997,** *56,* 16010–16015. doi:10.1103/PhysRevB.56.16010

22. Gross, L.; Mohn, F.; Moll, N.; Liljeroth, P.; Meyer, G. *Science* **2009,** *325,* 1110–1114. doi:10.1126/science.1176210
23. Fukuma, T.; Onishi, K.; Kobayashi, N.; Matsuki, A.; Asakawa, H. *Nanotechnology* **2012,** *23,* 135706. doi:10.1088/0957-4484/23/13/135706
24. Rahe, P.; Schütte, J.; Schniederberend, W.; Reichling, M.; Abe, M.; Sugimoto, Y.; Kühnle, A. *Rev. Sci. Instrum.* **2011,** *82,* 063704. doi:10.1063/1.3600453
25. Private communication with S. Porthun, RHK Technology Inc., Troy, MI, USA.
26. Shinners, S. M. *Modern Control System Theory and Design,* 2nd ed.; Wiley-Interscience: New York, NY, U.S.A., 1998.
27. Witte, R. A. *Spectrum and Network Measurements;* SciTech Publishing, 2001.
28. Butterworth, S. *Exp. Wireless Wireless Eng.* **1930,** *7,* 536–541.
29. Kauppinen, J.; Partanen, J. *Fourier Transforms in Spectroscopy;* Wiley-VCH: Berlin, Germany, 2001. doi:10.1002/3527600299
30. Valsa, J.; Brančik, L. *Int. J. Numer. Model.: Electron. Networks Devices Fields* **1998,** *11,* 153–166. doi:10.1002/(SICI)1099-1204(199805/06)11:3<153::AID-JNM299>3.0.CO;2-C
31. Giessibl, F. J.; Bielefeldt, H. *Phys. Rev. B* **2000,** *61,* 9968–9971. doi:10.1103/PhysRevB.61.9968
32. Pérez, R.; Štich, I.; Payne, M. C.; Terakura, K. *Phys. Rev. B* **1998,** *58,* 10835–10849. doi:10.1103/PhysRevB.58.10835

License and Terms